Fluorescent and Photocaged Lipids to Probe the Ceramide-Mediated Reorganization of Biological Membranes

By

Daniel Marcelo Carter Ramirez

Thesis submitted to the Faculty of Graduate and Postdoctoral Studies

University of Ottawa

In partial fulfillment of the requirements for the

PhD Degree in the

Ottawa Carleton Chemistry Institute

University of Ottawa

Candidate

Daniel Marcelo Carter Ramirez

Supervisors

Linda J. Johnston

William Ogilvie

Abstract

This thesis describes the development of novel fluorescent and photocaged lipids, and their application as tools to probe the morphological effects of ceramide (Cer)-mediated membrane reorganization in supported lipid bilayers.

Cer is a sphingolipid found in eukaryotic cells that plays a key role in regulating biological processes such as apoptosis, cell-to-cell communication, differentiation and some types of pathogenesis. Sphingolipid and cholesterol-rich lipid rafts in the plasma membrane are thought to be the point of origin for many of this lipid second messenger's effects. Cer is formed in the exoplasmic leaflet of the plasma membrane via the enzymatic hydrolysis of sphingomyelin. The compositional complexity of biological membranes has prompted the adoption of simpler model systems to study the effects of Cer generation. When it is directly incorporated into model membranes, Cer segregates into highly ordered domains with physical properties that are distinct from those of the surrounding fluid environments. However, enzymatic generation of Cer induces complex and dynamic membrane heterogeneity that is difficult to interpret and reconcile with its direct incorporation.

Here I describe the synthesis of 4-nitrobenzo-2-oxa-1,3-diazol-7-yl (NBD)-labelled cholesterol (Chol) and Cer analogs, and their use as probes in model membranes exhibiting liquid-disordered (L_d) and liquid-ordered (L_o) phase coexistence. The Chol probes reproduce the modest enrichment of Chol in L_o membrane domains as well as the Cer-induced displacement of cholesterol. One of the NBD Chol probes is used to

provide direct visualization of Chol redistribution during enzymatic Cer generation, and assists in identifying new features as Cer-rich regions. The NBD-labelled Cer quantifies membrane order using orientational order parameter measurements derived from polarized total internal reflection fluorescence microscopy (pTIRFM) images. The probe reports on changes in membrane order upon enzymatic generation of Cer, and indicates a significant increase in the molecular order of L_d membrane regions that is consistent with the redistribution of Chol into these areas. The probe also identifies *de novo* Cer-rich domains as areas of particularly high molecular order.

In the final project area, 6-Bromo-7-hydroxycoumarin-4-ylmethyl (Bhc)-caged Cers are shown to release Cer rapidly and efficiently upon irradiation with near-visible UV light. The caged lipids are then incorporated into supported membranes and photolyzed to release Cer with a high degree of spatial and temporal control. Controlled Cer generation is then used to drive protein-ganglioside clustering in lipid bilayers.

Acknowledgements

From the perspective of a twenty seven year-old who moved six times before the age of sixteen, six years is a long time to have worked in any one place. Between my fourth-year honours project, four-and-a-half years of research towards my PhD, and the summer in between, that's how long I've had at the NRC building on Sussex Drive. I still can't claim to know all of it's nooks and crannies, but after all the hours I've spent there, it almost feels like a home away from home. Without a doubt this is largely true thanks to the people I've had the privilege of working with there. Their support and encouragement made it easier to be one of the "off-campus" kids- one of the few who would trek to the U of O campus to TA, attend class or grad seminar, and occasionally play hooky for an afternoon.

First and foremost I'd like to thank my supervisors, Linda Johnston and Bill Ogilvie. Linda, you took me in as a last-minute honours student on a recommendation from Tony Durst, and saw me on my way with a PhD and bound for medical school. I will always be grateful for the freedom I enjoyed in setting the course of my projects, never more so than when you agreed to let me spend the best part of a year doing synthesis! You were frequently there for me with sound advice and realistic expectations, and were very indulgent of my often naïve and opinionated remarks in group meeting. Most tellingly, you also instilled in me the importance of conducting research that was reproducible, well-understood, and clearly presented. Bill, you are the reason I made chemistry such a big part of my life. I haven't had, and probably will never have, a teacher who comes close to being as good as you are at making a subject so interesting,

exciting and relevant. In lecture or in the lab, you've always had a knack for understanding your audience, and placing even exceedingly complex concepts within your students' grasp. As my on-campus advocate you also helped me negotiate the tricky waters of graduate seminars, comprehensive exams, and getting this thesis submitted under difficult circumstances.

To my colleagues at the NRC, thank you so much for your support, camaraderie and ever-present goodwill. Zygmunt, in the beginning I understood less than half of what you said, and even now I'm not sure I follow everything you say when we talk about optics or anything else in the realms of physics. You were always there when I had a late night, ready with a killer story or help troubleshooting my experiments and data analysis. Zhengfang, you are the microscopy and specialty fabrication wizard. Whenever I encountered what seemed like an insurmountable problem with an experimental setup or lab apparatus, without fail you were invaluable in engineering a solution. Maohui, keeper of the AFMs, lab quartermaster and soccer star- it's been a pleasure to work with you, and great kicking a ball around on those extended summer lunch breaks.

Captain Kirk, we've been in this grad school adventure together since the start and no one could have made the lab life and downtime quite as interesting as you did. Thanks for keeping the ball rolling when stuff wasn't working, I didn't feel like writing/marking/studying, or I just needed to vent a bit. An, Shan Zou, Jenna, it's been my pleasure to work with all of you, to exchange ideas and share opinions about work and life in general. To my former RISE students, Jack and Spencer, thank you for the

time and effort you put towards the projects we worked on together. I'd like to wish you both the best in your ongoing endeavours in medicine and chemistry respectively.

Robyn, you've been my constant liaison with Bill and the goings-on at the university for as long as you've been in grad school. What is more, you've been a good friend, a great listener, and a hard-working chemist and teacher- may all your dreams come true. Chemistry aside, Skidmore, Bernius and Jen, together with Robyn you've been the core of the Ottawa crew that let me get away from it all when I needed to. Thank you all for being there for me in the good and happy times, but also in the more difficult moments of life beyond the lab.

To my parents, thank you for not judging and always supporting me, for allowing me the freedom to dream, and raising me to be a critical thinker, but to also appreciate kindness and compassion. Your love for me shines through in everything you've done for me, and I feel incredibly proud and fortunate to be your son. To my sister Ally: you've been my rock in some of the hardest times I've gone through in my adult life thus far. Each day I am more in awe of the intelligence, wisdom, charisma and kindness of spirit that you embody. This world needs more people like you.

And last but definitely not least, I'd like to thank my darling Shannon. Our paths crossed late in my grad studies, but you helped me through the roughest, and most introspective part of this journey, when I often felt so alone and completely spent. You've taught me a lot about myself, and I've taken so much pleasure from experiences that we've shared. Here's to the future!

Table of Contents

List of Abbreviations

AFM	atomic force microscopy
Bhc	6-bromo-7-hydroxycoumarin
BLM	black lipid membrane
Bnz	benzoin
Boc	*tert*-butyloxycarbonyl
Bodipy	4,4-difluoro-4-bora-3a,4a-diaza-s-indacene
Bz	benzyl
CCD	charge coupled device
CDI	carbonyldiimidazole
Cer	ceramide
Chc	6-chloro-7-hydroxycoumarin
Chol	cholesterol
CT	charge transfer
Ctx-B	cholera toxin B subunit
DCM	dichloromethane
DCVJ	4-(dicyanovinyl)julolidine
DEACM	7-diethylaminocoumarin
DHPE	1,2-dihexadecanoyl-*sn*-glycero-3-phosphoethanolamine
DiI-C_{20}	1,1'-Dieicosanyl-3,3,3',3'-tetramethylindocarbocyanine perchlorate
DIPEA	*N,N*-diisopropylethylamine
DMAP	4-dimethylaminopyridine

DMF	*N,N*-dimethylformamide
DMPC	1,2-dimyristoyl-*sn*-glycero-3-phosphocholine
DOPC	1,2-dioleoyl-*sn*-glycero-3-phosphocholine
DPH	1,6-diphenyl-1,3,5-hexatriene
DPPC	1,2-dipalmitoyl-*sn*-glycero-3-phosphocholine
EPC	egg phosphatidylcholine
ESM	egg sphingomyelin
ESR	electron spin resonance
EtOAc	ethyl acetate
FCS	fluorescence correlation spectroscopy
FITC	fluorescein isothiocyanate
FRET	Förster/fluorescence resonance energy transfer
FTIR	Fourier transform infrared spectroscopy
GM1	ganglioside GM1
GPI	glycophosphatidylinositol
GPL	glycerophospholipid
GSL	glycosphingolipid
GUV	giant unilamellar vesicle
HCM	7-hydroxycoumarin
HEPES	4-(2-hydroxyethyl)-1-piperazineethanesulfonic acid
HOMO	highest occupied molecular orbital
HPLC	high performance liquid chromatography

I	intensity of fluorescence
L_β	solid-ordered, crystalline or gel phase
L_d	liquid-ordered phase
L_o	liquid-disordered phase
LUMO	lowest unoccupied molecular orbital
LUV	large unilamellar vesicle
MLV	multilamellar vesicle
moc	methoxy carbonate
MOMCl	methoxymethyl chloride, chloromethyl methyl ether
Mops	3-(*N*-morpholino)propanesulfonic acid
MS	mass spectrometry
NA	numerical aperture
NB	2-nitrobenzyl, *ortho*-nitrobenzyl
NBD	4-nitrobenzo-2-oxa-1,3-diazole
NIR	near infrared
nm	nanometer
ns	nanosecond
NMR	nuclear magnetic resonance
NPE	1-(2-nitrophenyl)ethyl
NSOM	near-field scanning optical microscopy
NVOC	4,5-dimethoxy-2-nitrobenzyl
$[P_2]$	orientational order parameter, pTIRM detected

PAINT	points accumulation for imaging in nanoscale topography
PALM	photo-activated localization microscopy
PC	phosphatidylcholine
PE	phosphatidylethanolamine
PG	phosphatidylglycerol
pHP	*para*-hydroxyphenacyl
PI	phosphatidylinositol
PMA	phosphomolybdic acid
POPC	1-palmitoyl-2-oleoyl-*sn*-glycero-3-phosphocholine
PS	phosphatidylserine
pTIRFM	polarized total internal reflection fluorescence microscopy
Q	quencher
R^{FD}	fluorescence detected dichroic ratio
ROI	region of interest
S_0	singlet electronic ground state
S_1	first or lowest energy singlet excited state
S_2	second singlet excited state
SFG	sum frequency generation
SIMS	secondary ion mass spectrometry
SLB	supported lipid bilayer
SM	sphingomyelin
SMase	spingomyelinase

SPR	surface plasmon resonance
STED	stimulated emission depletion
SUV	small unilamellar vesicle
T_1	first or lowest energy triplet excited state
TFA	trifluoroacetic acid
THF	tetrahydrofuran
TIRF	total internal reflection fluorescence
TLC	thin layer chromatography
T_m	phase transition temperature
T_{mix}	miscibility transition temperature
TR	Texas Red
TrCl	trityl chloride
UV-Vis	ultraviolet-visible
WF	wide-field
ε	molar absorption coefficient
θ_c	absorption dipole tilt angle with respect to substrate normal
λ	wavelength
μm	micrometer
τ	lifetime
Φ	quantum yield
Ψ	polarization angle of excitation light

List of Figures

List of Schemes

List of Tables

Chapter 1

Introduction: Ceramide-Mediated Membrane Reorganization

1.1 Lipid Rafts and Ceramide: Their Roles in Cellular Membranes

1.1.1 The Plasma Membrane[1-2]

Biological membranes define the major interfaces found in living organisms by posing a barrier between the interior and exterior of cells, and by demarcating many sub-cellular compartments or organelles. Membranes regulate the exchange of nutrients and metabolites necessary for homeostasis, and maintain concentration gradients of soluble species needed for neurotransmission and cell-to-cell communication. Compartmentalization effected by membranes also results in effective enzyme and substrate localization, which dramatically enhances the rates of catabolic and metabolic processes necessary to support life.

The plasma or cell membrane separates the interior of the cell or cytosol from the external environment or extracellular matrix in the case of a multicellular organism (Figure 1-1).[3] Comprising a hundred or more distinct lipid species, cholesterol, and many more integral and peripheral membrane proteins, the components of the plasma membrane are specific to particular organisms, tissues and cell types. Membrane composition is also highly dynamic, reflecting the evolution of a cell's life cycle and functional needs at a given point in time. Amphiphilic lipids do constitute a ubiquitous and key part of the membrane matrix, however.

1.1.2 Lipids of the Plasma Membrane[4]

Membrane lipids consist of a hydrophilic polar or charged head group and hydrophobic hydrocarbon tails. In aqueous solutions these molecules self-assemble into aggregates wherein the nonpolar moieties are grouped together to reduce their contact area with water molecules. The close packing of the hydrophobic chains is energetically and entropically favoured because these hydrocarbons cannot form hydrogen bonds with water, and therefore are not solvated by

water molecules. Lipid molecules in the plasma membrane are organized as an extended two-dimensional lipid bilayer (Figure 1-1). This structure comprises two leaflets or monolayers of closely packed lipid molecules oriented with the polar head groups facing out, so as to shield the hydrophobic tails from the bulk water.

Figure 1-1. The plasma membrane and its components.[3] Cells are enclosed by a membrane that segregates the intracellular fluid or cytoplasm from the external environment. Although there is a great diversity in the structure, function and distribution of membrane-associated proteins, the phospholipid bilayer is an integral and essential part of all biological membranes.

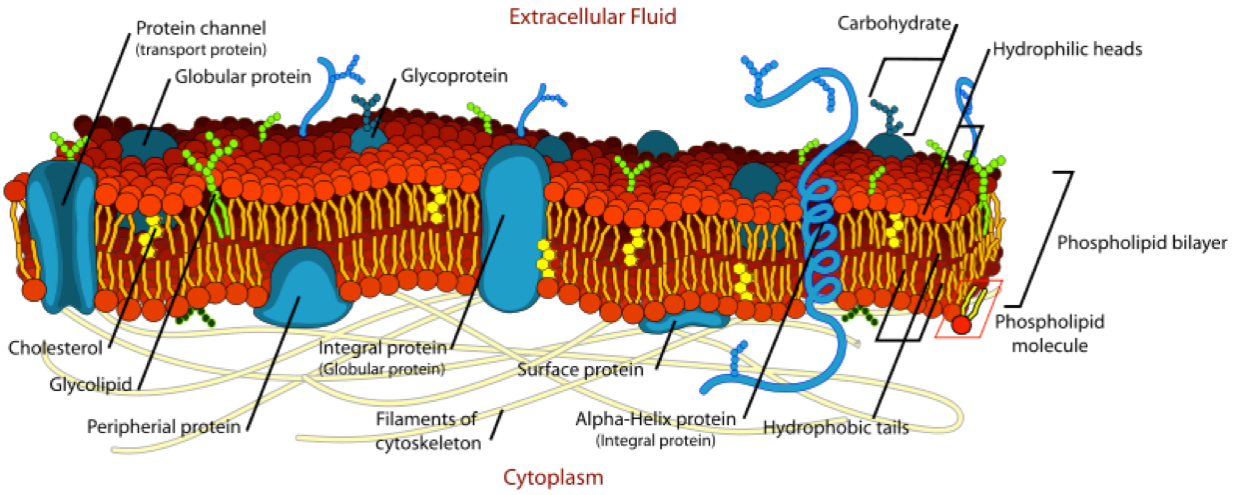

Most lipid molecules in the plasma membrane can be structurally classified as glycerolipids or sphingolipids depending on whether their carbon skeletons are glycerol or sphingosine. Lipids containing phosphate-ester headgroups are broadly categorized as phospholipids, and comprise a significant portion of the plasma membrane lipid population. Figure 1-2 illustrates chemical structures of some of the most commonly occurring phospholipid headgroup moieties. The net charge on the lipid headgroups under physiological conditions (typically pH 7) influences the extent of electrostatic interactions between these molecules and ions, other lipids or proteins in the environment. In glycerophospholipids hydrophobic, long-chain fatty

acids are esterified to the 1- and 2-positions of the glycerol backbone. The head group, consisting of a phosphate and any moieties esterified to it, is attached at the 3-position.

Figure 1-2. Structures of some common membrane glycerophospholipids. (A) Phosphatidylcholine (PC); (B) phosphatidylethanolamine (PE); (C) phosphatidylserine (PS); (D) phosphatidylglycerol (PG); (E) phosphatidylinositol (PI). In most naturally occurring chemical species R_1 is usually a saturated fatty acid, and R_2 an unsaturated fatty acid.

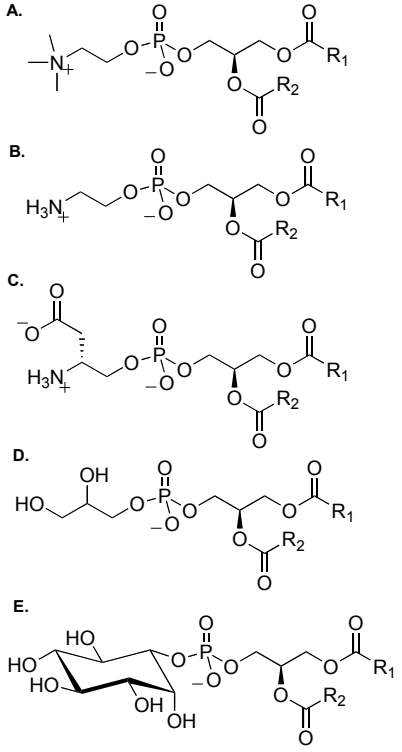

The nature of the fatty acids can greatly affect the chemical and physical properties of these phosphatides and the membranes that contain them. In most naturally occurring membranes glycerol phosphatides have a saturated fatty acid at position 1 and an unsaturated fatty acid at position 2. The most common saturated fatty acids in nature are palmitic acid (16:0) and stearic acid (18:0). Oleic acid, or 18:1 (9), is the most abundant unsaturated fatty acid, although fatty acids with up to four unsaturations are also found in most eukaryotes. Naturally occurring unsaturated fatty acids are almost always in the *cis* configuration, which introduces a bend in the fatty acid chain. This “kink” has important consequences for the structure of biological

membranes, because it disfavours tight packing of lipid molecules and thus induces fluidity and increased lateral mobility.

Figure 1-3. Structures of representative raft-associated lipids: sphingolipids and cholesterol. (A) Ceramide (Cer); (B) sphingomyelin (SM); (C) glucosyl(β) ceramide (cerebroside); (D) cholesterol (Chol); (E) ganglioside GM1. R is typically a long chain (C16 or greater) saturated fatty acid.

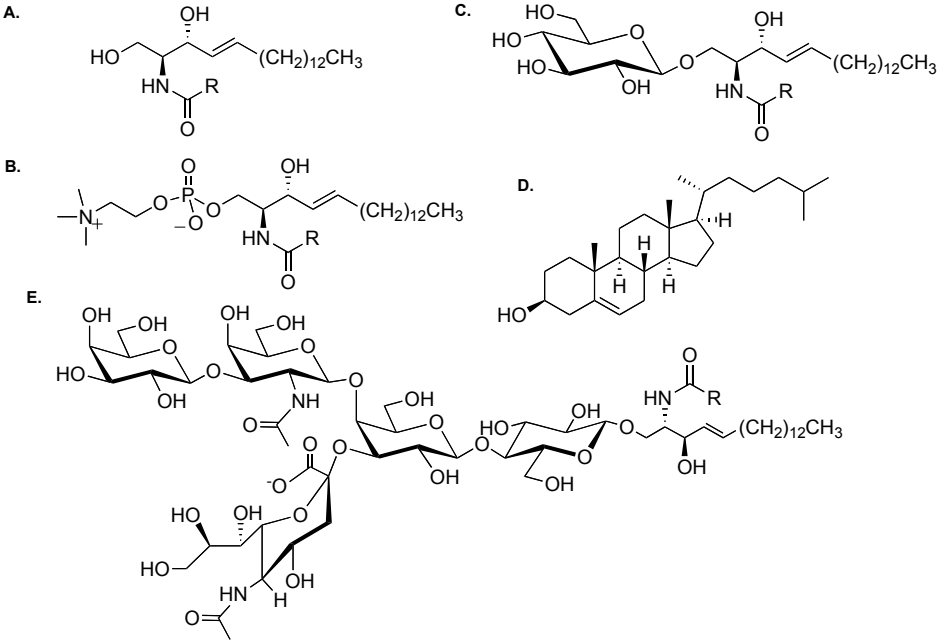

Sphingosine, an 18-carbon amino alcohol, forms the backbone of sphingolipids (Figure 1-3) rather than glycerol. When a fatty acid is joined to the 2-amino group of sphingosine via an amide linkage, the molecule formed is referred to as a ceramide (Cer). Sphingomyelin (SM) is formed by the esterification of phosphorylcholine to the 1-hydroxy group of ceramide. Glycosphingolipids consist of Cer with one or more sugar residues in a β-glycosidic linkage at the 1-hydroxyl moiety. When a single glucose or galactose is bound in this manner the molecule is termed a cerebroside. Gangliosides, a more complex class of sphingolipids, consist of a Cer backbone with three or more sugars esterified, one of which is a sialic acid. In the context of the plasma membrane, cholesterol (Chol) is intrinsically associated with the sphingolipids. The relatively rigid fused ring system of Chol and the weakly polar alcohol group at the C3 position

are critical structural elements in modulating membrane fluidity and compartmentalization-concepts that will be explored in some detail below.

1.1.3 Lipid Rafts and Membrane Compartmentalization

In order to perform the functions cells require, plasma membranes exhibit a high degree of complexity in their lipid and protein composition. These biological membranes must also be able to laterally segregate their constituents to execute and coordinate such functions. The lipid raft hypothesis postulates that these lipid bilayers are not structurally homogeneous and passive solvents for proteins.[5] Rather, preferential association between sphingolipids, Chol and specific proteins confers on cellular membranes the potential for lateral segregation into discrete domains (Figure 1-4).[6] As such, lipid rafts are essentially a nonrandom distribution of constituents geared to organize the many functions of the plasma membrane.[7] Rafts primary role was initially thought to be limited to membrane trafficking. Currently, however, rafts are believed to play a role in the organization of a much broader range of biological membrane activities.[6, 8]

The raft hypothesis was originally developed as an explanation for the enrichment of glycosphingolipids in the apical membrane of polarized epithelial cells.[9] Subsequent studies established that clusters enriched in sphingolipids, Chol, and glycosylphosphatidylinositol (GPI)-anchored proteins tend to be insoluble in Triton X-100, form detergent resistant membrane clusters, and have light buoyant density on sucrose gradients.[10] Seminal biophysical experiments indicated that the size of rafts should be on the order of 50 nm.[11] For several years the raft hypothesis was considered contentious due to the difficulties associated with directly visualizing dynamic processes on such small length scales with existing tools.[8]

Figure 1-4. Lipid rafts: lateral membrane heterogeneity is promoted by preferential interactions between cholesterol, sphingomyelin (SM) and glycosphingolipids (GSL). These fluctuating nanoscale assemblies facilitate localization of raft-associated proteins into discrete functional domains.[6]

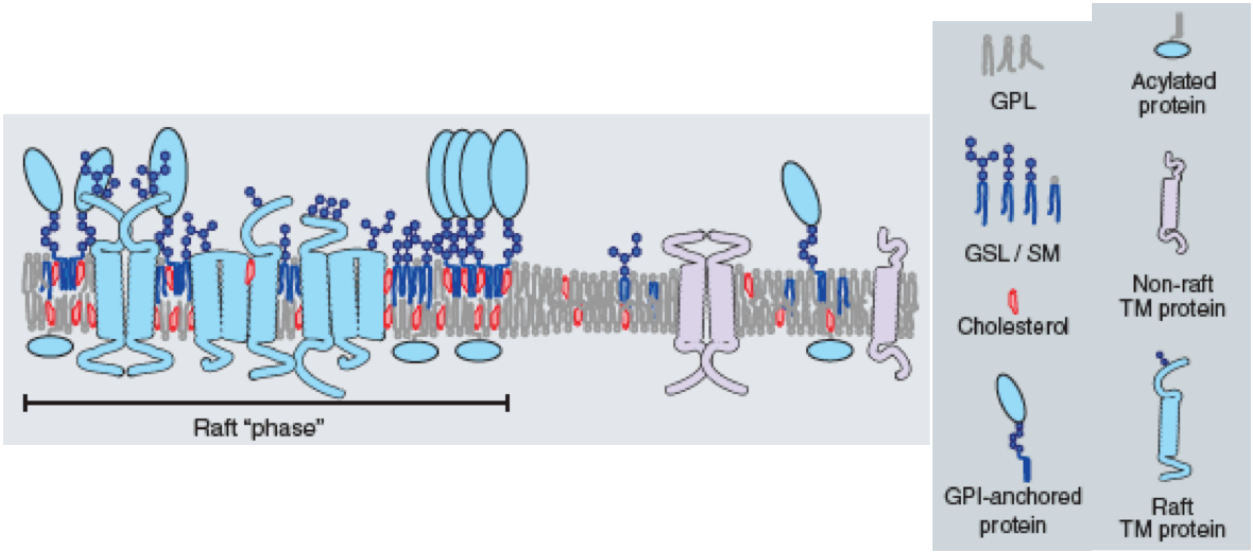

However, support for the raft hypothesis arose from the observation that synthetic membranes composed of sphingolipids and Chol recapture the detergent-resistant characteristics of the "native" clusters.[12-13] This suggested that lateral heterogeneity could occur spontaneously via self-association of the lipid components of a membrane, a fundamental advance on the "fluid mosaic" proposed in Singer and Nicolson's seminal model.[14] More recently, a provisional definition of rafts emerged from the 2006 Keystone Symposium: "Membrane rafts are small (10-200 nm), heterogeneous, highly dynamic, sterol- and sphingolipid-enriched domains that compartmentalize cellular processes. Small rafts can sometimes be stabilized to form larger platforms through protein-protein and protein-lipid interactions."[15] Since then high spatial and temporal resolution fluorescence resonance energy transfer experiments have generated a more conservative size estimate for rafts, with GPI-anchored receptors residing in temporally stable clusters of ~10 nm in diameter.[16]

Liquid phase coexistence observed in vitro has been proposed as the physical principle behind the existence of dynamic liquid-liquid immiscibility, in the form of lipid rafts, in vivo.[17] The discovery of model membrane systems that exhibit phase separation in wholly liquid bilayers[18-19] was thus an important development in the field of membrane biophysics. This lateral segregation is Chol-dependent, in that the flatness of the steroid skeleton favours interactions with the straighter, stiffer hydrocarbon chains of saturated lipids and disfavours interactions with bulkier unsaturated species.[20] Interactions with Chol also force neighbouring fatty acid chains into more extended trans conformations, increasing membrane thickness and driving further segregation via hydrophobic mismatch.[21]

In model membrane systems the cumulative effect of these interactions is physical segregation in the bilayer plane. A thicker or taller liquid-ordered (L_o) phase coexists with a thinner, liquid-disordered (L_d) phase.[22] The physical properties of these two distinct lipid environments can be measured and contrasted in terms of parameters relating to translational order (lateral diffusion) and conformational order (trans/gauche ratio in the acyl chains).[20] Sphingolipids tend to display longer and more saturated hydrocarbon chains than most naturally occurring glycerophospholipids. Consequently, extended hydrophobic interactions between sphingolipid hydrocarbon chains and interactions with Chol are favoured, both of which promote formation of an ordered phase.[23] Moreover, unlike glycerophospholipids, the polar region of sphingosine-derived lipids contains both acceptors and donors of hydrogen bonds, which increase their ability to associate with each other and with Chol.[20]

Phase separation in simple systems at thermodynamic equilibrium cannot be directly equated with membrane domain formation in living cells.[24] Model systems exhibit domains that

can range in size from nanoscale[25-27] to microscale[12-13] depending on the lipid mixture, a fundamental difference with respect to cells. A comparison of lipid packing in vesicles formed from lipids extracted from the plasma membrane versus the plasma membrane itself reveals that lipid domain-forming order is closely regulated by the presence of protein.[28] Thus while preferential lipid-lipid associations do underpin raft clustering in cells, specific lipid-protein interactions that further modify lipid organization also come into play.[6] Ultimately this implies that biological membranes may manifest short- or long-range molecular order on far shorter time and length scales than those observed in model membranes.[8] As such, the terms L_d and L_o are not strictly applicable to cellular membranes, because the parameters that define these phase states cannot be readily measured in vivo.[20] However, model membranes provide a framework for understanding how heterogeneity in cell membranes may arise.[29] They also afford valuable insight into the roles of specific intermolecular forces and interactions between membrane components in achieving functional membrane compartmentalization.

1.1.4 Ceramide: a Biophysical Perspective

In cells Cer can be either synthesized de novo in the endoplasmic reticulum or generated within the plasma membrane from SM through the action of sphingomyelinase (SMase, Figure 1-5 A).[30] Cer was initially identified as a major component of the stratum corneum. In this context the lipid is associated with the formation a hydrophobic barrier that prevents evaporation of water through the skin.[31] More recently Cer has been identified as an important second messenger and is involved in regulating biological processes such as cellular responses to stress stimuli, programmed cell death (apoptosis), some types of pathogenesis, growth and differentiation.[30, 32-33] While it is typically present in low levels, Cer in the plasma membranes of

apoptotic cells can reach levels as high as ~10%.[34] Many of the biological effects attributed to Cer are linked to its ability to modulate the biophysical properties of membranes. Notably, Cer is thought to play a pivotal role in concentrating signalling molecules in ordered lipid raft domains (Figure 1-5 B), thus providing one mechanism for enhancing the efficiency of signal transduction across the plasma membrane.[30, 33]

Figure 1-5. Ceramide (Cer) generation promotes raft coalescence. (A) Hydrolysis of sphingomyelin by sphingomyelinase (SMase) generates Cer in cellular raft domains. (B) Cer aggregation in rafts promotes their coalescence into larger signalling platforms.

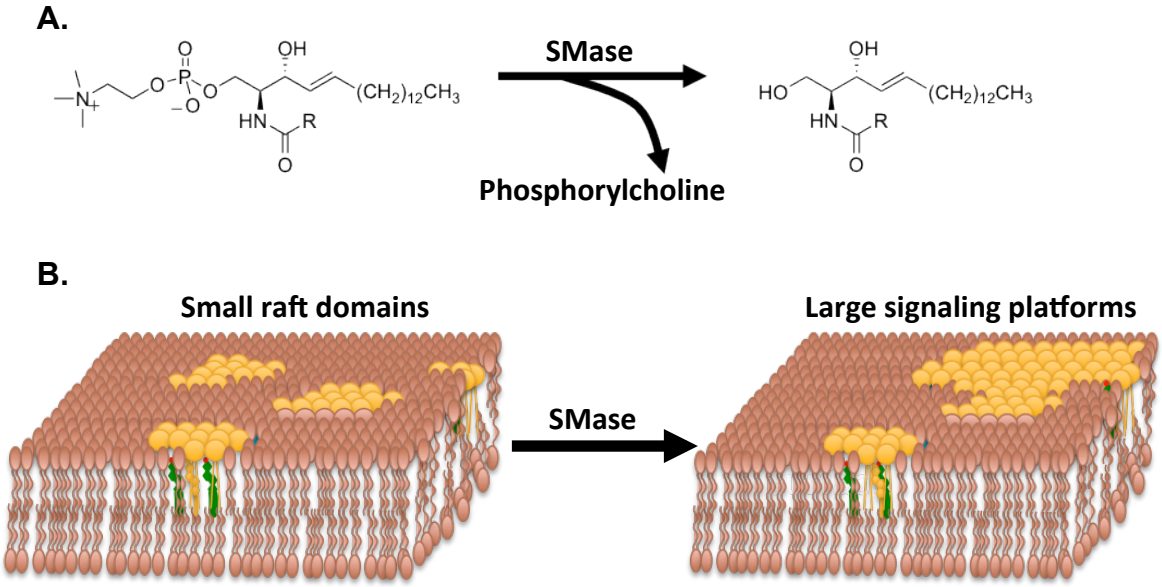

As with other sphingolipids, Cer molecules can form hydrogen bonds that promote lateral segregation to form stable domains in model membranes. Moreover, the low affinity of Cer for Chol, its high degree of hydrophobicity, and its high melting temperature give rise to very tight lipid packing and the formation of domains with solid or gel phase (L_β) character at physiological temperatures.[35-36] Within these domains the lipid molecules form a two-dimensional crystalline array and their lateral diffusion is dramatically reduced relative to liquid lipid phases. Given the lack of clearly elucidated mechanisms behind many of its signalling

functions, the physicochemical properties of Cer suggest that clusters or domains of the lipid could exert these effects by locally altering the mechanical properties of the plasma membrane. Broadly speaking, the effects of Cer generation in cells can be considered in terms of three types of membrane-associated event: 1) domain clustering and protein aggregation, 2) membrane blebbing or vesiculation, and 3) lipid scrambling between membrane leaflets.[37] Work in model lipid bilayers thus aims to provide biophysical data that is useful for understanding the impact of Cer on lateral segregation, and on the mechanical properties of biological membranes. Relevant precedents emerging in this field up until the culmination of the present work are reviewed in section 1.5.

1.2 Biomimetic Model Membrane Formats

Given that cellular membranes are compositionally complex and dynamic entities, it can be difficult to resolve certain aspects of their molecular structure and function *in vivo*. This has stimulated the widespread usage of simplified models of the cell membrane as integral parts of a reductionist approach to understanding membrane-related processes. Currently, these so-called biomimetic membranes are extensively employed to interrogate specific lipid-lipid and lipid-protein interactions, and to investigate the structure and function of membrane proteins. Lipid bilayers are a fundamental component of biomimetic membranes, however, a variety of model formats exist the most prevalent of which are shown in Figure 1-6.[38] The development over time of several distinct model systems has been driven by the requirements of the system under study, and of the analytical, spectroscopic or imaging techniques that experimenters have sought to apply.

1.2.1 Black Lipid Membranes

First prepared in 1962 by "painting" an organic solution of lipids across an aperture in a hydrophobic Teflon scaffold, free-standing lipid membranes are also known as black lipid membranes (BLMs).[39] These models lack interactions with a supporting substrate and so are accessible from either side of the lipid bilayer. Destructive interference of reflected light occurs at the two hydrophobic/hydrophilic interfaces, and accounts for the "black" color that gives these membranes their name. BLMs have been particularly useful for conducting electrochemical measurements on proton pumps,[40] ion channels,[41] and other membrane pores.[42] However, with most methods used to form BLMs residual amounts of organic solvent remain trapped in the hydrophobic core of the membrane. In turn this can disrupt lipid packing, and affect less robust membrane proteins.[43] Another general disadvantage of BLMs is their poor mechanical and temporal stability.[44]

Figure 1-6. Biomimetic membrane formats.[38] (A) A free-standing black lipid membrane (red) spans an aperture in a hydrophobic scaffold (green separating two aqueous compartments. An incorporated transmembrane protein is represented by the white rods. (B) Vesicular membranes separate an internal aqueous compartment (blue) from the external bulk solution. The white squares denote incorporated proteins or other biomolecules of interest. (C) Planar supported membranes can be deposited directly in contact with a solid support.

1.2.2 Vesicular Membranes

While also comprising a bilayer structure, vesicles are spherical particles where the membrane separates an internal aqueous compartment from the bulk solution. The lamellarity

or number of bilayers comprising the vesicular walls can be determined by the method used for their preparation. Vesicles composed of lipids are often termed liposomes, and they can be further categorized in terms of their size with diameters ranging from ~20 nm to 100 μm depending on how they are prepared. Unilamellar vesicles can be broadly classified as small unilamellar vesicles (SUVs) with diameters < 100 nm, large unilamellar vesicles (LUVs) 100 nm – 1 μm, or giant unilamellar vesicles (GUVs) > 1 μm.[45] Ensemble-averaged measurements obtained from SUVs have been used to study reconstituted protein function,[46] and for spectroscopic investigations probing membrane order (as I have done here), hydration, and permeability to various ions and other solutes.[47] They are also employed as precursors for the formation of supported membranes as discussed below (section 1.2.3). Due to their small size SUVs are not generally suitable for optical imaging or single vesicle measurements. In contrast, LUVs and GUVs are large enough to be resolved with a light microscope, and to be tethered, corralled or otherwise manipulated on an individual basis to some extent. As such, GUVs labeled with fluorescent probes have been extensively used to examine lipid phase behaviour[48] and to quantify lateral diffusion in the membrane.[49-50] GUVs have also been applied towards *in vitro* studies of membrane proteins[51] and the assessment of lipid-protein interactions.[52] With lifetimes on the order of days to weeks, vesicles are generally more stable than BLMs. However, due to their high degree of membrane curvature, SUVs are inherently unstable and can spontaneously fuse to form larger vesicles when stored below their phase transition temperature. One drawback of vesicular models is the limited applicability of surface analytical methods to characterize the topology and mechanical properties of these non-planar

membranes. That said, vesicles tethered to or in close interaction with planar supported membranes have been studied using surface sensitive techniques.[53-54]

1.2.3 Planar Supported Membranes

A third type of biomimetic membrane consists of a hydrated, single bilayer film in close association with a planar solid support or substrate, and separated only by an ultrathin (1-2 nm) water layer.[55-56] First developed in the 1980s, common techniques for preparing supported membranes include Langmuir film transfers,[57-59] vesicle spreading,[60-61] and vesicle fusion/deposition.[62-63] The latter method calls for a concentrated suspension of SUVs, which is prepared by the hydration of a dry lipid film followed by either sonication or extrusion. When vesicles are deposited on a hydrophilic support such as freshly cleaved mica, or a hydroxylated silicon or glass slide, they can adsorb and burst to form membrane patches on the planar surface. High lateral mobility allows extended bilayers to form as individual patches fuse together to minimize solvent exposure of the hydrophobic lipid moieties.[64-66] The planar solid support confers additional stability to the membrane structure, but more importantly surface characterization techniques can be readily applied to this membrane format. Atomic force microscopy (AFM), total internal reflection fluorescence microscopy (TIRFM), near-field scanning optical microscopy (NSOM), sum frequency generation spectroscopy (SFG), and surface plasmon resonance spectroscopy (SPR) are among the surface or interfacial methods used to examine supported membranes.[67-73] As models of cellular membranes, supported lipid bilayers (SLBs) have been used by many groups including our own to study lipid phase behaviour, membrane order, mechanical properties, dynamics, probe lipid-protein interactions, and for biosensing applications.[74-78]

One significant limitation of this class of model is that the membrane-substrate distance is often not large enough to prevent strong interactions between incorporated membrane components and the solid surface.[56, 79] Physical coupling between the SLB and the solid support is particularly problematic for investigations involving integral membrane proteins, for which loss of functionality or complete denaturation can occur. This has led to various modifications of the supported membrane format that seek to reduce unfavourable contacts between the support and bilayer by increasing the distance between them while maintaining the mechanical stabilization. Thus, lipid bilayers can be cushioned on polymer or polyelectrolyte films, covalently tethered to the substrate by anchor or spacer groups, or formed on porous supports that create an array of small cavities under the membranes (Figure 1-7).[64, 79-81]

Figure 1-7. Biomimetic supported membrane formats.[38] (A) Cushion-supported biomimetic membranes introduce a polymer cushion (blue) between the solid support (green) and the lipid bilayer (red). The polymer interacts with both non-covalently. (B) Hydrophilic spacers (yellow) can be covalently linked to the support and interact non-covalently with the bilayer, or be covalently attached to lipids or proteins in the membrane. (C) Lipid membranes can also be mounted on a porous support (green) that introduces nanoscale cavities below the membrane to better accommodate transmembrane proteins (white).

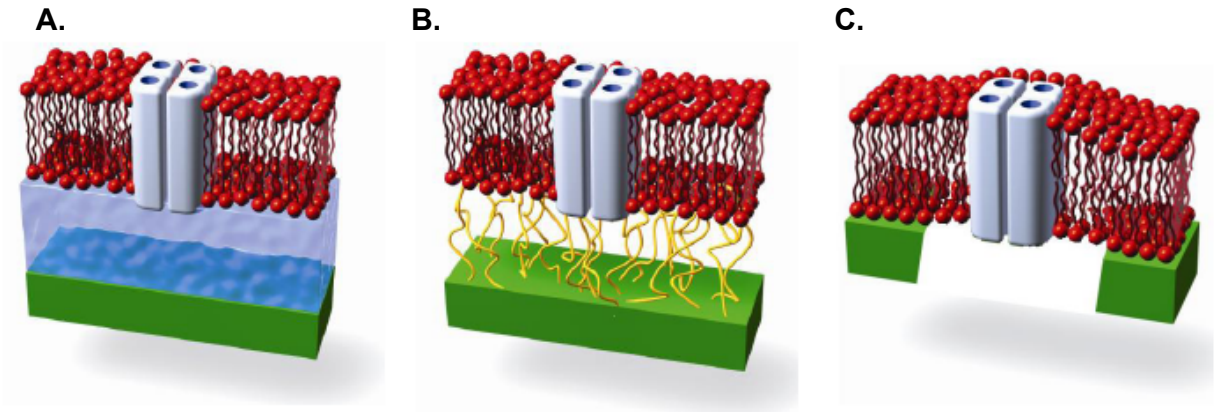

1.2.4 Model Membrane Composition

The lipid composition of a biomimetic or model membrane is usually tailored to meet the requirements of the system being studied. In a biological context possible considerations

include the thickness of the membrane, its net surface charge, polarizability, fluidity and extent of observable phase separation. Membrane stability is also a factor, and can be assessed in terms of tolerance to changes in parameters such as pH, ionic strength, and temperature. Free-standing BLMs can be made from phospholipids and typically also contain residual quantities of a nonpolar solvent such as decane. Vesicular and supported lipid membranes are also largely phospholipid-based, but are more readily formed without organic solvent contaminants.[66]

Models of cellular lipid rafts call for biomimetic membranes that exhibit L_d and L_o phase coexistence at room temperature- i.e. below the miscibility transition temperatures (T_{mix}) of the lipids in the two phases. Several so-called "raft mixtures" of synthetic and/or naturally occurring lipids have been adopted to produce raft-like domains in GUVs and supported lipid bilayers. The synthetic systems typically comprise binary or ternary lipid mixtures of an unsaturated glycerophospholipid, and saturated glycerophospholipid or SM, with the addition of Chol in the ternary mixtures.[48, 82-86] Three commonly used ternary lipid mixtures in model membrane studies are: 1,2-dioleoyl-*sn*-glycero-3-phosphocholine (DOPC, where the phase transition temperature of the pure lipid or T_m = -20 °C),[87] 2-dipalmitoyl-*sn*-glycero-3-phosphocholine (DPPC, T_m = 41 °C),[88] and Chol; 1-palmitoyl-2-oleoyl-*sn*-glycero-3-phosphocholine (POPC, T_m = -2 °C),[89] *N*-palmitoyl-*D-erythro*-sphingomyelin (C16:0 sphingomyelin, C16 SM, T_m = 41.1 °C),[90] and Chol; and DOPC, C16 SM and Chol. Phase diagrams have been constructed for these three mixtures in GUVs using both NMR order parameters and fluorescence microscopy.[86, 91-93] From these diagrams it is possible to predict the molar ratios of the three lipid components for which L_o/L_d phase separation will be observed, and the relative

composition and area coverage of each phase. The conclusions drawn in GUVs from these mixtures regarding phase coexistence regimes are also broadly applicable to SLBs.

Our group has adopted a ternary mixture of DOPC, egg sphingomyelin (ESM) and Chol as our primary model system to study Cer-induced membrane reorganization in SLBs. A naturally occurring sphingomyelin mixture isolated from chicken eggs, the predominant species in ESM is C16 SM (86%, the remainder being long chain saturated lipids).[94] The physicochemical properties of C16, C18 SM and ESM are very similar, and SLBs prepared with ESM or C18 SM in comparable molar fractions have comparable morphologies when imaged by AFM or fluorescence microscopy.[85, 95] In the body of work described here, I have also used the ESM-containing mixture to examine the effects of Cer on SLBs via its enzymatic generation *in situ*, direct incorporation of *N*-palmitoyl-*D-erythro*-sphingosine (C16:0 ceramide, C16 Cer, T_m = 90 °C)[96] into the membranes, and photorelease from caged Cers. The photolytic studies have additionally been extended to binary mixtures of POPC and C16 Cer.

1.2.5 Biomimetic Membrane Formation

Liposomes are commonly formed using the film-hydration method.[97] Lipids are first dissolved in organic solvent and mixed in the required molar ratios. The solvent is then evaporated under a stream of nitrogen or argon gas, and residual solvent is removed using a vacuum pump. Subsequently, the dried lipid film is hydrated with an aqueous solution and agitated or vortexed to form a suspension. Dry lipid films form stacks of liquid crystalline bilayers which, when hydrated, become fluid and swell (Figure 1-8).[98]

Figure 1-8. Mechanism of vesicle formation.[98] Liposomes or lipid vesicles are formed when thin lipid films are hydrated and stacks of crystalline bilayers become fluid and swell. The hydrated lipid sheets detach during agitation and self-close to form large, multilamellar vesicles (MLVs). Once these structures have formed vesicle size and/or lamellarity can be reduced by sonication or mechanical extrusion.

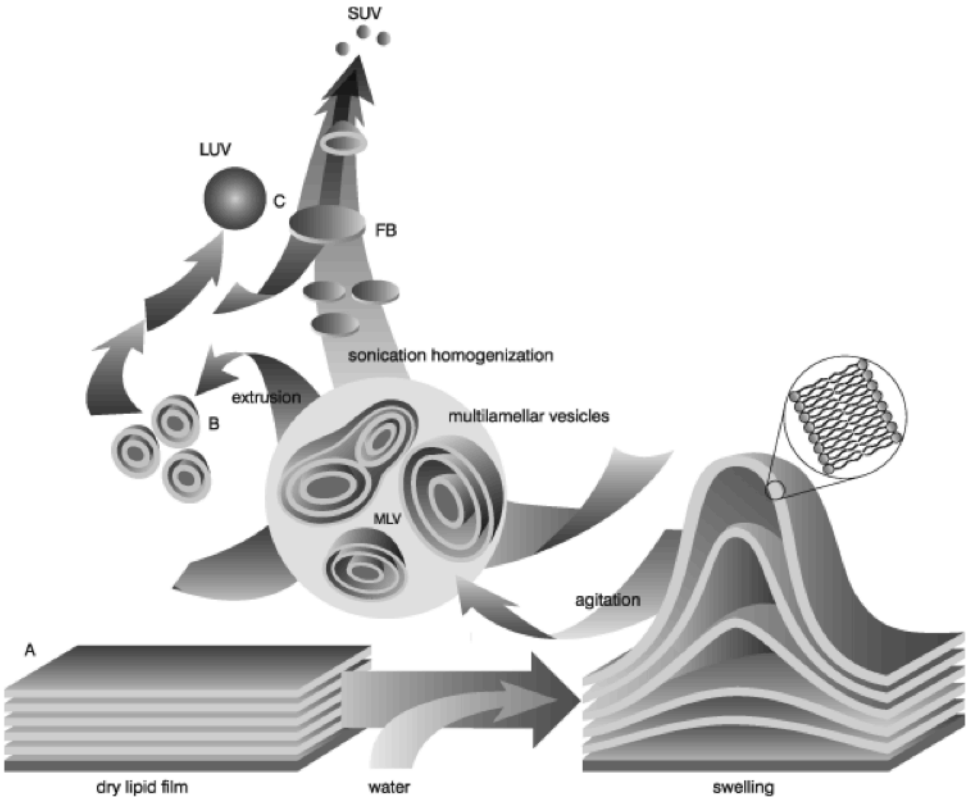

The swollen lipid sheets detach during agitation and spontaneously close in upon themselves to form large, multilamellar vesicles (MLVs) in order to minimize interaction of the hydrophobic core of the lipids at the edges of the sheets with water. Energy must be expended to reduce the size of the MLVs, and this input can take the form of mechanical energy (extrusion) or sonic energy (sonication). Disruption of MLVs with sonication typically gives rise to SUVs with diameters of 15-50 nm. Bath sonicators are commonly used to sonicate MLV solutions. A vial of the vesicle solution is placed in the bath and sonicated to clarity (typically 30-60 min for DOPC/ESM/Chol mixtures) at a temperature exceeding the gel-phase transition temperature of the lipid. The mean size distribution of vesicles produced by sonication varies

between batches, and vesicle populations with compositional heterogeneity can form when using lipid mixtures .

In the extrusion method an MLV solution is placed in an extruder and forced through a polycarbonate membrane with defined pore size. Accordingly, extrusion typically produces LUVs with a diameter similar to the pore diameter used, and good reproducibility is observed from batch to batch.[99] GUVs can be prepared by electroformation.[100] In this approach lipids dissolved in an organic solvent are sprayed onto electrodes, the solvent is removed under a stream of nitrogen, and the electrodes are then immersed in aqueous solution. Applying an alternating current between the electrodes with a potential difference of about 3 volts subsequently forms the GUVs.[101]

SLBs can be made by sequential Langmuir-Blodgett (vertical) and Langmuir-Schaeffer (horizontal) transfers of lipid monolayers from an air-water interface onto a solid support, or by vesicle deposition. The SLB experiments described in the following chapters were conducted using membranes formed by vesicle deposition onto mica in aqueous calcium chloride. Under these conditions, the presence of Ca^{2+} ions in the medium is thought to induce SLB formation by masking the negative net surface charge, and promoting vesicle rupture.[72]

1.3 Fluorescence Techniques in Model Membranes

Fluorescence microscopy and spectroscopy are among the most widely applied tools in the chemical and biological sciences. Perhaps the most attractive aspects of fluorescence are its high sensitivity of detection, up to a single molecule level, and good temporal resolution. Fluorescence techniques can provide information on a wide range of processes including diffusion rates, molecular distances, interactions between solvent molecules and fluorophores,

conformational or orientational changes, and binding interactions. A further advantage is their ability to operate in biological systems of varying complexity, from model membranes up to the level of living cells and tissues. In the context of lipid bilayers fluorophores can report on membrane phase behaviour, order, microviscosity, hydration, and the lateral diffusion of membrane-associated molecules.[47, 102] Fluorescence-based methods can also assess the insertion, folding and function of membrane proteins.[103-105] The investigations presented in the subsequent chapters of this thesis have made extensive use of spectroscopic measurements in SUVs and fluorescence imaging of supported bilayers. Accordingly, I will give a brief overview of fluorescence and the principles behind the techniques I have employed herein.

1.3.1 Molecular Basis of Fluorescence[106-107]

When a substance emits light in a phenomenon broadly termed as luminescence, electrons in an excited state undergo relaxation to a lower energy state through the release of electromagnetic radiation. Luminescence can take the form of fluorescence or phosphorescence depending on the nature of the excited state involved in the process. Fluorescence is the emission arising from a singlet excited state, where an electron in the excited orbital (sometimes referred to as the lowest unoccupied molecular orbital or LUMO) has the opposite spin to a second electron in the ground state orbital (highest occupied molecular orbital or HOMO). Return of the excited state electron to the ground state is spin allowed and occurs rapidly at a rate of about 10^8 s^{-1}. Defined as the average time elapsed between excitation and return to the ground state, the fluorescence lifetime (τ) is therefore on the order of tens of nanoseconds (ns) for most fluorophores.

Jablonski diagrams such as the one shown in Figure 1-9 are used to illustrate the molecular processes occurring between the absorption and emission of light, and the pathways that interconnect distinct electronic states.[108] Ranked according to increasing electronic energy, the ground, first and second singlet electronic states are identified by S_0, S_1, and S_2 respectively. Within each of these electronic energy levels molecules can populate a number of vibrational energy levels which are denoted 0, 1, 2, and so forth. The Franck-Condon principle states that electronic transitions (indicated by the vertical arrows) between these states occur on timescales (~10^{-15} s) far shorter than those on which displacements of atomic nuclei take place.

Figure 1-9. Jablonski energy diagram with approximate time scales for radiative and nonradiative processes. Adapted from the *Olympus Microscopy Resource Center*.[108]

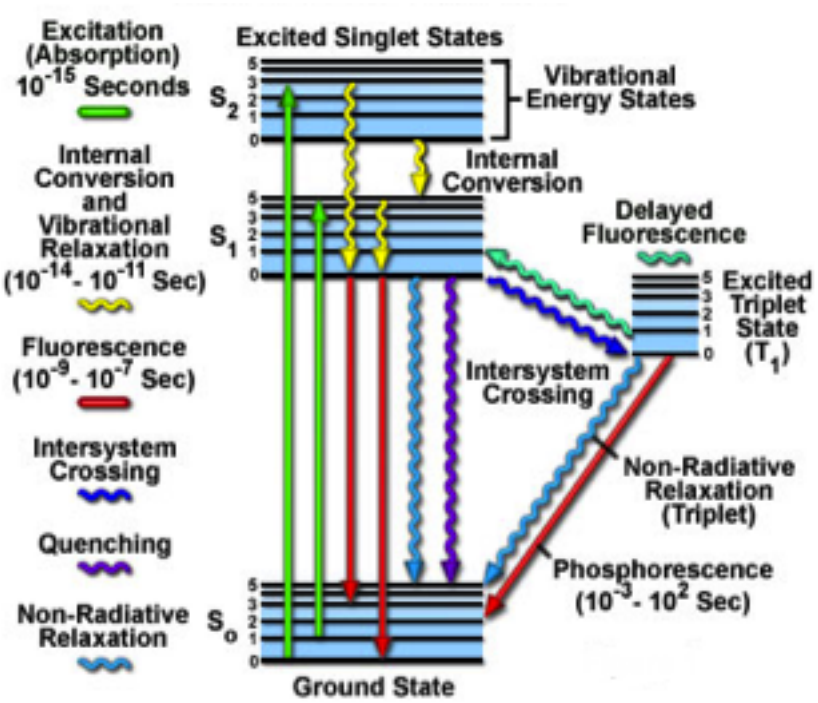

Although absorption and emission of light occur mostly from molecules populating the lowest vibrational energy levels, the energy differences between the various energy levels are apparent in well-resolved examples of absorption and emission spectra (Figure 1-10).[109] When a

fluorophore absorbs light it is usually excited to a higher vibrational energy level of S_1 or S_2. According to the Franck-Condon principle, absorption occurs so quickly that there is no time for molecular motion during the absorption process. In most instances excited molecules in a condensed phase then undergo internal conversion, a rapid ($\leq 10^{-12}$ s) relaxation to the lowest vibrational energy level of S_1, prior to emission from this thermally equilibrated state. Emission is to higher vibrational energy levels of the S_o state, and this accounts for the vibrational structure observed in emission spectra (Figure 1-10).

Figure 1-10. Absorption and emission spectra of perylene in benzene.[109] Perylene is notable as one of relatively few fluorophores that produce spectra with well-resolved bands depicting discrete vibrational energy levels in solution. Figure by MIT OpenCourseWare.

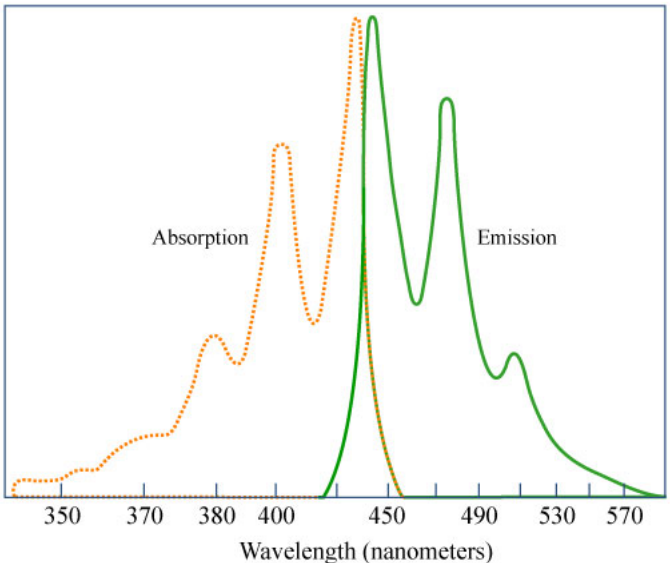

Certain general characteristics apply to most fluorophores. As the Jablonski diagram in Figure 1-9 indicates, the energy of emission is generally less than that of absorption, meaning that fluorescence typically occurs at longer wavelengths than excitation. This decrease in energy, known as the Stokes shift, is observed for all fluorescent molecules in solution. Losses in excitation energy accounting for the shift can occur through thermal processes such as internal conversion, solvent effects, excited-state reactions, complex formation, and energy

transfer. Internal conversion to the lowest vibrational level of S_1 after excitation accounts for another general property of fluorescence formally known as Kasha's rule. The rule states that the same fluorescence emission spectrum is generally observed independent of the excitation wavelength, reflecting a rapid dissipation of excess energy following excitation into higher electronic and vibrational levels. As such, and consistent with the Franck-Condon principle, the fluorescence emission spectrum of a given fluorophore is often a mirror image of the absorption spectrum for its $S_0 \rightarrow S_1$ transition. However, deviations from this mirror symmetry rule can arise from excited-state processes such as proton dissociation, charge-transfer and/or complex formation.

Molecules in the S_1 excited state can also undergo intersystem crossing, or a spin conversion to the first triplet state T_1. Emission from a triplet excited state is termed phosphorescence, and it is usually observed at longer wavelengths and hence lower energies than fluorescence. In this type of process, transition of the electron in the excited orbital to the ground state is spin forbidden, as it has the same spin as the electron already present in the ground state orbital. Consequently, emission rates from triplet states are slow, normally ranging from 10^3 to 10^0 s^{-1}, with corresponding lifetimes in the ms to s range. Molecules containing heavy atoms such as bromine and iodine, and other structural elements that facilitate intersystem crossing by diminishing the $S_1 \rightarrow T_1$ energy gap, are frequently phosphorescent.

Several nonradiative pathways compete with fluorescence or phosphorescence to deactivate singlet and triplet excited states. They include other photophysical processes such as quenching, energy transfer and solvent interactions, but also photochemical transformations.

The molecular environment occupied by a fluorophore plays a significant role in determining the interplay between competing photophysical processes. As such, changes in the fluorescent properties of a molecule can be exploited to report on the nature of its surroundings. In the sections that follow I have expanded on these photophysical concepts as they relate to my studies involving lipid membranes. However, I have confined my discussion of photochemistry to Chapter 4, where I present the portion of this work involving caged ceramides.

1.3.2 Fluorescence Quantum Yields and Lifetimes[110]

Two of the most important characteristics of a fluorophore are its fluorescence lifetime (τ) and quantum yield (Φ). Through the use of fluorescent membrane probes, changes in these two parameters can provide indirect but nonetheless valuable insights into the physicochemical properties and dynamics of distinct lipidic environments.

Together with a molecule's extinction coefficient or molar absorptivity, the fluorescence quantum yield is the major determinant of emission brightness. Defined as the ratio of photons emitted to the number absorbed, fluorescence quantum yield can also be described in terms of the emissive rate constant of the fluorophore (k_{em}), and its rate constant for nonradiative decay to the ground state S_0 (k_{nr}):

$$\Phi = k_{em} / (k_{em} + k_{nr}) \qquad \text{(Equation 1-1)}$$

This expression is simplified in that k_{nr} encompasses all possible nonradiative processes. If the radiationless decay rate is much smaller than the rate of radiative decay, such that $k_{nr} << k_{em}$, the quantum yield can approach unity.

In practice quantum yields of fluorescence can be experimentally determined via the comparative method of Williams *et al.*,[111] as I have done here. This approach involves the use of

well-characterized standard samples with known Φ values. The standard samples should be selected to ensure that they absorb at the excitation wavelength chosen for the test sample, and if possible, emit in a similar region as well. Relative fluorescence quantum yields for the unknown sample (Φ_X) can be calculated with respect to a known standard (Φ_{St}) according to the following relationship:

$$\Phi_X = \Phi_{St} (I_X / I_{St}) (A_{St} / A_X) \quad \text{(Equation 1-2)}$$

Where I_X and I_{St} are the integrated steady-state fluorescence intensities of the sample and standard respectively, and A_X and A_{St} are their corresponding matched absorbances.

The fluorescence lifetime determines the time available for the fluorophore to interact with or diffuse in its environment, and as such dictates the information available from its emission. Defined as the average time the molecule spends in the excited state prior to returning to the ground state, lifetime (τ) can be expressed as follows:

$$\tau = 1 / (\Phi + k_{nr}) \quad \text{(Equation 1-3)}$$

Measured fluorescence lifetimes are ensemble-averaged values of the time spent in the excited state, and so few molecules emit at precisely τ. Even samples containing a single type of fluorophore can display complex intensity decays due to factors such as conformational heterogeneity, fluorophore-solvent interactions, transient quenching effects, and resonance energy transfer. As such, mean or apparent lifetime values are typically defined by mathematical functions that best reflect their distributions: single-exponential, multi-exponential, or non-exponential.

The fluorescence lifetimes reported in this work have been obtained from intensity decays obtained using time-resolved frequency-domain measurements. In this method the sample is

excited with light that is intensity-modulated at a high frequency- comparable to the reciprocal of the anticipated lifetime. This has the effect of modulating the emission intensity at the same frequency. However, the emission exhibits time delays and amplitude changes relative to the excitation, according to the sample's intensity decay law. The time delay between excitation and emission is measured as a phase angle shift (ϕ_ω) where ω is the modulation frequency in radians s^{-1} (Figure 1-11). In the case of a single exponential decay, these two quantities are related to the lifetime by the expression given below:

$$\tan \phi_\omega = \omega\tau \qquad \text{(Equation 1-4)}$$

Figure 1-11. Definitions of the phase angle and modulation of emission for fluorescence lifetime determination by the frequency-domain method. In this example the assumed time decay is 5 ns and the light modulation frequency is 80 MHz. Excitation is traced in green and emission in red. Adapted from *Principles of Fluorescence Spectroscopy*.[110]

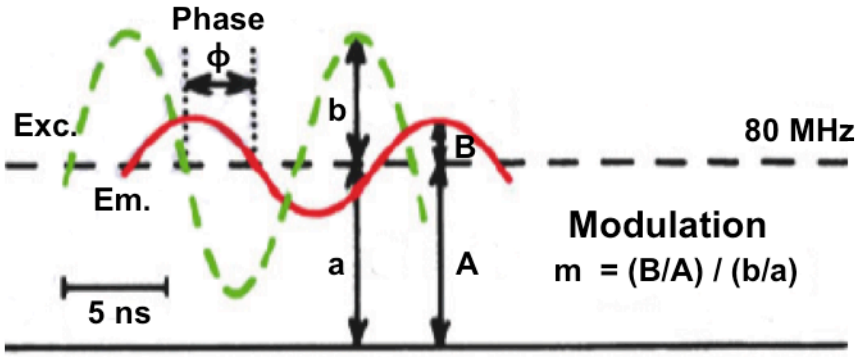

Due to the finite lifetime of the excited state, the emission does not precisely follow the excitation. As such, the peak-to-peak height ratio of the modulated emission is decreased relative to the modulated excitation, and this provides a second independent measure of the lifetime via a frequency dependent modulation factor (m_ω) such that:

$$m_\omega = (1 + \omega^2\tau^2)^{-1/2} \qquad \text{(Equation 1-5)}$$

Frequency-domain data plots typically depict phase angle and/or modulation as functions of the frequency range under examination (Figure 1-12). In the case of multi-exponential decays, these frequency response curves assume a different shape. The form of these intensity decays is determined via a nonlinear least-squares analysis of the frequency response curves.[112-113]

Figure 1-12. Simulated frequency-domain data for a single-exponential decay. The phase angle increases and the modulation decreases with increasing modulation frequency. The data points indicate the simulated data, and the solid lines show the best fits to a single decay time. Adapted from *Principles of Fluorescence Spectroscopy*.[110]

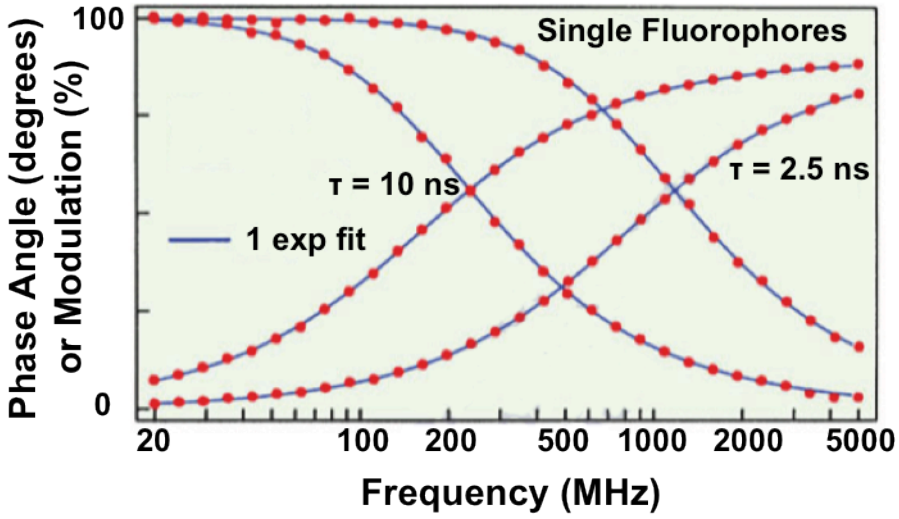

1.3.3 Fluorescence Quenching[114]

Quenching encompasses a range of processes that lead to decreased fluorescence intensity. I have not explicitly examined quenching in this work, other than in a very specific application of fluorescence resonance energy transfer (see section 1.3.4 and Chapter 2). However, it is a broadly significant factor that merits some consideration, because fluorophores in a membrane will interact with other embedded species, in addition to solute and solvent molecules as they experience varying degrees of hydration. Dissolved species such as molecular oxygen, halogens and amines, or polar protic solvents such as water can all act as collisional quenchers of fluorescence.

Collisional quenching occurs when the excited-state fluorophore is deactivated upon contact with some other molecule in solution, which is termed the quencher. The molecules are not chemically altered by the process shown, but the fluorophore is returned to the ground state without emitting a photon. The decrease in intensity arising from collisional quenching is described by the Stern-Volmer equation:

$$F_0 / F = 1 + k_q \tau_0 [Q] \qquad \text{(Equation 1-6)}$$

Where k_q is the bimolecular quenching constant, τ_0 is the unquenched lifetime of the fluorophore, and [Q] is the quencher concentration. The product of k_q and τ_0 is often expressed as *K* the Stern-Volmer quenching constant. In the presence of a soluble quencher, larger values of *K* are expected for a fluorophore situated on the surface of a biomolecule or that is otherwise accessible to the solvent.

At 10 ns in duration, a prototypical singlet excited state is relatively long-lived when compared to the motions of small molecules in aqueous solution. With a diffusion coefficient in water of 2.5 x 10^{-5} $cm^2 s^{-1}$ (at 25 °C) oxygen can diffuse about 7 nm in this time window, a distance which is comparable to the thickness of a lipid bilayer. The effects of quenching on the fluorescence properties of membrane probes can therefore manifest as changes in Φ and τ. For example, increases in vesicular membrane fluidity can increase the exposure of membrane-associated fluorophores to the aqueous milieu, with concomitant increases in collisional quenching with molecules in solution.

Quenching can occur through a variety of other processes and mechanisms, some of which arise from the formation of nonfluorescent complexes of fluorophores and quenchers. This type of process is referred to as static quenching since it does not rely on diffusion or molecular

collisions, and occurs by excitation of a ground state complex. Other absorbing or light scattering species can also attenuate fluorescence via non-molecular mechanisms, and this can be a concern in concentrated solutions of liposomes, particularly if the fluorophores employed are excited at shorter wavelengths (< 400 nm).

1.3.4 Resonance Energy Transfer[115]

Resonance energy transfer (RET) is an excited state process that occurs whenever the emission spectrum of a fluorophore overlaps with the absorption spectrum of a second fluorophore.[116] The two species are referred to as the donor and acceptor respectively, and the aforementioned interaction between them is also commonly termed fluorescence resonance energy transfer (FRET). RET does not involve emission of light by the donor, and the acceptor does not need to be fluorescent. Since RET is not the result of donor emission being absorbed by the acceptor, there is no intermediate photon involved in the process. Rather, the donor and acceptor are coupled by a dipole-dipole interaction.

The extent of energy transfer is determined by the distance separating the donor and acceptor, and by the extent of spectral overlap that exists between them. The Förster distance (R_0) is the distance at which energy transfer occurs with 50 % efficiency. R_0 is dependent on the overlap integral of the donor emission spectrum with the acceptor absorption spectrum, as well as their mutual molecular orientations. The rate of energy transfer $k_T(r)$ is given by:

$$k_T(r) = (1 / \tau_D) (R_0 / r)^6 \qquad \text{(Equation 1-7)}$$

Where r is the distance between the donor (D) and the acceptor, and τ_D is the lifetime of the donor in the absence of energy transfer. Defined in terms of a fixed distance, the efficiency of energy transfer for a single donor-acceptor pair is:

$$E = R_0^6 / (R_0^6 + r^6) \quad \text{(Equation 1-8)}$$

Efficiency can also be defined in terms of τ_D and the fluorescence lifetime of the donor in the presence of an acceptor (τ_D'), or in terms of the measured fluorescence intensities of the donor in the absence (F_D) and presence (F_D') of an acceptor.

$$E = 1 - (\tau_D' / \tau_D) \quad \text{(Equation 1-9)}$$

$$E = 1 - (F_D' / F_D) \quad \text{(Equation 1-10)}$$

Förster distances are typically on the order of 30 to 60 Å, which makes them well suited to report on events occurring on a biomolecular scale, and for use as spectroscopic rulers. As such energy transfer measurements have been used to report on conformational changes in proteins, binding between enzymes and substrates, and nucleic acid hybridization among others. However, the theory differs somewhat according to the specific situation: i.e. donors and acceptors that are free in solution versus covalently linked to macromolecules, contained in a membrane or intercalated with DNA.[115, 117] RET also effectively results in the quenching of donor fluorescence in a manner that is proportional to the proximity and concentration of the acceptor species. In a heterogeneous environment, such as a phase-separated membrane where the distribution of donor and acceptor molecules is not equal, RET can occur with different efficiencies. This property can be exploited in order to enhance fluorescence contrast between the l_d and l_o phases of the membrane, as described in Chapter 2.

1.3.5 Fluorescence Anisotropy[118]

Fluorescence anisotropy measurements can provide information on the rigidity of various molecular environments by reporting on the rotational diffusion of fluorophores. Although I have not conducted fluorescence anisotropy experiments as part of the work described here

the technique has been used for several decades in the membrane biophysics field.[119-121] The rotational rates of membrane-embedded fluorophores occur on a nanosecond timescale, and therefore the associated anisotropy values can be sensitive to membrane composition.

The technique relies on the selective excitation of fluorophore molecules whose absorption transition dipoles are parallel to the electric field vector of polarized light from an excitation source. In an isotropic solution this excitation results in photoselection for a partially oriented population of fluorophores, and thus in partially polarized fluorescence emission – because the light emitted is also polarized along a fixed dipole axis in the fluorophore. The relative angle between these dipole moments determines the maximum measured anisotropy (r_0). When a sample is excited with vertically polarized light, the fluorescence anisotropy is defined by:

$$r = (I_v - I_h) / (I_v + 2I_h) \qquad \text{(Equation 1-11)}$$

Where I_v and I_h are the fluorescence intensities of the vertically and horizontally polarized emission. Fluorophores in fluid solution will typically rotate extensively on a very short timescale (50-100 ps) relative to the excited-state lifetime. Under such conditions fluorescence anisotropies will be near zero, because the orientation of emission will be randomized. When fluorophores are bound to larger molecules such as proteins or membrane-associated lipids, rotational diffusion should decrease. In such a case the anisotropy can be calculated from the Perrin equation:[122]

$$r = r_0 / [1 + (\tau / \theta)] \qquad \text{(Equation 1-12)}$$

Where the anisotropy that would be measured in the absence of rotational diffusion is r_0, and θ is the rotational correlation time for the diffusion process.

Another fluorescence-based, orientation-sensitive method, polarized total internal reflection fluorescence microscopy (pTIRFM) is a surface characterization technique that can be used to indirectly measure membrane order and quantify structural changes. Chapter 4 of this thesis describes the use of pTIRFM on supported model membranes. The principles behind TIR and its application to fluorescence microscopy are discussed below, in section 1.3.8.

1.3.6 Fluorescent Reporters in Lipid Membranes and the Parameters They Probe

Fluorescent probes for biomembranes are designed to investigate structure, dynamics, and molecular interactions by reporting on a range of physical membrane parameters. In order to favour their distribution into lipidic environments, membrane-probing fluorophores are generally intrinsically hydrophobic, conjugated to native lipid scaffolds, or functionalized with long chain alkyl groups. The relative position or location of the fluorophore and its orientation in the membrane influence a given probe's spectroscopic response, and therefore its ability to report on a particular membrane property.[47]

Some fluorophores do not exhibit a significant spectroscopic response to changes in membrane environments, but can nonetheless provide useful information regarding phase behaviour and lateral organization. For example, our group has made extensive use of a sulforhodamine head group-labelled phospholipid, Texas Red DHPE (Figure 1-13 A), as a marker for the L_d phase in supported bilayers exhibiting L_o/L_d phase coexistence.[123-124] In this case the fluorescence contrast between L_d and L_o phases is a good indicator of the probe's relative distribution, because its fluorescence quantum yield and spectral properties do not vary significantly between the two lipid environments.[125] Texas Red and several other dye-labelled lipids incorporate bulky fluorophores that disrupt the intrinsic packing properties of the lipid,

and so may favour preferential partitioning into disordered environments in phase-separated vesicles and supported membranes.[102, 126] However, for a number of probes partitioning between coexisting L_o and L_d phases is highly sensitive to composition, and cannot be reliably predicted on the basis of probe structure alone.[102]

Figure 1-13. A selection of fluorescent probes used in model membrane studies. (A) Texas Red DHPE; (B) diphenylhexatriene (DPH); (C) 4-(dicyanovinyl)julolidine (DCVJ); (D) laurdan; (E) NBD DHPE; (F) Nile Red NR12S; (G) di-4-ANEPPDHQ.

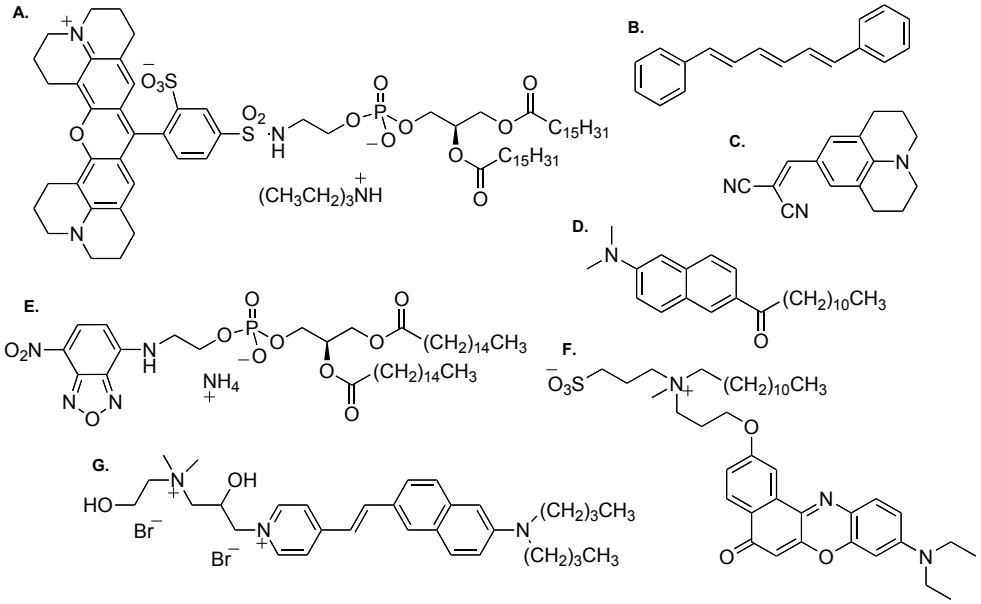

Environment-sensitive membrane probes typically provide information on their molecular environment by changing their fluorescence properties such as absorption or emission maxima, fluorescence intensity or fluorescence lifetime. The interrogated properties may include microviscosity, molecular order, polarity, hydration, environment relaxation and electrostatic potentials. Microviscosity is the reciprocal of fluidity, and it quantifies the frictional resistance encountered by molecules undergoing translational and rotational motions. The rotational motion of rod-shaped probes such as diphenyl hexatriene (DPH, Figure 1-13 B) can be measured by fluorescence anisotropy, and this permits estimation of membrane

microviscosity.[127] Anisotropy also provides a measure of lipid order or packing in the membrane, and so can differentiate between membrane phase states.[47] Environmental viscosity can also be assessed by molecular rotors such as 4-(dicyanovinyl)julolidine (DCVJ, Figure 1-13 C). The environment in which these probes are situated determines the extent of molecular rotation they experience, and can induce diagnostically useful variations in their fluorescence quantum yields.[128]

In solution fluorophores' ground and excited state energies, and their dipole interactions with solvent molecules can be used to characterize and quantify their spectroscopic responses to changes in the polarity of the isotropic environment.[129-130] Lipid bilayers, however, are highly isotropic structures exhibiting polarity gradients that extend on similar length scales to the dimensions of the reporting fluorophores. Polarity sensing on the basis of spectral shifts is more challenging in such an environment. Many membranes also possess ordered charges that create strong local electric fields and dipoles that induce spectroscopic effects similar to those observed in isotropic polar solvents. Therefore, probe responses in lipid membranes are strongly orientation dependent, and cannot be readily calibrated or interpreted using polarity measurements acquired in isotropic solutions.[47]

The depth-dependent distribution and dynamics of water molecules in a lipid bilayer collectively account for the membrane's degree of hydration.[131] The polar phosphate and carbonyl groups of the membrane lipids are solvated by water molecules in an ordered hydrogen bond network. The resulting oriented water dipoles thus contribute to the electric fields present in a bilayer.[132] Water molecules proximal to the reporting fluorophore give rise to wavelength shifts[133] or quenching-based effects[134] on fluorescence lifetime via dipolar and

hydrogen bonding interactions. These can be exploited to sense varying degrees of membrane hydration.

Polarity and hydration in lipid membranes can be assessed using solvatochromic dyes that exhibit shifts in their emission spectra. Examples of such fluorophores are Laurdan, Prodan, NBD, Nile Red and 3-hydroxyflavone derivatives (Figure 1-13 D-F).[133, 135-139] Following electronic excitation of these dyes intramolecular charge transfer (ICT) gives rise to large increases in their dipole moments. The dyes' excitation and emission spectra are shifted by dipole-dipole and hydrogen bonding interactions with their surroundings that increase or reduce the energy of their electronic transitions. Therefore, these dyes exhibit red-shifted emission in response to an increase in solvent polarity and the relaxation rate of their surroundings.

Static electric fields associated with lipid bilayers can be categorized as surface, dipole or transmembrane potentials.[140-141] Surface potential spans the membrane surface and bulk water, and are generated by the charged headgroups of phospholipids and ions adsorbed at the interface. The dipole potential is localized between the membrane surface and the hydrophobic central regions of the membrane, and arises from the ordered lipid dipoles (ester groups and dipolar headgroups) and the associated ordered water molecules. Spanning the entire length of the bilayer, the transmembrane potential arises from the difference in ionic strength on the two sides of the membrane. Electrochromic dyes that also operate by an ICT mechanism can report on electric fields in lipid membranes.[47] When the ground- and excited-state dipoles of naphthylstyryl-piridinium dyes such as di-4-ANEPPDHQ (Figure 1-13 G) interact with an external electric field, they experience electrochromic shifts in their absorption and emission.[142] Excitation spectra are commonly used, however, as shifts in the emission spectra of these

probes are often altered by molecular relaxations.[143] Moreover, with many probes composition- and phase state-dependent hydration effects can be convoluted with membrane electric potentials as the excitation spectra are affected by solvation of the polar ground states.[142-144]

1.3.7 Epi-fluorescence Microscopy[145-146]

Fluorescence microscopy posses features absent in other modes of traditional optical microscopy that have allowed it to become an important tool in the biomedical and materials science fields. Although the spatial resolution of conventional fluorescence microscopes is limited to approximately 200 nm for visible light, detection sensitivity is excellent. The charge coupled device (CCD) cameras that are now in widespread use as detectors on fluorescent microscopes are routinely capable of detecting and localizing single fluorescing molecules and reporting on their dynamics with millisecond temporal resolution. Several distinct molecular targets can be simultaneously tracked or identified with a high degree of specificity through the use of multiple probes with distinct spectral characteristics.

A fluorescence microscope operates by illuminating a sample containing fluorophores with a particular band of wavelengths. The comparatively weak emitted fluorescence is then separated from the excitation light such that only the emitted light reaches the user's eye or the camera detector. Under these conditions the resulting fluorescent structures should appear bright against a very dark background with high contrast. The excitation light is on the order of a million times brighter than the emitted fluorescence, and as such the limits of detection are typically determined by the "darkness" of the background.

Reflected light or episcopic illumination is currently the foremost method in contemporary fluorescence microscopy. The technique is also known as incident light or simply epi-

fluorescence microscopy. In collecting the epi-fluorescence images of supported lipid bilayers presented in this work, I have exclusively used microscopes with an inverted configuration. Figure 1-14 illustrates a schematic diagram for a similar inverted microscope.

Figure 1-14. Cut-away component diagram for an Olympus IX 70 inverted tissue culture microscope. This epifluorescence microscope has a similar configuration and layout to the IX 81 instruments used in data acquisition for this thesis. Adapted from the *Olympus Microscopy Resource Center*.[146]

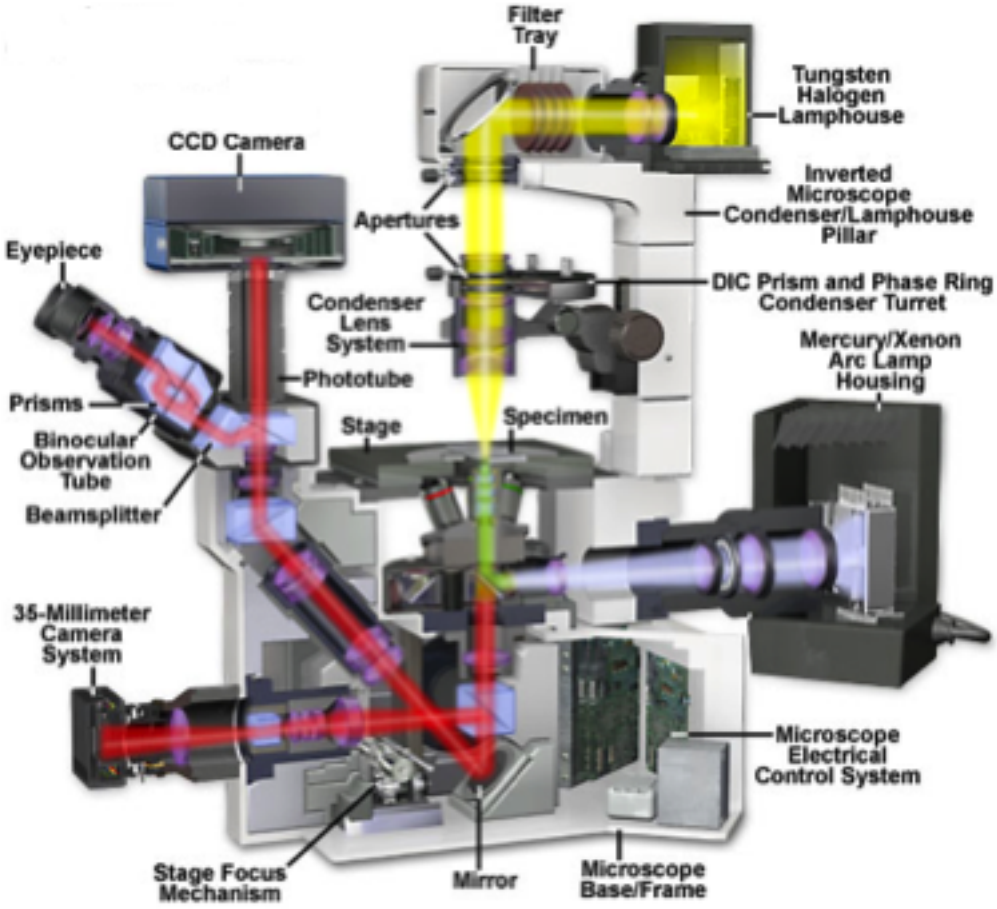

This design operates as a reflected light microscope in which the wavelength of the reflected (emitted) light is longer than that of the excitation. Epi-illuminators typically consist of a mercury or xenon lamp or a laser system stationed in a port at the rear end of the microscope frame. Broad-spectrum fluorescence illumination from this source passes through a collector lens and into a cube containing a wavelength selective excitation filter, a dichromatic (or

dichroic) mirror, and an emission filter. Wavelengths passed by the excitation filter reflect from the surface of the dichroic mirror, and through the microscope objective to the sample. The objective condenses the excitation light to bathe the sample in a cone of illumination whose size and shape is determined by the objective numerical aperture. Secondary fluorescence, emitted by fluorophores in the sample, returns through the objective, dichroic mirror and emission filter, which blocks out the unwanted excitation wavelengths. The filtered light is then routed through the microscope optical train to the detecting CCD device or the oculars.

Epi-fluorescence illumination schemes confer several advantages by using the same objective to condense the excitation light and then capture the emitted fluorescence. As the objective/condenser are a single component proper alignment is readily maintained and so the excitation light passes through the objective with minimal losses to reach the sample. On most instruments the irradiated area is limited to that which is observed through the oculars, which helps to reduce inadvertent fluorophore bleaching. Typically an epi-fluorescence microscope can also readily alternate between or combine reflected light fluorescence and transmitted light observation through the eyepieces with the capture of digital images.

As with most focusing light microscopy techniques, resolution (Δr) in the focal plane is limited by the wavelength of light (λ) and the aperture angle of the lens (α) of the objective:[147]

$$\Delta r = \lambda / (2n \sin \alpha) \qquad \text{(Equation 1-13)}$$

Where n is the refractive index of the medium through which the light is travelling. The quantity $2n \sin \alpha$ also corresponds to the numerical aperture of the objective (NA). The resolution along the optical axis (Δz) is poorer, as is apparent from its dependence on the same parameters:[147]

$$\Delta z = \lambda / (n \sin^2 \alpha) \qquad \text{(Equation 1-14)}$$

In practice, when working at wavelengths > 350 nm, the lateral and axial resolution are limited to about 200 nm and 500 nm respectively.

1.3.8 Total Internal Reflection Fluorescence Microscopy (TIRFM)[148-149]

Our group's interest in total internal reflection fluorescence microscopy (TIRFM) is rooted in its ability to selectively excite fluorophores in very thin sample regions, such as planar supported model membranes. Eliminating fluorescence from outside the focal plane improves the signal-to-background noise ratio, and therefore also the spatial resolution of the features of interest. The technique exploits the properties of an evanescent wave that is formed upon total internal reflection of light at the interface between two media possessing different refractive indices. This evanescent field extends into a limited region of the sample adjacent to the interface that is typically less than 100 nm in depth. Consequently, only fluorophores closest to the interface will be excited upon interaction with the evanescent field (Figure 1-15), and the secondary fluorescence from these molecules can be collected through the microscope objective.

Figure 1-15. Total internal reflection fluorescence microscopy (TIRFM). Only fluorophores closes to the interface will be excited upon interaction with the evanescent field, which is typically less than 100 nm in depth. Adapted from the *Olympus Microscopy Resource Center*.[149]

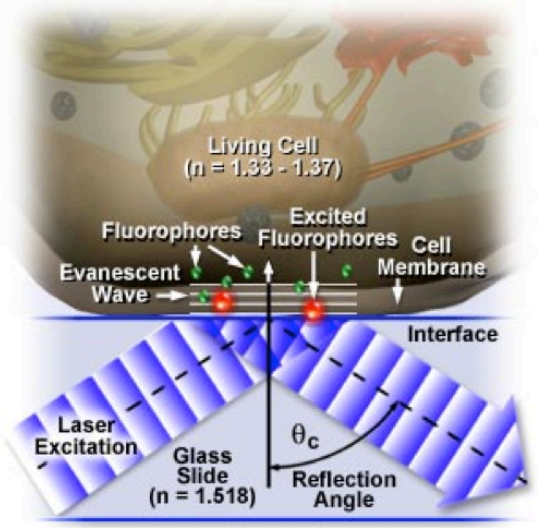

The phenomenon of total internal reflection can be understood in terms of Snell's law, which governs the refractive behaviour of light propagation between media. When light passing through a material with a high refractive index, n_1, encounters a medium with a lower refractive index, n_2, it is refracted or bent. Snell's Law describes how the angle of the incident light beam (θ_1) with respect to the interface normal (z-axis) is related to the refracted beam angle within the lower-index medium (θ_2):

$$n_1 \sin\theta_1 = n_2 \sin\theta_2 \quad \text{(Equation 1-15)}$$

When light strikes the interface joining the two materials at a sufficiently high angle, termed the critical angle (θ_c), it is refracted at 90 degrees relative to the normal ($\sin\theta_2 = 1$), and is thus parallel to the interface. Under these conditions Snell's Law reduces accordingly, such that the two indices of refraction defining the interface can be used to predict θ_c:

$$\sin\theta_c = n_2 / n_1 \quad \text{(Equation 1-16)}$$

At angles exceeding θ_c, the light is reflected entirely back into the first medium. However, total internal reflection does not abruptly originate at the critical angle. Rather, a continuous transition takes place as the angle of incidence increases: from predominant refraction with a small degree of reflection, to total internal reflection at angles greater than θ_c.

Although light no longer propagates into the second medium under TIR conditions, reflected light propagates parallel to the surface, and creates an electromagnetic field in the region of the second medium directly bordering the interface. The range over which this evanescent field can excite fluorophores is limited by the exponential decay of its wave energy in the direction perpendicular to the interface (z-axis, Figure 1-16):

$$E_z = E_0^{(-z/d)} \quad \text{(Equation 1-17)}$$

Where E_z is the energy at perpendicular distance z from the interface, and E_0 is the energy at the interface, and d is the penetration depth of the field. This last quantity is in turn dependent on the wavelength of the incident light (λ_i), the angle of incidence, and the refractive indices of the two media at the interface:

$$d = (\lambda_i/4\pi)\,(n_1^2 \sin^2\theta_1 - n_2^2)^{-1/2} \qquad \text{(Equation 1-18)}$$

Two approaches are used to configure instruments for TIRFM: a prism-based method and an objective lens-based method. I have used the latter approach on an inverted microscope platform to conduct the TIRFM experiments described in the following chapters. In this TIR scheme the objective is employed to introduce coherent laser illumination to the substrate-sample interface. Incidence angles greater than the critical angle are achieved through the use of high numerical aperture objectives (NA 1.45 or higher).

Figure 1-16. Schematic illustration of evanescent wave exponential decay for total internal reflection (TIR) at a glass-water interface. Adapted from *Nikon MicroscopyU*.[148]

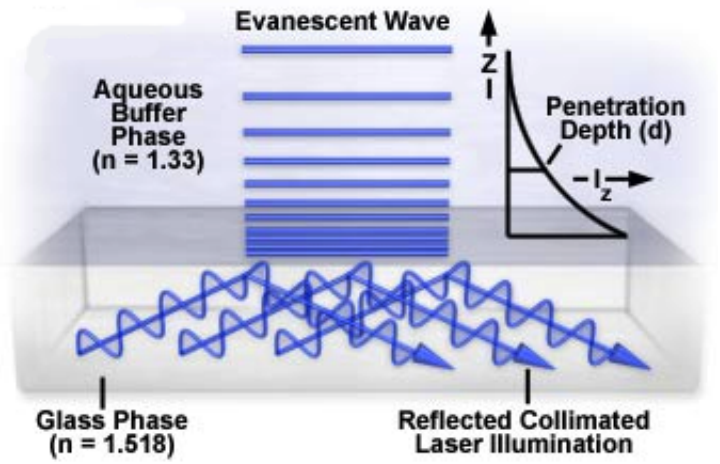

In addition to providing a measure of the light collecting capability of the lens, the numerical aperture of the objective also determines the range of angles at which excitation

light can exit the objective. Accordingly, the achievable range of illumination incidence angles is defined by the objective's NA:

$$NA = n \sin\theta \qquad \text{(Equation 1-19)}$$

Where θ is one-half the objective angular aperture. In order to ensure that light exits the front optical surface of the objective at an angle greater than or equal to θ_c, the coherent laser illumination must first be focused at the periphery of the objective's rear focal plane. Objective-based evanescent field excitation offers more flexibility in terms of sample manipulation than a prism-based approach, although precise control of the incident illumination angle is more difficult to achieve.

1.4 Atomic Force Microscopy (AFM)[150-151]

Throughout this work I have employed atomic force microscopy (AFM) to complement and support my fluorescence microscopy-based studies of supported model membranes. I have used the technique to independently validate the identity of discrete lipid phases and characterize the topology of lateral membrane reorganization that has otherwise been monitored with fluorescent membrane probes. AFM is a scanning probe technique that is able to measure surface topography, mechanical properties and specific probe-sample interactions, all with nanometer resolution. The probe consists of a very finely pointed tip (with a typical width of some 40 nm) attached to a cantilever with a well-defined spring constant. Feedback is provided optically via a laser beam that is directed onto the back face of the scanning tip, and reflected onto a position-sensitive photodiode (Figure 1-17). As the tip is scanned over the sample surface, interactions with features provoke deflections of the cantilever. In turn this gives rise to changes in the position of the laser spot on the photodiode. As the probe raster

scans the entire region of interest, these electronic signals are successively converted into line scans and then entire images by software on the controlling computer.

Figure 1-17. Schematic depiction of atomic force microscopy (AFM) performed on a phase-separated supported lipid bilayer. AFM is a scanning probe technique that is able to image surface topography with nanoscale spatial resolution.

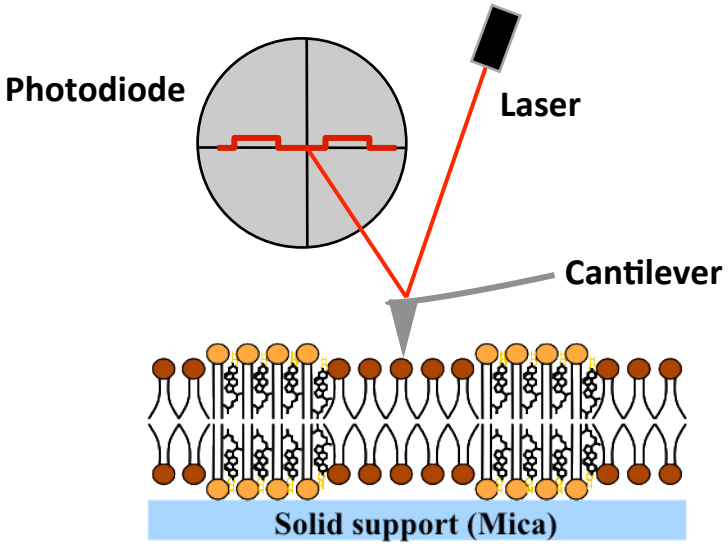

Three basic AFM imaging modes are most commonly applied. In my experiments I have almost exclusively employed contact mode AFM where the tip is scanned over the surface at a constant force setpoint. Comparatively insensitive to environment-related perturbations, this mode is most commonly employed to characterize hard, dry samples. Herein I have routinely used contact mode to image supported bilayers that have been formed on mica in water or buffered aqueous solutions. One limitation that can arise with contact mode imaging is that the tip can alter delicate samples by scratching or otherwise removing material from the imaged surface. Sample damage can be prevented or reduced by decreasing the force that is exerted with the scanning tip.

Non-contact AFM provides an alternative route to imaging delicate samples such as cells. In this mode the cantilever is made to oscillate at a defined frequency that is usually close to its

resonance frequency. The oscillating cantilever is then brought into close proximity with the surface, but without actually making contact. Van-der-Waals and other molecular interactions between the cantilever and sample will dampen its vibration as it is scanned across the surface. Images are subsequently generated by mapping this vibrational damping relative to the lateral position of the cantilever. Although non-contact AFM can generate high resolution images this requires low oscillation amplitudes and very flat sample surfaces. Furthermore, the technique is also particularly susceptible to environmental factors, such as humidity when imaging in air, that interfere with measurements at the lower forces that are typically applied.

Intermittent contact or tapping mode also operates with an oscillating cantilever, but unlike non-contact AFM the tip is brought close enough to the surface to tap the sample as it vibrates. This intermittent contact with the sample has the effect of lowering the cantilever's resonance amplitude, and thus the height of surface features can be determined by mapping amplitude as a function of lateral position. Reduced tip contact reduces the likelihood of damaging the sample while imaging in this mode. Furthermore, the application of larger oscillation amplitudes makes the approach less sensitive to environmental perturbation.

AFM instruments can also be configured to perform force spectroscopy, a method of measuring surface interactions as a function of tip-sample separation, through the generation of force-distance curves.[152] These curves are often recorded by repeatedly approaching and retracting the cantilever at a fixed lateral position. Force-distance curves can quantitatively probe a range of different interactions including capillary, Coulombic, and van der Waals forces, in addition to solvation or hydration effects. In a biological context force-distance

measurements have been used to investigate forces between proteins or DNA strands,[153] and to characterize the thickness and mechanical properties of lipid bilayers.[77]

1.5 Setting the Stage: Ceramide in Model Membranes

1.5.1 Direct Incorporation of Ceramide in Biomimetic Membranes

This section provides an overview of the state of the art in model membrane work with Cer as it pertains to the investigations that I describe in subsequent chapters. I have focused on the lateral phase behaviour of Cer in mixtures that form raft-like domains, some other ternary mixtures, and a few simple lipid systems lacking Chol. I also briefly examine protein sorting in Cer-rich model membrane domains. Lastly, I have revisited previous work on phase-separated supported bilayers involving the use of SMase to generate Cer in situ. I hope to highlight some of the gaps in the contemporary understanding of Cer-mediated membrane reorganization that have prompted our group to develop novel probes and phototriggers.

Ceramides with long *N*-acyl chains typically segregate into lateral domains when mixed with phosphatidylcholines (DMPC or POPC) over a wide range of Cer molar ratios and temperatures.[84, 154-155] As an example, only about 5 mol% C16 Cer is required to form gel domains in POPC bilayers. For Langmuir monolayers formed from mixtures of DMPC with short-chain ceramides (C2 Cer, C6 Cer and C8 Cer) in molar ratios of 2/1, all ceramides are miscible at all surface pressures examined.[156] For the longer chain ceramides domain morphology was dependent on acyl chain length. For C10 Cer, C12 Cer and C14 Cer flower-like gel domains were observed. For even longer ceramides (from C16 Cer to C24:1 Cer) circular domain shapes predominated. In an example that is closer to our group's own work in supported bilayers, Fidorra et al. performed AFM imaging of POPC/C16 Cer bilayers (5/1 molar ratio) and reported

that they exhibit solid flower-like domains within a bulk fluid phase.[157] Furthermore, they showed that in GUVs of POPC/Cer/Chol (5/1 with up to 20 mol% Chol) ceramides form solid domains within a fluid phase. Increasing the Chol content resulted in Chol-driven Cer solubilization, as the solid domains disappeared and a single fluid phase was observed.[158] These data indicate that naturally occurring long chain ceramides form solid domains when present in a fluid matrix at physiologically relevant concentrations, but subject to the relative Chol content.

Direct incorporation of Cer into lipid mixtures that form raft-like domains has been studied in supported bilayer model systems by both AFM and fluorescence microscopy. Schwille's group found that substituting C18 Cer for C18 SM in the ternary mixture of DOPC/C18 SM/Chol (molar ratios of 1/1/1) produced lipid bilayers with three distinct phases when above 8 mol% Cer incoporation.[95] The lowest or thinnest regions were assigned to the DOPC-rich L_d phase, while the domains projecting ~0.8 nm above the bulk corresponded to a SM-rich L_o phase. The highest domains (~1.2 nm above fluid), which were not observed in the absence of Cer or below the 8 mol% threshold, were identified as Cer-rich L_β or solid ordered domains. Our group has observed similar morphological features in supported bilayers of DOPC/ESM/Chol upon direct incorporation of C16 Cer at similar levels (10 mol%, Figure 1-18).[85] The aforementioned investigation by Schwille and coworkers also revealed that the diffusion coefficient associated with the L_d phase decreased as Cer content was increased, which would be consistent with Chol-enrichment of this fluid phase. It was suggested that this effect could arise via selective displacement of Chol from the SM-rich domains with increasing amounts of Cer.[159] The displacement of Chol from L_o domains by Cer may arise from the latter's strong interaction with

SM in PC/SM/Chol mixtures. Further to this, a study exploring the effects of Cer acyl chain length revealed that only long chain ceramides (C16 Cer and C18 Cer) segregate from L_o domains to form Cer-rich domains.[160]

Figure 1-18. AFM images of bilayers of DOPC/ESM/Chol (2/2/1 molar ratios). (A) with no Cer added. (B) 5 mol% Cer. (C) 10 mol % Cer. At this loading taller, gel phase Cer-rich domains can be observed. The total sphingolipid mol% (i.e. ESM + Cer) was constant for all lipid mixtures. Adapted from *Ira and Johnston*.[85]

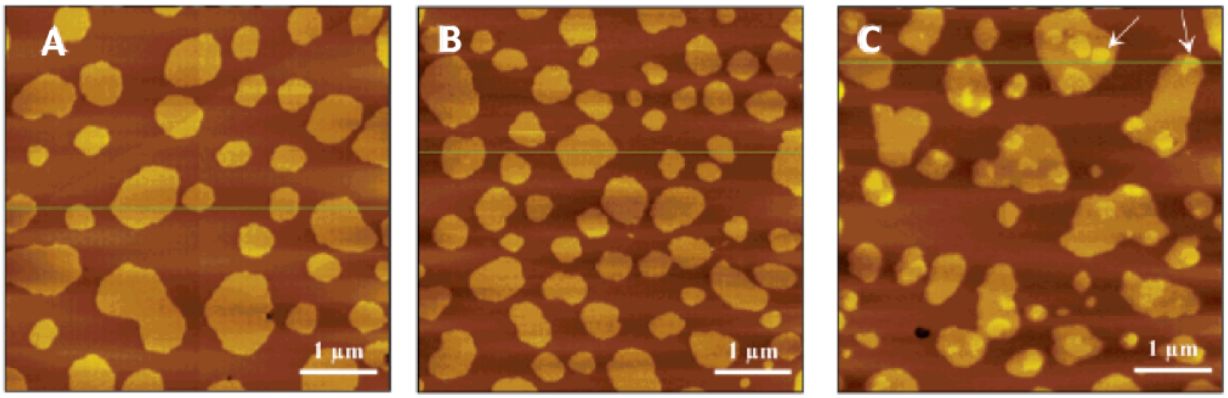

The Schwille group has also combined AFM with confocal microscopy and fluorescence correlation spectroscopy (FCS) to to examine the role of Cer in protein distribution in supported lipid bilayers. Their work showed that the ganglioside GM1-cholera toxin (Ctx-B) complex, which is used as a marker for raft domains in cell and model membranes, partitions into Cer-rich domains.[161] In a second example, GPI-anchored placental alkaline phosphatase (GPI-PLAP) was partially immobilized in Cer-rich domains. Together, these experiments offer support for the suggested role of Cer domains in signal amplification, by acting as loci for the aggregation of raft-associated receptor proteins.[37]

1.5.2 Enzymatic Generation of Ceramide in Sphingomyelin-Containing Membranes

GUVs containing SM and exhibiting coexisting L_o and L_d phases have been treated with SMase to generate Cer.[162-164] In these experiments the enzyme could only access SM in the outer leaflet of the vesicles, which lead to asymmetric Cer generation. The conversion of SM to

Cer in these systems first induced coalescence of L_o domains. As enzymatic activity progressed the boundaries between L_o and L_d phases as defined by fluorescent probe distribution started to undulate, until eventually the probe was homogeneously distributed. Further exposure to SMase produced membrane invaginations and led to vesicle rupture.

Supported bilayers showing L_o and L_d phase coexistence (DOPC/C18 SM/Chol in molar ratios of 1/1/1) were also incubated with SMase from *S. aureus* and imaged by AFM.[95] These samples evolved extensively over the course of the enzymatic treatment. The resulting domain morphology was very distinct from that observed when a comparable amount of Cer was directly incorporated into the initial lipid mixture. The enzymatic conversion of SM led to the formation of a third thicker (taller) Cer-rich phase surrounding the L_o domains, indicating that SMase acted at the phase boundary marking the periphery of the SM-rich domains. Our group undertook similar SMase experiments in bilayers of DOPC/ESM/Chol (2/2/1 molar ratio) which led to the visualization of three distinct membrane topographies: a) larger open areas of the fluid phase with occasional defects, b) areas of L_o domains with Cer-rich perimeters, and c) areas with clusters of these domains surrounded by an intermediate phase (Figure 1-19).[85, 124]

Figure 1-19. AFM images of a bilayer of DOPC/ESM/Chol (2/2/1 molar ratios). (A) Before treatment with SMase two topography levels are observed, consistent with l_d (brown) and l_o (yellow) phases. (B) Following treatment with SMase taller Cer-rich fences surround the domains. (C) A larger area image indicates the presence of an intermediate phase (blue circle) and membrane defects (green). Adapted from *Ira and Johnston*.[85]

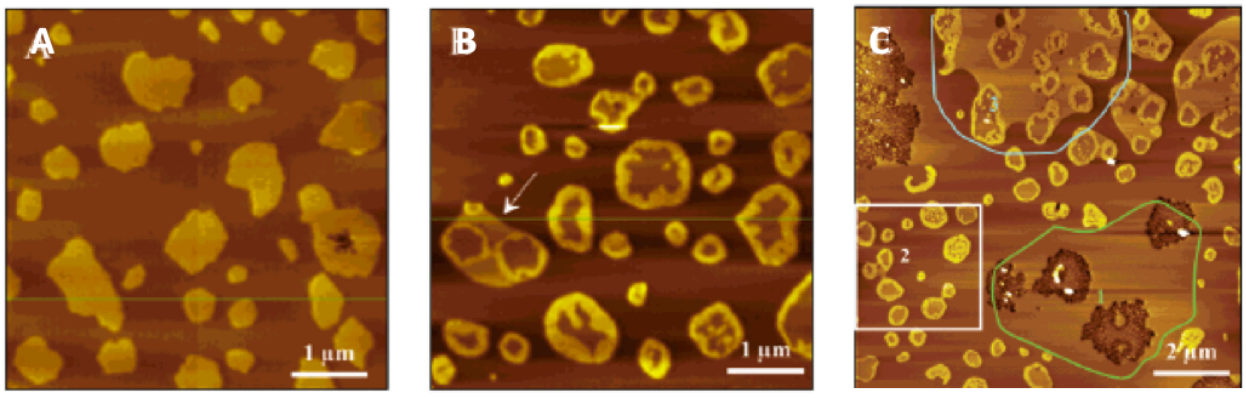

Similar morphological changes were observed with SMase from both *S. aureus* and *B. cereus*, and in both cases enzyme activity seemed to be most pronounced at the interface between L_d and L_o domains. Our group also showed that for bilayers of DOPC/ESM/Chol (5/5/1 molar ratio) exhibiting small nanoscale SM-rich domains SMase activity promoted clustering of existing condensed domains into larger patches.[123] Experiments by Maggio and coworkers using a fluorescently labelled SMase in monolayers support the assessment that its activity is centered on areas enriched in SM, the enzymatic substrate.[165] Another investigation by the same group suggests that lateral segregation of Cer in the membrane occurs after SMase activity disrupts the initial membrane equilibrium by over-saturating the liquid expanded phase with Cer. The rate of Cer production was also shown to be a determinant in the evolution and morphology of Cer-rich domains.[166] The presence of Chol in these membranes appears to enhance enzymatic activity as SM in L_o domains may be more accessible to SMase than SM in the gel domains that would be formed in the absence of Chol.[167-168]

In summation, enzymatic Cer production in model membranes has kinetic and dynamic characteristics that are absent when domains are formed by pre-incorporating Cer into the lipid mixture. These include: a) different domain morphology, b) changes in membrane stability such as the appearance of defects, and c) enzymatic activity that is modulated by the physical state (phase or surface tension) of the membrane.[37, 85] Our group's experience working with SMase in model membranes uncovered several factors that limited our ability to interpret its effects on membrane structure: 1) the difficulty of reconciling data acquired from independent AFM and fluorescence imaging experiments, 2) a lack of fluorescence probes to label L_o phases or reliably model Chol and sphingolipid behaviour, and 3) limited ability to control the temporal and

spatial distribution of SMase activity. The overarching objective of my research has been to design, synthesize and evaluate tools that seek to address these particular limitations.

The first point has been addressed through the implementation of a parallelized or correlated fluorescence-AFM imaging approach which allowed us to image the same region of an enzyme-treated SLB sequentially using both techniques.[124] In Chapter 2 I describe the use of this approach in my characterization of novel fluorescent Chol derivatives. These probes help to address the second point by allowing direct visualization of Cer-rich membrane regions, an improvement over the previously utilized probe, Texas Red DHPE. Chapter 3 introduces a new fluorescent Cer which enabled us to indirectly probe SMase-induced changes in membrane order by monitoring orientational order parameters determined using polarized total internal reflection fluorescence microscopy (pTIRFM). This technique provides some structural information with superior time-resolution to AFM, and without needing to physically interact with the sample. Lastly Chapter 4 presents caged Cer analogs which have allowed us to generate Cer in situ with greater spatial and temporal control than can be achieved via SMase treatments. We have applied this capability towards the photochemically-directed clustering of a ganglioside-protein complex in Cer-rich domains.

1.6 References

1. Karp, G., The structure and function of the plasma membrane. In *Cell and molecular biology*, Third ed.; John Wiley & Sons, Inc.: Hoboken, NJ, 2003; pp 122-158.

2. Garrett, R. H.; Grisham, C. M., Membranes and membrane transport. In *Biochemistry*, Third ed.; Thomson Brooks/Cole: Belmont, CA, 2005; pp 267-290.

3. Hill, M. Cell Membranes and Compartments. http://php.med.unsw.edu.au/cellbiology/index.php?title=Cell_Membranes_and_Compartments.

4. Garrett, R. H.; Grisham, C. M., Lipids. In *Biochemistry*, Third ed.; Thomson Brooks/Cole: Belmont, CA, 2005; pp 247-264.

5. Simons, K.; Ikonen, E., Functional rafts in cell membranes. *Nature* **1997,** *387*, 569-572.

6. Lingwood, D.; Simons, K., Lipid rafts as a membrane-organizing principle. *Science* **2010,** *327*, 46-50.

7. Lingwood, D.; Kaiser, H. J.; Levental, I.; Simons, K., Lipid rafts as functional heterogeneity in cell membranes. *Biochem. Soc. Trans.* **2009,** *37*, 955-960.

8. Jacobson, K.; Mouritsen, O. G.; Anderson, R. G. W., Lipid rafts: at a crossroad between cell biology and physics. *Nat. Cell Biol.* **2007,** *9*, 7-14.

9. Simons, K.; van Meer, G., Lipid sorting in epithelial cells. *Biochemistry* **1988,** *27*, 6197-6202.

10. Brown, D., GPI-anchored proteins and detergent-resistant membrane domains. *Braz. J. Med. Biol. Res.* **1994,** *27*, 309-315.

11. Pralle, A.; Florin, E.-L.; Simons, K.; Horber, J. K. H., Sphingolipid-cholesterol rafts diffuse as small entities in the plasma membranes of mammalian cells. *J. Cell Biol.* **2000,** *148*, 997-1007.

12. Dietrich, C.; Bagatolli, L. A.; Volovyk, Z. N.; Thompson, N. L.; Levi, M.; Jacobson, K.; Gratton, E., Lipid rafts reconstituted in model membranes. *Biophys. J.* **2001,** *80*, 1417-1428.

13. Dietrich, C.; Volovyk, Z. N.; Levi, M.; Thompson, N. L.; Jacobson, K., Partitioning of Thy-1, GM1, and cross-linked phospholipids into lipid rafts reconstituted into supported model membrane monolayers. *Proc. Natl. Acad. Sci. USA* **2001,** *98*, 10642-10647.

14. Singer, S. J.; Nicolson, G. L., The fluid mosaic model of the structure of cell membranes. *Science* **1972,** *175*, 720-731.

15. Pike, L. J., Rafts defined: a report on the Keystone symposium on lipid rafts and cell function. *J. Lipid Res.* **2006,** *47*, 1597-1598.

16. Goswami, D.; Gowrishankar, K.; Bilgrami, S.; Ghosh, S.; Raghupathy, R.; Chadda, R.; Vishwakama, R.; Rao, M.; Mayor, S., Nanoclusters of GPI-anchored proteins are formed by cortical actin-driven activity. *Cell* **2008,** *135*, 1085-1097.

17. Schroeder, R.; London, E.; Brown, D., Interactions between saturated acyl chains confer detergent resistance on lipids and glycosylphosphatidylinositol (GPI)-anchored proteins: GPI-anchored proteins in liposomes and cells show similar behavior. *Proc. Natl. Acad. Sci. USA* **1994,** *91*, 12130-12134.

18. Lentz, B. R.; Barrow, D. A.; Hoechli, M., Cholesterol-phosphatidylcholine interactions in multilamellar vesicles. *Biochemistry* **1980,** *19*, 1943-1954.

19. Ipsen, J. H.; Karlstrom, G.; Mouritsen, O. G.; Wennerstrom, H.; Zuckermann, M. J., Phase equilibria in the phosphatidylcholine-cholesterol system. *Biochim. Biophys. Acta* **1987,** *905*, 162-172.

20. Simons, K.; Vaz, W. L. C., Model systems, lipid rafts, and cell membranes. *Annu. Rev. Biophys. Biomol. Struct.* **2004,** *33*, 269-295.

21. Garcia-Saez, A. J.; Chiantia, S.; Schwille, P., Membrane transport, structure, function and biogenesis. *J. Biol. Chem.* **2007,** *282*, 33537-33544.

22. Veatch, S. L.; Keller, S. L., Miscibility phase diagrams of giant vesicles containing sphingomyelin. *Phys. Rev. Lett.* **2005,** *94*, 148101-148104.

23. Niemela, P. S.; Hyvonen, M. T.; Vattulainen, I., Influence of chain length and unsaturation on sphingomyelin bilayers. *Biophys. J.* **2006,** *90*, 851-863.

24. Munro, S., Lipid rafts. *Cell* **2003,** *115*, 377-388.

25. de Almeida, R. F. M.; Loura, L.; Fedorov, A.; Prieto, M., Lipid rafts have different sizes depending on membrane composition: A time-resolved fluorescence resonance energy transfer study. *J. Mol. Biol.* **2005,** *346*, 1109-1120.

26. Hsueh, Y. W.; Gilbert, K.; Trandum, C.; Zuckermann, M.; Thewalt, J., The effect of ergosterol on dipalmitoylphosphatidylcholine bilayers: a deuterium NMR and calorimetric study. *Biophys. J.* **2005,** *88*, 1799-1808.

27. Veatch, S. L.; Polozov, I. V.; Gawrisch, K.; Keller, S. L., Liquid domains in vesicles investigated by NMR and fluorescence microscopy. *Biophys. J.* **2004,** *86*, 2910-2922.

28. Ge, M.; Gidwani, A.; A.B., B.; Holowka, D.; Baird, B.; Freed, J. H., Ordered and disordered phases coexist in plasma membrane vesicles of RBL-2H3 mast cells. An ESR study. *Biophys. J.* **2003,** *85*, 1278-1288.

29. Feigenson, G. W., Phase diagrams and lipid domains in multicomponent lipid bilayer mixtures. *Biochim. Biophys. Acta* **2009,** *1788*, 47-52.

30. Cremesti, A. E.; Goni, F. M.; Kolesnick, R. N., Role of sphingomyelinase and ceramide in modulating rafts: do biophysical properties determine biologic outcome? *FEBS Lett.* **2002,** *531*, 47-53.

31. Parrott, D. T.; Turner, J. E., Mesophase formation by ceramides and cholesterol: a model for stratum corneum lipid packing? *Biochim. Biophys. Acta* **1993,** *1147*, 273-276.

32. Hannun, Y. A.; Obeid, L. M., Many ceramides. *J. Biol. Chem.* **2011,** *286*, 27855-27862.

33. Bollinger, C. R.; Teichgraber, V.; Gulbins, E., Ceramide-enriched membrane domains. *Biochim. Biophys. Acta* **2005,** *1746*, 284-294.

34. Hannun, Y. A., Functions of ceramide in coordinating cellular responses to stress. *Science* **1996,** *274*, 1855-1859.

35. Goni, F. M.; Alonso, A., Effects of ceramide and other simple sphingolipids on membrane lateral structure. *Biochim. Biophys. Acta* **2009,** *1788*, 169-177.

36. Goni, F. M.; Alonso, A., Effects of ceramide and other simple sphingolipids on membrane lateral structure. *Biochim. Biophys. Acta* **2006,** *1788*, 178-183.

37. Lopez-Montero, I.; Monroy, F.; Velez, M.; Devaux, P. F., Ceramide: From lateral segregation to mechanical stress. *Biochim. Biophys. Acta* **2010,** *1798*, 1348-1356.

38. Ibragimova, S. Supporting and stabilizing biomimetic membranes. Technical University of Denmark (DTU), Lyngby, Denmark, 2011.

39. Mueller, P.; Rudin, D. O.; Ti Tien, H.; Wescott, W. C., Reconstitution of cell membrane structure in vitro and its transformation into an excitable system. *Nature* **1962,** *194*, 979-980.

40. Schmies, G.; Luttenberg, B.; Chizhov, I.; Engelhard, M.; Becker, A.; Bamberg, E., Sensory rhodopsin II from the haloalkaliphilic *natronobacterium pharaonis*: light-activated proton transfer reactions. *Biophys. J.* **2000,** *78*, 967-976.

41. Heimburg, T., Lipid ion channels. *Biophys. Chem.* **2010,** *150*, 2-22.

42. Schulte, A.; Ruamchan, S.; Khunkaewla, P.; Suginta, W., The outer membrane protein VhOmp of *Vibrio harveyi*: pore-forming properties in black lipid membranes. *J. Memb. Biol.* **2009,** *230*, 101-111.

43. Finol-Urdaneta, R. K.; McArthur, J. R.; Juranka, P. F.; French, R. J.; Morris, C. E., Modulation of KvAP unitary conductance and gating by 1-alkanols and other surface active agents. *Biophys. J.* **2010,** *98*, 762-772.

44. Schmitt, E. K.; Vrouenraets, M.; Steinem, C., Channel activity of OmpF monitored in nano-BLMs. *Biophys. J.* **2006,** *91*, 2163-2171.

45. Marsh, D., *Handbook of Lipid Bilayers*. Second ed.; CRC Press: 2012; p 1130.

46. Kalmbach, R.; Chizhov, I.; Schumacher, M. C.; Friedrich, T.; Bamberg, E.; Engelhard, M., Functional cell-free synthesis of a seven helix membrane protein: *in situ* insertion of bacteriorhodopsin into liposomes. *J. Mol. Biol.* **2007,** *371*, 639-648.

47. Demchenko, A. P.; Mely, Y.; Duportail, G.; Klymchenko, A. S., Monitoring biophysical properties of lipid membranes by environment-sensitive fluorescent probes. *Biophys. J.* **2009,** *96*, 3461-70.

48. Veatch, S. L.; Keller, S. L., Seeing spots: complex phase behaviour in simple membranes. *Biochim. Biophys. Acta* **2005,** *1746*, 172-185.

49. Korlach, J.; Schwille, P.; Webb, W. W.; Feigenson, G. W., Characterization of lipid bilayer phases by confocal microscopy and fluorescence correlation spectroscopy. *Proc. Natl. Acad. Sci. USA* **1999,** *96*, 8461-8466.

50. Kahya, N.; Scherfeld, D.; Bacia, K.; Poolman, B.; Schwille, P., Probing lipid mobility of raft-exhibiting model membranes by fluorescence correlation spectroscopy. *J. Biol. Chem.* **2003,** *278*, 28109-28115.

51. Nomura, S. M.; Kondoh, S.; Asayama, W.; Asada, A.; Nishikawa, S.; Akiyoshi, K., Direct preparation of giant proteo-liposomes by *in vitro* membrane protein synthesis. *J. Biotechnol.* **2008,** *133*, 190-195.

52. Sanchez, S. A.; Gratton, E., Lipid-protein interactions revealed by two-photon microscopy and fluorescence correlation spectroscopy. *Acc. Chem. Res.* **2005,** *38*, 469-477.

53. Yoshina-Ishii, C.; Boxer, S. G., Arrays of mobile tethered vesicles on supported lipid bilayers. *J. Am. Chem. Soc.* **2003,** *125*, 3696-3697.

54. Kiessling, V.; Domanska, M. K.; Tamm, L. K., Single SNARE-mediated vesicle fusion observed in vitro by polarized TIRFM. *Biophys. J.* **2010,** *99*, 4047-4055.

55. Sackmann, E., Supported membranes: scientific and practical applications. *Science* **1996,** *271*, 43-48.

56. Tanaka, M.; Sackmann, E., Supported membranes as biofunctional interfaces and smart bionsensor platforms. *Phys. Stat. Sol.* **2006,** *203*, 3452-3462.

57. Blodgett, K. B., Films built by depositing successive monomolecular layers on a solid surface. *J. Am. Chem. Soc.* **1935,** *57*, 1007-1022.

58. Langmuir, I.; Schaefer, V. J., Salted-out protein films. *J. Am. Chem. Soc.* **1938,** *60*, 2803-2810.

59. Wagner, M. L.; Tamm, L. K., Tethered polymer-supported planar lipid bilayers for reconstitution of integral membrane proteins: silane-polyethyleneglycol-lipid as a cushion and covalent linker. *Biophys. J.* **2000,** *79*, 1400-1414.

60. Radler, J.; Strey, H.; Sackmann, E., Phenomenology and kinetics of lipid bilayer spreading on hydrophilic surfaces. *Langmuir* **1995,** *11*, 4539-4548.

61. Dorn, J.; Belegrinou, S.; Kreiter, M.; Sinner, E. K.; Meier, W., Planar block copolymer membranes by vesicle spreading. *Macromol. Biosci.* **2011,** *11*, 514-525.

62. Brian, A. A.; McConnell, H. M., Allogeneic stimulation of cytotoxic T cells by supported planar membranes. *Proc. Natl. Acad. Sci. USA* **1984,** *81*, 6159-6163.

63. Tamm, L. K.; McConnell, H. M., Supported phospholipid bilayers. *Biophys. J.* **1985,** *47*, 105-113.

64. Richter, R. P.; Berat, R.; Brisson, A. R., Formation of solid-supported lipid bilayers: an integrated view. *Langmuir* **2006,** *22*, 3497-3505.

65. Morigaki, K.; Tawa, K., Vesicle fusion studied by surface plasmon resonance and surface plasmon resonance spectroscopy. *Biophys. J.* **2006,** *91*, 1380-1387.

66. Richter, R.; Mukhopadhyay, A.; Brisson, A., Pathways of lipid vesicle deposition on solid surfaces: A combined QCM-D and AFM study. *Biophys. J.* **2003,** *85*, 3035-3047.

67. Shaw, J. E.; Epand, R. F.; Epand, R. M.; Li, Z.; Bittman, R.; Yip, C. M., Correlated fluorescence-atomic force microscopy of membrane domains: structure of fluorescence probes determines lipid localization. *Biophys. J.* **2006,** *90*, 2170-2178.

68. Johnston, L. J., Nanoscale imaging of domains in supported lipid membranes. *Langmuir* **2007,** *23*, 5886-5895.

69. Salamon, Z.; Tollin, G., Surface plasmon resonance studies of complex formation between cytochrome c and bovine cytochrome c oxidase incorporated into a supported planar bilayer. I. Binding of cytochrome c to cardiolipin/phosphatidylcholine membranes in the absence of oxidase. *Biophys. J.* **1996,** *71*, 848-857.

70. Kett, P. J. N.; Casford, M. T. L.; Davies, P. B., Sum frequency generation (SFG) vibrational spectroscopy of planar phosphatidylethanolamine hybrid bilayer membranes under water. *Langmuir* **2010,** *26*, 9710-9719.

71. El Kirat, K.; Morandat, S.; Dufrene, Y. F., Nanoscale analysis of supported lipid bilayers using atomic force microscopy. *Biochim. Biophys. Acta* **2010,** *1798*, 750-765.

72. Goksu, E. I.; Vanegas, J. M.; Blanchette, C. D.; Lin, W.; Longo, M. L., AFM for structure and dynamics of biomembranes. *Biochim. Biophys. Acta* **2009,** *1788* (254-266).

73. Burns, A. R.; Frankel, D. J.; Buranda, T., Local mobility in lipid domains of supported bilayers characterized by atomic force microscopy and fluorescence correlation spectroscopy. *Biophys. J.* **2005,** *89*, 1081-1093.

74. Zhong, J., From simple to complex: investigating the effects of lipid composition and phase on the membrane interactions of biomolecules using in situ atomic force microscopy. *Integr. Biol.* **2011,** *3*, 632-644.

75. Bally, M.; Bailey, K.; Sugihara, K.; Grieshaber, D.; Voros, J.; Stadler, B., Liposome and lipid bilayer arrays towards biosensing applications. *Small* **2010,** *6*, 2481-2497.

76. Garcia-Saez, A. J.; Schwille, P., Surface analysis of membrane dynamics. *Biochim. Biophys. Acta* **2010,** *1798*, 766-776.

77. Garcia-Manyes, S.; Sanz, F., Nanomechanics of lipid bilayers by force spectroscopy with AFM: A perspective. *Biochim. Biophys. Acta* **2010,** *1798*, 741-749.

78. Marsh, D., Cholesterol-induced fluid membrane domains: a compendium of lipid-raft ternary phase diagrams. *Biochim. Biophys. Acta* **2009,** *1788*, 2114-2123.

79. Tanaka, M.; Sackmann, E., Polymer-supported membranes as models of the cell surface. *Nature* **2005,** *437*, 656-663.

80. Kuhner, M.; Tampe, R.; Sackmann, E., Lipid mono- and bilayers supported on polymer films: composite polymer-lipid films on solid substrates *Biophys. J.* **1994,** *67*, 217-226.

81. Simon, A.; Girard-Egrot, A.; Sauter, F.; Pudda, C.; D'Hahan, N. P.; Blum, L.; Chatelain, F.; Fuchs, A., Formation and stability of a suspended biomimetic lipid bilayer on silicon submicrometer-sized pores. *J. Colloid Interf. Sci.* **2007,** *308*, 337-343.

82. Holopainen, J. M.; Angelova, M. I.; Kinnunen, P. K. J., Vectorial budding of vesicles by asymmetrical enzymatic formation of ceramide in giant liposomes. *Biophys. J.* **2000,** *78*, 830-838.

83. Sot, J.; Bagatolli, L. A.; Goni, F. M.; Alonso, A., Detergent-resistant, ceramide-enriched domains in sphingomyelin/ceramide bilayers. *Biophys. J.* **2006,** *90*, 903-914.

84. Silva, L.; De Almeida, R. F. M.; Fedorov, A.; Matos, A. P. A.; Prieto, M., Ceramide-platform formation and -induced biophysical changes in a fluid phospholipid membrane. *Mol. Membr. Biol.* **2006,** *23*, 137-148.

85. Ira; Johnston, L. J., Ceramide promotes restructuring of model raft membranes. *Langmuir* **2006,** *22*, 11284-11289.

86. De Almeida, R. F. M.; Borst, J.; Fedorov, A.; Prieto, M.; Visser, A., Complexity of lipid domains and rafts in giant unilamellar vesicles revealed by combining imaging and microscopic and macroscopic time-resolved fluorescence. *Biophys. J.* **2007,** *93*, 539-553.

87. Avanti Polar Lipids: 18:1 (9-Cis) PC (DOPC); Cas Number: 4235-95-4. http://www.avantilipids.com/index.php?option=com_content&view=article&id=231&Itemid=207&catnumber=850375.

88. Avanti Polar Lipids: 16:0 PC (DPPC); Cas Number: 63-89-8. http://www.avantilipids.com/index.php?option=com_content&view=article&id=216&Itemid=206&catnumber=850355.

89. Avanti Polar Lipids: 16:0-18:1 (9-Cis) PC (POPC); Cas Number: 26853-31-6. http://www.avantilipids.com/index.php?option=com_content&view=article&id=243&Itemid=208&catnumber=850457.

90. Ramstedt, B.; Slotte, J. P., Comparison of the biophysical properties of racemic and *d-erythro-N*-acyl sphingomyelins. *Biophys. J.* **1999,** *77*, 1498-1506.

91. Filippov, A.; Oradd, G.; Lindblom, G., Sphingomyelin structure influences the lateral diffusion and raft formation in lipid bilayers. *Biophys. J.* **2006,** *90*, 2086-2092.

92. Shahedi, V.; Oradd, G.; Lindblom, G., Domain-formation in DOPC/SM bilayers studied by pfg-NMR: Effect of sterol structure. *Biophys. J.* **2006,** *91*, 2501-2507.

93. Veatch, S. L., From small fluctuations to large-scale phase separation: lateral organization in model membranes containing cholesterol. *Semin. Cell Dev. Biol.* **2007,** *18*, 573-582.

94. The predominant species in ESM is *N*-palmitoyl-sphingosylphosphorylcholine (86%), see: *Avanti Polar Lipids*, 2011 Catalog, B 91.

95. Chiantia, S.; Kahya, N.; Ries, J.; Schwille, P., Effects of ceramide in liquid-ordered domains investigated by simultaneous AFM and FCS. *Biophys. J.* **2006,** *90*, 4500-4508.

96. Shah, J.; Atienza, J. M.; Duclos, J., R.I.; Rawlings, A. V.; Dong, Z.; Shipley, G. G., Structural and thermotropic properties of synthetic C16:0 (palmitoyl) ceramide: effect of hydration. *J. Lipid Res.* **1995,** *36*, 1936-1944.

97. Woodle, M. C.; Papahadjopoulos, D., Liposome preparation and size characterizaiton. *Methods Enzymol.* **1989,** *171*, 193-217.

98. Lasic, D. D., *Liposomes in gene delivery*. CRC Press: Boca Raton, FL, 1997; p 295.

99. Kolchens, S.; Ramaswami, V.; Birgenheier, J.; Nett, L.; O'Brien, D. F., Quasi-elastic light scattering determination of size distribution of extruded vesicles. *Chem. Phys. Lipids* **1993,** *65*, 1-10.

100. Angelova, M. I.; Dimitrov, D. S., Liposome electroformation. *Faraday Discuss. Chem. Soc.* **1986,** *81*, 303-311.

101. Lee, J. C. M.; Bermudez, H.; Discher, B. M.; Sheehan, M. A.; Won, Y. Y.; Bates, F. S.; Discher, D. E., Preparation, stability, and in vitro performance of vesicles made with diblock copolymers. *Biotech. Bioeng.* **2001,** *73*, 135-145.

102. Baumgart, T.; Hunt, G.; Farkas, E. R.; Webb, W. W.; Feigenson, G. W., Fluorescence probe partitioning between L_o/L_d phases in lipid membranes. *Biochim. Biophys. Acta* **2007,** *1768*, 2182-2194.

103. Murakoshi, H.; Iino, R.; Kobayashi, T.; Fujiwara, T.; Ohshima, C.; Yoshimura, A.; Kusumi, A., Single-molecule imaging analysis of Ras activation in living cells. *Proc. Natl. Acad. Sci. USA* **2004,** *101*, 7317-7322.

104. Lohse, M. J.; Nuber, S.; Hoffmann, C., Fluorescence/bioluminescence resonance energy transfer techniques to study G-protein-coupled receptor activation and signaling. *Pharmacol. Rev.* **2012,** *64*, 299-336.

105. Bains, G.; Patel, A. B.; Narayanaswami, V., Pyrene: a probe to study protein conformation and conformational changes. *Molecules* **2011,** *16*, 7909-7935.

106. Lakowicz, J. R., Introduction to fluorescence. In *Principles of fluorescence spectroscopy*, Third ed.; Springer Science+Business Media, LLC: New York, NY, 2006; pp 1-25.

107. Turro, N. J.; Ramamurthy, V.; Scaiano, J. C., Chapter 4: Radiative transitions between electronic states. In *Principles of molecular photochemistry, an introduction*, University Science Books: Sausalito, CA, 2009; pp 169-264.

108. Johnson, I. D.; Davidson, M. W. Jablonski energy diagram. http://www.olympusmicro.com/primer/java/jablonski/jabintro/index.html.

109. Manalis, S.; So, P.; Shusteff, M. Emission and absorption spectra for perylene. http://www.flickr.com/photos/mitopencourseware/3681890353/in/set-72157620866436826/.

110. Lakowicz, J. R., Frequency-domain lifetime measurements. In *Principles of fluorescence spectroscopy*, Springer Science+Business Media, LLC: New York, NY, 2006; pp 158-203.

111. Williams, A. T. R.; Winfield, S. A.; Miller, J. N., Relative fluorescence quantum yields using a computer controlled luminescence spectrometer. *Analyst* **1983,** *108*, 1067-1071.

112. Lakowicz, J. R.; Laczko, G.; Cherek, H.; Gratton, E.; Limkeman, M., Analysis of fluorescence decay kinetics from variable-frequency phase shift and modulation data. *Biophys. J.* **1984,** *46*, 463-477.

113. Gratton, E.; Limkeman, M.; Lakowicz, J. R.; Maliwal, B.; Cherek, H.; Laczko, G., Resolution of mixtures of fluorophores using variable-frequency phase and modulation data. *Biophys. J.* **1984,** *46* (479-486).

114. Lakowicz, J. R., Quenching of fluorescence. In *Principles of fluorescence spectroscopy*, Springer Science+Business Media, LLC: New York, NY, 2006; pp 278-300.

115. Lakowicz, J. R., Energy transfer. In *Principles of fluorescence spectroscopy*, Springer Science+Business Media, LLC: New York, NY, 2006; pp 443-468.

116. Förster, T., Intermolecular energy migration and fluorescence. *Ann. Phys. (Leipzig)* **1948,** *2*, 55-75.

117. Stryer, L., Fluorescence energy transfer as a spectroscopic ruler. *Annu. Rev. Biochem.* **1978,** *47*, 819-846.

118. Lakowicz, J. R., Fluorescence anisotropy. In *Principles of fluorescence spectroscopy*, Springer Science+Business Media, LLC: New York, NY, 2006; pp 353-378.

119. Jahnig, F., Structural order of lipids and proteins in membranes: Evaluation of fluorescence anisotropy data. *Proc. Natl. Acad. Sci. USA* **1979,** *76*, 6361-6365.

120. Lakowicz, J. R.; Gryczynski, I.; Kusba, J.; Danielsen, E., Two photon-induced fluorescence intensity and anisotropy decays of diphenylhexatriene in solvents and lipid bilayers. *J. Fluoresc.* **1992,** *2*, 247-258.

121. Stott, B. M.; Vu, M. P.; McLemore, C. O.; Lund, M. S.; Gibbons, E.; Brueseke, T. J.; Wilson-Ashworth, H. A.; Bell, J. D., Use of fluorescence to determine the effects of cholesterol on lipid behavior in sphingomyelin liposomes and erythrocyte membranes. *J. Lipid Res.* **2008,** *49*, 1202-1215.

122. Berberan-Santos, M. N., Pioneering contributions of Jean and Francis Perrin to molecular luminescence. In *New trends in fluorescence spectroscopy: applications to chemical and life sciences*, Valeur, B.; Brochon, J.-C., Eds. Springer: New York, NY, 2001; Vol. 18, pp 7-33.

123. Ira; Johnston, L. J., Sphingomyelinase generation of ceramide promotes clustering of nanoscale domains in supported bilayer membranes. *Biochim. Biophys. Acta* **2008,** *1778*, 185-197.

124. Ira; Zou, S.; Carter Ramirez, D. M.; Vanderlip, S.; Ogilvie, W. W.; Jakubek, Z. J.; Johnston, L. J., Enzymatic generation of ceramide induces membrane restructuring: correlated AFM and fluorescence imaging of supported bilayers. *J. Struct. Biol.* **2009,** *168*, 78-89.

125. Carter Ramirez, D. M.; Ding, J.; Guan, J.; Vobornik, D.; Carnini, A.; Ogilvie, W. W.; Jakubek, Z. J.; Johnston, L. J., A Forster resonance energy transfer (FRET) approach for enhancing fluorescence contrast in phase-separated membranes. *Can. J. Chem.* **2011,** *89*, 423-432.

126. Wustner, D., Fluorescent sterols as tools in membrane biophysics and cell biology. *Chem. Phys. Lipids* **2007,** *146*, 1-25.

127. Lentz, B. R., Membrane 'fluidity' as detected by diphenylhexatriene probes. *Chem. Phys. Lipids* **1989,** *50*, 171-190.

128. Haidekker, M. A.; Theodorakis, E. A., Molecular rotors - fluorescent biosensors for viscosity and flow. *Org. Biomol. Chem.* **2007,** *5*, 1669-1678.

129. Lippert, E. L., Laser-spectroscopic studies of reorientation and other relaxation processes in solution. In *Organic molecular photophysics*, Birks, J. B., Ed. Wiley: New York, NY, 1975; pp 1-31.

130. Reichart, C., Solvatochromic dyes as solvent polarity indicators. *Chem. Rev.* **1994,** *94*, 2319-2358.

131. Disalvo, E. A.; Lairion, F.; Martini, F.; Tymczyszyn, E.; Frias, M.; Almaleck, H.; Gordillo, G. J., Structural and functional properties of hydration and confined water in membrane interfaces. *Biochim. Biophys. Acta* **2008,** *1778*, 2655-2670.

132. Gawrisch, K.; Ruston, D.; Zimmerberg, J.; Parsegian, V. A.; Rand, R. P.; Fuller, N., Membrane dipole potentials, hydration forces, and the ordering of water at membrane surfaces. *Biophys. J.* **1992,** *61*, 1213-1223.

133. Parasassi, T.; Di Stefano, M.; Loiero, M.; Ravagnan, G.; Gratton, E., Cholesterol modifies water concentration and dynamics in phospholipid bilayers: a fluorescence study using Laurdan probe. *Biophys. J.* **1994,** *66*, 763-768.

134. Ho, C.; Slater, S. J.; Stubbs, C. D., Hydration and order in lipid bilayers. *Biochemistry* **1995,** *34*, 6188-6195.

135. Chattopadhyay, A., Chemistry and biology of N-(7-nitrobenz-2-oxa-1,3-diazol-4-yl)-labeled lipids: fluorescent probes of biological and model membranes. *Chem. Phys. Lipids* **1990,** *53*, 1-15.

136. Mazeres, S.; Schram, V.; Tocanne, J. F.; Lopez, A., 7-Nitrobenz-2-oxa-1,3-diazole-4-yl-labeled phospholipids in lipid membranes: differences in fluorecence behaviour. *Biophys. J.* **1996,** *71*, 327-335.

137. Sykora, J.; Kapusta, P.; Fidler, V.; Hof, M., On what time scale does solvent relaxation in phospholipid bilayers happen? *Langmuir* **2002,** *18*, 571-574.

138. Kucherak, O. A.; Oncul, S.; Darwich, Z.; Yushchenko, D. A.; Arntz, Y.; Didier, P.; Mely, Y.; Klymchenko, A. S., Switchable nile red-based probe for cholesterol and lipid order at the outer leaflet of biomembranes. *J. Am. Chem. Soc.* **2010,** *132*, 4907-4916.

139. Oncul, S.; Klymchenko, A. S.; Kucherak, O. A.; Demchenko, A. P.; Martin, S.; Dontenwill, M.; Arntz, Y.; Didier, P.; Duportail, G.; Mely, Y., Liquid ordered phase in cell membranes evidenced by a hydration-sensitive probe: Effects of cholesterol depletion and apoptosis. *Biochim. Biophys. Acta* **2010,** *1798*, 1436-1443.

140. Cevc, G., Membrane electrostatics. *Biochim. Biophys. Acta* **1990,** *1031*, 311-382.

141. Wang, L., Measurements and implications of the membrane dipole potential. *Annu. Rev. Biochem.* **2012,** *81*, 615-35.

142. Jin, L.; Millard, A. C.; Wuskell, J. P.; Dong, X.; Wu, D.; Clark, H. A.; Loew, L. M., Characterization and application of a new optical probe for membrane lipid domains. *Biophys. J.* **2006,** *90*, 2563-2575.

143. Clarke, R. J.; Kane, D. J., Optical detection of membrane potential: avoidance of fluidity and dye-induced effects. *Biochim. Biophys. Acta* **1997,** *1323*, 223-239.

144. Vitha, M. F.; Clarke, R. J., Comparison of excitation and emission ratiometric fluorescence methods for quantifying the membrane dipole potential. *Biochim. Biophys. Acta* **2007,** *1768*, 107-114.

145. Spring, K. R.; Davidson, M. W. Introduction to fluorescence microscopy. http://www.microscopyu.com/articles/fluorescence/fluorescenceintro.html.

146. Abramowitz, M.; Herman, B.; Murphy, D. B.; Davidson, M. W. Anatomy of the fluorescence microscope. http://www.olympusmicro.com/primer/techniques/fluorescence/anatomy/fluoromicroanatomy.html.

147. Born, M.; Wolf, E., *Principles of Optics*. Cambridge University Press: Cambridge, 2002.

148. Ross, S. T.; Schwartz, S.; Fellers, T. J.; Davidson, M. W. Total internal reflection fluorescence (TIRF) microscopy. http://www.microscopyu.com/articles/fluorescence/tirf/tirfintro.html.

149. Axelrod, D.; Davidson, M. W. TIRF: Introduction and theoretical aspects. http://www.olympusmicro.com/primer/techniques/fluorescence/tirf/tirfintro.html.

150. Wiesendanger, R., *Scanning probe microscopy and spectroscopy: methods and applications*. Cambridge University Press: Cambridge, 1994.

151. Jalili, N.; Laxminarayana, K., A review of atomic force microscopy imaging systems: application to molecular metrology and biological sciencea. *Mechatronics* **2004,** *14*, 907-945.

152. Cappella, B.; Dietler, G., Force-distance curves by atomic force microscopy. *Surf. Sci. Rep.* **1999,** *34*, 1-104.

153. Clausen-Schaumann, H.; Seitz, M.; Krautbauer, R.; Gaub, H. E., Force spectroscopy with single bio-molecules. *Curr. Opin. Chem. Biol.* **2000,** *4*, 524-530.

154. Holopainen, J. M.; Lehtonen, J. Y. A.; Kinnunen, P. K. J., Lipid microdomains in dimyristoylphosphatidylcholine-ceramide liposomes. *Chem. Phys. Lipids* **1997,** *88*, 1-13.

155. Holopainen, J. M.; Brockman, H. L.; Brown, R. E.; Kinnunen, P. K. J., Interfacial interactions of ceramide with dimyristoylphosphatidylcholine: impact of the N-acyl chain. *Biophys. J.* **2001,** *80*, 765-775.

156. Kartunnen, M.; Hataja, M. P.; Saily, M.; Vattulainen, I.; Holopainen, J. M., Lipid domain morphologies in phosphatidylcholine-ceramide monolayers. *Langmuir* **2009,** *25*, 4595-4600.

157. Fidorra, M.; Duelund, L.; Leidy, C.; Simonsen, A. C.; Bagatolli, L. A., Absence of fluid-ordered/fluid-disordered phase coexistence in ceramide/POPC mixtures containing cholesterol. *Biophys. J.* **2006,** *90*, 4437-4451.

158. Castro, B. M.; Silva, L. C.; Fedorov, A.; de Almeida, R. F. M.; Prieto, M., Cholesterol-rich fluid membranes solubilize ceramide domains: implications for the structure and dynamics of mammalian intracellular and plasma membranes. *J. Biol. Chem.* **2009,** *284*, 22978-22987.

159. Megha; London, E., Ceramide selectively displaces cholesterol from ordered lipid domains (rafts). *J. Biol. Chem.* **2004,** *279*, 9997-10004.

160. Chiantia, S.; Kahya, N.; Schwille, P., Raft domain reorganization driven by short- and long-chain ceramide: a combined AFM and FCS study. *Langmuir* **2007,** *23*, 7659-7665.

161. Chiantia, S.; Ries, J.; Chwastek, G.; Carrer, D.; Li, Z.; Bittman, R.; Schwille, P., Role of ceramide in membrane protein organization investigated by combined AFM and FCS. *Biochim. Biophys. Acta* **2008,** *1778*, 1356-1364.

162. Staneva, G.; Momchilova, A.; Wolf, C.; Quinn, P. J.; Koumanov, K., Membrane microdomains: role of ceramides in the maintenance of their structure and functions. *Biochim. Biophys. Acta* **2009,** *1788*, 666-675.

163. Taniguchi, Y.; Ohba, T.; Miyata, H.; Ohki, K., Rapid phase change of lipid microdomains in giant vesicles induced by conversion of sphingomyelin to ceramide. *Biochim. Biophys. Acta* **2006,** *1758*, 145-153.

164. Lopez-Montero, I.; Velez, M.; Devaux, P. F., Surface tension induced by sphingomyelin to ceramide conversion in lipid membranes. *Biochim. Biophys. Acta* **2007,** *1768*, 553-561.

165. De Tullio, L.; Maggio, B.; Fanani, M. L., Sphingomyelinase acts by an area-activated mechanism on the liquid-expanded phase of sphingomyelin monolayers. *J. Lipid Res.* **2008,** *49*, 2347-2355.

166. Fanani, M. L.; De Tullio, L.; Hartel, S.; Jara, J.; Maggio, B., Sphingomyelinase-induced domain shape relaxation driven by out-of-equilibrium changes of composition. *Biophys. J.* **2009,** *96*, 67-76.

167. Jungner, M.; Ohvo, H.; Slotte, J. P., Interfacial regulation of bacterial sphingomyelinase activity. *Biochim. Biophys. Acta* **1997,** *1344*, 230-240.

168. Contreras, F. X.; Sot, J.; Ruiz-Arguello, M. B.; Alonso, A.; Goni, F. M., Cholesterol modulation of sphingomyelinase activity at physiological temperatures. *Chem. Phys. Lipids* **2004,** *130*, 127-134.

Chapter 2

Novel Fluorescent Probes for Cholesterol in Supported Membranes

This Chapter Contains Material Adapted from the Following Manuscripts

1. Carter Ramirez, D.M.; Ogilvie, W.W.; Johnston, L.J., NBD-cholesterol probes to track cholesterol distribution in model membranes. *Biochim. Biophys. Acta* **2010**, *1798*, 558-568
2. Carter Ramirez, D.M.; Ding, J.; Guan, J.; Vobornik, D.; Carnini, A.; Ogilvie, W.W.; Jakubek, Z.J.; Johnston, L.J., A Förster resonance energy transfer (FRET) approach for enhancing fluorescence contrast in phase-separated membranes. *Can. J. Chem.* **2011**, *89*, 423-432

2.1 Introduction: Assessing Cholesterol Distribution in Lipid Membranes

2.1.1 Characterizing Membrane Reorganization With a Multi-Modal Imaging Approach

The raft hypothesis postulates that cellular membranes contain discrete regions enriched in sphingomyelin (SM) and cholesterol (Chol).[1-2] These domains, termed lipid rafts, are thought to exist in a liquid-ordered (L_o) phase; as such they have a different composition from the remainder of the lipid bilayer, which is thought to be in a fluid or liquid-disordered (L_d) phase. As introduced in more detail in Chapter 1, lipid rafts are implicated in processes involving membrane protein compartmentalization and lipid sorting such as cell signalling, membrane trafficking and viral infection.[3] It has been proposed that the enzymatic generation of ceramide (Cer) promotes coalescence of small raft domains to give larger platforms, providing a mechanism for organizing signalling molecules to facilitate and amplify signaling.[4-5] Cer is a small hydrophobic sphingolipid that is generated in vivo by sphingomyelinase (SMase) mediated hydrolysis of SM.[4-5] The role of Cer in cell-signalling is well documented and its involvement in apoptosis, differentiation and internalization of viruses and bacteria has been extensively studied.[6-7] Cer also has a pronounced effect on membrane properties, forming gel phase, Cer-rich domains in both cells and model membranes.[5-6, 8]

The inherent difficulties in studying small, dynamic membrane domains in cells have inspired many studies of the partitioning of lipids and proteins between ordered and disordered phases in model membranes.[1, 9-11] This approach has provided valuable information on the factors that lead to membrane compartmentalization and the preference of various biomolecules for specific membrane environments. For example, a variety of studies have shown that direct incorporation of Cer in ternary lipid mixtures with coexisting liquid phases

leads to gel-phase Cer rich domains and to the expulsion of cholesterol from liquid-ordered phases.[12-22] Although the consequences of direct Cer incorporation are reasonably well-understood, enzymatic Cer generation is more complex, even in model membranes.[12, 14, 21, 23-27] Recently, our group has used a combination of atomic force microscopy (AFM) and fluorescence to demonstrate that enzymatic generation of Cer leads to significant membrane restructuring of phase separated lipid bilayers with coexisting L_o and L_d phases.[24-25] These changes include formation of Cer enriched regions in the original L_o domains and the disappearance of some domains with the concomitant formation of new membrane regions that exclude dye and have different thickness and higher lateral adhesion than the initial L_o and L_d phases. The multi-modal imaging approach allowed my predecessor on the project to probe changes on the nanometer scale using AFM and to follow the dynamics of the larger scale bilayer restructuring using fluorescence, providing significant insight into this complex process. Nevertheless, it was not possible to draw definitive conclusions on the composition (Cer-rich vs Chol-rich) of new regions of high lateral adhesion that were generated.[25] Although we considered the possibility of probing Chol distribution with an antibody, the group's previous work had shown that labelling L_o domains with GM1 cholera toxin significantly reduced enzyme-induced membrane restructuring. Thus, we employed an alternate approach using a dye-labelled Chol to evaluate Chol redistribution during enzymatic reaction.

2.1.2 Fluorescent Cholesterol Analogs and Their Use in Model Membrane Studies

Fluorescence microscopy has been widely used to visualize L_o - L_d phase separation for ternary lipid mixtures that model some aspects of membrane raft behaviour but there are few probes that can selectively label ordered Chol and sphingolipid-rich domains.[28-29] As

demonstrated recently by Feigenson and Webb, most fluorescent lipid analogs partition strongly into the L_d phase based on fluorescence microscopy studies in giant unilamellar vesicles (GUVs).[28] The membrane partitioning behaviour of a number of fluorescent Chol derivatives has been examined with three main strategies employed for fluorophore incorporation (Figure 2-1).[30] First, naturally fluorescent sterols such as dehydroergosterol and cholestatrienol (Figure 2-1 B, C) have been shown to mimic Chol in lipid trafficking and in sterol-rich domains in lipid bilayers.[31-32] This approach avoids modification of the hydroxyl group and the alkyl chain, thus minimizing disruption of Chol packing in L_o phases, but has significant limitations due to rapid photobleaching and the requirement for UV excitation.[28, 33] Second, Chol analogs with dyes such as NBD attached to the aliphatic side chain (Figure 2-1 D) have been shown to partition into disordered phases and do not duplicate the membrane condensation effect of native Chol.[28-29, 32] By contrast, attachment of a hydrophobic fluorophore to the aliphatic side chain is more successful since a Bodipy-Chol analog (Figure 2-1 E) was shown to condense phosphatidylcholine (PC) monolayers and support formation of a SM-Chol ordered phase.[34] However, fluorescence microscopy of supported bilayers of DOPC/SM/Chol mixtures indicates that this probe is very sensitive to the bilayer composition, localizing in either ordered (brain SM) or disordered (C16 SM) phases or showing no contrast (C18 SM).[35] Direct measurements of partition coefficients by fluorescence correlation spectroscopy confirm these qualitative conclusions from fluorescence intensity ratios, with K_p (L_o/L_d) of 1.9 and 0.8 for DOPC/egg SM/Chol GUVs and DOPC/C_{18}-SM/Chol supported bilayers.[13, 36] Third, several studies indicate variable results for hydroxyl-labelled Chols. For example, replacement of the 3-hydroxyl with a doxyl spin label did not significantly modify the behaviour

compared to natural Chol based on NMR order parameters,[32] whereas a Bodipy-labelled Chol ester (Figure 2-1 F) partitioned strongly into liquid-disordered domains.[37] The above results demonstrate that the choice and method of attachment of the dye require careful adjustment to design a fluorescent analog that reproduces the behaviour of natural Chol.

Figure 2-1. Structures of (A) cholesterol (Chol) and a selection of fluorescent sterols used in biophysical membrane research. (B) dehydroergosterol; (C) cholestatrienol; (D) 25-NBD-cholesterol; (E) Bodipy-FChol; (F) Bodipy(C_{12})-Chol ester. Adapted from Chem. Phys. Lipids, 2007, *146*, 1-25.[30]

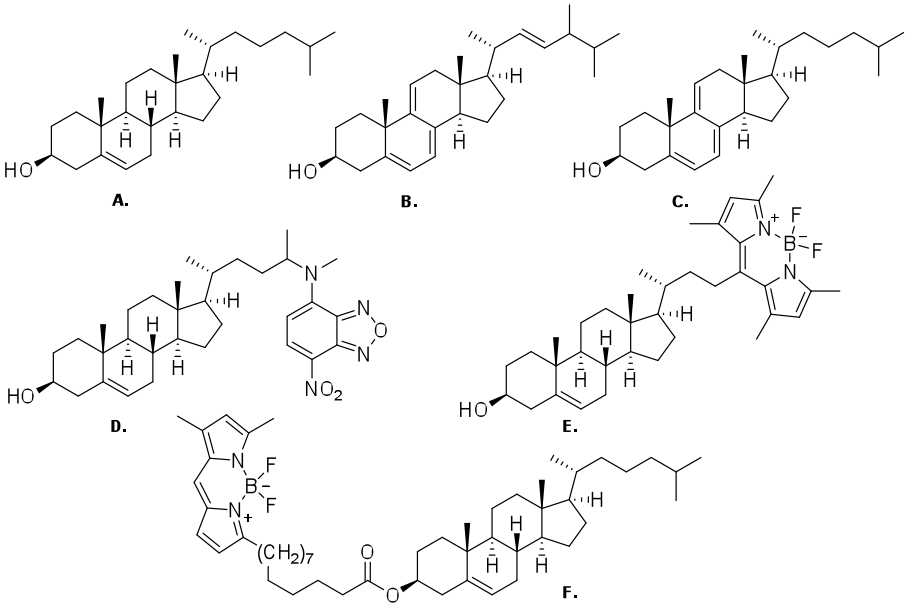

2.1.3 Novel Fluorophore-Labelled Cholesterol Probes

This chapter describes the synthesis of 4 novel fluorescent Chols (Figure 2-2, **1-4**) that are labelled with fluorophores at the 3β-OH position. We have characterized their fluorescence behaviour in vesicles and examined their suitability for visualization of phase separation in supported bilayers with coexisting L_o and L_d phases. A combination of fluorescence and AFM imaging in model membranes shows that the various Chol analogs have modest preferences for either L_o or L_d phases, depending on the lipid composition, the fluorophore and the length of the linker. One derivative has been used to probe Chol displacement by direct Cer incorporation

in bilayers containing SM. The same probe was employed to follow the dynamics of membrane reorganization during enzymatic generation of Cer, providing the first direct visualization of enzyme-mediated Chol redistribution, as well as information on the bilayer composition after *in situ* Cer generation.

Figure 2-2. Structures of the labeled Chols and the *N*-NBD-DHPE standard used in this study.

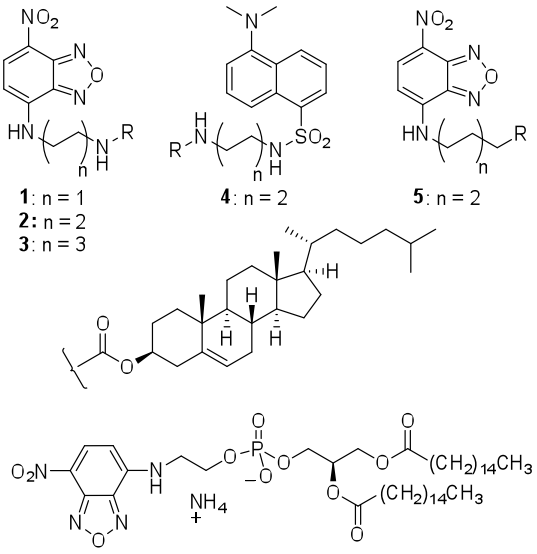

2.2 NBD- and Dansyl-labeled Cholesterols

2.2.1 Design and Synthesis of Cholesterol Analogs

Based on the advantages and limitations of the fluorescent sterols that have been examined previously, we chose to synthesize Chol probes with dyes conjugated at the 3-hydroxyl position. This choice was based on the observation that Chols with polar fluorophores attached to the aliphatic tail show a preference for labelling disordered phases,[28] while partitioning of the tail-labelled Bodipy-Chol (Figure 2-1 E) is very sensitive to the membrane composition, specifically the chain length and heterogeneity of the SM component.[13, 35-36] We selected the small, polar NBD fluorophore, reasoning that the failure of the Bodipy-Chol esters (Figure 2-1 F) to partition into ordered domains[37] was due to insertion of the hydrophobic Bodipy moiety into the

membrane, disrupting lipid packing. NBD is an environment sensitive dye with fluorescence quantum yields that vary with solvent polarity, and has been widely used as a probe in cells and model membranes.[38-39] The NBD fluorophore was attached via a carbamate group, as used previously to attach a Dansyl chromophore to the C-6 position;[40] the carbamate group is resistant to hydrolysis and retains some of the hydrogen bonding capability of the free hydroxyl group. Diamine linkers with 2, 4 and 6 carbons were used to determine the optimal linker length to minimize disruption of the polar head group packing by the fluorophore. NBD Chols **1-3** have intramolecular distances between C-3 of the sterol and C-4 of the fluorophore ranging from 8.5 to 13.5 Å, based on calculations for the lowest energy, anti-staggered linker conformation. We also synthesized one analog with a Dansyl fluorophore, **4**, which is similar in size to NBD but less hydrophilic.

Scheme 2-1 illustrates the synthetic approach employed to prepare probes **1**-**3**. Ethyl, butyl and hexyl alkylendiamines were mono-protected as tert-butyl carbamates under conditions developed by Krapcho.[41] The mono-protected diamines were then conjugated to 7-nitrobenzo-2-oxa-1,3-diazol-4-yl chloride (NBD-Cl) via nucleophilic aromatic substitution in the presence of triethylamine.[42] Subsequent removal of the *N*-tert-butoxy carbonyl groups was achieved in trifluoroacetic acid (TFA). Phosgene was used to activate cholesterol for coupling with the NBD-alkylendiamines. NBD-cholesterols **1**-**3** were then obtained by introducing the triflate salt of the appropriate NBD-alkylendiamine to a solution of the cholesteryl chloroformate in the presence of N,N-diisopropylethylamine (DIPEA). Dansyl-Chol **4** was synthesized in a similar fashion.

Scheme 2-1. Synthesis of NBD-Chols. (a) Boc_2O, dioxane, rt, 22 h; (b) Et_3N, DMF, 30 min; (c) TFA/CH_2Cl_2, rt, 30 min; (d) $C(O)Cl_2$, DIPEA, CH_2Cl_2, 0 °C, 1 h; (e) **I**, DIPEA, CH_2Cl_2, 12 h, rt.

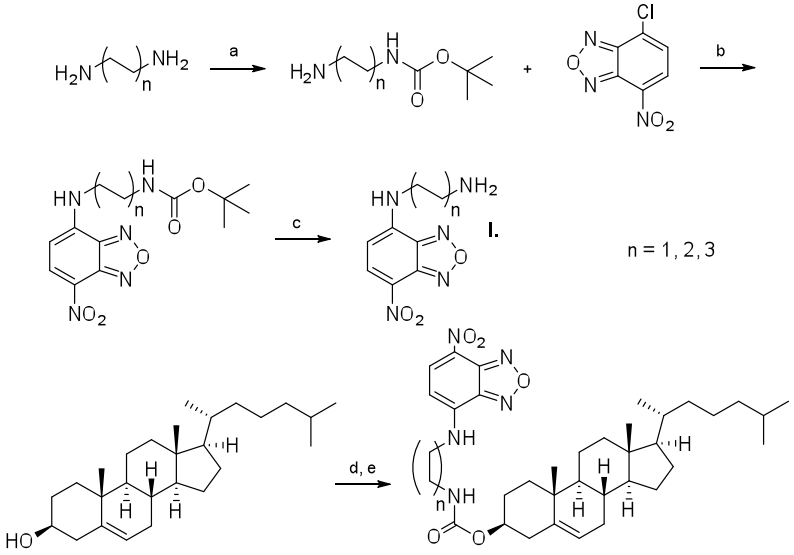

2.2.2 Fluorescence Spectroscopy

Absorption and fluorescence spectra were measured for NBD Chols **1**-**3** and **5** and N-NBD-DHPE in aqueous vesicle solutions of DOPC, DOPC/Chol in molar ratios of 2/1, DPPC/Chol 2/1, and ESM/Chol 2/1. Figure 2-3 shows representative spectra for probe **2** acquired in vesicles. These mixtures were selected to approximate the composition of the L_d and L_o phases in the domain-forming bilayers used for fluorescence microscopy; representative data for several probes in DOPC were also measured. The absorption spectra for all four probes were similar with maxima at 335 and 470 (±5) nm, corresponding to the π, π* and charge transfer bands, respectively. The maximum of the fluorescence emission spectra varied by ~10 nm for the various probe/lipid combinations, ranging from 527 to 537 nm (Table 2-1). The emission maxima are similar to literature values of 541 and 535 nm for N-NBD-DHPE and several acyl chain labelled phospholipids in fluid vesicles.[38-39] They are significantly blue-shifted from the

566 nm emission maximum reported for n-propylamino-NBD in water, reflecting the less polar environment of the lipid bilayer.[43]

Figure 2-3. (A) absorption spectra of NBD-DHPE and NBD-Chol 2 in lipid SUVs: I) DOPC with 2 mol% NBD-DHPE; II) DOPC 0.5% NBD-DHPE; (III) DOPC/Chol in 2/1 molar ratios and 0.5% NBD-Chol **2**; IV) ESM/Chol in 2/1 molar ratios and 0.5% **2**; V) DPPC/Chol in 2/1 molar ratios and 0.5% **2**. Traces shown here are uncorrected for vesicle scattering. (B) Emission spectra for the same vesicle suspensions.

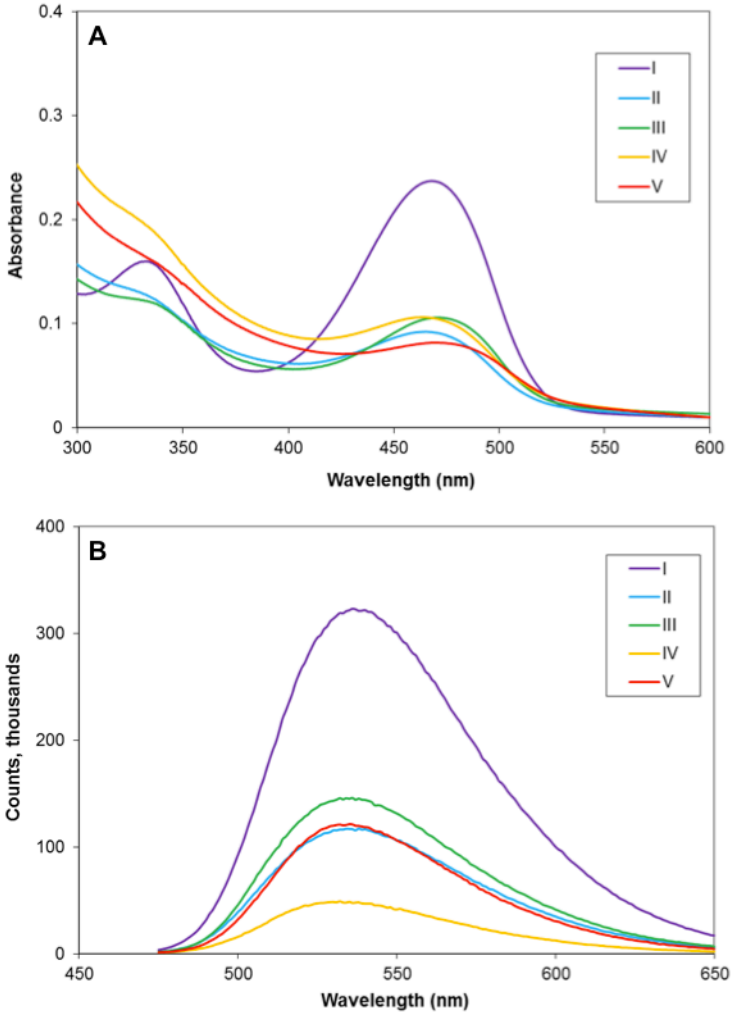

Fluorescence quantum yields, Φ, were determined in the same lipid vesicles (Table 2-2) using *N*-NBD-DHPE in DOPC vesicles (Φ of 0.16 at 2.0 mol % dye in egg PC vesicles) as a standard.[38] Φ values for the NBD-labelled lipids ranged from 0.12 to 0.26 for the different lipid compositions, indicating relatively modest changes in the polarity experienced by the NBD

fluorophore as a function of either probe structure or lipid composition. The effect of probe concentration in ESM/Chol was examined for **2** (Table 2-2); the quantum yield decreased by less than a factor of two over a probe concentration range of 0.1 to 1 mol percent.

Table 2-1. Absorption and emission maxima (in nm) for the NBD derivatives and lipid mixtures used in this study.

NBD-labeled lipid	Absorption/Emission Maxima (nm) Vesicle Composition			
(0.5 mol %)	DOPC	DOPC/Chol 2/1	DPPC/Chol 2/1	ESM/Chol 2/1
NBD-DHPE	468 / 537	464 / 536	467 / 532	463 / 529
NBD-Chol **1**	-	469 / 537	470 / 533	467 / 530
NBD-Chol **2**	471 / 536	472 / 535	475 / 534	466 / 530
NBD-Chol **3**	-	467 / 534	467 /535	464 / 524
NBD-CE **5**	473 / 534	466 / 533	467 / 535	467 / 527

Table 2-2. Fluorescence quantum yields (Φ) for NBD-Chols **1**-**3** and **5** in vesicles with various lipid compositions measured using NBD-DHPE as a reference standard.

Dye (mol %)	Vesicle Composition Φ			
	DOPC	DOPC/Chol 2/1	DPPC/Chol 2/1	ESM/Chol 2/1
NBD-DHPE (2.0)	0.16[a]	-	-	-
NBD-DHPE (0.5)	0.18	0.16	0.23	0.26
NBD-Chol **1** (0.5)	-	0.16	0.19	0.12
NBD-Chol **2** (0.5)	0.21	0.19	0.26	0.24
NBD-Chol **2** (0.1, 1.0)	-	-	-	0.38, 0.22
NBD-Chol **3** (0.5)	-	0.17	0.12	0.16
NBD-CE **5** (0.5)	0.16	0.15	0.24	0.25

[a] Quantum yield in egg PC vesicles, from: S. Mazeres, V. Schram, J.-F. Tocanne and A. Lopez, 7-Nitrobenz-2-oxa-1,3-diazole-4-yl-labeled phospholipids in lipid membranes: differences in fluorescence behavior, *Biophys. J*. **1996**, *71*, 327-335.

2.2.3 Partitioning of dye-labelled cholesterols in ternary lipid mixtures

Lipid mixtures of DOPC, DPPC or ESM, and Chol in a 2/2/1 mol ratio and containing 0.5 mol% of the dye-labelled lipids were used as a starting point to study the partitioning behaviour

of the new Chol analogs. Supported lipid bilayers of these mixtures display coexisting L_o/L_d phases and afford L_o domains large enough to visualize using fluorescence microscopy, as reported in previous studies.[14, 25, 44] Representative images for bilayers of DOPC/ESM/Chol and DOPC/DPPC/Chol containing 0.5 mol% probe **2** are shown in Figure 2-4 A, B. The bilayer for the ESM mixture has many small dye-excluded regions that correspond well to the dark domains observed for this mixture using Texas Red-DHPE to visualize phase-separation in our earlier work.[14, 25] The contrast between domains and fluid phase is much lower than that observed for Texas Red-DHPE which shows approximately 3-fold higher intensity in the fluid phase than in the domains. The image in Figure 2-4 A provides qualitative evidence for a modest preference of the labelled Chol for the fluid phase. By contrast, the image in Figure 2-4 B for the DOPC/DPPC/Chol bilayer shows small bright domains, indicating that probe **2** preferentially stains the ordered domains; AFM was used to verify that the bright regions corresponded to the taller liquid-ordered domains.

Since the two raft mixtures showed different partitioning behaviour for probe **2**, we examined several additional compositions within the L_d/L_o co-existence region for DOPC/ESM/Chol membranes (Figure 2-4).[44-45] The bilayer morphology changed as the lipid composition was varied and AFM was used to verify the assignment of dye excluded areas to either fluid or ordered regions. Representative data for correlated fluorescence and AFM imaging of a bilayer of DOPC/ESM/Chol in molar ratios of 7/9/4 are shown in Figure 2-5. The darker regions in the optical image (Figure 2-5 A) correspond to raised domains and higher frictional contrast in the AFM height and lateral deflection scans, respectively (Figure 2-5 B, C), consistent with their assignment to areas of L_o phase. Similarly, the areas of stronger

fluorescence match the phase with lower height and lower frictional contrast observed by AFM, and are identified as the fluid or L_d phase (Figure 2-5 D).

Figure 2-4. Fluorescence images illustrating the partitioning of NBD-Chol **2** (0.5 mol%) between liquid-ordered and liquid-disordered phases in supported lipid bilayers prepared from ternary lipid mixtures: (A) DOPC/ESM/Chol 2/2/1; (B) DOPC/DPPC/Chol 2/2/1; (C) DOPC/ESM/Chol 3/5/2; (D) DOPC/ESM/Chol 5/3/2; (E) DOPC/ESM/Chol 7/9/4; (F) DOPC/ESM/Chol 1/1/1. Scale bar = 5 μm.

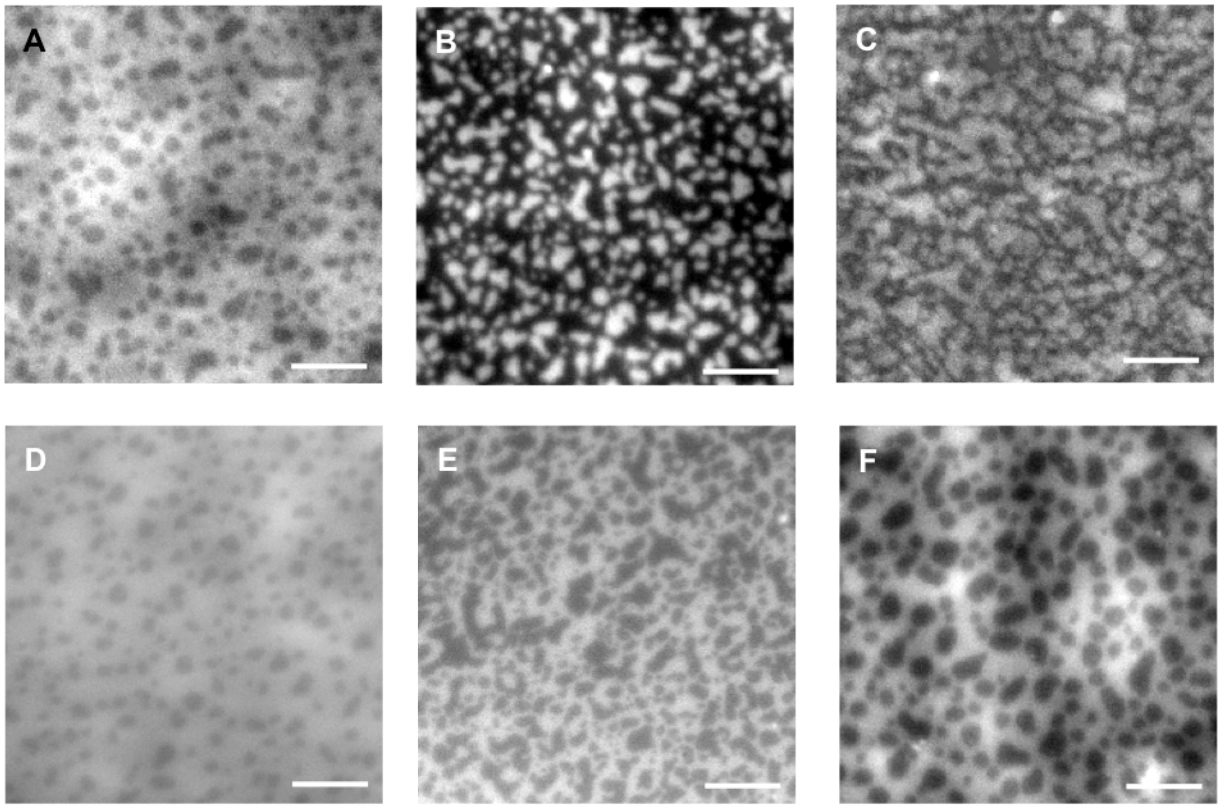

Comparison of AFM and fluorescence images for the other compositions indicates that probe **2** partitions more strongly into the L_d phase in all but one of the ESM mixtures (see representative fluorescence images in Figure 2-4 C-F). The exception is the bilayer with the highest fraction of ESM (DOPC/ESM/Chol in mol ratios of 3/5/2, 50% ESM, fluorescence in Figure 2-4 C, AFM not shown) where the ordered phase has the stronger fluorescence; this composition gave interconnected domains, making it difficult to distinguish L_o and L_d phases based solely on the fluorescence images. The AFM and fluorescence images for mixtures with

variable ESM ratios indicate that domains of the higher ordered phase become less round and increasingly irregular in shape and cover a larger fraction of the surface area as the fraction of ESM increases. The 1/1/1 bilayers typically exhibited smooth, round domains (Figure 2-4 F) that were consistently larger than those for the other ESM mixtures.

Figure 2-5. Correlated fluorescence and AFM images for a DOPC/ESM/Chol (7/9/4) supported lipid bilayer containing 0.5 mol% NBD-Chol **2**: (A) Fluorescence image; (B, C) Height and lateral deflection AFM images, respectively; (D) Intensity and height cross sections for the lines indicated in A and B. The cross sections indicate that the raised L_o domains observed by AFM are ~ 0.8 nm higher than the surrounding L_d phase and correspond to the dark, dye-excluded regions in the fluorescence image. Scale bar = 5 μm.

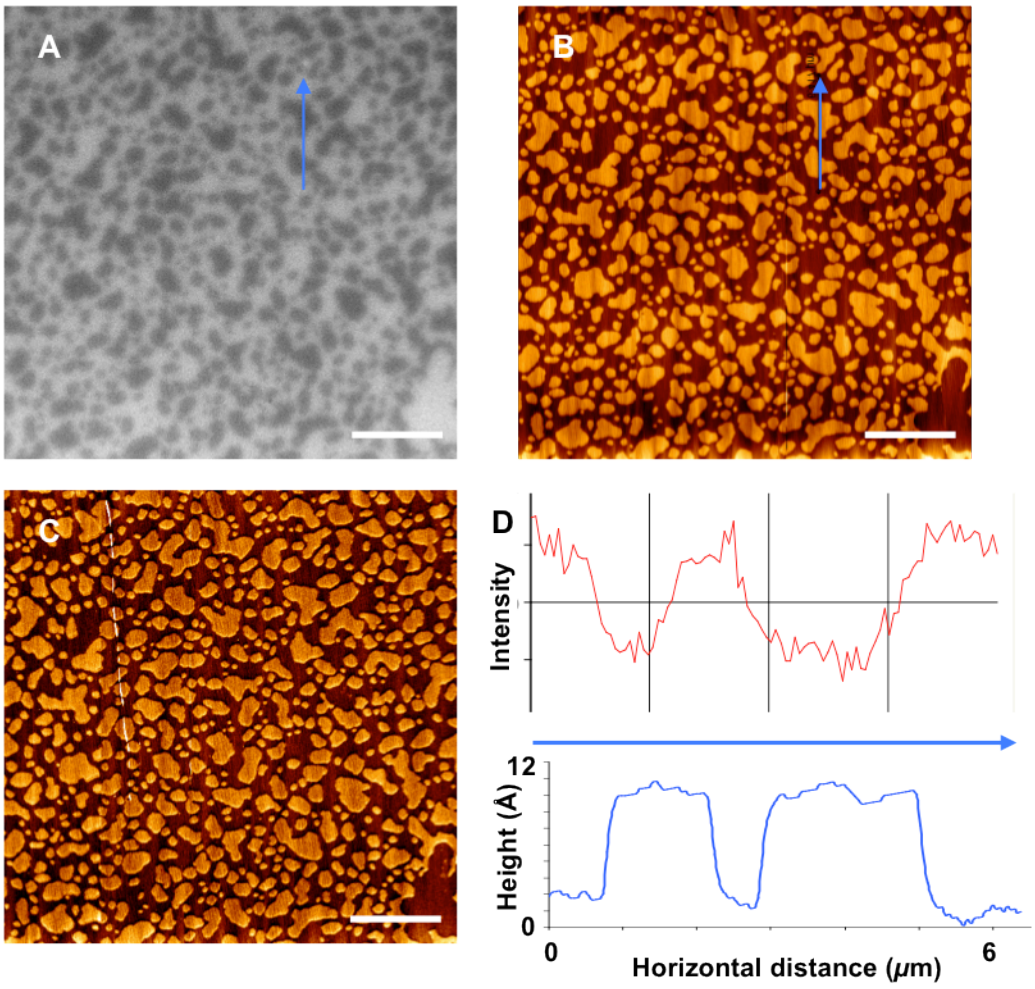

For comparison to literature data,[46] DOPC/brain SM/Chol bilayers (in molar ratios of 3/2/1 and 4/2/1) containing 0.5 mol% probe **2** were imaged by fluorescence microscopy and AFM. These mixtures gave higher liquid-ordered domains (as visualized by AFM) that were slightly

darker than the surrounding membrane in fluorescence images; representative images are shown in Figure 2-6. Thus, both egg and brain SM have qualitatively similar partitioning for the NBD-Chol **2**.

Figure 2-6. Fluorescence (A) and AFM (B) images for a DOPC/brain SM/Chol bilayer (4/2/1 stained with 0.5 mol% **2**). The images are for different areas of the same bilayer. The cross section below the AFM image indicates that the domains are ~1 nm higher than the surrounding fluid phase. Scale bar = 5 μm.

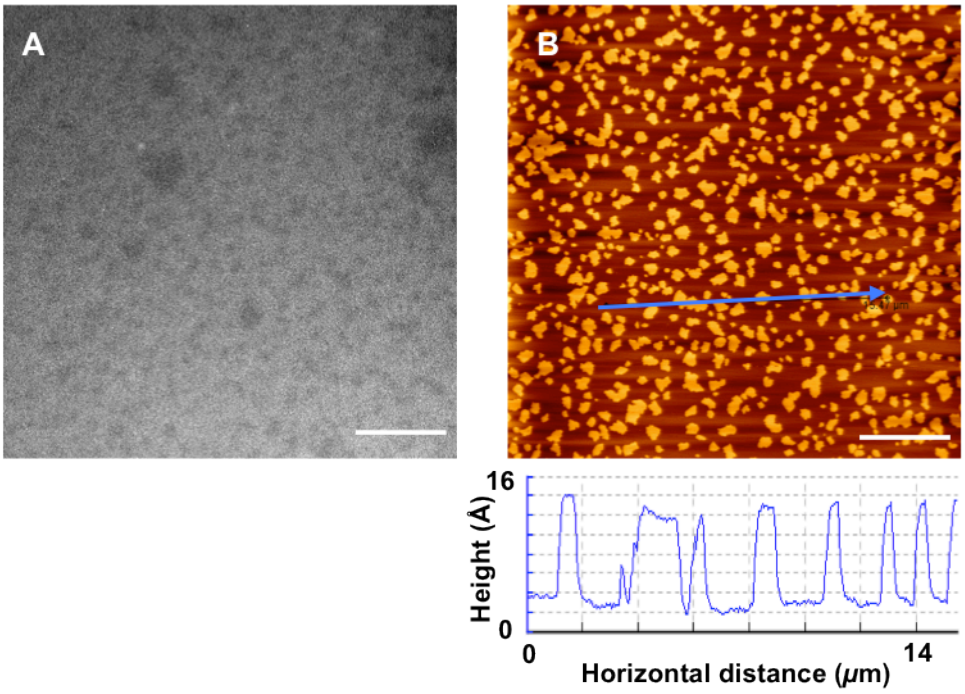

The ratios of intensities (I_{Lo}/I_{Ld}) for L_o and L_d phases in bilayers of various ternary lipid mixtures with 0.5 mol% of probes **1-5** were measured for multiple bilayers for each probe/lipid composition (Table 2-3). The differences between probes and for different lipid compositions are modest, with a slight preference for localization in the L_d phase in most cases. Intensity ratios are one of the most important factors for assessing the utility of probes for labelling specific membrane domains for microscopy experiments. However, the intensity ratios reflect changes in both probe concentration and probe brightness and thus provide only qualitative information on the partitioning of probes between lipid environments. For example, a probe

may show stronger fluorescence in one phase due to changes in its photophysical properties, rather than a higher concentration.

Table 2-3. Ratio of fluorescence (I_{Lo}/I_{Ld}) intensities and partition coefficients (K_p) for liquid-ordered/liquid-disordered phases for Chol analogs **1**-**5** in bilayers with various lipid compositions. Data from TIRF microscopy, except for probe 4 and Cer and brain SM mixtures, which were measured by epifluorescence.

Vesicle Composition[a]	Dye	I_{Lo}/I_{Ld}	K_p[b]
DOPC/DPPC/Chol			
2/2/1	**1**	0.77 ± 0.04	0.65
2/2/1	**2**	1.37 ± 0.08	1.0
2/2/1	**3**	1.26 ± 0.07	1.8
2/2/1	**4**	0.55 ± 0.03	
2/2/1	**5**	0.69 ± 0.04	0.4
DOPC/ESM/Chol			
2/2/1	**1**	0.83 ± 0.04	1.1
2/2/1	**2**	0.94 ± 0.02	0.7
2/2/1	**3**	0.90 ± 0.02	1.0
2/2/1	**4**	0.49 ± 0.04	
2/2/1	**5**	0.73 ± 0.05	0.4
3/5/2	**1**	0.79 ± 0.04	1.0
3/5/2	**2**	1.11 ± 0.02	0.8
3/5/2	**3**	0.79 ± 0.03	0.8
5/3/2	**2**	0.89 ± 0.02	0.6
7/9/4	**2**	0.89 ± 0.04	0.6
1/1/1	**2**	0.86 ± 0.04	0.6
DOPC/ESM/Chol/Cer			
7/7/4/2	**2**	0.53 ± 0.05[c]	
DOPC/brain SM/Chol			
3/2/1	**2**	0.88 ± 0.05	
4/2/1	**2**	0.90 ± 0.04	

[a] Molar ratios. [b] K_p for probe **2** was estimated using relative quantum yields from supported bilayer experiments; for other probes quantum yield ratios for vesicles solutions were used. [c] I_{gel}/I_{Ld} for ceramide-enriched domains is 0.27 ± 0.06.

Changes in probe brightness may be caused by variation in quantum yields, concentration-dependent self-quenching or excitation efficiency (due to different molecular orientations) as a function of lipid environment.[28] Although many investigations of probe partitioning are based solely on a comparison of fluorescence intensities, others report directly measured partition coefficients, making a quantitative comparison between the two types of measurements problematic.

Differences in probe brightness between L_o and L_d phases for **2** were measured in order to estimate partition coefficients from the fluorescence intensity data for this probe in supported bilayers. First, plots of fluorescence intensity as a function of [**2**] in DOPC bilayers were linear between 0 and 1% (Figure 2-7), demonstrating that self-quenching does not occur at the dye concentration (0.5%) used for the phase separated bilayers. Although self-quenching has been reported for NBD-labelled lipids in vesicles, it occurs over a higher range of concentrations (eg, between 3-9% for C_{12}-NBD-PC).[47] Second, the relative quantum yields for probe **2** in different lipid environments were estimated from fluorescence intensity measurements for single phase DOPC, DOPC/Chol, DPPC/Chol and ESM/Chol bilayers under matched conditions, as outlined in the materials and methods section of this chapter (2.5.6). PC or SM/Chol mixtures with 2/1 molar ratios were used, providing an upper limit for the fraction of Chol in the L_o and L_d phases. The intensity ratios provide an estimate for the ratio of quantum yields for L_o vs L_d phases of 0.72 and 0.76 for ESM and DPPC mixtures, respectively. The ratio of quantum yields measured for vesicles of the same composition in solution gives similar results (0.73 and 0.79 for ESM and DPPC mixtures, respectively). This serves to validate the approach based on quantification of intensities from supported lipid bilayers. The agreement between the two approaches indicates

either that the solid support does not affect the photophysics of the probe or that the effect of the support is similar for both ordered and disordered phases. The quantum yield ratios for probe **2** were then used to estimate K_p from the (I_{Lo}/I_{Ld}) data for phase-separated bilayers of ternary lipid mixtures (Table 2-3). Note that this approach assumes that self-quenching is negligible (consistent with the linear dependence of intensity on probe concentration) but does not account for any changes in excitation due to different orientations in the supported bilayer.[48] Based on the similarity in quantum yield ratios for probe **2** in L_o and L_d phases measured for supported bilayers and vesicles, K_p values for the other NBD-Chol probes were obtained using the quantum yield data for vesicles.

Figure 2-7. Plot of fluorescence intensity as a function of [**2**] for DOPC bilayers.

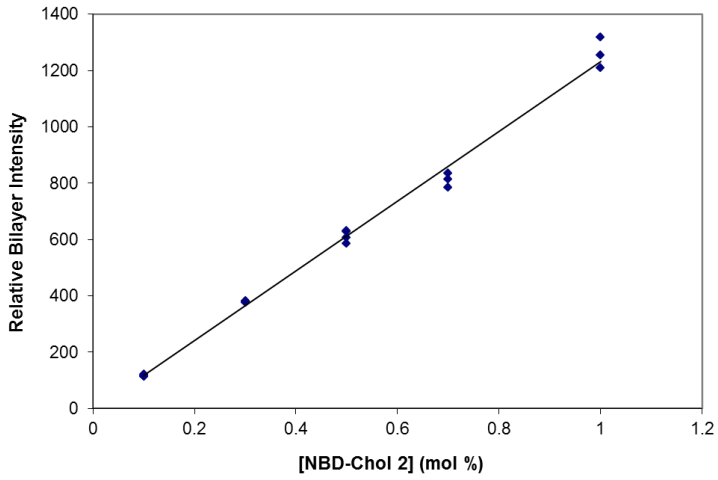

2.2.4 Partitioning of NBD-Cholesterol 2 in Ceramide-Containing Lipid Bilayers

Bilayers prepared from vesicle solutions of DOPC, ESM, Chol, and synthetic ceramide (16:0 Cer) in a 3/4/2/1 ratio containing 0.5 mol% NBD Chol **2** were imaged by AFM and fluorescence microscopy (Figure 2-8 A, B). The AFM height image shows irregularly shaped domains with two distinct heights. The lower domains are ~1 nm higher than the surrounding DOPC-rich phase

(Figure 2-8 C), consistent with results for L_o domains in bilayers without Cer (Figure 2-5). The higher features are assigned to Cer-rich domains, based on earlier studies that have shown that direct incorporation of Cer leads to Cer-enriched domains adjacent to or within the initial liquid-ordered domains for ternary lipid mixtures containing SM.[12-14, 24] As described previously,[25, 49] the apparent height of the Cer rich-subdomains is extremely sensitive to the force applied, varying from as much as 3-4 nm at relatively high setpoint (cross section in Figure 2-8 C) and decreasing to ~1 nm at lower setpoint/force.

Figure 2-8. Correlated AFM and fluorescence images for a DOPC/ESM/Chol/Cer (7/7/4/2) supported lipid bilayer containing 0.5 mol% NBD-Chol **2**: (A) AFM topography; (B) Fluorescence image; (C) Height and fluorescence intensity cross sections for the lines indicated in images A and B. The highest domains are assigned to a Cer-rich gel phase and correspond to the darkest domains in the fluorescence image, while L_o domains with intermediate height correspond to areas of intermediate intensity in the fluorescence image. Scale bar = 5 μm.

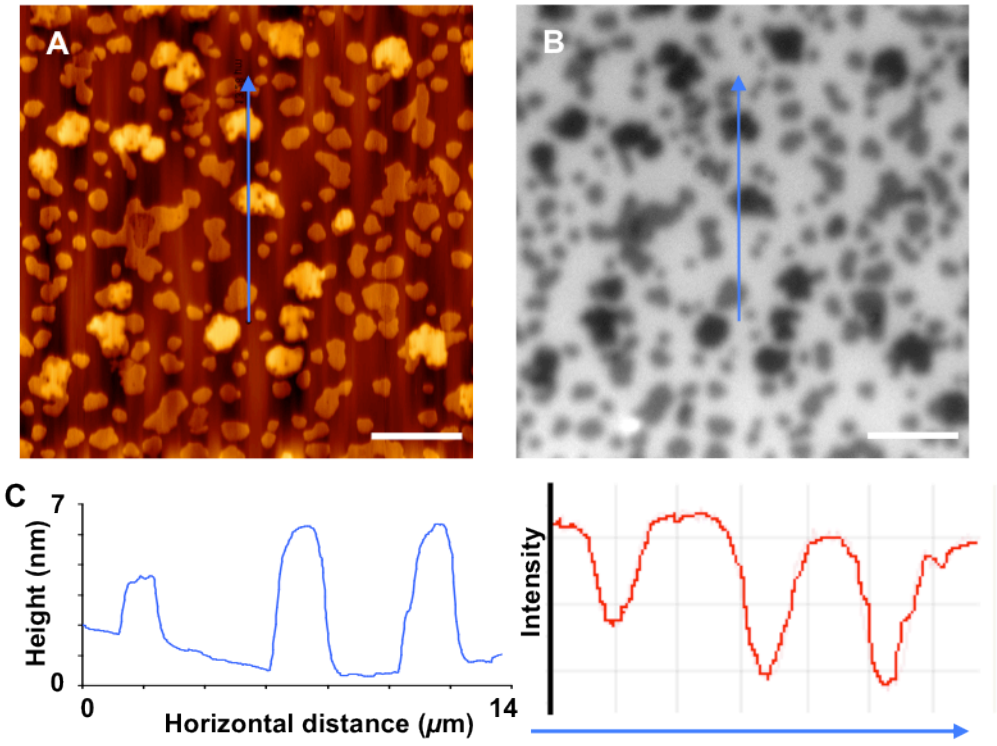

The fluorescence image of the same region scanned by AFM shows two different intensity levels associated with the domains (Figure 2-8 B, C). The Cer-enriched regions observed by AFM

correspond to the darkest domains while the intermediate height L_o domains have an intensity intermediate between those of the Cer-rich domains and the bright L_d phase. The correlated AFM and fluorescence images provide qualitative evidence that probe **2** has a lower preference for the Cer-enriched regions than for the L_o domains (Table 2-3). Furthermore, the I_{Lo}/I_{Ld} ratio (Table 2-3) suggests an increased preference for probe **2** to partition into the L_d phase in the presence of Cer, possibly reflecting a small fraction of Cer in the L_o domains.

2.2.5 NBD-Cholesterol 2 in Sphingomyelinase-Treated Bilayers

Probe **2** was used to follow membrane restructuring during SMase treatment of supported bilayers prepared from DOPC/ESM/Chol 7/9/4 lipid mixtures. Prior to enzyme addition AFM shows higher L_o domains that correspond to the slightly darker areas visualized by fluorescence microscopy in a correlated imaging experiment (Figure 2-4). The bilayer was treated with SMase, and fluorescence images of the same area were recorded over a period of 20 minutes (Figure 2-9). Changes in the bilayer appeared shortly after enzyme addition, with the most dramatic restructuring events occurring on the timescale of a few minutes. Dark, dye-excluded patches formed within the first minute and grew rapidly in diameter over the first five minutes following enzyme addition (areas 1 and 2 in Figure 2-9 B, C). Whereas bilayers prior to enzyme addition show only two levels of fluorescence, an intensity cross section for the bilayer 5 minutes after enzyme addition demonstrates that the dark dye-excluded regions have considerably lower fluorescence intensity than the surrounding L_o domains, which are in turn less intense than the fluid phase (compare cross sections I and II in Figure 2-9). The original domains are no longer visible in the dye-excluded patches (areas 1 and 2) that form after enzyme addition, but in other areas the original domains persist largely unchanged (area 3).

Figure 2-9. Fluorescence images for a DOPC/ESM/Chol (7/9/4 with 0.5 mol% **2**) supported lipid bilayer before and during incubation with 0.33 U/ml SMase: (A) Bilayer before enzyme addition; (B- F) Bilayer imaged at 2.5, 5, 10, 15 and 19 minutes after SMase addition. The features outlined in blue are conserved throughout the time course experiment. One of the large dye-excluded areas formed by enzyme activity is outlined in green. (I, II and III) Cross sections are shown for the lines indicated in images A, C and F. Only two levels of fluorescence intensity are observed before (A, I) and at longer times after enzyme addition (F, III), while three intensity levels are evident at intermediate times (C, II). Scale bar = 5 μm.

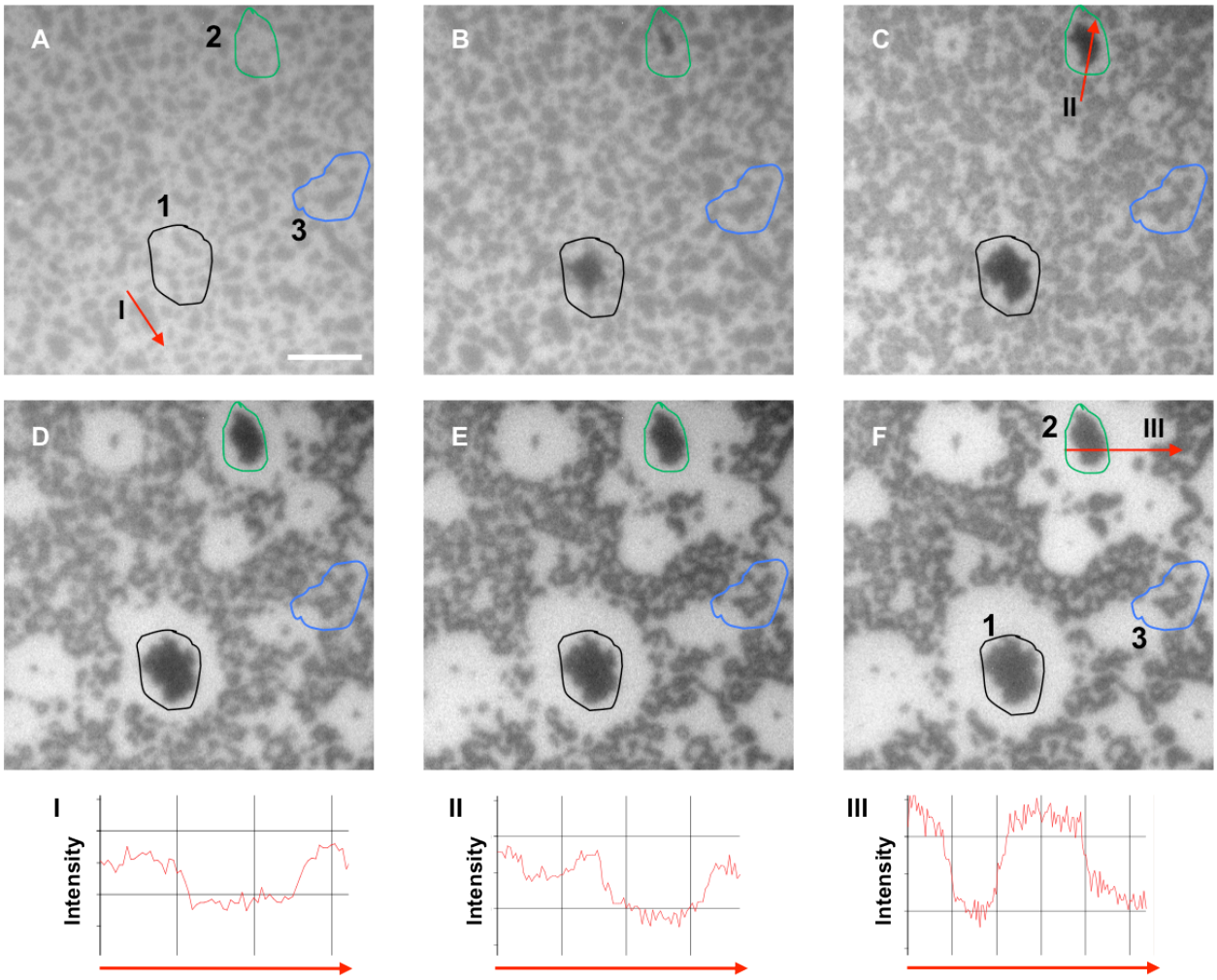

Images recorded after 10 minutes show the presence of bright, steadily expanding rings that surround the large dark regions (see the bright rings around areas 1 and 2 in Figure 2-9 D, E). Other regions of the bilayer have a mixture of bright and dark areas that retain the outlines of the original domains. By the end of the time course, the small dark domains are of similar intensity to the large dye-excluded patches that grow in, rather than of intermediate intensity

as for the image recorded at 5 minutes (Figure 2-9 F and cross section III for area 2). The dark patches and bright rings in the fluorescence images recorded during enzyme treatment for 7/9/4 DOPC/ESM/Chol bilayers are qualitatively similar to our earlier observations for bilayers prepared with different ratios of the same lipids and using Texas Red-DHPE to visualize bilayer morphology.[24-25] However, the NBD-labelled Chol probe provides additional information on changes in Chol distribution, suggesting that Chol is excluded from the dark patches that form during enzyme action, as well as from the domains.

To confirm the above hypothesis, the bilayer was washed to inactivate/remove enzyme and correlated AFM and fluorescence images were recorded (Figure 2-10). Although a different area is imaged after washing, the fluorescence image (Figure 2-10 A) has similar features to those in Figure 2-9 F; cross sections (Figure 2-10 D, E) show 3 intensity levels with the large dye-excluded patches being the least intense. This confirms that a difference in dye bleaching efficiency in L_o and L_d phases is not responsible for the observed intensity variations in Figure 2-9. The correlated images allow us to draw three conclusions on the restructured bilayer. First, the AFM image shows many small raised features that are similar in size and shape to domains observed prior to enzyme treatment (Figure 2-10 B, areas outlined in blue). Some of these domains have raised edges, analogous to those assigned to Cer rich sub-domains in earlier AFM studies.[14, 25] The domain heterogeneity is also visible by fluorescence for the larger domains, as indicated by the intensity cross sections shown in Figure 2-10 E, F. Note that small dark domains with brighter centers are found in other areas, for example area 3 in Figure 2-9.

Figure 2-10. Correlated fluorescence and AFM images for a DOPC/ESM/Chol (7/9/4 with 0.5% mol% **2**) bilayer that was treated with 0.33 U/ml SMase for 22 min and washed prior to imaging: (A) Fluorescence; (B, C) AFM height and lateral deflection images; (D-F) Intensity and height cross sections for the lines indicated in images A and B. The large dark patches have lower fluorescence intensity than regions that retain the outlines of the initial domains (D) and show enhanced contrast in lateral deflection (C). Superimposed fluorescence intensity and height cross-sections (E) confirm that the domain perimeters are taller and brighter than the dye-excluded patches. Another superposition of intensity and height (F) shows that the domain perimeter (brown arrow) has lower fluorescence than the domain interior. Scale bar = 4 μm.

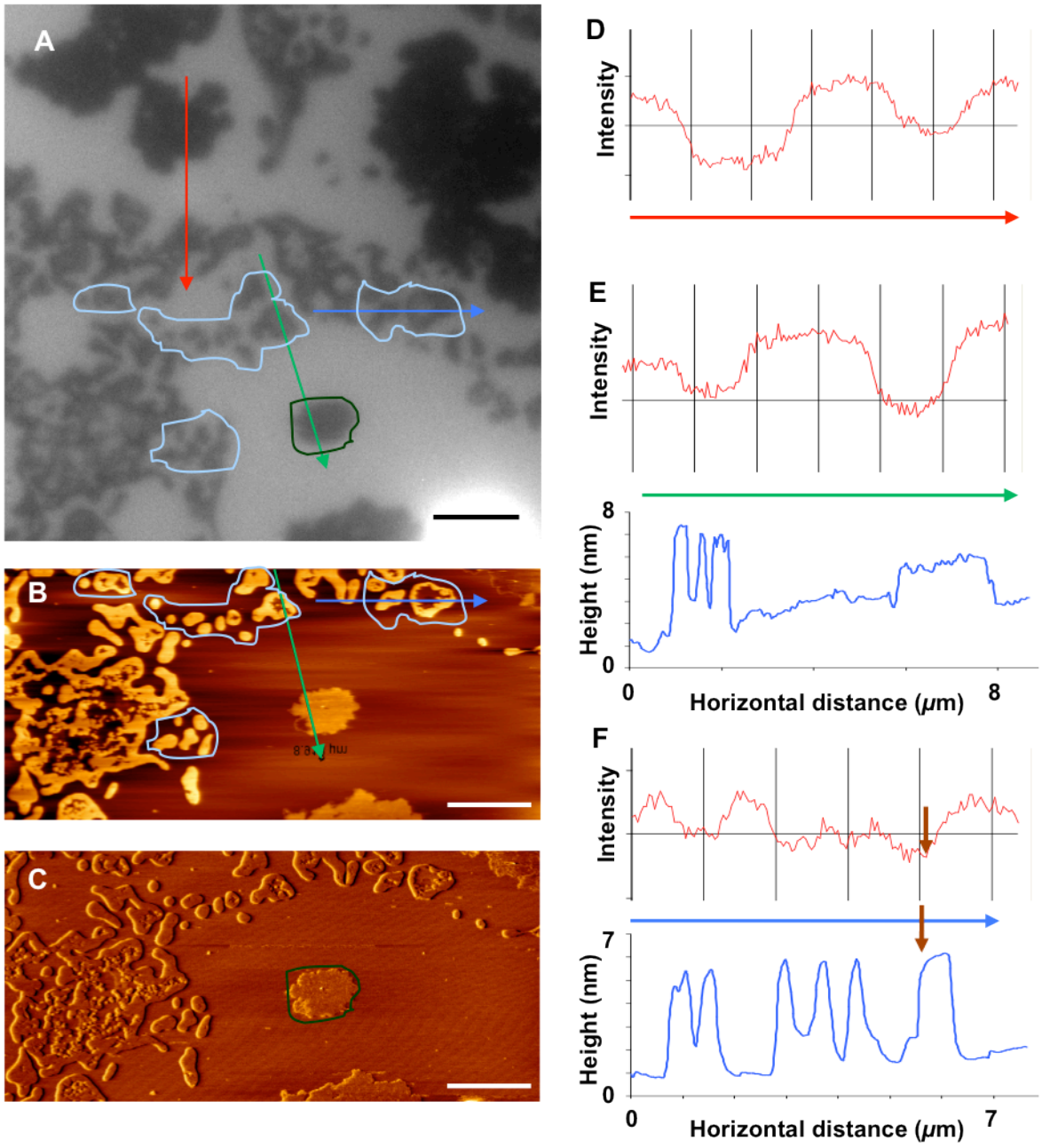

Second, the bright fluorescent rings correspond to uniform lower regions in the AFM image, consistent with a disordered DOPC-rich phase. Third, the dark patch (circled in green) in the center of the bright ring in the fluorescence image has a height intermediate between those of the small Cer-enriched domains and the lower DOPC-rich regions. This feature shows up clearly in lateral deflection scans (Figure 2-10 C), and probe **2** suggests that this region is depleted in Chol. The combination of different imaging modes demonstrates that the dark patches in the center of the bright rings have properties that are different from other regions of the bilayer, consistent with Cer enriched platforms formed by enzyme activity. Elsewhere Cer localizes in small subdomains within and surrounding the original L_o domains. The composition of the two Cer-enriched regions is likely to be significantly different.

The reorganization of the enzyme treated bilayers varies for different regions of an individual sample (and from sample to sample) and is attributed to variable numbers of active enzymes in specific regions.[25] The complexity of the enzyme-initiated bilayer restructuring makes it essential to correlate AFM and fluorescence images for the same bilayer area. Correlated AFM and fluorescence images for a second SMase-treated bilayer are presented in Figure 2-11 to illustrate the range of morphologies produced by enzyme treatment. The results are qualitatively similar to those in Figures 2-9 and 2-10 in that 3 intensity levels are evident in the fluorescence image (Figure 2-11 A, B) with large dark patches and areas of intermediate intensity that correspond to the initial L_o domains. However, the bright rings of fluid phase are not observed, possibly due to lower enzyme activity. A lateral deflection AFM image (Figure 2-11 D) shows that the dark areas have high frictional contrast and the smaller domains are

heterogeneous with raised edges; both of these effects are attributed to Cer-rich bilayer regions.

Figure 2-11. Correlated fluorescence and AFM images for a DOPC/ESM/Chol (7/9/4 with 0.5% mol% **2**) bilayer that was treated with 0.33 U/ml SMase for 16 min and washed prior to imaging: (A, B) Fluorescence image and cross section show three intensity levels assigned to 'bright' fluid phase, 'dark' domains, and dye-excluded patches (outlined in green); (C, D) AFM height and lateral deflection images indicate that the dye-excluded patches have high contrast in lateral deflection and a height intermediate between those of the fluid phase and small domains. Scale bar = 2 μm.

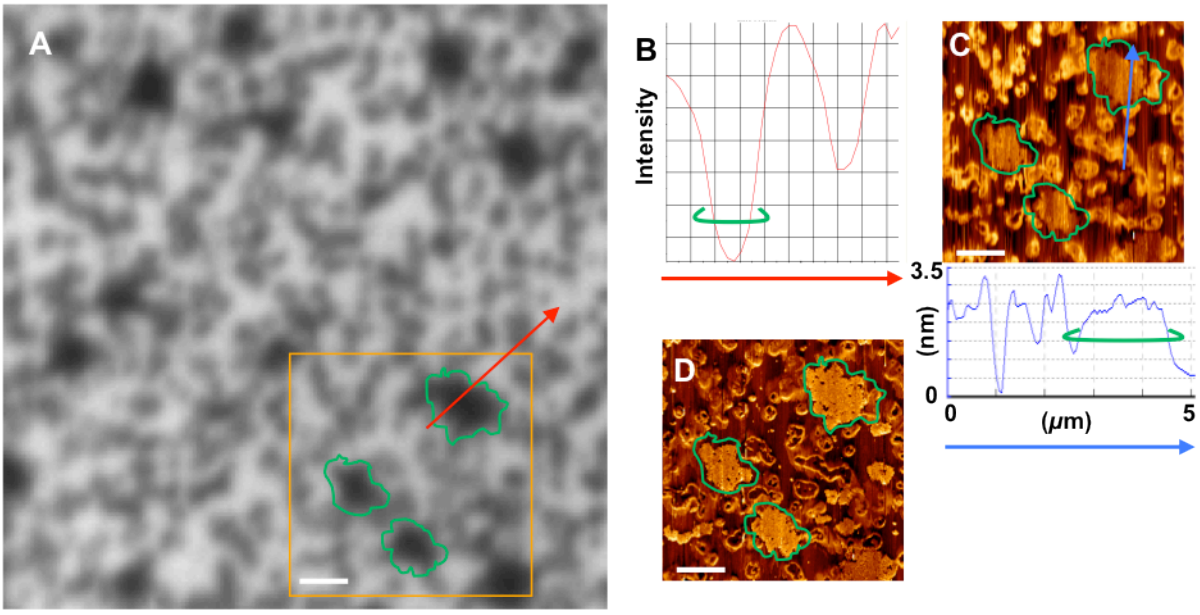

2.2.6 Contrast-Enhanced Imaging to Follow the Dynamics of SMase-Mediated Bilayer Reorganization

In another study our group had examined the partitioning of the dye-labelled lipid probe NBD-DHPE by fluorescence microscopy in phase separated lipid bilayers with coexisting liquid-ordered and fluid phases.[50] This probe showed slightly higher fluorescence intensity in the ordered domains but underwent a contrast reversal to give a more strongly fluorescent fluid phase in the presence of >0.2% Texas Red-DHPE (TR-DHPE). The change in contrast was shown to result from Forster resonance energy transfer between the NBD donor and TR acceptor in the fluid phase, which had a TR concentration that is approximately 3 times higher than in the

domains. An alternate approach using a nitroxide-substituted lipid that partitions into the fluid phase as a quencher was also examined as a means to enhance the contrast; however, the quencher modified the domain-forming behaviour of the bilayer. Here I describe the application of the energy transfer method for enhancing the contrast between ordered and fluid phases when examining the morphology of enzyme-treated bilayers.

A labelling strategy using a NBD-Chol/TR-DHPE FRET pair has some advantages for resolving the complex changes that occur during enzymatic generation of Cer in supported bilayers. Figure 2-12 illustrates a representative time course experiment recording the evolution of a supported bilayer of DOPC/ESM/Chol (molar ratios of 7/9/4) following SMase treatment. The bilayer was labelled with 0.5% NBD-Chol **2** and 0.2% TR-DHPE, and incubated with 0.33 U/mL of enzyme. Figure 2-12 A shows the bilayer before enzyme addition. The L_o domains appear bright relative to the L_d phase; this is in contrast to bilayers labelled with **2** alone for which the fluid phase is brighter, but is consistent with contrast reversal owing to FRET, as described for NBD-DHPE and TR-DHPE in membranes of similar composition.[50] In an image (Figure 2-12 B) of the same sample region taken 3 min after SMase addition, the domains appear slightly darker than the surrounding membrane. Control experiments confirmed that this change was not due to accelerated NBD photobleaching in the domain relative to the fluid phase. In section 2.2.5, we reported that as Cer is generated in the domains, NBD-Chol **2** is gradually ejected from these features into the fluid phase. The domain darkening observed here is consistent with this earlier observation. Recorded 9 min after enzyme addition, Figure 2-12 C reveals domains that exhibit two levels of fluorescence intensity. Although the features retain their overall rounded shape and can be matched to domains in the initial untreated bilayer, they now appear as dark

rings enclosing bright regions at their centers. Over time, these rings continue to darken and thicken, and the bright regions at the domain centers decrease in size (see Figure 2-12 D, 16 min; note that the intensities are weaker in both phases owing to probe bleaching).

Figure 2-12. Fluorescence time course for a DOPC/ESM/Chol (7/9/4) bilayer labeled with 0.5% **2** and 0.2% TR-DHPE and treated with 0.5 U SMase in a final volume of 1.5 mL. (A) Before SMase addition, (B) 3 min after SMase addition, (C) 9 min after SMase addition, and (D) 16 min after SMase addition. The sample was illuminated so as to excite the NBD chromophore of **2**. Scale bar = 5 μm.

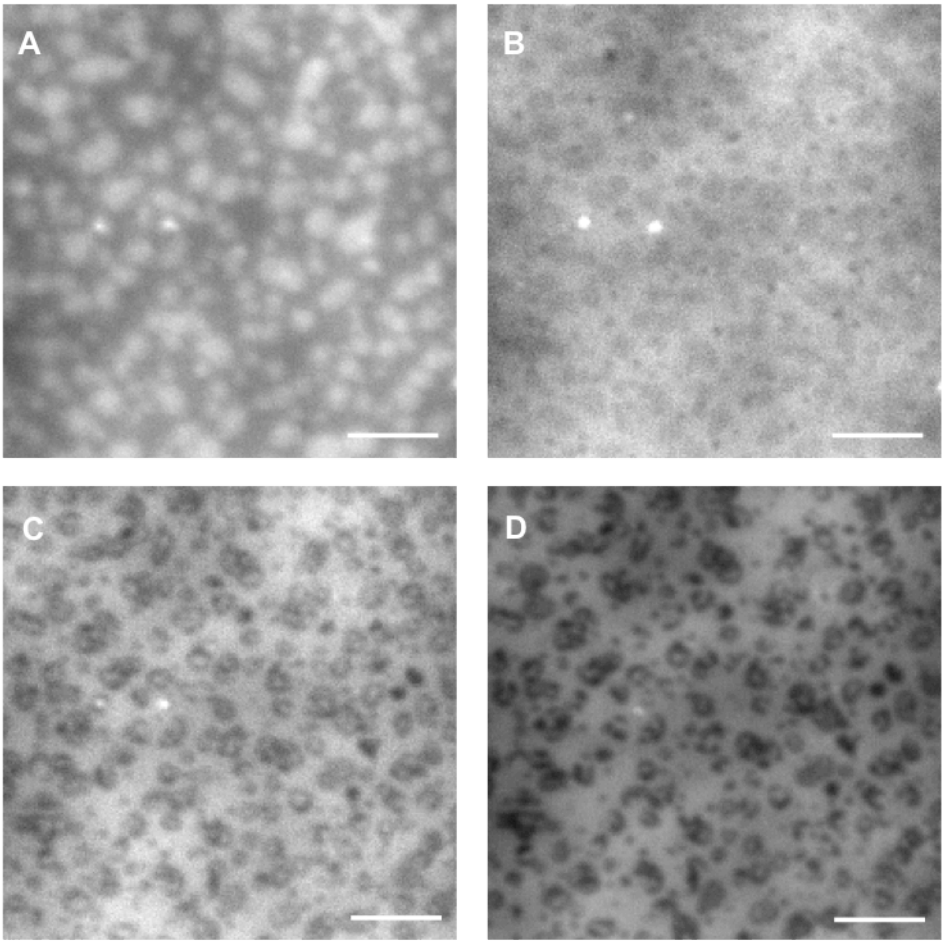

Based on the correlated fluorescence–AFM imaging of similar SMase-treated bilayers described above, the dark border and bright central regions that appear in the domains correspond to a raised, fencelike gel-phase perimeter and a liquid-ordered core that is lower in height. The taller gel-phase regions have been assigned to Cer-enriched regions that are depleted in cholesterol,[14, 51] and so should exclude a probe for cholesterol. The dark domain

perimeters in Figure 2-12 C and D show that this is in fact the case with the NBD-Chol **2**. The domain centers remain bright indicating that they retain the probe and therefore also conserve significant cholesterol content, consistent with previous AFM results. Such heterogeneity within domains was not observed by fluorescence with NBD-Chol **2** in the absence of TR-DHPE (Figure 2-9), illustrating the advantage of the FRET method for enhancing fluorescence contrast.

2.3 Discussion

2.3.1 NBD-Chol Photophysics in Lipid Bilayers

NBD has strong solvatochromic properties with a quantum yield that decreases with increasing solvent polarity, a property that has been exploited to assess the location and orientation of fluorophore labelled lipids in membranes.[38-39] In the present study we have observed quantum yields ranging from 0.12 to 0.26 for the various NBD-labelled Chols (Table 2-2). By comparison to earlier studies on the solvatochromic properties of n-propylamino-NBD in organic solvents and water-dioxane mixtures, these data indicate a relatively polar environment with dielectric constants between 30 and 40.[38, 43] A wider variation in quantum yields was observed previously for acyl chain labelled NBD-phospholipids that adopt a looping configuration with the NBD group in the relatively polar headgroup region of the bilayer.[38]

NBD Chols **1-3** show only small variations in quantum yield as a function of the linker length in DOPC/Chol and the observed values are similar to those in DOPC as well as to those for NBD-DHPE and the ester linked NBD Chol, **5** (Table 2-2). This suggests that, in the L_d phase, the polarity of the NBD environment is insensitive to the linker length and the method of fluorophore attachment, consistent with the disordered lipid packing in a fluid bilayer. By contrast, the quantum yields for the DPPC/Chol and ESM/Chol vesicles show larger changes

when the linker length is varied from 2 to 6 carbons. Probe **2** with the 4-carbon linker has significantly higher quantum yields, indicative of a less polar environment, than do **1** and **3** which have shorter and longer linkers, respectively. The more polar environment for **3** (with the 6-carbon linker) is consistent with positioning of the NBD closer to the bilayer interface in a more aqueous environment. It is less obvious why the short two-carbon linker also places the NBD in a more polar environment; one possibility is that the short linker causes significant disruption of headgroup packing, leading to greater water penetration. Interestingly, quantum yields for NBD-DHPE and **5** follow the same trend as **2** in DPPC/Chol and ESM/Chol vesicles, indicating that, despite the change in lipid and method of linker attachment, the fluorophore senses a similar and slightly less polar environment (compared to DOPC) for all three probes. Note that the distance between the Chol oxygen and the dye in ester **5** is almost the same as for probe **2**.

The observation of a less polar environment for **2**, **5** and NBD-DHPE in liquid-ordered vesicles is in contrast to the conclusion that the NBD group in acyl chain labelled lipids is expelled from the bilayer toward the aqueous phase in a gel phase relative to a fluid phase.[38] We attribute this difference to disruptions to lipid packing caused by the looping conformation assumed by the NBD fluorophore for chain labelled phospholipids. Variations in lipid packing and hydration for a Chol-enriched L_o phase, compared to a gel phase, may also play a role.[52]

2.3.2 Fluorescent Analogs for Modelling Free Cholesterol

The qualitative partitioning data obtained from fluorescence intensity ratios indicate that the four NBD-Chols show modest preferences for either L_o or L_d phases, depending on the lipid composition and the length and method of attachment of the linker (Table 2-3). The estimated

partition coefficients for the most part lead to the same conclusions. For the DOPC/DPPC/Chol bilayers, probe **3** shows a significant preference (K_p = 1.8) for the L_o domains in DOPC/DPPC/Chol bilayers, whereas probe **1** with the short carbamate linker and ester **5** partition more strongly into the L_d phase. Probe **2** is similar to probe **3** in terms of fluorescence intensity data but after taking changes in probe brightness into account, it actually shows no preference for L_o over L_d phase (K_p of 1). Although the variation in partitioning behaviour is relatively modest, the results suggest that the length of the linker and the use of an ester vs carbamate linker do influence probe partitioning. A carbamate linker with approximately 13.5 Å between C-3 of cholesterol and C-4 of NBD (probe **3**) gives the highest L_o partitioning.

The data for DOPC/DPPC/Chol mixtures can be compared to recent studies that have used NMR and/or fluorescence to examine phase separation in DOPC, DPPC and Chol mixtures, demonstrating that the L_o phase is strongly enriched in DPPC and moderately enriched in Chol [53-54]. For example, a partition coefficient for Chol of 1.4 was measured for a 1:1 mixture of DOPC/DPPC with 30 mol % Chol at 20 °C[54] and it was concluded that Chol concentrations ranged from 10-20 mol% in the L_d phase and 30-40% in the L_o phase for 1:1 DOPC/DPPC mixtures with 15 or 30% Chol.[53] These data indicate that **2** and **3** provide remarkably good models for the behaviour of native Chol in DOPC/DPPC/Chol mixtures, significantly better than either **1** or **5**. It is evident that relatively small changes to the linker and method of attachment can modulate the partitioning of the NBD-labeled lipids between L_o and L_d phases.

The 3 carbamate linked NBD Chols have a reduced preference for the L_o phase for 2:2:1 DOPC/ESM/Chol bilayers compared to the corresponding DPPC mixtures. Probe **2** does not show a preference for localization in the L_o phase for any of the SM mixtures (including brain

SM) that we have examined. The reduced preference for the L_o phase for ESM mixtures compared to DPPC mixtures is consistent with results for several carbocyanine dyes that were shown to partition into the L_d phase for ternary lipid mixtures containing SM but into the L_o phase for DSPC mixtures.[28] By contrast, the ester linked NBD Chol, **5**, has a K_p value of 0.4 in both ESM and DPPC ternary lipid mixtures. Interestingly, the Dansyl probe (**4**) has the strongest preference for the L_d phase based on fluorescence intensities in both DPPC and ESM mixtures, consistent with the hypothesis that the less hydrophilic probe may interact more strongly with the bilayer, leading to a preference for the disordered phase.

A recent NMR study of lipid diffusion in DOPC/ESM/Chol mixtures has concluded that Chol partitions to roughly the same extent into both L_o and L_d phases and that the driving force for phase separation in this system is the increasing difficulty of incorporating DOPC into an ordered phase.[55] This observation is in good agreement with the probe partitioning that we observe for **1-3**. However, other studies have shown a strong affinity of cholesterol for ESM or brain SM L_o domains when the unsaturated lipid component is POPC and have concluded that the interaction between Chol and SM is at least as favourable as that between a long chain saturated PC and Chol.[56-57] The lack of quantitative information on the ratio of Chol in L_o and L_d phases for DOPC/ESM/Chol precludes a direct assessment of the ability of the NBD Chol probes to mimic the behaviour of native Chol in the ESM mixture. Nevertheless, the stronger preference of **1-3** for the L_o phase, relative to the ester-linked derivative, is encouraging.

NBD-Chol probes **1-3** have advantages over other fluorescent sterols that have been used to mimic the behaviour of free Chol in model membranes.[30] Intrinsically fluorescent sterols, such as cholestatrienol and dehydroergosterol (Figure 2-1, B, C), are generally accepted to be

reasonably good models for native Chol. However, they do show differences in NMR order parameters relative to Chol, and their rapid photobleaching and requirement for UV excitation limit their utility for studying biological samples.[28, 30, 32-33] The two alternate approaches of attaching a fluorophore to either the alkyl side chain or the hydroxyl group of the sterol backbone have met with limited success. As summarized in the introduction, the attachment of polar fluorophores to the alkyl chain generally decreases the affinity for ordered domains and has the added complication of reversing the orientation of Chol so that the fluorophore labelled tail, rather than the hydroxyl group, is positioned in the polar headgroup region of the bilayer. This limitation can be overcome by conjugation of the relatively non-polar Bodipy to the alkyl chain (so-called Bodipy "free" cholesterol, Bodipy-FChol, Figure 2-1 E). The "upright" orientation of this probe in the bilayer is maintained and its partitioning behaviour in supported bilayers varies significantly different for mixtures containing C_{16}-SM, C_{18}-SM and brain SM, based on qualitative measurements of fluorescence intensities.[35] Measured partition coefficients, $K_p(L_o/L_d)$, of 1.9 and 0.8 for DOPC/ESM/Chol GUVs and DOPC/C_{18}-SM/Chol supported bilayers confirm the strong dependence on the chain length and heterogeneity of the SM component.[13, 36] Interestingly, the three carbamate linked NBD-Chols studied here show a similar reversal in partitioning for DPPC vs SM, but not for ESM vs brain SM. Although the Bodipy-FChol has the advantage of a higher quantum yield, the use of hydroxyl-labelled Chols may be advantageous in cases where it is preferable to avoid introducing a dye in the bilayer interior.

Although several Chol analogs with doxyl spin labels attached to the hydroxyl group adequately model the behaviour of natural Chol,[32] hydroxyl labelling is not a generally

successful strategy. For example, a Bodipy Chol ester with the dye attached via a C_{12} alkyl chain (Figure 2-1 F) partitions strongly into L_d domains (K_p (L_o/L_d) = 0.16) in DOPC/SM/Chol supported bilayers as measured by FCS).[37] By contrast, the carbamate-linked NBD Chols that we have synthesized show significantly stronger preferences for the L_o phase in both DPPC and ESM ternary lipid mixtures. This confirms our hypothesis that the partitioning of the Bodipy Chol ester is dominated by the propensity for Bodipy to insert into the alkyl chain region of the membrane, disrupting lipid packing. The carbamate linked NBD probes also show close to 2-fold higher partitioning into L_o domains than does the commercial ester-linked NBD probe, **5**. Like hydroxyl groups, carbamates can act as both hydrogen bond donors and acceptors, and the presence of this functional group may allow these probes to behave more like free Chol in model membranes. The Dansyl analog, **4**, has a considerably lower I_{Lo}/I_{Ld} than any of the NBD-Chol analogs in both ESM and DPPC mixtures. This is likely due to incorporation of the less polar Dansyl into the hydrophobic region of the bilayer, similar to Bodipy. Although quantum yields for **4** in vesicles were not measured, literature data on solvatochromic properties of Dansyl fluorophores suggest that variations in fluorescence efficiency will be comparable to those for NBD.[58]

The ability of probe **2** to mimic the well-known exclusion of Chol from Cer-rich membrane domains was also examined. The displacement of **2** from Cer domains was confirmed by correlated AFM and fluorescence imaging. A number of methods have provided convincing evidence for the expulsion of Chol by Cer[12, 16-19] and Bodipy-FChol has recently provided the first direct optical visualization of this phenomenon in DOPC/SM/Chol/Cer supported bilayers.[13] However, unlike Bodipy-FChol, NBD-Chol **2** has the advantage of allowing simultaneous

visualization of all three coexisting phases (Cer-rich, L_o and L_d) produced by direct incorporation of Cer in DOPC/ESM/Chol bilayers with a single probe. Together, our work plus the previous study using Bodipy-FChol, suggest that designing a probe to reproduce the exclusion of Chol from Cer-rich domains is more straightforward than designing one to mimic the more subtle interactions of Chol with PC or SM in L_o domains.

2.3.3 Probing Cholesterol Redistribution During *in Situ* Generation of Ceramide

NBD-Chol **2** was used to follow changes in bilayer morphology and Chol redistribution during enzymatic generation of Cer in DOPC/ESM/Chol bilayers. Although the initial fluorescence intensities for probe **2** are similar in L_o domains and the surrounding L_d phase, the contrast is adequate to visualize the domains and to show that the overall bilayer restructuring induced by SMase is analogous to that observed in our earlier studies using Texas Red-DHPE, which has a strong preference for the L_d phase.[24-25] The use of NBD-Chol **2** has two important advantages, as discussed below: (1) it allows visualization of the dynamic reorganization of Chol during enzyme activity and (2) it provides information on the composition of various regions of the restructured bilayer.

Bilayers that initially have only two levels of fluorescence intensity, corresponding to L_d and L_o phases identified by AFM, evolve to show greater heterogeneity upon exposure to SMase. The L_o domains show progressively lower fluorescence intensity, with concomitant formation of bright rings of fluid phase around large dye-excluded patches (Figure 2-10). This provides the first direct visualization of the dynamic displacement of Chol from liquid-ordered domains in response to *in situ* enzymatic Cer production. Changes in domain structure and evolution from a mixture of L_o and L_d phases to a gel and liquid phase has been reported after enzymatic

generation of Cer in GUVs of ternary lipid mixtures.[26] A related fluorescence microscopy study has provided evidence for pore formation and vesicle collapse for SMase-treated GUVs.[23] Of particular interest, Silva et al have examined enzymatic hydrolysis of SM in PSM/POPC/Chol vesicles, a lipid mixture for which a detailed phase diagram is available.[27] This work demonstrated that the physical properties of the membrane strongly modulate SMase activity with phase-separated (L_o/L_d) mixtures showing higher activity. The effects of Cer were dependent on the Chol concentration, leading to the hypothesis that Chol in particular, and lipid rafts in general, function as modulators of SMase in cells.[27] The development of specific probes to track Chol will facilitate a better understanding of the complex bilayer changes that occur after enzymatic Cer generation, as illustrated here for one lipid mixture.

The domain heterogeneity produced by Cer generation and concomitant Chol expulsion are clearly visualized by AFM which shows raised Cer-enriched regions around many of the initial L_o domains. These Cer "fences" are believed to form at the perimeter of the SM-rich domains because the interface between the two phases is disordered, facilitating access of the enzyme to its substrate.[14, 59-60] Although the domain heterogeneity is typically below the resolution limit of fluorescence microscopy, there are some larger domains that do show two levels of fluorescence after enzyme treatment (Figure 2-10), with the darker domain perimeter corresponding to raised domain edges in the AFM. Moreover, the implementation of a contrast-enhanced imaging approach, through the use of the NBD-Chol **2** and TR-DHPE FRET pair, enables improved optical visualization of these heterogeneous features within the domains (Figure 2-12). The loss of **2** from the Cer-enriched regions in enzyme-treated bilayers is

consistent with the exclusion of probe **2** from Cer-enriched domains when Cer is directly incorporated in DOPC/ESM/Chol bilayers.

In addition to observing the dynamic reorganization of Chol, probe **2** provides insight on the composition of the large dye-excluded patches that form during enzyme activity. In earlier studies using AFM and fluorescence imaging with Texas Red-DHPE as a probe, it was not possible to assign the composition of these new membrane regions. Although we initially hypothesized that the dye-excluded patches were enriched in Chol, AFM showed that they had high lateral adhesion, more consistent with Cer-enriched regions.[14, 25] The use of probe **2** demonstrates that the large dye-excluded patches that form during enzyme activity exclude Chol, leading to the conclusion that they are Cer enriched membrane regions. The hypothesis that SMase activity causes coalescence of small raft domains to form larger Cer platforms has been postulated to provide a mechanism for modulating signalling processes.[4-5] Nevertheless, most of the available evidence suggests that Cer forms small gel phase domains that are unlikely to localize membrane proteins. The recent study of Cer-induced membrane alterations by Silva *et al.* has suggested that platforms may be Chol-enriched SM-depleted L_d domains.[27] Our work indicates that larger Cer-enriched regions can form, at least in supported bilayers. Additional studies of the properties of these Cer-enriched regions and their ability to include signalling molecules will be necessary to assess their relevance to the Cer-enriched platforms that are hypothesized to form in cells.

2.4 Summary of Findings and Outlook

A series of Chol probes with NBD attached to the 3-hydroxyl position via carbamate linkers with variable lengths has been synthesized based on rational-design principles. The photophysical properties of the probes have been characterized and their partitioning in phase-separated supported bilayers quantified based on L_o/L_d fluorescence intensity ratios. The carbamate-linked NBD Chols show a stronger preference for partitioning into L_o domains than does a structurally similar probe with an ester linkage, **5**, illustrating the importance of careful optimization of probe and linker to provide the best mimic of free Chol. Comparison of the partitioning of NBD probes to available literature data for Chol indicates that the probes reproduce well the relatively modest enrichment of Chol in L_o vs L_d domains for DOPC/DPPC/Chol mixtures as well as the Cer-induced displacement of Chol. Probe **2** was used to follow the dynamic redistribution of Chol in phase-separated membrane in response to *in situ* Cer generation. This provides the first direct optical visualization of Chol redistribution during enzymatic Cer generation and allows the assignment of new bilayer regions that exclude dye and have high lateral adhesion to Cer-rich regions. Furthermore, we observed that labelling the bilayers with an NBD-Chol and TR-DHPE probe combination allowed us to resolve domain heterogeneity owing to Cer-enriched subdomains that was not evident when using either of the two dyes independently. Overall this study illustrates the feasibility of the rational design of fluorophore-labelled lipids to track specific bilayer components and the utility of a correlated AFM-fluorescence imaging approach for probing complex bilayer morphology.

2.5 Experimental

2.5.1 Materials

Dioleolylphosphatidylcholine (DOPC), dipalmitoylphosphatidylcholine **(**DPPC), chicken egg sphingomyelin (ESM), C16:0 ceramide (Cer), cholesterol (Chol), 1,2-dipalmitoyl-*sn*-glycero-3-phospho ethanolamine-*N*-(7-nitro-2-1,3-benzoxadiazol-4-yl) (ammonium salt) (*N*-NBD-DHPE), and 5-cholesten-3ß-ol 6-[(7-nitro-2-1,3-benzoxadiazol-4-yl)amino]caproate (NBD-6 Chol, **5**) were purchased from Avanti Polar Lipids (Alabaster, AL) and were used as received. Texas Red 1,2-dihexadecanoyl-*sn*-glycero-3-phosphoethanolamine, triethyl-ammonium salt (TR-DHPE) was obtained from Invitrogen (Eugene, OR). Chol analogues **1**-**4** were synthesized from Chol and NBD-alkylendiamines as described in section 2.5.2. Sphingomyelinase (SMase) isolated from *Staphylococcus aureus* was obtained from Sigma-Aldrich. All aqueous solutions were prepared using 18.3 MΩ·cm *Milli-Q* water. SMase buffer: 125 mM NaCl, 10 mM $CaCl_2$, 2 mM $MgCl_2$, 10 mM HEPES, pH 7.4.

2.5.2 Synthesis of Fluorescent Cholesterol Analogs

All ^{1}H NMR and ^{13}C NMR spectra were recorded in $CDCl_3$ on a Bruker AVANCE 400 instrument at room temperature. Chemical shifts are reported relative to TMS. Complete NMR spectra can be found in the appendix found at the end of this volume.

Synthesis of mono-protected diamines; general procedure for *N*-*tert*-butoxycarbonyl-α,ω-alkanediamines [$H_2N(CH_2)_xNHBOC$; x = 2, 4, 6]

A solution of di-tert-butyl dicarbonate (Boc_2O, 50 mg, 229 μmol) in dioxane (5 mL) was added over a period of 2.5 h to a solution of 1,2-diaminoethane (108.8 mg, 1.8 mmol) in dioxane (5 mL). The mixture was allowed to stir for 22 h and the solvent was then removed

using a rotary evaporator. Water (10 mL) was added to the residue and the insoluble bis-substituted product was removed by filtration. The filtrate was extracted with dichloromethane (DCM, 3 x 10 mL) and the DCM evaporated to yield the mono-protected diamine as an oil (32.5 mg, 89%).

1,4-diaminobutane and 1,6-diaminohexane were mono-protected following a similar procedure with comparable yields obtained.

General procedure for the synthesis of *N*-(*tert*-Butoxycarbonyl)-*N'*-(4-nitrobenz-2-oxa-1,3-diazole)alkylendiamines

A solution of 7-nitrobenzo-2-oxa-1,3-diazol-4-yl chloride (NBD-Cl, 50 mg, 251 μmol) in 0.5 mL of anhydrous DMF was added dropwise in 5 min., under a nitrogen atmosphere at room temperature, to a stirred solution of the appropriate mono-BOC protected diamine (*N*-BOC-1,2-diaminoethane) (52.3 mg, 363 μmol) and triethylamine (51 μL, 377 μmol) in 0.5 mL of the same solvent. The dark solution was stirred at room temperature with the exclusion of light for 30min at which time complete consumption of NBD-Cl was confirmed (TLC analysis). The mixture was diluted with water and extracted with DCM. The organic phase was dried over MgSO4 and evaporated prior to purification by column chromatography (hexane/EtOAc 3:7) to afford 64 mg (79%) of the NBD-functionalized derivative.

N-BOC-1,4-diaminobutane and *N*-BOC-1,6-diaminohexane were also treated with NBD-Cl under the same conditions to give the corresponding NBD-alkylendiamines in similar yields.

NBD-Cholesterols 1-3 from cholesterol and NBD-diamines; general procedure

A solution of cholesterol (50.3 mg, 130 μmol) and N,N-diisopropylethylamine (DIPEA, 33.6 mg, 260 μmol) in DCM (5 mL) was cooled to 0 °C under a nitrogen atmosphere; to this was

added in a drop-wise manner a phosgene solution (10% w/v in toluene, 320 μL, 650 μmol) with stirring. The reaction was allowed to stir to completion following a gradual rise to room temperature (~1 hr, monitored by TLC using hexane/EtOAc, 4:1). After the solvent and the excess phosgene were removed under reduced pressure, the crude cholesteryl chloroformate was re-suspended in DCM (2mL) under a nitrogen atmosphere. In a separate flask, BOC-NBD-diaminobutane (38.0 mg, 108 μmol) was dissolved in 4:1 DCM:trifluoroacetic acid (TFA, 1 mL) and allowed to stir for 30 min at room temperature (TLC hexane/EtOAc, 4:6). The de-protected NBD-diamine was concentrated under reduced pressure; it was then re-suspended in benzene and once again concentrated at low pressure to remove residual TFA (repeated twice). Subsequently the NBD-diaminobutane (27.2 mg, 108 μmol) and DIPEA (55.8 mg, 432 μmol) were dissolved in DCM (2 mL). This preparation was slowly added by syringe to the solution of cholesteryl chloroformate; the mixture was then allowed to stir overnight to completion (TLC hexane/EtOAc, 1:1). The solution was then diluted with DCM, washed with water, then saturated $NaHCO_3$, and finally brine before being dried over $MgSO_4$. 49.3 mg (69%) of compound **2** was obtained following purification by column chromatography (hexane/EtOAc, 4:1).

Compounds **1** and **3** were prepared following the same procedure as **2** and were obtained in similar yields.

***N*^{1}- Cholesterylcarbamoyl-*N*^{2}-(4-nitrobenzo-2-oxa-1,3-diazole)-ethyl-1,2-diamine**

(NBD-cholesterol 1) IR (neat) 3330, 1713 cm^{-1}; ^{1}H NMR δ 8.48 (d, 1H, *J* = 8.9 Hz), 7.53 (br, 1H), 6.18 (d, 1H, *J* = 8.8 Hz), 5.39-5.38 (m, 1H), 5.13 (br, 1H), 4.59-4.52 (m, 1H), 3.67-3.58 (m, 4H), 2.38-2.21 (m, 2H), 2.05-0.82 (m, 38H), 0.67 (s, 3H); ^{13}C NMR δ 157.9 s, 144.3 s, 143.9 s, 139.4 s,

136.4 d, 125.1 s, 123.0 d, 99.1 d, 75.6 d, 56.7 d, 56.1 d, 50.0 d, 42.3 t, 39.7 t, 39.5 t, 38.4 t, 36.9 t, 36.6 s, 36.2 t, 35.8 d, 32.0 d, 31.9 t, 31.0 d, 29.8 t, 28.3 t, 28.0 t, 24.3 t, 23.9 t, 22.8 q, 22.6 q, 21.1 t, 19.3 q, 18.7 q, 11.9 q; MS (ES+) 636.2 (MH^+)

N^1- Cholesterylcarbamoyl-N^4-(4-nitrobenzo-2-oxa-1,3-diazole)-butyl-1,4-diamine

(NBD-cholesterol 2) IR (neat) 3340, 1697 cm^{-1}; ^1H NMR δ 8.46 (d, 1H, *J* = 8.4 Hz), 6.73 (br, 1H), 6.19 (d, 1H, *J* = 8.8 Hz), 5.35-5.34 (m, 1H), 4.79 (br, 1H), 4.52-4.46 (m, 1H), 3.57-3.55 (m, 2H), 3.27 (m, 2H), 2.37-2.20 (m, 2H), 2.03-0.84 (m, 42H), 0.67 (s, 3H); ^{13}C NMR δ 156.5 s, 144.2 s, 143.9 s, 139.6 s, 136.5 d, 123.7 s, 122.6 d, 98.7 d, 74.6 d, 56.6 d, 56.1 d, 50.0 d, 43.7 t, 42.3 s, 39.7 t, 39.5 t, 38.5 t, 36.9 t, 36.5 s, 36.1 t, 35.8 d, 31.9 t, 31.8 d, 28.2 t, 28.1 t, 28.0 d, 27.8 t, 25.4 t, 24.2 t, 23.8 t, 22.8 q, 22.5 q, 21.0 t, 19.3 q, 18.7 q, 11.8 q; MS (ES+) 664.5 (MH^+)

N^1- Cholesterylcarbamoyl-N^6-(4-nitrobenzo-2-oxa-1,3-diazole)-hexyl-1,6-diamine

(NBD-cholesterol 3) IR (neat) 3360, 1701 cm^{-1}; ^1H NMR δ 8.41 (d, 1H, *J* = 8.4 Hz), 7.03 (br, 1H), 6.15 (d, 1H, *J* = 8.4 Hz), 5.28 (br, 1H), 4.81 (br, 1H), 4.43 (br, 1H), 3.50 (br, 2H). 3.16-3.14 (m, 2H), 2.35-2.16 (m, 2H), 2.02-0.77 (m, 46H), 0.62 (s, 3H); ^{13}C NMR δ 156.6 s, 144.4 s, 144.2 s, 140.0 s, 137.0 d, 123.3 s, 122.6 d, 98.8 d, 74.5 d, 56.8 d, 56.3 d, 50.2 d, 44.1 t, 42.5 s, 40.7 t, 39.9 t, 39.7 t, 38.8 t, 37.2 t, 36.7 s, 36.4 t, 36.0 d, 32.1 t, 32.0 d, 30.1 t, 28.4 t, 28.3 t, 28.2 d, 26.5 t, 26.3 t, 24.4 t, 24.0 t, 23.0 q, 22.8 q, 21.2 t, 19.5 q, 18.9 q, 12.0 q; MS (ES+) 692.5 (MH^+)

Procedure for the synthesis of N^1-(*tert*-Butoxycarbonyl)-N^4-(5-(dimethylamino) naphthalene-1-sulfonamide)-butyl-1,4-diamine

A solution of mono-protected BOC-diaminobutane (723.3 mg, 3.8 mmol) and triethylamine (1125 mg, 11.1 mmol) was prepared in DCM (20 mL) under a nitrogen atmosphere. In a separate flask Dansyl chloride (700 mg, 2.5 mmol) was dissolved in DCM (20 ml); it was then

transferred slowly by canula into the first flask, and allowed to sit for 30 min at room temperature with stirring (TLC hexane/EtOAc, 1:1). The solution was subsequently diluted with EtOAc, washed with 10% HCl, then saturated $NaHCO_3$, and lastly brine before being dried over $MgSO_4$. Purification was by column chromatography (hexane/EtOAc, 6:4) to obtain 758 mg (72%) of BOC-Dansyl-diaminobutane.

Dansyl-Cholesterol 4 from cholesterol and BOC-Dansyl-diaminobutane

A solution of cholesterol (76 mg, 198 μmol) and triethylamine (40 mg, 396 μmol) in DCM (4 mL) was cooled to 0 ºC under a nitrogen atmosphere; to this was added in a drop-wise manner a phosgene solution (10% w/v in toluene, 490 μL, 990 μmol) with stirring. The reaction was allowed to stir to completion following a gradual rise to room temperature (~ 1 hr, monitored by TLC using hexane/EtOAc, 4:1). After the solvent and the excess phosgene were removed under reduced pressure, the crude cholesteryl chloroformate was re-suspended in DCM (2 mL) under a nitrogen atmosphere. In a separate flask, BOC-Dansyl-diaminobutane (50 mg, 119 μmol) was dissolved in 4:1 DCM:TFA (5 mL) and allowed to stir for 30 min at room temperature (TLC hexane/EtOAc, 1:1). The de-protected NBD-diamine was concentrated under reduced pressure; it was then re-suspended in benzene and once again concentrated at low pressure to remove residual TFA (repeated twice). Subsequently the Dansyl-diaminobutane (35.6 mg, 108 μmol) and triethylamine (113 mg, 1.1 mmol) were dissolved in DCM (2 mL). This preparation was slowly added by syringe to the solution of cholesteryl chloroformate; the mixture was then allowed to stir overnight to completion (TLC hexane/EtOAc, 1:1). The solution was then diluted with EtOAc, washed with water, followed by saturated $NaHCO_3$, and finally brine before being

dried over $MgSO_4$. 43.9 mg (51%) of compound **4** was obtained following purification by column chromatography (hexane/EtOAc, 7:3).

***N*^{1}- Cholesterylcarbamoyl-*N*^{4}-(dimethylamino) naphthalene-1-sulfonamide)-butyl-1,4-diamine (Dansyl-cholesterol 4**) IR (neat) 3350, 1703 cm^{-1}; 1H NMR δ 8.55 (d, 1H, *J* = 8.4 Hz), 8.29 (d, 1H, *J* = 8.8 Hz), 8.24 (dd, 1H, *J* = 7.2, 1.2 Hz), 7.56 (dd, 1H, *J* = 8.8, 8.0 Hz), 7.52 (dd, 1H, *J* = 8.4, 7.6 Hz), 7.19 (d, 1H, *J* = 7.6 Hz), 5.36-5.35 (m, 1H), 4.94 (br, 1H), 4.52-4.50 (m, 1H), 4.46-4.45(m, 1H), 3.01-3.00 (m, 2H), 2.90-2.89 (m, 8H), 2.33-2.24 (m, 2H), 2.03-0.85 (m, 42H), 0.67 (s, 3H); ^{13}C NMR δ 156.3 s, 140.0 s, 134.8 s, 130.5 d, 129.7 d, 129.6 s, 128.5 d, 123.3 d, 122.6 d, 115.3 d, 74.3 d, 56.8 d, 56.2 d, 50.1 d, 45.5 q, 43.0 t, 42.4 s, 39.8 t, 39.6 t, 38.6 t, 37.1 t, 36.6 s, 36.3 t, 35.9 d, 32.0 t, 31.9 d, 28.3 t, 28.2 t, 28.1 d, 27.1 t, 26.7 t, 24.4 t, 23.9 t, 22.9 q, 22.6 q, 21.1 t, 19.4 q, 18.8 q, 11.9 q; MS (ES+) 734.5 (MH^+).

2.5.3 Preparation of Bilayers

Small unilamellar vesicles were prepared with minor adjustments to a previously described protocol [14]. Briefly, chloroform solutions of phospholipids and dye-labelled lipids were mixed in the appropriate ratios and the lipid films obtained after evaporating the solvent were hydrated in water. The samples were then sonicated in a bath sonicator to clarity to form SUVs with a final lipid concentration of 0.5 mg/mL. All vesicle solutions were sonicated at temperatures above the T_m of the constituent lipids and were used immediately or stored at 4 ºC for up to 1 week prior to use.

Planar supported bilayers were formed on mica via vesicle fusion. Vesicle solution (60 µl) and 750 µl $CaCl_2$ (15 mM) were added to freshly cleaved mica (15- 25 µm thick for fluorescence imaging) clamped in a liquid cell. After incubation at 45 °C for 60 min, bilayers were gradually

cooled to RT over a period of two hours, and then gently washed with Milli-Q water to remove unattached vesicles before imaging. The presence of occasional defects allowed us to measure the bilayer thickness, confirming the presence of a single bilayer.

2.5.4 Spectroscopic Measurements

Absorption spectra were measured with a Cary 5000 UV-Vis-NIR spectrophotometer at 22 °C, using a 1-cm-path length quartz cuvette. Absorption spectra for NBD-labelled Chols **1**-**3** and **5**, and *N*-NBD-DHPE were measured in water at 0.5 mol percent dye to total lipid in vesicles, with the total lipid concentration at 1.3 x 10^{-3}M. The spectra of vesicle solutions containing dye-labelled lipids were corrected for scattering using a vesicle solution of the same lipid composition in the absence of dye. Emission spectra were recorded at 22 °C using a Horiba Jobin Yvon FL3-21 2tau spectrofluorometer with slit widths of 1 nm. Fluorescence quantum yields Φ were obtained with reference to N-NBD-DHPE in vesicles of egg yolk PC (Φ = 0.16 [38]) at an excitation wavelength of 470 nm and absorbance < 0.2.

2.5.5 Fluorescence Microscopy

Fluorescence images of bilayers were measured in total internal reflection fluorescence (TIRF) mode on an Olympus 1X81 microscope equipped with a high resolution CCD camera (CoolSNAP, Photometrics, US) and a 60x/1.45 NA Plan Apochromat objective. The NBD-labelled Chols were excited at 488 nm and emission collected at 530 (±20) nm. Dansyl-Chol fluorescence images were obtained using an arc lamp and a UV excitation/visible emission filter set (Semrock). For SMase treatment, the bilayers were washed with SMase buffer and imaged. The effect of enzyme on the bilayer was followed in time by imaging the same area before and after addition of buffered enzyme solution at room temperature. Control experiments indicated that

irradiation of bilayers containing NBD-Chol **2** for similar time periods to those used for the SMase treatments led to no changes in bilayer morphology, although significant photobleaching of the dye was observed. The use of TIRF microscopy is an advantage, even for thin bilayer samples, because background fluorescence from residual vesicles in solution does not contribute to the bilayer signals. This is particularly useful for studies of SMase-treated bilayers since enzyme activity frequently leads to release of fluorescent vesicles into solution.

For the fluorescence intensity analysis, the intensity counts of adjacent domain and fluid phase regions were obtained using ImagePro software. A background fluorescence count was obtained by either completely bleaching an area immediately adjacent to the area of interest or by using a bilayer defect in the region of interest. Care was taken to ensure that background, domain and fluid phase intensities were measured in areas of uniform excitation intensity to minimize effects due to variation in excitation intensity across the field of view. Several different areas were imaged for each sample. The relative intensities of adjacent L_d fluid-phase and L_o domains were taken from intensity cross-sections of the area-of-interest. These values were then corrected for background fluorescence to give an L_d/L_o intensity ratio (I_{Lo}/I_{Ld}). A minimum of ten corrected I_{Lo}/I_{Ld} values were collected per region (approximately 100 μm^2), and a number of different samples were measured for each analog to check for reproducibility.

2.5.6 Quantification of Bilayer Standards

Relative quantum yield measurements for supported bilayers were measured using a recently reported procedure for quantifying fluorescence microscopy data using supported bilayer standards [48]. First, plots of fluorescence intensity vs [probe **2**] in DOPC bilayers were measured (in epifluorescence mode on an IX81 inverted optical microscope using lamp

excitation) and shown to be linear between 0.1 and 1.0 mol% dye. Then fluorescence intensities for single phase bilayers of DOPC, DOPC/Chol, DOPC/ESM and DOPC/DPPC (all 2/1 molar ratios) containing 0.5 mol% **2** were measured under matched conditions. To account for variations in spectral properties of the probe in different lipid environments the intensity data was corrected using a scaling factor measured on the same microscope. This was accomplished by measuring the fluorescence intensity of vesicle solutions used to prepare the supported bilayers by focusing the excitation laser deep into the sample and verifying that the intensity measured did not vary with small changes in the focus. The ratio of corrected intensities for DOPC/Chol and DPPC (or ESM)/Chol bilayers provides an estimate of the relative quantum yields for probe **2** in L_o/L_d phases.

2.5.7 Correlated Fluorescence-Atomic Force Microscopy

Correlated images were recorded using a JPK NanoWizard®II BioAFM (JPK Instruments, Berlin, Germany) integrated with an Olympus IX81 inverted optical microscope. AFM was performed in contact mode and images were captured using DNP-S (Veeco, CA) AFM cantilever/tips with spring constants of 0.15-0.32 N/m. Images were recorded in both topographic and lateral deflection modes. The contrast in lateral deflection scans depends strongly on the normal force applied to the sample and the scan speed. Fluorescence images were obtained using lamp excitation with a 100x oil immersion objective (Olympus), FITC WF filter set (Chroma Technology) and a high resolution CCD camera (CoolSNAP, Photometrics).

Solid-supported bilayers of the desired composition were prepared and AFM and fluorescence images of the same sample area were recorded sequentially, after locating a suitable sample region. Fluorescence images had acquisition times of < 3 s, much shorter than

the ~10 minutes required to obtain the AFM images. Typically fluorescence images were recorded both before and after AFM images of the same area to verify that the membrane morphology had not changed dramatically during the time required for AFM imaging. For SMase treatment the bilayer was imaged in water (using both techniques) prior to replacing the water with a known volume of buffered enzyme solution; this was followed by incubating the sample at room temperature for 10-20 min while following its evolution by fluorescence microscopy. The sample was then rinsed extensively with water and re-imaged by both AFM and fluorescence.

2.6 References

1. Simons, K.; Vaz, W. L., Model systems, lipid rafts and cell membranes. *Annu. Rev. Biophys. Biomol. Struct.* **2004,** *33*, 269-295.

2. Simons, K.; Ikonen, E., Functional rafts in cell membranes. *Nature* **1997,** *387*, 569-572.

3. Mayor, S.; Rao, M., Rafts: scale-dependent, active lipid organization at the cell surface. *Traffic* **2004,** *5*, 231-240.

4. Cremesti, A. E.; Goni, F. M.; Kolesnick, R., Role of sphingomyelinase and ceramide in modulating rafts: do biophysical propoerties determine biologic outcome? *FEBS Lett.* **2002,** *531*, 47-53.

5. Bollinger, C. R.; Teichgraber, V.; Gulbins, E., Ceramide-enriched membrane domains. *Biochim. Biophys. Acta* **2005,** *1746*, 284-294.

6. Kolesnick, R. N.; Goni, F. M.; Alonso, A., Compartmentalization of ceramide signaling: physical foundations and biological effects. *J Cell Physiol.* **2000,** *184* (3), 285-300.

7. Hannun, Y. A.; Luberto, C.; Argraves, K. M., Enzymes of sphingolipid metabolism: from modular to integrative signaling. *Biochem.* **2001,** *40* (16), 4893-903.

8. Goni, F. M.; Alonso, A., Effects of ceramide and other simple sphingolipids on membrane lateral structure. *Biochim. Biophys. Acta* **2009,** *1788*, 169-177.

9. Lagerholm, B. C.; Weinreb, G. E.; Jacobson, K.; Thompson, N. L., Detecting microdomains in intact cell membranes. *Annu. Rev. Phys. Chem.* **2005,** *56*, 309-336.

10. London, E., How principles of domain formation in model membranes may explain ambiguities concerning lipid raft formation in cells. *Biochim Biophys Acta* **2005,** *1746*, 203-220.

11. Veatch, S. L.; Keller, S. L., Seeing spots: Complex phase behavior in simple membranes. *Biochim Biophys Acta* **2005,** *1746*, 172-185.

12. Chiantia, S.; Kahya, N.; Ries, H.; Schwille, P., Effects of ceramide on liquid-ordered domains investigated by simultaneous AFM and FCS. *Biophys. J.* **2006,** *90*, 4500-4508.

13. Chiantia, S.; Ries, J.; Chwastek, G.; Carrer, D.; Li, Z.; Bittman, R.; Schwille, P., Role of ceramide in membrane protein organization investigated by combined AFM and FCS. *Biochim. Biophys. Acta* **2008,** *1778*, 1356-1364.

14. Ira; Johnston, L. J., Ceramide promotes restructuring of model raft membranes. *Langmuir* **2006,** *22*, 11284-11289.

15. Silva, L.; de Almeida, R. F. M.; Federov, A.; Matos, A. P. A.; Prieto, M., Ceramide-platform formation and induced biophysical changes in a fluid phospholipid membrane. *Mol. Membr. Biol.* **2006,** *23*, 137-148.

16. Silva, L. C.; de Almeida, R. F. M.; Castro, B. M.; Fedorov, A.; Prieto, M., Ceramide-domain formation and collapse in lipid rafts: Membrane reorganization by an apoptotic lipid. *Biophys. J.* **2007,** *92*, 502-516.

17. Megha; Sawatzki, P.; Kolter, T.; Bittman, R.; London, E., Effect of ceramide N-acyl chain and polar headgroup structure on the properties of ordered lipid domains (lipid rafts). *Biochim. Biophys. Acta* **2007,** *1768*, 2205-2212.

18. Megha; London, E., Ceramide selectively displaces cholesterol from ordered lipid domains (rafts): implications for lipid raft structure and function. *J. Biol. Chem.* **2004,** *279* (11), 9997-10004.

19. Ali, M. R.; Cheng, K. H.; Huang, J., Ceramide drives cholesterol out of the ordered lipid bilayer phase into the crystal phase in 1-palmitoyl-2-oleoyl-sn-glycero-3-phosphocholine/cholesterol/ceramide ternary mixtures. *Biochem.* **2006,** *45*, 12629-12638.

20. Sot, J.; Ibarguren, M.; Busto, J. V.; Montes, L.-R.; Goni, F. M.; Alonso, A., Cholesterol displacement by ceramide in sphingomyelin-containing liquid-ordered domains, and in generation of gel regions in giant lipidic vesicles. *FEBS Lett.* **2008,** *582*, 3230-3236.

21. Nurminen, T. A.; Holopainen, J. M.; Zhao, H.; Kinnunen, P. K., Observation of topical catalysis by sphingomyelinase coupled to microspheres. *J. Am. Chem. Soc.* **2002,** *124* (41), 12129-34.

22. Carrer, D. C.; Maggio, B., Phase behavior and molecular interactions in mixtures of ceramide with dipalmitoylphosphatidylcholine. *J. Lipid Res.* **1999,** *40*, 1978-1989.

23. Lopez-Mentero, I.; Velez, M.; Devaux, P. F., Surface tension induced by sphingomyelin to ceramide conversion in lipid membranes. *Biochim. Biophys. Acta* **2007,** *1768*, 553-561.

24. Ira; Johnston, L. J., Sphingomyelinase generation of ceramide promotes clustering of nanoscale domains in supported bilayer membranes. *Biochim. Biophys. Acta* **2008,** *1778*, 185-197.

25. Ira; Zou, S.; Carter Ramirez, D.; Vanderlip, S.; Ogilvie, W.; Jakubek, Z.; Johnston, L. J., Enzymatic Generation of Ceramide Induces Membrane Restructuring: Correlated AFM and Fluorescence Imaging of Supported Bilayers. *J. Struct. Biol.* **2009,** *in press*.

26. Taniguchi, Y.; Ohba, T.; Miyata, H.; Ohki, K., Rapid phase change of lipid microdomains in giant vesicles induced by conversion of sphingomyelin to ceramide. *Biochim. Biophys. Acta* **2006,** *1758*, 145-153.

27. Silva, L. C.; Futerman, A. H.; Prieto, M., Lipid raft composition modulates sphingomyelinase activity and ceramide-induced membrane physical alterations. *Biophys. J.* **2009,** *96*, 3210-3222.

28. Baumgart, T.; Hunt, G.; Farkas, E. R.; Webb, W. W.; Feigenson, G. W., Fluorescence probe partitioning between Lo/Ld phases in lipid membranes. *Biochim. Biophys. Acta* **2007,** *1768*, 2182-2194.

29. Sengupta, P.; Hammond, A.; Holowka, D.; Baird, B., Structural determinants for partitioning of lipids and proteins between coexisting fluid phases in giant plasma membrane vesicles. *Biochim. Biophys. Acta* **2008,** *1778*, 20-32.

30. Wustner, D., Fluorescent sterols as tools in membrane biophysics and cell biology. *Chem. Phys. Lipids* **2007,** *146*, 1-25.

31. Bjorkqvist, Y. J. E.; Nyholm, T. K. M.; Slotte, J. P.; Ramstedt, B., Domain formation and stability in complex lipid bilayers as reported by cholestatrienol. *Biophys. J.* **2005,** *88*, 4054-4063.

32. Scheidt, H. A.; Muller, P.; Herrmann, A.; Huster, D., The potential of fluorescent and spin-labeled steroid analogs to mimic natural cholesterol. *J. Biol. Chem.* **2003,** *278*, 45563-45569.

33. Wustner, D., Improved visualization and quantitative analysis of fluorescent membrane sterol in polarized hepatic cells. *J. Micros.* **2005,** *220*, 47-64.

34. Li, Z.; Mintzer, E.; Bittman, R., First synthesis of free cholesterol-BODIPY conjugates. *J. Org. Chem.* **2006,** *71*, 1718-1721.

35. Shaw, J. E.; Epand, R. F.; Epand, R. M.; Li, Z.; Bittman, R.; Yip, C. M., Correlated Fluorescence-Atomic Force Microscopy of Membrane Domains: Structure of Fluorescence Probes Determines Lipid Localization. *Biophys. J.* **2006,** *90*, 2170-2178.

36. Ariola, F. S.; Li, Z.; Cornejo, C.; Bittman, R.; Heikal, A. A., Membrane fluidity and lipid order in ternary giant unilamellar vesicles using a new Bodipy-cholesterol derivative. *Biophys. J.* **2009,** *96*, 2696-2708.

37. Chiantia, S.; Ries, J.; Kahya, N.; Schwille, P., Combined AFM and two-focus SFCS study of raft-exhibiting model membranes. *ChemPhysChem* **2006,** *7*, 2409-2418.

38. Mazeres, S.; Schram, V.; Tocanne, J.-F.; Lopez, A., 7-Nitrobenz-2-oxa-1,3-diazole-4-yl-labeled phospholipids in lipid membranes:differences in fluorescence behavior. *Biophys. J.* **1996,** *71*, 327-335.

39. Chattopadhyay, A., Chemistry and biology of N-(7-nitrobenz-2-oxa-1,3-diazol-4-yl)-labeled lipids: fluorescent probes of biological and model membranes. *Chem. Phys. Lipids* **1990,** *53*, 1-15.

40. Wiegand, V.; Chang, T.-Y.; Strauss, J. F.; Fahrenholz, F.; Gimpl, G., Transport of plasma membrane-derived cholesterol and the function of Niemann-Pick C1 protein. *FASEB J.* **2003,** *17*, 782-784.

41. Krapcho, A. P.; Kuell, C. S., Mono-protected diamines. N-tert-butoxylcarbonyl-α,ω-alkanediamines from α,ω-alkanediamines. *Synth. Commun.* **1990,** *20*, 2559-2564.

42. Taliani, S.; Simorini, F.; Segianni, V.; La Motta, C.; Da Settimo, F.; Cosimelli, B.; Abignente, E.; Greco, G.; Novellino, E.; Rossi, L.; Gremigni, V.; Spinetti, F.; Chelli, B.; Martini, C., New fluorescent 2-phenylindolglyoxylamide derivatives as probes targeting the peripheral-type benzodiazepine receptor: design, synthesis, and biological evaluation. *J. Med. Chem.* **2007,** *50*, 404-407.

43. Fery-Forgues, S.; Fayet, J.-P.; Lopez, A., Drastic changes in the fluorescence properties of NBD probes with the polarity of the medium: involvement of a TICT state? *J. Photochem. Photobiol. A: Chem.* **1993,** *70*, 229-243.

44. Veatch, S. L.; Keller, S. L., Separation of liquid phases in giant vesicles of ternary mixtures of phospholipids and cholesterol. *Biophys. J.* **2003,** *85*, 3074-3083.

45. Veatch, S. L.; Keller, S. L., Miscibility phase diagrams of giant vesicles containing sphingomyelin. *Phys. Rev. Lett.* **2005,** *94*, 148101-1-4.

46. Shaw, J. E.; Oreopoulos, J.; Wong, D.; Hsu, J. C. Y.; Yip, C. M., Coupling evanescent-wave fluorescence imaging and spectroscopy with scanning probe microscopy: challenges and insights from TIRF-AFM. *Surf. Interface Anal.* **2006,** *38*, 1459-1471.

47. Coste, V.; Puff, N.; Lockau, D.; Quinn, P. J.; Angelova, M. I., Raft-like domain formation in large unilamellar vesicles probes by the fluorescent phospholipid analogue, C12NBD-PC. *Biochem. Biophys. Acta* **2006,** *1758*, 460-467.

48. Galush, W. J.; Nye, J. A.; Groves, J. T., Quantitative fluorescence microscopy using supported lipid bilayer standards. *Biophys. J.* **2008,** *95*, 2512-2519.

49. Sullan, R. M. A.; Li, J. K.; Zou, S., Direct correlation of structures and nanomechanical properties of multicomponent lipid bilayers. *Langmuir* **2009,** *25*, 7471-7477.

50. Carter Ramirez, D. M.; Ding, J.; Guan, J.; Vobornik, D.; Carnini, A.; Ogilvie, W. W.; Jakubek, Z. J.; Johnston, L. J., A Forster resonance energy transfer (FRET) approach for enhancing fluorescence contrast in phase-separated membranes. *Can. J. Chem.* **2011,** *89*, 423-432.

51. Chiantia, S.; Kahya, N.; Ries, J.; Schwille, P., Effects of ceramide in liquid-ordered domains investigated by simultaneous AFM and FCS. *Biophys. J.* **2006,** *90*, 4500-4508.

52. Demchenko, A. P.; Mely, Y.; Duportail, G.; Klymchenko, A. S., Monitoring biophysical properties of lipid membranes by environment-sensitive fluorescent probes. *Biophys. J.* **2009,** *96*, 3461-70.

53. Oradd, G.; Westerman, P. W.; Lindblom, G., Lateral diffusion coefficients of spearate lipid species in a ternary raft-forming bilayer: a pfg-NMR multinuclear study. *Biophys. J.* **2005,** *89*, 315-320.

54. Veatch, S. L.; Polozov, I. V.; Gawrisch, K.; Keller, S. L., Liquid domains in vesicles investigated by NMR and fluorescence microscopy. *Biophys. J.* **2004,** *86*, 2910-2922.

55. Lindblom, G.; Oradd, G.; Filipov, A., Lipid lateral diffusion in bilayers with phopphatidylcholine, spingomylein and cholesterol. An NMR study of dynamics and lateral phase separation. *Chem. Phys. Lipids* **2006,** *141*, 179-184.

56. Frazier, M. L.; Wright, J. R.; Pokorny, A.; Almeida, P. F. F., Investigation of domain formation in sphingomyelin/cholesterol/POPC mixtures by fluorescence resonance energy transfer and Monte Carlo simulations. *Biophys. J.* **2007,** *92*, 2422-2433.

57. Tsamaloukas, A.; Szadkowska, H.; Heerklotz, H., Thermodynamic comparison of the interactions of cholesterol with unsaturated phospholipid and sphingomyelins. *Biophys. J.* **2006,** *90*, 4479-4487.

58. Li, Y.-H.; Chan, L.-M.; Tyer, L.; Moody, R. T.; Himel, C. M.; Hercules, D. M., Study of solvent effects on the fluorescence of 1-(Dimethylamino)-5-naphthalenesulfonic acid and related compounds. *J. Am. Chem. Soc.* **1975,** *97*, 3118-3126.

59. You, H. X.; Yu, L.; Qi, X., Phospholipid membrane restructuring induced by saposin C: a topographic study using atomic force microscopy. *FEBS Lett.* **2001,** *503*, 97-102.

60. Grandbois, M.; Clausen-Schaumann, H.; Gaub, H., Atomic force microscope imaging of phospholipid bilayer degradation by phospholipase A2. *Biophys. J.* **1998,** *74*, 2398-2404.

Chapter 3

Quantitative Fluorescence: Measuring Orientational Membrane Order with NBD-Cer

This Chapter Contains Material Adapted from the Following Manuscript

1. Carter Ramirez, D.M.; Jakubek, Z.J.; Lu, Z.; Ogilvie, W.W.; Johnston, L.J., A new probe to measure changes in orientational order associated with ceramide-mediated membrane reorganization. *Manuscript in Preparation*.

3.1 Introduction: Probing Orientational Order in Lipid Membranes

3.1.1 A Move Towards Quantitative Imaging Approaches

Fluorescence-based imaging has been widely used to examine phase separation and domain dynamics in lipid membranes.[1-6] The relative availability of basic fluorescence microscopes with millisecond-to-second temporal resolution and good detection sensitivity has made them a tool of first resort in descriptive or qualitative membrane studies. However, a thorough understanding of membrane microdomains and protein-lipid interactions also requires quantifiable data that can define molecular conformations and order/alignment, probe intermolecular forces, determine phase composition, or quantify lateral mobility within a membrane. We felt that having the ability to quantitatively assess order in planar supported bilayers could further our understanding of ceramide-dependent membrane reorganization in these model systems.[7-8] In this chapter we describe the synthesis and characterization of a novel fluorescent ceramide (Cer) analog, and evaluate its utility as a probe for monitoring changes in membrane order.

To date a number of established and emerging imaging techniques have been used to provide more quantitative characterization of lipid membranes. They include: coherent anti-Stokes Raman scattering microscopy, fluorescence lifetime imaging, fluorescence interference contrast microscopy, and secondary ion mass spectrometry imaging (SIMS).[9-14] Near-field scanning optical microscopy (NSOM) is a fluorescence-based imaging technique that has been used to probe membrane morphology and protein localization, and measure lateral diffusion with nanoscale resolution.[15-16] Far-field fluorescence super-resolution imaging methods including stimulated emission depletion microscopy (STED), photo-activated localization

microscopy (PALM), and point accumulation for imaging in nanoscale topography (PAINT) have also been applied to biological membrane studies.[17-18]

As discussed at length in Chapter 2, a coupled fluorescence and atomic force microscopy (AFM) approach can be used to examine membrane morphology and probe lipid-lipid and lipid-protein interactions in model membranes and cells.[8, 19-21] Parallelized fluorescence and AFM can also identify discrete lipid phases, and map the distribution of fluorescently labelled lipids and proteins against topography. Some recent investigations have supplemented this combinatorial approach by implementing fluorescence correlation spectroscopy (FCS), alongside or in place of AFM, to measure the lateral diffusion rates of fluorescently labelled lipids and proteins.[22-24] Coupling with AFM helps to offset the diffraction-limited nature of conventional optical microscopy and its reliance on fluorescent reporters. In its most widely used imaging modes, AFM lacks chemical specificity, and therefore structures can usually only be identified by size, shape, and bulk physical properties such as elasticity or compressibility. However, differences in optical properties of the reporter fluorophores such as emission wavelength, florescence lifetime, and the polarization anisotropy or linear dichroism can provide additional quantitative information regarding the probes' environment.[25] As such, this parallelized imaging approach can be extended to assess molecular orientations or conformations in membranes. One such combination of techniques is polarized total internal reflection fluorescence microscopy (pTIRFM)-AFM, which has been applied to parallelized imaging of orientational order and topography in model membranes.[21, 26-27] pTIRFM has also been widely used in a stand-alone approach to quantify topological changes and vesicular fusion in model lipid membranes and the plasma membranes of live cells.[28-32] The body of work presented here employs this

technique, complemented in some situations by AFM, to measure lipid order in some of the model membranes routinely studied in our group, and to quantify sphingomyelinase (SMase)-induced changes in their orientational order.

3.1.2 Order Parameters and Orientation Sensitive Techniques

The function of membrane-associated molecules stems in large part from their structure, interactions with other membrane components, and their alignment or orientation in the membrane. Orientational order in membranes can be quantitatively assessed through a time- and ensemble-averaged quantity defined as the order parameter. Order parameter measurements have contributed significantly to the characterization of membrane structure and dynamics, both in models and *in vivo*, and particularly to the study of lipid-protein interactions.[33-35] A number of orientation-sensitive techniques have been used to calculate orientational order parameters: ESR and NMR spectroscopy, wide angle x-ray scattering, optical birefringence, ultraviolet-visible linear dichroism spectroscopy, polarized attenuated total internal reflection Fourier transform infrared (pATR-FTIR) spectroscopy, polarized Raman spectroscopy, and time-resolved fluorescence polarization anisotropy.[36-42] These techniques differ from each other in terms of the molecular dipole interactions that they probe, their temporal resolution, and the number of order parameters they can assess.

Deuterated lipids have seen widespread use as probes in NMR measurements of membrane order. The carbon-deuterium NMR order parameter (S_{CD}) has been a particularly useful tool for characterizing the phase behaviour and molecular dynamics of mixtures of lipids and cholesterol in model membranes.[34, 43-47] The effect of cholesterol content and distribution on the phase state and order of naturally occurring lipids has also been assessed in fluorescence

polarization anisotropy studies on liposomes prepared from cellular membrane extracts.[33] Fluorophore-labelled lipids and proteins have also been employed to quantify molecular order and compartmentalization dynamics in membranes for over thirty years using a range of polarized fluorescence imaging approaches.[48-53] These techniques spatially detect fluorescent probes by relying on their dichroic absorption and/or anisotropic emission of polarized light, and can report on their orientation, conformation and rotational mobility.

3.1.3 Polarized Total Internal Reflection Fluorescence Microscopy (pTIRFM)

A theoretical overview of pTIRFM is presented here which draws on the work of Axelrod, Thompson, Yip and their respective research groups to briefly outline the principles behind the technique.[21, 54-55] Polarized light can be used to determine the orientational order of membrane components because photon absorption is dependent on the reporter's molecular orientation with respect to the polarization axis. As described in Chapter 1, in TIRFM of planar supported bilayers a surface-travelling electromagnetic wave is generated following TIR at the substrate/water interface (Figure 3-1). By measuring the dichroism of fluorescence as a function of the polarization angle ψ of the excitation light, we can probe the orientational order of fluorophores embedded in the supported membrane. Fluorescent molecules are excited if the electric field vector of this evanescent wave is aligned to the same polar angle as their absorption dipoles. Fluorophores oriented at different tilt angles relative to the substrate normal will therefore be preferentially excited at different polarization angles. The probe tilt angle (θ_c) can theoretically range from 0° indicating alignment with the substrate normal (the reference z-axis) to 90° which is indicative of an absorption dipole lying parallel to the substrate (Figure 3-1).

Figure 3-1. Polarized total internal reflection fluorescence microscopy (pTIRFM) exploits polarization-dependent differences in detected fluorescence intensity to quantify membrane order. Preferential excitation of fluorophores oriented at different angles with respect to the sample normal (z-axis) is achieved by systematically varying the polarization of the illuminating beam. Excitation occurs when the electric field vector of the light and the absorption dipole of the fluorophores are aligned.

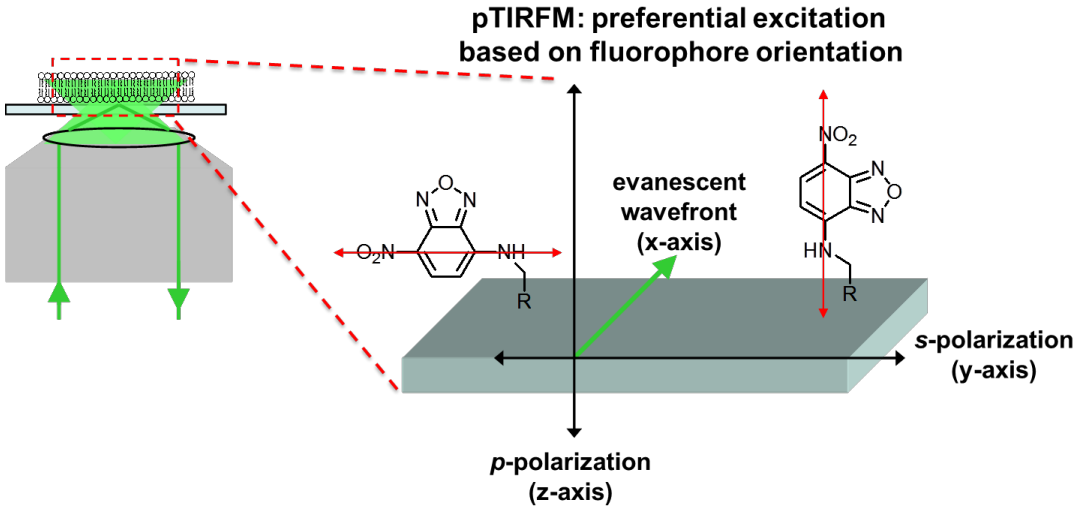

For reporters with uniaxial symmetry the steady-state fluorescence intensity as a function of the evanescent wave's polarization angle, $F(\psi)$, is given by:

$$F(\psi) = 1 + B(\cos^2\psi - \cos^2\psi_0) \quad \text{(Equation 3-1)}$$

Where ψ_0 is the experimentally determined polarization angle at which $F(\psi)$ is a maximum (restricted to 0° or 90°). The parameter B describes the distribution of fluorophore orientations in the detection volume, and is related to the pTIRF order parameter $[P_2]$ by:

$$B = \frac{(I_z - I_y + I_x) + [P_2]\,(2I_z + I_y - I_x)}{I_y(1-[P_2]) + \cos^2\psi_0(I_z - I_y + I_x) + [P_2]\,(2I_z + I_y - I_x)} \quad \text{(Equation 3-2)}$$

Where I_x, I_y, and I_z are the intensity directional components of the evanescent field, which can be calculated when the relative index of refraction of the TIR interface and the illumination beam's incidence angle are known. The orientational order parameter $[P_2]$ can be defined in

terms of the fluorescence-detected dichroic ratio R^{FD}, which is experimentally acquired from *p*- and *s*-polarized pTIRFM images of the sample on a pixel-by-pixel basis:

$$[P_2] = \frac{I_x - R^{FD} I_y + I_z}{I_x - R^{FD} I_y - 2I_z}$$

(Equation 3-3)

$$R^{FD} = \frac{F_p}{F_s}$$

(Equation 3-4)

Where F_p is the fluorescence intensity obtained with *p*-polarized excitation where the electric field vector aligned with the membrane normal (0°), and F_s is the intensity measured with *s*-polarized excitation (90°). As such, $[P_2]$ is a time- and ensemble-averaged quantity, but it is independent of fluorophore concentration. [21] The relationship between the orientation parameter $[P_2]$ and the tilt angle (θ_c) of the fluorophore's absorption dipole with respect to the membrane normal (z-axis) is given by the following expression:

$$[P_2] = \frac{1}{2}(3[\cos^2\theta] - 1)$$

(Equation 3-5)

For a planar solid-supported membrane the possible range of tilt angles (θ_c) extends from 0° to 90° meaning that $[P_2]$ values of -0.5 to 1.0 can be calculated from pTIRFM images. $[P_2]$ = 0 suggests an isotropic or randomly oriented distribution of molecules. A $[P_2]$ value of -0.5 is consistent with an absorption dipole oriented perpendicular to the membrane normal, whereas a value of 1.0 indicates a dipole aligned with the z-axis. In practice values between these end points, which indicate degrees of dipole ordering intermediate to the two extremes, are typically observed (Figure 3-2).

Figure 3-2. Schematic depiction of pTIRFM imaging of a phase-separated supported lipid membrane. Order parameter [P_2] values for fluorophores in the membrane can be calculated from the *p*- and *s*-polarized TIRF images of the bilayer. [P_2] allows determination of the fluorophore tilt angles (θ_c) with respect to the membrane normal. $\theta_c L_d$ and $\theta_c L_o$ shown here are the average tilt angles measured for the probe NBD-Cer **10** in the liquid-disordered and liquid-ordered phases of DOPC/ESM/Chol bilayers (see section 3.2.4). 'X' denotes the *s*-polarization electric field vector projecting into and out of the page.

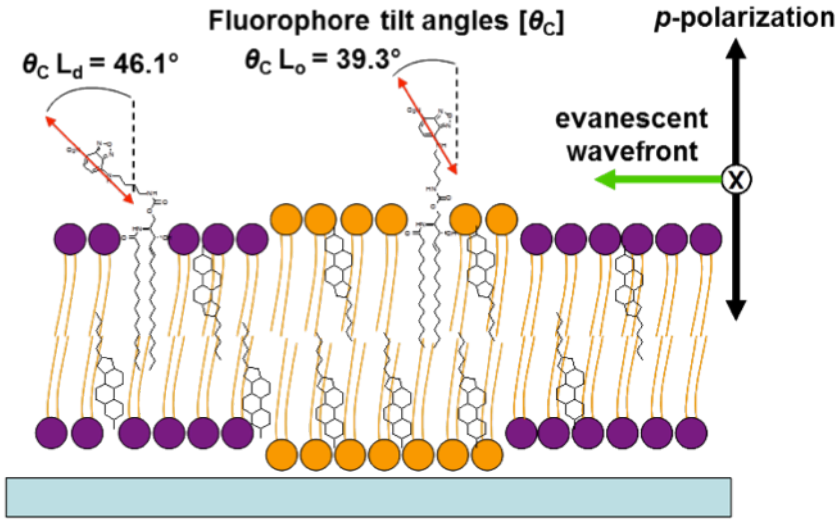

3.2 Results

3.2.1 Synthesis of NBD-Ceramide

NBD-labeled ceramide (NBD-Cer) **10** was synthesized from commercially sourced N-palmitoyl-D-erythro-sphingosine **1** as described in Scheme 3-1. Chemoselective protection of the C_1 hydroxyl moiety of **1** with trityl chloride (TrCl, **2**) in the presence of *N*,*N*-diisopropylethylamine (DIPEA) gave 1-trityl ceramide **3** in 65% yield. The C_3 hydroxyl group was then masked as a benzoate ester upon reaction with benzoyl chloride **4** in the presence of triethylamine (Et_3N) and 4-dimethylaminopyridine (DMAP) to afford **5**. Lewis acid-mediated methanolysis of the C_1 trityl group was achieved with boron trifluoride diethyl etherate ($BF_3{\cdot}Et_2O$) to give 3-benzoyl ceramide **6** in 70% yield. The unprotected primary hydroxyl group of **6** was then treated with carbonyldiimidazole (CDI) to activate it for a subsequent coupling reaction. The amine coupling partner, **8**, was prepared via the deprotection of *tert*-butyl 4-(4-

nitrobenzo-2-oxa-1,3-diazol-7-ylamino)butylcarbamate **7** in neat trifluoroacetic acid (TFA). Carbamate **9** was formed in 38% yield from the reaction of the amine and CDI-activated alcohol in the presence of of Et_3N. Hydrolysis of the C_3 benzoate ester with LiOH afforded ((*E*,2*S*,3*R*)-3-hydroxy-2-(palmitamido)octadec-4-enyl)-4-(4-nitrobenzo-2-oxa-1,3-diazol-7-ylamino)butylcarbamate (NBD-ceramide, **10)** in an overall yield of 10% from **1**.

Scheme 3-1. Synthesis of NBD-ceramide. (a) DIPEA, CH_2Cl_2, rt, 2 d, 65%; (b) Et_3N, DMAP, CH_2Cl_2, 12 h, 92%; (c) $BF_3{\cdot}Et_2O$, toluene/MeOH, rt, 2 h, 70%; (d) CDI, toluene, rt, 1 h; (e) TFA, 0.5 h, rt; (f) **8**, Et_3N, CH_2Cl_2, 12 h, rt, 38%; (g) LiOH, THF/MeOH/H_2O, 1 h, 60%.

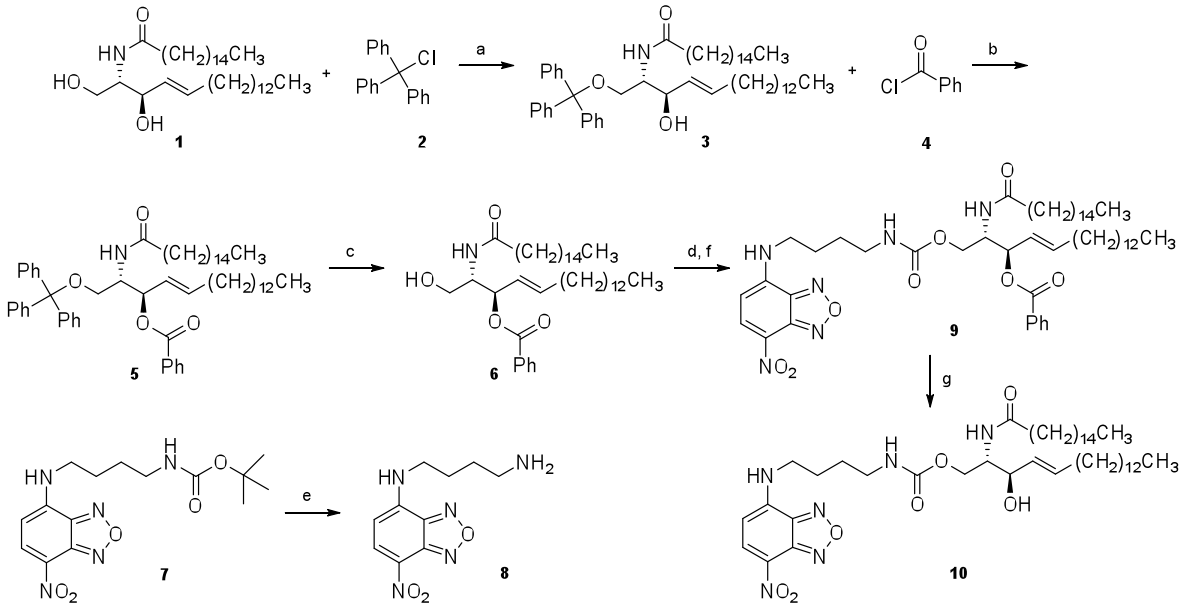

3.2.2 Spectroscopic Characterization

Previous model membrane investigations have shown that the photophysical properties of the NBD fluorophore are environment-sensitive, and particularly responsive to changes in solvent polarity.[56] Membranes with coexisting lipid phases will exhibit two or more distinct environments where differences in lipid order and packing behaviour may be apparent from changes in NBD's absorption, emission, fluorescence quantum yield (Φ_{fl}) or lifetime (τ). Few head-group labelled NBD lipids have been described to date, so we elected to compare NBD-

Cer **10** spectroscopically to one such probe, NBD-DHPE. Figure 3-3 shows absorption and emission spectra for small unilamellar vesicles (SUVs) prepared from lipid films incorporating NBD-DHPE or **10**. Egg phosphatidylcholine (EPC) incorporating 2 mol% NBD-DHPE (Φ_{fl} = 0.16) was used as a standard for determining quantum yields of fluorescence for NBD in lipid SUVs (Table 3-1).

Figure 3-3. (A) absorption spectra of NBD probes in lipid SUVs: I) EPC with 2 mol% NBD-DHPE; II) EPC 0.5% NBD-DHPE; (III) EPC 0.5% NBD-Cer **10**; IV) DOPC/Chol in 2/1 molar ratios and 0.5% **10**; V) PSM/Chol in 5/4 molar ratios and 0.5% **10**. Traces shown here are uncorrected for vesicle scattering. (B) Emission spectra for the same vesicle suspensions.

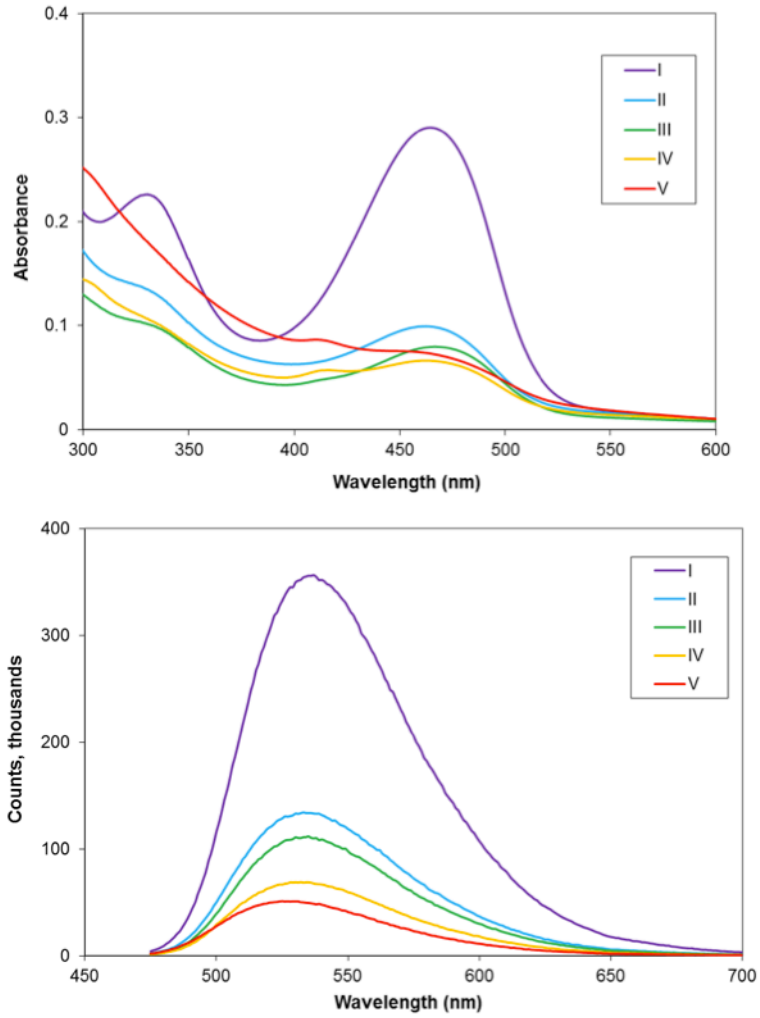

Table 3-1. Photophysical properties of NBD-DHPE and NBD-Cer **10** in SUVs.

Lipid, dye x mol%[a]	λ_{abs}	λ_{em}	Φ_{fl}[b]	τ (ns)[c]	w (ns)[d]
EPC 2% NBD-DHPE	468	536	0.16	6.9 ± 0.1	2.7 ± 0.2
EPC 0.5% NBD-DHPE	468	533	0.19	7.7 ± 0.2	1.9 ± 0.5
EPC 0.5% **10**	470	535	0.20	7.5 ± 0.1	2.4 ± 0.3
DOPC/Chol 2/1[e] 0.5% **10**	466	532	0.20	7.9 ± 0.1	2.5 ± 0.5
PSM/Chol 5/4[f] 0.5% **10**	468	525	0.19	11.1 ± 0.5	1.4 ± 0.7

[a] Spectra obtained in *Milli-Q* H_2O. [b] Quantum yields of fluorescence determined against the reference (2% NBD-DHPE in EPC; *Biophys. J*. **1996**, *71*, 327-335) for excitation at 370 nm. [c] Lifetimes were measured by the frequency domain method. [d] Gaussian fits of the raw data were supplied by Dr. Z. J. Jakubek, where *w* is the width of the distribution. [e,f] These mixtures approximate the composition of L_d and L_o phases respectively for the lipid mixture of DOPC/PSM/Chol in molar ratios of 2/2/1.

The absorption spectrum of this mixture (Figure 3-3A, I) showed clear peaks at 335 and 468 nm assigned to the π, π^* and charge transfer (CT) bands of the fluorophore respectively. At 536 nm, the emission peak for NBD-DHPE in this mixture was also consistent with previously reported values. When the loading of NBD-DHPE in EPC was decreased to 0.5 mol%, the quantum yield of fluorescence increased to 0.19 and the calculated fluorescence lifetime also increased from 6.9 to 7.7 ns (Table 3-1), suggesting that at 2 mol% some self-quenching may occur in the lipid vesicles. However, previous supported membrane experiments we have performed with NBD indicate that in the range of 0.1-1 mol% its fluorescence intensity increases linearly with increasing concentration (see Chapter 2).

Spectra for NBD-Cer **10** in SUVs of EPC at 0.5 mol% were similar to those for NBD-DHPE in the same lipid mixture. No significant shifts were observed in absorption or emission, and fluorescence quantum yield and lifetime were essentially unchanged (Table 3-1). Taken together these results suggest that the NBD chromophore occupies a similar environment when attached to the head-group of phosphatidylethanolamine or the C_1-hydroxyl group of Cer via a

short, hydrophilic linker. From a phase diagram for ternary mixtures of DOPC/PSM/Chol[57] we selected a mixture of DOPC/Chol in molar ratios of 2/1 to model the L_d phase of our supported membranes in spectroscopic SUV experiments incorporating 0.5 mol% **10**. A mixture of PSM/Chol in molar ratios of 5/4 was used to simulate the L_o phase. Photophysical properties and spectra for **10** in these two mixtures are shown in Table 3-1 and Figure 3-3. Spectra and the fluorescence quantum yield in the DOPC/Chol mixture were similar to those obtained in EPC. A small increase was observed in the fluorescence lifetime, possibly reflecting the ordering effect of cholesterol in these vesicles. The PSM/Chol absorption spectrum showed a marked increase in lipid absorbance that was not confined to the two NBD absorption bands (verified with a sample that did not contain dye), and that we attribute to vesicular light scattering. We have observed that at these working concentrations (~1 mg/mL) lipid suspensions rich in SM or other sphingolipids require extended sonication at elevated temperatures to reach clarity. Moreover, even when these suspensions appear clear by inspection, they consistently show stronger absorption across all wavelengths examined than do mixtures of unsaturated, fluid-phase PCs. Probe **10** in the PSM/Chol mixture also exhibited a blue-shift in emission of about 10 nm with respect to the PC mixtures, although its fluorescence quantum yield did not differ dramatically. However, at 11.1 ns the fluorescence lifetime increased significantly, providing good evidence that the probe was situated in a more highly ordered environment.

3.2.3 pTIRFM Calibration

An aqueous fluorescein solution (~3 μM) on a mica-glass substrate was used to calibrate the half-wave plate needed to systematically vary the polarization of the excitation light on our fluorescence microscope. Stacks of 20 pTIRFM images were captured incrementing ψ by 20°

between successive images. Plots of fluorescence intensity as a function of the evanescent wave's polarization angle $F(\psi)$ derived from these images defined the positions of the half-wave plate that gave *p*- (0° or ψ_0 at which $F(\psi)$ is a maximum) and *s*-polarization (90°). Figure 3-4A shows 4 half-wave plate calibration curves that were sequentially recorded over the course of approximately 1 hour.

Figure 3-4. Half-wave plate calibration for pTIRFM implementation. (A) Four calibration curves acquired sequentially with a dilute solution of fluorescein in water. The sample was prepared on a mica-glass sandwich substrate such as was used in the supported model membrane studies (see section 3.2.4), and the half-wave plate angle rotated in 20° increments between acquisitions. (B) Calibration curve fitted to the theoretical expression for fluorescence intensity as a function of the polarization angle $F(\psi)$ of the excitation light. The maximum for $F(\psi)$ is found at ψ_0 which here is found to be to -6.3° on the half-wave plate.

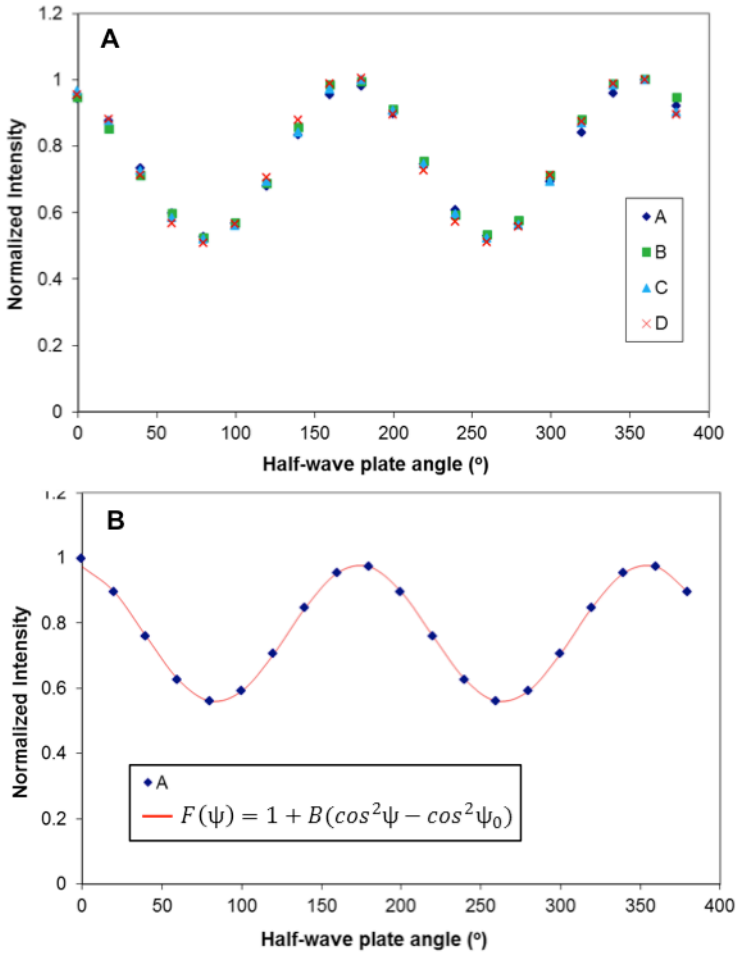

Good overlap between the four sets of points suggests that the angular positions on the plate are well defined, and that the intensity and polarization of the excitation laser are well conserved throughout the acquisition interval. As indicated in Figure 3-4B these experimentally measured fluorescence intensities were in good agreement with the theoretical curve for $F(\psi)$ (Equation 3-5; $(\theta_c) = 54.7°$, $[P_2] = 0$, $B = 0.27$). The *p*- and *s*-polarized images obtained for the dye solution were then analyzed with the order parameter $[P_2]$ macro to detect and correct for dichroism in the microscope optics. For randomly oriented fluorophores, such as dye molecules in dilute solution, $[P_2]$ should theoretically equal zero if no instrumental bias exists. For the order parameter images in Figure 3-5 a mean $[P_2]$ value of 0.04 ± 0.01 ($(\theta_c) = 53.1° \pm 0.4°$) was obtained. This suggests that the raw pTIRFM images did not require significant polarization corrections.

Figure 3-5. Calibration of the pTIRF microscope. (A) pTIRFM image acquired with *p*-polarized light; (B) *s*-polarized image of the same region of interest (ROI) shown on the same intensity scale. (C) Orientational order parameter $[P_2]$ image calculated on a pixel-by-pixel basis from A and B. (D) $[P_2]$ histogram with a pixel-average value of 0.04 ± 0.01 corresponding to $(\theta_c) = 53.1° \pm 0.4°$. Scale bar = 5 μm.

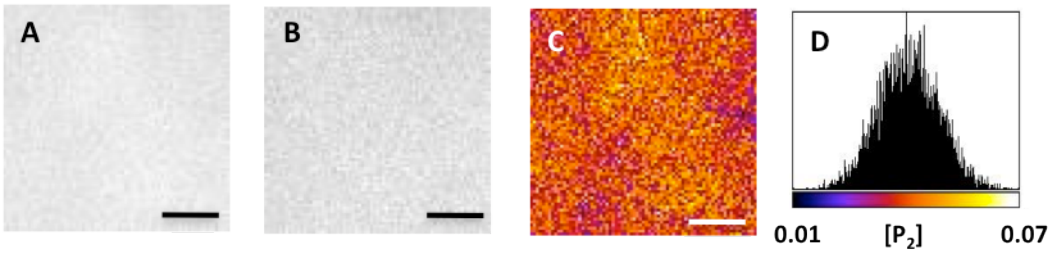

3.2.4 Probing Membrane Order Using NBD-Cer

3.2.4.1 Order Parameter Measurements in Phase-Separated Model Membranes

Our application of NBD-Cer **10** towards measuring membrane order by pTIRFM was prompted by a serendipitous observation made when switching between epifluorescence and TIR modes on the TIRF microscope. The characterization of **10** in supported model membranes

involved assessing its partitioning behaviour in bilayers of DOPC/ESM/Chol in molar ratios of 2/2/1, at a probe loading of 0.5 mol%. This ternary lipid mixture exhibits coexisting L_d and L_o phases, with the latter presenting as rounded, micron-scale, ESM- and Chol-rich domains (Figure 3-6). We first observed that when visualized in epifluorescence mode these domains appeared dark relative to the surrounding membrane (Figure 3-6A). However, when the incidence angle of the excitation light was adjusted to achieve TIR at the mica substrate-water interface, we saw a striking inversion of the two phases' relative fluorescence intensity (Figure 3-6B). Not only did the L_o domains appear brighter in the TIRFM images, the fluorescence intensity of the entire sample was also significantly increased.

Figure 3-6. A qualitative observation of polarization-dependent fluorescence contrast in a phase-separated supported membrane of DOPC/ESM/Chol in molar ratios of 2/2/1 labelled with 0.5 mol% **10**. (A) Epifluorescence image; (B) TIRFM image of the same ROI. Scale bar = 5 μm.

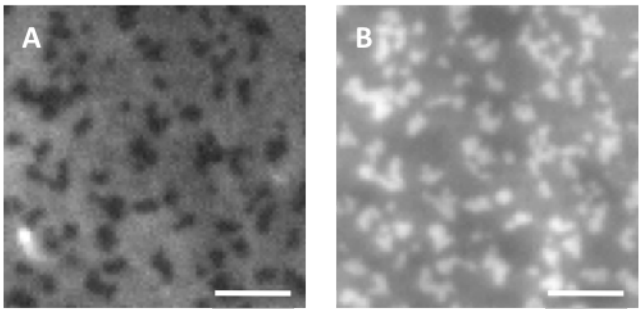

Consequently, pTIRFM imaging capability was first implemented to assess the dependence of **10**'s fluorescence intensity in these supported membranes on the polarization of the excitation light. For bilayers of DOPC/ESM/Chol stained with 0.5 mol% **10**, pTIRFM images acquired upon excitation with *s*-polarized light gave relative contrast (Figure 3-7A) similar to that observed in epifluorescence images. pTIRFM images obtained with *p*-polarized light showed higher intensity overall and also reproduced the inversion of contrast observed with

the switch from epifluorescence to TIRFM, whereby the L_o domains appeared bright relative to the L_d phase (Figure 3-7B).

Figure 3-7. pTIRFM imaging of orientational order parameter [P_2] distribution for probe **10** in a bilayer of DOPC/ESM/Chol in molar ratios of 2/2/1. (A) *p*-polarized image; (B) *s*-polarized; the corner insets are displayed on the same intensity scale. (C) Calculated order parameter [P_2] image of the same region. Scale bar = 5 μm.

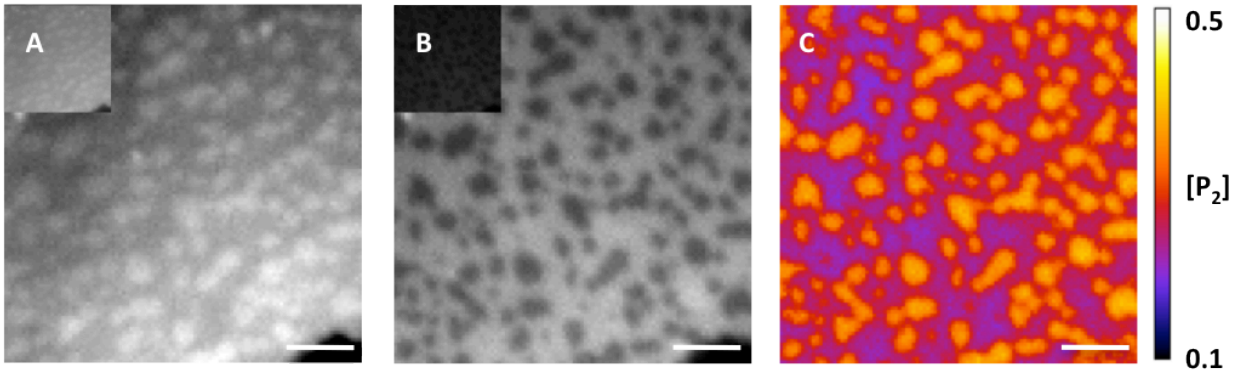

Orientational order parameter [P_2] maps (Figure 3-7C) were then generated for these supported membranes from *s*- and *p*-polarized images acquired in several representative regions of interest (ROI). The order parameter images exhibited two [P_2] populations corresponding to the L_d and L_o phases respectively (Table 3-2). For images obtained in *Milli-Q* water we calculated [P_2] = 0.22 ± 0.02 with a corresponding (θ_c) = 46.1° ± 0.7° for the L_d phase. For the L_o domains the corresponding [P_2] and (θ_c) values were 0.40 ± 0.03 and 39.3° ± 1.0° respectively. The (θ_c) values for our head-labelled probe **10** report on the mean orientation of the fluorophore's absorption dipole (Figure 3-8) with respect to the membrane normal. The absorption dipole moment for N-substituted nitrobenzoxadiazole (NBD) fluorophores such as NBD-Cer **10** is offset by 9.5° relative to the C_7-N bond (Figure 3-8).[58] In the idealized, lowest energy and highest order all-trans conformation[59] available to probe **10** in a planar supported bilayer, we expected that this dipole should be oriented at a small angle with respect to the membrane normal. In practice, a larger angle for the L_d phase indicates a less upright or erect

dipole orientation, which is suggestive of looser packing or increased disorder in this lipid environment as compared to the L_o domains (Figure 3-2).

Table 3-2. Orientational order parameter [P_2] and fluorophore absorption dipole tilt angles (θ_c) measured by pTIRFM in phase separate supported lipid membranes. All measurements we performed on mica-glass sandwich substrates and in *Milli-Q* water unless otherwise stated.

Lipid Composition	Probe	Lo		Ld	
		[P_2]	θ	[P_2]	θ
DOPC/ESM/Chol					
2:2:1	NBD-Cer **10**	0.40 ± 0.03	39.3 ± 1.0	0.22 ± 0.02	46.1 ± 0.7
2:2:1	BODIPY-PC	0.28 ± 0.03	43.9 ± 1.0	0.20 ± 0.02	46.8 ± 0.6
[a]2:2:1	NBD-Cer **10**	0.35 ± 0.02	41.1 ± 0.9	0.22 ± 0.02	46.3 ± 0.6
[b]2:2:1	NBD-Cer **10**	0.36 ± 0.01	41.0 ± 0.3	0.30 ± 0.01	43.0 ± 0.2
DOPC/DPPC/Chol					
2:2:1	NBD-Cer **10**	0.43 ± 0.01	38.0 ± 0.5	0.33 ± 0.02	42.1 ± 0.6

[a]Bilayers imaged in SMase buffer: 125mM NaCl, 10mM $CaCl_2$, 2mM $MgCl_2$, 10mM HEPES, pH 7.4.
[b] Bilayer in buffer treated with SMase for 21min to generate ceramide from ESM- these are data obtained from the sample shown in figures 3-11 and 3-12.

BODIPY-PC is an acyl-chain labelled probe (Figure 3-8) which has been previously used to measure fluorescence-detected order parameters in phase-separated model membranes.[21] We incorporated 0.5 mol% BODIPY-PC in bilayers of DOPC/ESM/Chol in molar ratios of 2/2/1, and recorded pTIRFM images in several ROI (Figure 3-9). Bilayers stained with BODIPY-PC did not show an inversion of phase contrast for *s*- and *p*-polarized pTIRFM images. The L_o domains consistently appeared dark with respect to the L_d phase, although an overall increase in fluorescence intensity was observed for the *p*-polarized images. We subsequently compared [P_2] values obtained for this probe with those calculated for **10** (Table 3-2). Calculated [P_2] and (θ_c) values of 0.20 ± 0.02 and 46.8° ± 0.6° for the L_d phase were very similar to those obtained with **10**. For the L_o phase, however, [P_2] and (θ_c) differed significantly at 0.28 ± 0.03 and 43.9° ± 1.0°. The greater difference in [P_2] observed between the L_d and L_o phases with **10** suggested

that this probe could be a better candidate to report on order parameter changes occurring in the L_o phase.

Figure 3-8. Fluorescent lipid probes used in this study and their absorption dipole moments. (A) The hydrophilic linker and fluorophore of NBD-Cer **10** probes the polar head group region of the membrane; (B) conversely, the hydrophobic reporter of BODIPY-PC is embedded in the core of the membrane.

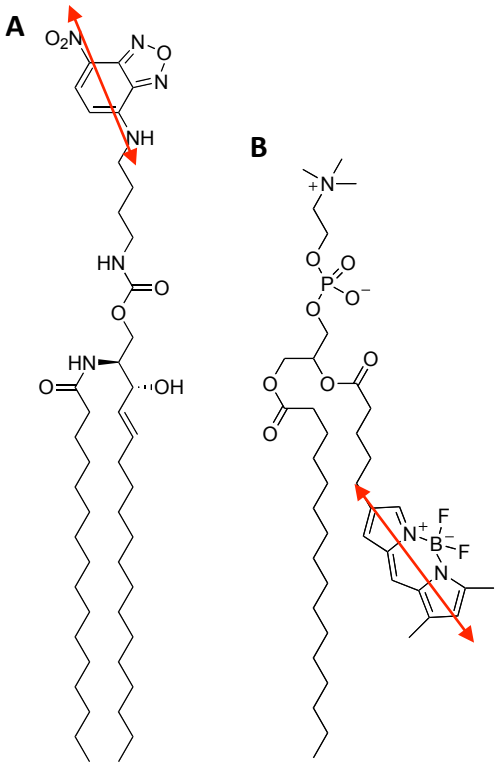

Probe **10** was also incorporated into model membranes of a second phase-separated lipid mixture: DOPC/DPPC/Chol in molar ratios of 2/2/1. In these bilayers the L_o domains appeared brighter than the surrounding L_d phase in both *s*- and *p*-polarized pTIRFM images (Figure 3-10). For this ternary lipid mixture [P_2] and (θ_c) were calculated at 0.33 ± 0.02 and 42.1° ± 0.6° for the L_d phase (Table 3-2). The DPPC and Chol-rich L_o domains presented [P_2] and (θ_c) values of 0.43 ± 0.1 and 38.0° ± 0.5° respectively. The [P_2] obtained for **10** in both phases indicated that the probe was oriented at smaller angles with respect to the membrane normal than in the analogous ordered and disordered environments in the DOPC/ESM/Chol bilayers. Furthermore,

the difference in orientational order between the two environments was significantly decreased for these DPPC-containing membranes.

Figure 3-9. pTIRFM imaging of orientational order parameter [P_2] distribution for BODIPY-PC in a bilayer of DOPC/ESM/Chol in molar ratios of 2/2/1. (A) *p*-polarized image; (B) *s*-polarized; both images are displayed on the same intensity scale. (C) [P_2] image of the same region. Scale bar = 5 μm.

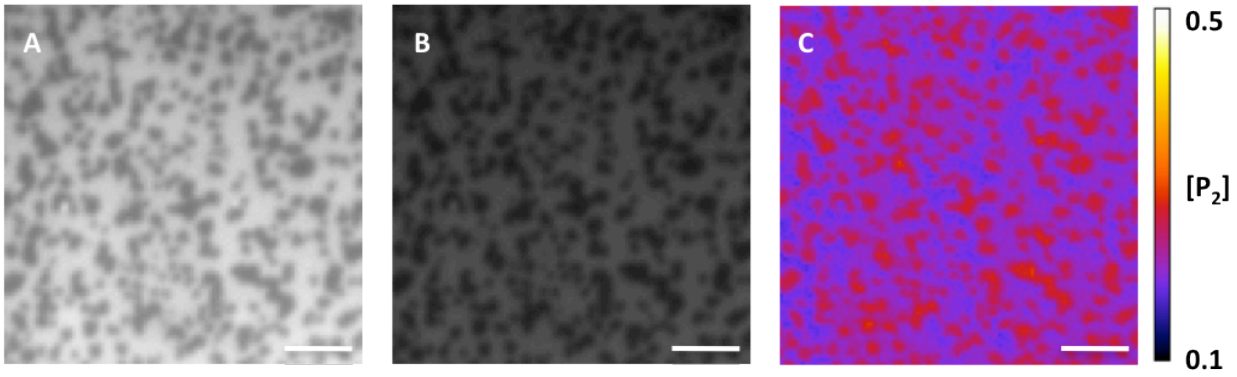

Figure 3-10. pTIRFM imaging of orientational order parameter [P_2] with reporter NBD-Cer **10** in a bilayer of DOPC/DPPC/Chol in molar ratios of 2/2/1. (A) *p*-polarized image; (B) *s*-polarized; the inset images are displayed on the same intensity scale. (C) [P_2] image of the same region. Scale bar = 4 μm.

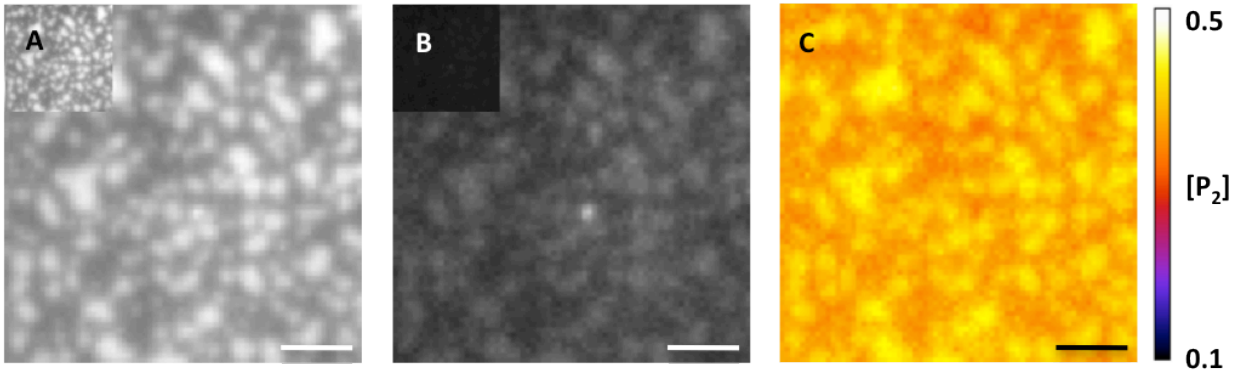

Several studies have shown that the NBD fluorophore photobleaches rapidly in oxygenated solutions.[60-61] Throughout our pTIRFM imaging experiments with NBD-Cer **10** we sought to minimize unnecessary exposure of our bilayer samples to the excitation laser or ambient light. We assessed the bleaching rate of **10** in supported bilayers upon exposure to 488 nm laser light in TIR mode by first irradiating a small ROI through a reduced iris aperture, and then acquiring an image of the entire area with the iris fully open. After repeating this procedure for several

sets of conditions, we determined that TIR excitation through a 6% transmission neutral density filter with a 1 s exposure time resulted in a loss in fluorescence intensity due to bleaching of less than 5% between two sequential exposures. Under these conditions, and with the camera gain set to zero, the mean fluorescence intensity of the bilayer was at least 5 times greater than the background signal (see section 3.5.5.2 for an explanation of how the background level was determined). We proceeded to use these acquisition parameters for all of our pTIRFM experiments. For two back-to-back sets of *s*- and *p*-polarized pTIRFM images in a given ROI, the corresponding [P_2] images were in good agreement with each other (not shown). Varying the order in which *s*- and *p*-polarized images were acquired did not vary this outcome. Taken together, these results suggest that the effects of NBD bleaching will be negligible for a pTIRFM bilayer experiment with **10** consisting of *s*- and *p*-polarized images recorded before and after an event of interest.

3.2.4.2 Using pTIRFM to Report on SMase-Dependent Membrane Reorganization

We sought to evaluate NBD-Cer **10**'s utility as a probe for pTIRFM by using it to report on Cer-mediated changes in membrane order resulting from *in situ* treatment with sphingomyelinase (SMase). For the measurements described above our supported bilayers of DOPC/ESM/Chol with 0.5 mol% **10** were formed in *Milli-Q* water; however, our SMase treatments have been routinely performed in a high ionic strength HEPES buffer. Therefore, we recorded pTIRFM images for these bilayers after first washing them with buffer, and allowing them to equilibrate for about 20 min (Figure 3-11 A-C, Table 3-2). Under these conditions we obtained [P_2] and (θ_c) values of 0.22 ± 0.02 and 46.3° ± 0.6° respectively for the L_d phase. In the L_o domains we calculated corresponding [P_2] and (θ_c) values of 0.35 ± 0.02 and 41.1° ± 0.9°. The

[P_2] values determined for both phases represent a decrease from those recorded in *Milli-Q* water, although the difference is only significant (i.e. greater than one standard deviation) in the L_o phase. Such a decrease in [P_2] for the L_o phase translates to an increase of about 2° in the average angle between the NBD transition dipole and the membrane normal, and may indicate a slight disordering effect.

Figure 3-11. Changes in membrane order ensuing from the SMase-mediated reorganization of DOPC/ESM/Chol (molar ratios of 2/2/1) bilayers stained with 0.5 mol% **10** were quantified using pTIRFM. The membranes were first imaged in SMase buffer (pH 7.4): (A) *p*-polarized, (B) *s*-polarized image, both of which are displayed on the same intensity scale. (C) [P_2] image of the same region. Following 21 min of treatment with SMase (0.2 U/mL), the ROI was reimaged (D-E) to reveal a striking contrast reversal between the two lipid phases in the *p*-polarized channel (D), and a significant increase in order for the L_d phase (F). Scale bar = 5 μm.

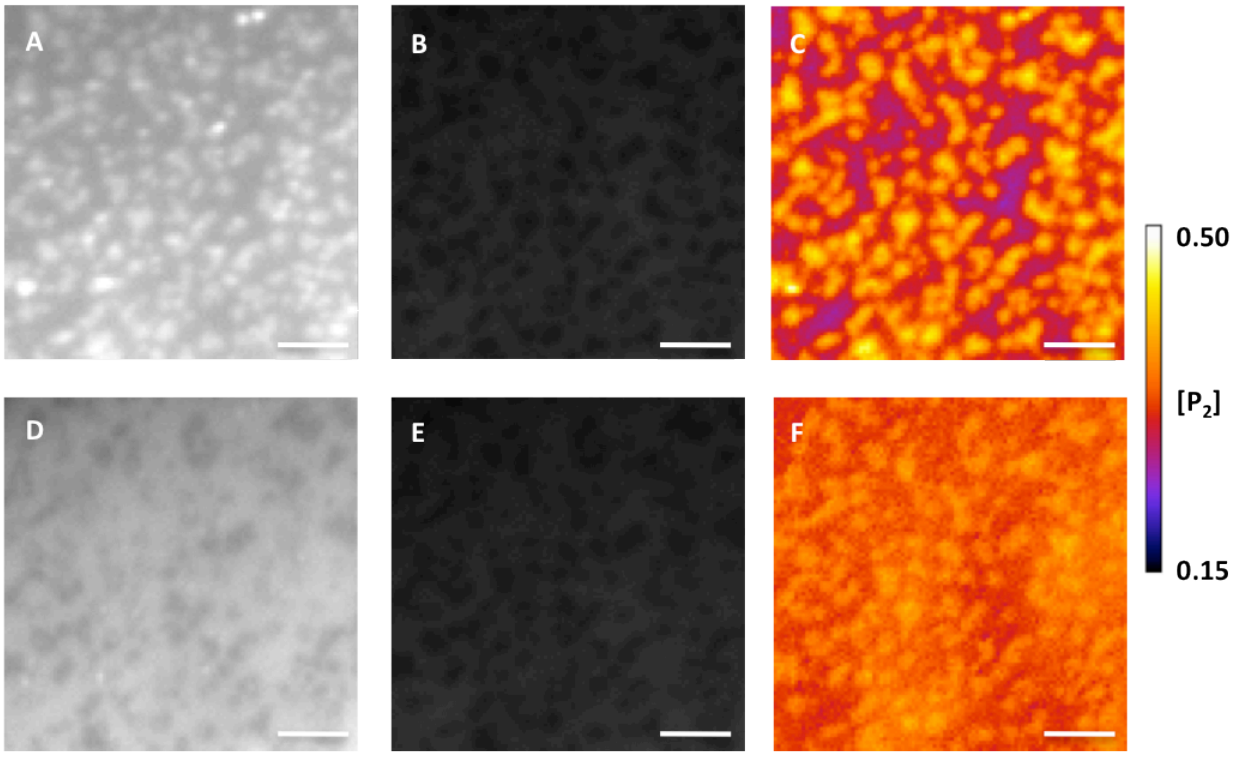

SMase-induced changes in the bilayer were observed by fluorescence within seconds of introducing the enzyme into the solution above the lipid membrane. Micron-scale lateral reorganization of the membrane progressed rapidly for the 15-20 min immediately following addition of SMase. The time-resolution for our pTIRFM acquisitions was about 30 s as in order

to sequentially acquire *s*- and *p*-polarized images the half-wave plate had to be removed from the microscope turret and manually adjusted to the required position. Due to this instrumental limitation, we were unable to obtain pTIRFM images during the rapid stage of membrane restructuring. Therefore, pTIRFM images were typically recorded approximately 20 min following SMase treatment, at which time it was possible to acquire *s*- and *p*-polarized images that exhibited good agreement in the position and size of membrane features.

Figure 3-11 shows pTIRFM and order parameter images for a DOPC/ESM/Chol bilayer before and 21 min after the addition of SMase. In this ROI the membrane domains appeared well conserved in size and shape after enzyme treatment, and no other indications of morphological changes were evident from the *s*-polarized pTIRFM image. However, a comparison of the *p*-polarized images recorded prior to SMase treatment and at the 21 min mark showed a clear inversion of the fluorescence contrast between the domains and the surrounding membrane (Figure 3-11 A, D). Prior to Cer generation in the bilayer, the L_o domains appeared bright relative to the L_d phase, although at the latter time point the domains were darker than the bulk membrane.

Order parameters for **10** calculated from these pTIRFM images also provided evidence of SMase-dependent changes in membrane structure (Figure 3-11 C, F; Table 3-2). Reduced contrast between the lipid phases in the post-SMase [P_2] image indicated that the transition dipoles of **10** in these two environments were more closely aligned than they had been in the untreated bilayer. Therefore, the probe indirectly indicated that the difference in lipid packing order between two phases had decreased. For the DOPC-rich phase [P_2] increased from 0.22 ± 0.02 to 0.30 ± 0.01 with a corresponding decrease in (θ_c) of about 3°. The decrease in the mean

tilt angle of the transition dipole of the fluorescent reporter with respect to the bilayer normal suggested that the DOPC-rich phase became more ordered following Cer generation in the membrane. Conversely, $[P_2]$ did not change significantly in the domains with calculated values of 0.35 ± 0.02 and 0.36 ± 0.01 before and after SMase-treatment respectively. We were able to rule out increased photobleaching of **10** in the L_o phase as the reason for these changes because the increase in $[P_2]$ for the L_d phase, and the distinctive reversal of fluorescence contrast between the two phases, were not confined to the initial ROI and were observed throughout the SMase-treated bilayer. Additionally, we observed an increase in the *p*-polarized absolute fluorescence intensity of the L_d phase following Cer generation, which would account for both the increase in $[P_2]$, and the marked reversal in fluorescence contrast with respect to the L_o phase.

SMase treatment of DOPC/ESM/Chol bilayers gave rise to heterogeneous, irregularly shaped features from which **10** seemed to be depleted, as they appeared darker than both the bulk membrane and the raft-like domains. The ROI in Figure 3-12 shows a region of the same bilayer sample discussed above in which a dye-depleted patch had formed after 21 min in the presence of SMase. As previously discussed in Chapter 2, we have identified cholesterol-depleted regions of similar size and shape based on the exclusion of our NBD-Chol probe from these features. Parallelized fluorescence and AFM experiments with the cholesterol probe indicated that these dye-excluded patches projected from the bulk membrane, but were not as tall as the raft-like domains. Correlated pTIRFM/AFM experiments performed on SMase-treated bilayers incorporating **10** (Figure 3-13) confirmed that the dye-depleted features observed with this NBD-Cer probe corresponded to the phase of intermediate height observed in the earlier

study. As can be seen from the order scale bars in the [P_2] images for Figures 3-12, 3-13 and 3-14, these irregularly shaped patches exhibited maximum [P_2] values ranging from about 0.40 to 0.50 depending on the size of the feature. As such the order parameters for the new phase were consistently higher than those measured for the rest of the membrane before and after SMase treatment.

Figure 3-12. A second ROI for the same bilayer sample shown in Figure 3-11 highlights the appearance of a new highly ordered dye-depleted phase. (A-C) pTIRFM images acquired in SMase buffer and the corresponding [P_2] map prior to SMase addition. (D-F) Domains appear well-conserved on the right side of the image same area 21 min after enzyme addition, but significant remodelling of the membrane is apparent from the irregularly-shaped dark feature that has replaced several domains on the left-hand side. Scale bar = 5 μm.

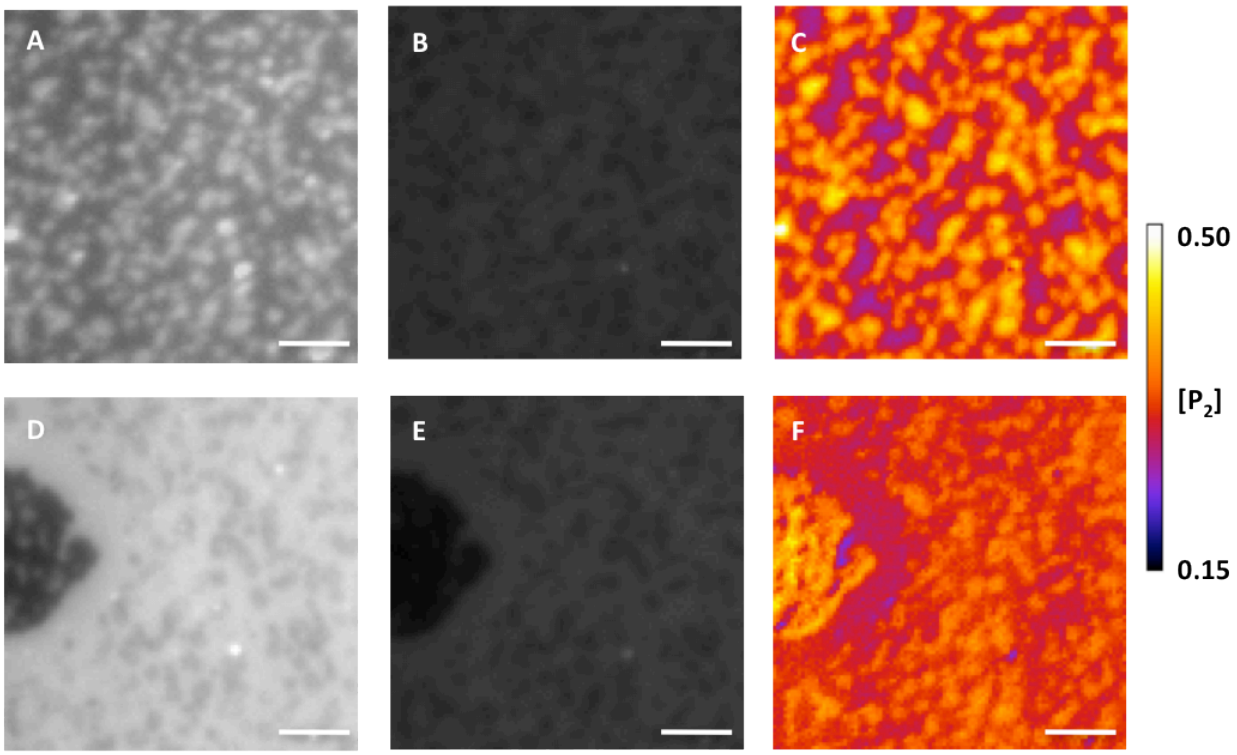

Figure 3-13. Parallelized pTIRFM-AFM images of a DOPC/ESM/Chol (2/2/1 molar ratios and 0.5% **10**) bilayer were acquired following a 33 min SMase treatment. Several dye-depleted features have been identified with green borders in *p*- and *s*-polarized fluorescence images (A and B with insets shown on the same intensity scale). The orientational order parameter [P_2] values for these features (C) suggest that they are more ordered than the bulk membrane. AFM performed in the same area (D, z-scale = 4 nm) indicates that these ordered regions correspond to a new phase with heights intermediate to those of the L_o and L_d phases. Scale bar = 5 μm.

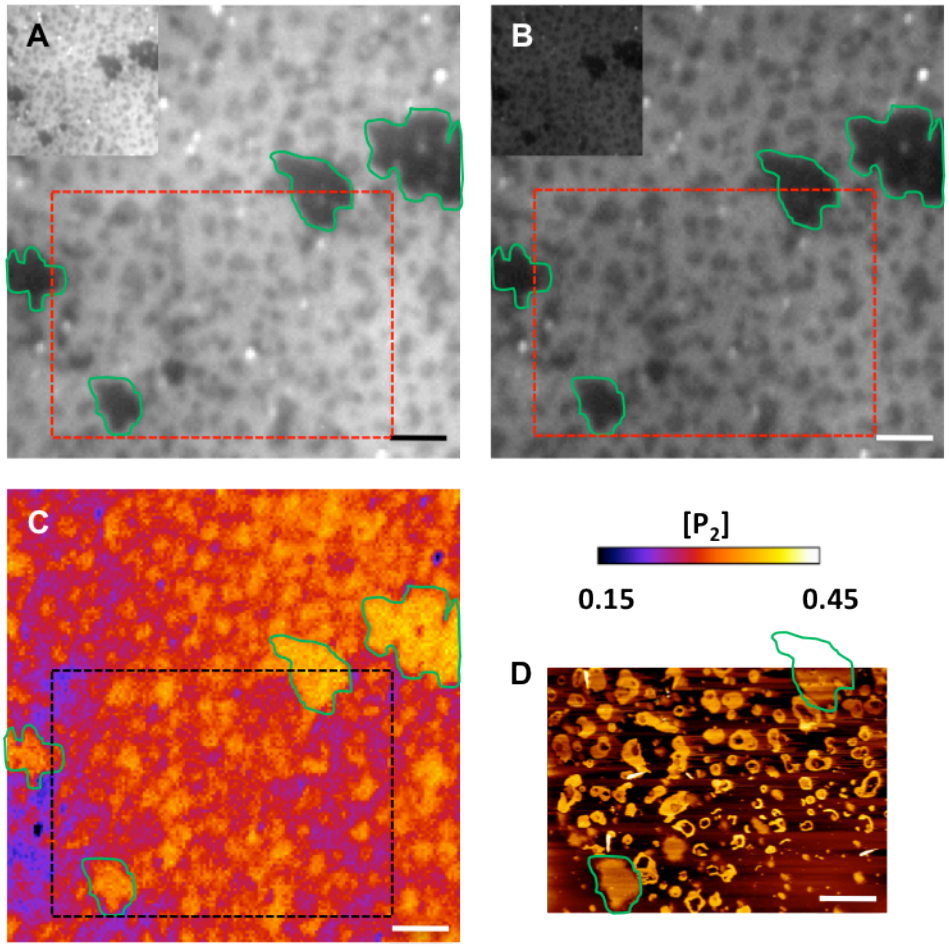

Figure 3-14. The dye-depleted features generated from SMase activity in bilayers of DOPC/ESM/Chol (2/2/1 molar ratio) vary considerably in their size and shape, perhaps reflecting a heterogeneous distribution of membrane-bound enzyme molecules. Larger examples of such features (A, B) exhibit [P_2] values for **10** almost two-fold higher than those for either the L_d or L_o phase (C, and cross-section D) which may be indicative of increasingly solid-ordered or crystalline character. Scale bar = 5 μm.

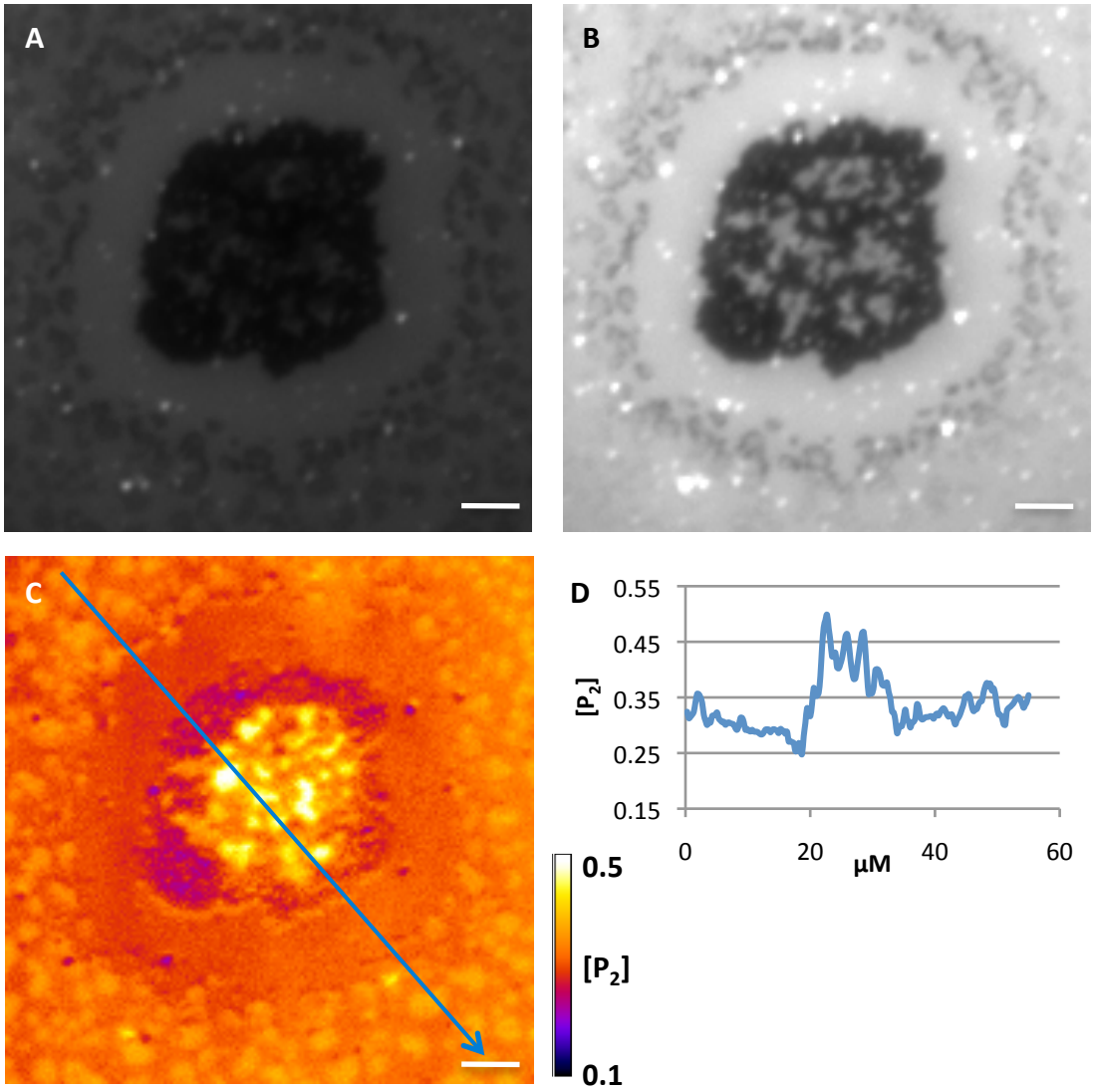

3.3 Discussion of pTIRFM Results Obtained Using NBD-Cer

3.3.1 NBD-Cer as a Probe for Measuring Orientational Order in Lipid Membranes

Order parameter measurements were obtained from pTIRFM images acquired with the probe NBD-Cer **10** in bilayers of DOPC/ESM/Chol and DOPC/DPPC/Chol (Table 3-2). Although calculated [P_2] values differ between the two lipid mixtures they follow a common trend in that [P_2] and (θ_c) for the respective L_d phases are consistent with a more disordered environment than that of the L_o domains. The highest order all-trans conformation[59] of **10** (Figure 3-8) should orient the NBD transition dipole almost perpendicular to the plane of the bilayer and solid support. Therefore, we expect to see greater [P_2] and smaller (θ_c) values for the more highly ordered L_o lipid phase, as is in fact the case. BODIPY-PC is another fluorescent probe that should exhibit a transition dipole that is aligned with the bilayer normal when in its most stable conformation. [P_2] measurements with this probe in bilayers of DOPC/ESM/Chol also indicate increased disorder for the L_d phase with respect to the L_o domains on the basis of a larger (θ_c) value in the bulk fluid phase.

Previous pTIRFM studies incorporating BODIPY-PC in bilayers with coexisting L_d and L_o phases reflect the same trend, and provide the basis for a more quantitative assessment of our pTIRFM data.[21, 26] Oreopoulos and Yip have performed order parameter measurements on supported membranes of DOPC/DSPC/Chol in molar ratios of 1/1/1 and 1/1 with 30 mol% cholesterol. In the former mixture they reported [P_2] values of 0.29 ± 0.01 and 0.26 ± 0.01 for the L_d and L_o phases respectively. For the latter case the corresponding [P_2] values were 0.22 ± 0.03 in the L_d phase and 0.30 ± 0.02 in the L_o domains. Our own results with BODIPY-PC in bilayers of DOPC/ESM/Chol are in good general agreement with the second data set: [P_2] = 0.20

± 0.02 in the bulk membrane and $[P_2]$ = 0.28 ± 0.03 in the ordered domains (Figure 3-9, Table 3-2). Although we obtained a similar $[P_2]$ value with NBD-Cer **10** for the L_d phase of this lipid mixture at 0.22 ± 0.02, the order parameter in the L_o domains was significantly higher at 0.40 ± 0.03 (Figure 3-7, Table 3-2). This difference may arise from the different location of the reporter moieties within the membrane. The BODIPY fluorophore is attached to one of the PC acyl chains, and is thus probably situated in the hydrophobic interior of the membrane. In contrast, NBD is attached to the primary hydroxyl group of Cer by a short hydrophilic linker, and is intended to probe the polar head-groups of the bilayer. The extensive hydrogen bonding network that characterizes this region of the membrane in sphingolipid- and Chol-rich domains contributes significantly to their ordered state,[62] and may thereby account for the higher $[P_2]$ value measured with **10** for the L_o phase.

In bilayers of DOPC/DPPC/Chol labelled with **10** we have calculated a $[P_2]$ value of 0.33 ± 0.02 for the L_d phase, which is considerably higher than that obtained for the analogous ESM-containing membranes (Figures 3-7 and 3-10, Table 3-2). Phase diagrams for this ternary lipid mixture indicate that for the molar ratios employed in this study the L_d phase of the DPPC-containing mixture is more Chol-rich than the L_d phase in the ESM-containing mixture.[1] Increased Chol in the fluid phase should exert an ordering effect that could account for the relative increase in $[P_2]$. By extension the DPPC-rich L_o phase will thus have a lower Chol fraction and should thus be more crystalline than an ESM- and Chol-rich phase. This may explain the modest increase in order for the DPPC-rich L_o phase: [P2] is 0.43 ± 0.01 versus 0.40 ± 0.03 for the ESM-containing bilayers.

3.3.2 Interpreting pTIRFM Results in SMase-Treated Bilayers

Supported model membranes of DOPC/ESM/Chol have been extensively used to study Cer-mediated membrane reorganization by several groups including our own. Cer is typically generated *in situ* via the enzymatic hydrolysis of sphingomyelin upon treatment of the bilayer with SMase. As described in Chapter 2 and elsewhere, parallelized fluorescence and atomic force microscopy (AFM) have been used to record changes in membrane morphology induced by SMase activity. In using NBD-Cer **10** to probe SMase-mediated membrane reorganization by pTIRFM, we hoped to address some of the limitations of this approach, in addition to furthering our understanding of the complex morphology produced by the enzyme.

While the fluorescence component of the correlated approach provides improved temporal resolution over stand-alone AFM of events occurring on timescales of seconds or minutes, it affords limited information regarding local membrane properties or the lipid composition of distinct phases. AFM imaging complements fluorescence by interrogating the physicochemical character of the membrane, mapping topography, and providing superior spatial resolution that is useful in visualizing sub-micron scale features. However, in our experience using AFM to monitor restructuring of SMase-treated bilayers is subject to two principal limitations. First, long acquisition times mean that AFM imaging cannot capture the initial rapidly progressing stage of membrane reorganization following SMase addition. Second, when imaging enzyme-treated bilayers AFM tips rapidly become contaminated and lose their ability to resolve membrane features. Furthermore, the scanning action of the AFM can redistribute bound enzyme molecules across the sample or mechanically damage the bilayer. Scanning with a

minimum applied force, working with dilute SMase solutions and washing out the enzyme prior to AFM imaging can attenuate these effects to some extent, although not completely.

The pTIRFM images we have recorded using **10** as a fluorescent reporter in SMase-treated DOPC/ESM/Chol bilayers provide structural information that is consistent with changes in the lipid composition and properties of these membranes. Order parameter values for the bulk membrane or L_d phase increase significantly following enzymatic generation of Cer (Table 3-2 and Figure 3-11). Our previous studies with the NBD-Chol probe suggest that a significant fraction of cholesterol is expelled from the L_o domains and into the L_d phase as the amount of Cer in these features increases.[8] The ordering effect of Chol on fluid membranes, and the displacement of Chol by Cer from SM-rich domains have been widely documented (for an overview see Chapters 1 and 2), and as such the observed increase in $[P_2]$ for the DOPC-rich bulk phase following SMase treatment is consistent with preceding work.

Calculated $[P_2]$ does not appear to change in the L_o domains that conserve their shape following addition of the enzyme. This indicates that the average orientation of the NBD transition dipole of **10** remains approximately constant throughout. However, the composition of these features is probably changing as $[P_2]$ in the adjacent L_d bulk membrane does increase significantly. We discarded increased photobleaching of **10** in the L_o phase as a possible explanation for this observation as the change in $[P_2]$ for the L_d phase and the distinctive reversal of fluorescence contrast between the two phases were not confined to the initial ROI, and were observed throughout the SMase-treated bilayer. Nonetheless, other photophysical effects must be considered. Previous spectroscopic studies report a direct relationship between increasing solvent polarity and the molar extinction coefficient for the CT band of NBD, but an

inverse relationship with respect to fluorescence quantum yield.[56, 63] Our own photophysical characterization of **10** (Table 3-1) indicates that quantum yields of fluorescence do not change significantly between L_d and L_o phases. We did not, however, determine a quantum yield in a gel phase that would allow us to directly rule out a significant decrease in the fluorescence efficiency of **10** in the domains upon Cer generation. Increasing Cer concentrations should result in more compact lipid packing in the domains due to its decreased molecular area with respect to sphingomyelin. Tighter packing could push the tethered NBD moiety of **10** further out from the bulk membrane into an increasingly polar aqueous environment, and result in decreased fluorescence. However, when we compare the absolute fluorescence intensities in pTIRFM images acquired before and after SMase treatment, no significant decrease is observed for the domains. Conversely, the intensity of fluorescence in the bulk L_d phase does increase in the *p*-polarized images acquired post-SMase treatment. This would be consistent with the more upright alignment of the NBD-Cer transition dipoles expected with the higher-level order of this fluid environment as its Chol content is increased.

Parallelized pTIRFM-AFM experiments (Figure 3-13) confirm that the heterogeneous dye-depleted features generated through the action of SMase exhibit large [P_2] values (Figures 3-12, 3-14) and correspond to a phase that is intermediate in height to the raft-like domains and the L_d phase. These new features and highly-ordered relative to the rest of the membrane, and thus the same as those observed in the NBD-Chol probe study described in Chapter 2; and so we can conclude that they are probably Chol-depleted. Cumulatively these results and the direct Cer incorporation experiments in Chapter 2 suggest that this new phase is also Cer-enriched.

Performing pTIRFM-AFM imaging of DOPC/ESM/Chol bilayers incorporating Cer and labelled with **10** could supply further evidence to support this particular interpretation.

Correlated AFM imaging in this study (Figure 3-13) also reveals sub-domain-level heterogeneity that is not discernible in the accompanying [P_2] image. In the AFM scan tall, fence-like perimeters encircle some of the domains, all on a length scale of a few hundred nanometers. The 60x TIRF objective used to acquire the pTIRFM images gave an effective pixel size of 0.27 x 0.27 μm. As such, detecting [P_2] changes within these domains may only be plausible with the use of a higher magnification objective. The pTIRFM apparatus used in these experiments could not acquire order parameter data during the rapid stages of SMase-mediated bilayer re-equilibration. This does not reflect an inherent limitation of the technique, rather the need to manually reposition the half-wave plate in order to sequentially acquire *s*- and *p*-polarized pTIRFM images. With modifications to the plate housing the acquisition time should decrease significantly, and allow for time-resolved pTIRFM imaging of processes occurring on the order of a few seconds.

Orepoulos and Yip have used pTIRFM to examine the effect of two variables on membrane order in phase-separated bilayers of DOPC/DSPC/Chol: the mole fraction of Chol present,[21] and the addition of an antimicrobial peptide, indolicidin (IL).[26] Two fluorescent probes were employed in these studies, the aforementioned BODIPY-PC, and DiI-C_{20}. The latter was assigned as having a transition dipole oriented mostly perpendicular to the membrane normal. Therefore, their results with BODIPY-PC offer a more direct comparison for our own results with **10**. Order parameters were calculated with BODIPY-PC for DOPC/DSPC membranes with Chol content increasing from 5 to 30 mol%. [P_2] values for the L_d phase ranged from a high of 0.31 at

15 mol% Chol down to 0.22 at 30 mol% Chol. In the L_o phase [P_2] was at a maximum of 0.30 at 30 mol% Chol and a minimum of 0.23 at 15 mol%. Following addition of IL to DOPC/DSPC/Chol bilayers (1/1/1 lipid molar ratio), [P_2] for the L_d phase decreased from 0.29 ± 0.01 to 0.16 ± 0.02. Order also decreased in the L_o phase with [P_2] dropping from 0.26 ± 0.01 to 0.22 ± 0.02. In our own measurements with **10** in bilayers of DOPC/ESM/Chol, [P_2] for the L_d phase increased from 0.22 ± 0.02 to 0.30 ± 0.01 upon treatment with SMase. [P_2] values in the L_o domains were essentially unchanged at 0.36 ± 0.01 post enzyme addition, but [P_2] values ≥ 0.40 were observed in the newly formed intermediate phase. A better comparison of BODIPY-PC and **10** requires that they be evaluated as reporters of the same process in a model membrane, for instance by applying the former probe to SMase experiments in our DOPC/ESM/Chol mixture. However, pTIRFM images we have acquired with BODIPY-PC (Figure 3-9) suggest that it does not partition as strongly into the ESM- and Chol-rich domains as **10**. The position of the bulky BODIPY label embedded among the lipid acyl chains may disfavor its distribution into the L_o phase. Moreover, the conversion of ESM to ceramide results in greatest changes in the head group region of the membrane as choline moieties are hydrolyzed to smaller hydroxyl groups. As such BODIPY-PC may not be as sensitive to changes in the orientational order of this environment as probe **10**.

3.4 Summary of Findings and Future Outlook

We have synthesized a novel fluorescent sphingolipid analog, NBD-Cer **10**, and have characterized its photophysical properties in liposomes with compositions selected to reflect L_d and L_o phase membrane environments. The probe has also been evaluated as a tool to assess orientational order in supported lipid membranes using a pTIRFM imaging approach. Order parameter [P_2] and (θ_c) values calculated for **10** are in good agreement with determinations obtained with BODIPY-PC in both our own work and the existing literature. These parameters are also consistent with lipid phase assignments inferred from topography from prior AFM imaging experiments (Chapter 2). Furthermore, we have used **10** to quantify Cer-dependent changes in the lipid order of model membranes treated with SMase. The probe identifies a significant increase in the order of the L_d phase and the appearance of a new, highly ordered and dye-depleted phase following enzyme treatment.

Going forward, several probe- and instrument-related improvements can broaden the scope of our pTIRFM capability. The NBD fluorophore was initially selected in our probe design due to its small size, hydrophilic nature and the ease with which it could be functionalized in organic synthesis. However, its environment-sensitive fluorescence and propensity to photobleaching make it a challenging probe to work with, and limit its utility for quantitative fluorescence imaging. The spatial and temporal resolution of the pTIRFM apparatus used in these studies can be respectively improved through the use of a higher magnification TIRF objective, and a motorized mount for the half-wave plate. At the time of writing these modifications are being implemented by other members of our group, along with the use of brighter and more photostable fluorescent probes.

3.5 Experimental

3.5.1 Chemicals

Egg yolk phosphocholine (EPC), 1,2-Dioleoyl-*sn*-glycero-3-phosphocholine (DOPC), 1,2-dipalmitoyl-*sn*-glycero-3-phosphocholine (DPPC), egg sphingomyelin (ESM), *N*-palmitoyl-*D*-*erythro*-sphingomyelin (C16:0 sphingomyelin, PSM), *N*-palmitoyl-*D*-*erythro*-sphingosine (C16:0 ceramide, C16-Cer), and cholesterol were purchased from Avanti Polar Lipids (Alabaster, AL) and used without further purification. The ammonium salt of 1,2-dipalmitoyl-sn-glycero-3-phosphoethanolamine-N-(7-nitro-2-1,3-benzoxadiazol-4-yl) (NBD-DHPE) was also obtained from Avanti Lipids. 2-(4,4-Difluoro-5,7-dimethyl-4-bora-3a,4a-diaza-*s*-indacene-3-pentanoyl)-1-hexadecanoyl-*sn*-glycero-3-phosphocholine (BODIPY-PC) was acquired from Molecular Probes (Eugene, OR). ((*E*,2*S*,3*R*)-3-hydroxy-2-(palmitamido)octadec-4-enyl)-4-(4-nitrobenzo-2-oxa-1,3-diazol-7-ylamino)butylcarbamate (NBD-Cer, **10**) was synthesized as described elsewhere in this chapter. The sodium salt of fluorescein used in the pTIRFM calibration experiments, sphingomyelinase (SMase) isolated from *S. aureus*, and all salts and synthetic reagents were purchased from Sigma-Aldrich (St. Louis, MO). Optical adhesive 88 was obtained from Norland Products (Cranbury, NJ) and used to glue freshly cleaved mica (grade V-1, Ted Pella, Redding, CA) onto cover glass (Fisher Scientific, Hampton, NH). All aqueous solutions were prepared using 18.3 MΩ cm *Milli-Q* water. SMase buffer (125 mM NaCl, 10 mM $CaCl_2$, 2 mM $MgCl_2$, 10 mM 4-(2-hydroxyethyl)piperazine-1-ethanesulfonic acid (HEPES), pH 7.4) was used for some imaging and SMase experiments. All buffered solutions were passed through a 0.22 μm filter (Millipore, Billerica, MA) before being used. Organic solvents used for preparing lipid films were HPLC grade from EMD Chemicals (Philadelphia, PA).

3.5.2 Synthesis of NBD-Ceramide

All ^{1}H NMR and ^{13}C NMR spectra were recorded in $CDCl_3$ on Bruker AVANCE 300 and 400 instruments at room temperature. Chemical shifts are reported relative to TMS. Complete NMR spectra can be found in the appendix found at the end of this volume.

N-palmitoyl-D-erythro-sphingosine (1) was used as purchased from Avanti Polar Lipids. Its ^{1}H NMR spectrum was obtained to facilitate the characterization of the synthetic intermediates described below. ^{1}H NMR (300 MHz; $CDCl_3$) δ_H 0.89 (6H, t, J = 6.6 Hz), 1.27-1.34 (46H, m), 1.64-1.67 (2H, m), 2.03-2.10 (2H, m), 2.24 (1H, t, J = 7.2 Hz), 2.70 (1H, br), 2.71 (1H, br), 3.68-3.75 (1H, m), 3.89-3.97 (1H, m), 3.95-4.00 (1H, m), 4.31-4.35 (1H, m), 5.54 (1H, ddt, J_1 = 15.3 Hz, J_2 = 6.3 Hz, J_3 = 1.2Hz), 5.80 (1H, dtd, J_1 = 15.3 Hz, J_2 = 6.6 Hz, J_3 = 0.9 Hz), 6.25 (1H, d, J = 7.2 Hz).

***N*-((*E*,2*S*,3*R*)-3-hydroxy-1-trityloxyoctadec-4-en-2-yl)palmitamide (3)** A solution of *N*-palmitoyl-D-*erythro*-sphingosine **1** (109.3 mg, 203 µmol) and *N*, *N*-diisopropylethylamine (DIPEA, 52.5 mg, 406 µmol) in CH_2Cl_2 (2 mL) was prepared at room temperature under a nitrogen atmosphere. A solution of trityl chloride (TrCl **2**, 0.7M in CH_2Cl_2, 96.1 mg, 345 µmol) was added drop-wise to the former, with stirring. The reaction was allowed to proceed to completion (~48 hrs) as determined by TLC (EtOAc/CH_2Cl_2, 75:25) visualized using UV and phosphomolybdic acid (PMA) staining. The solution was then diluted with EtOAc, washed with water, then saturated $NaHCO_3$, and finally brine before being dried over $MgSO_4$. 100.8 mg (65 %) of **3** was obtained following flash chromatography purification (CH_2Cl_2/EtOAc/Et_3N 98:2:0.5). ^{1}H NMR (400 MHz; $CDCl_3$) δ_H 0.86 (6H, t, J = 6.4 Hz), 1.24-1.29 (46H, m), 1.58-1.66 (2H, m), 1.89-1.91 (2H, m), 2.17 (2H, dd, J_1 = 8.0 Hz, J_2 = 7.2 Hz), 3.28 (1H, dd, J_1 = 10.0 Hz, J_2 = 4.0 Hz), 3.37 (1H, dd, J_1 = 9.6 Hz, J_2 = 4.0 Hz), 3.39 (1H, s), 4.02-4.07 (1H, m), 4.14-4.18 (1H, m), 5.24 (1H, ddt, J_1 = 15.6 Hz, J_2 = 6.4 Hz, J_3 = 1.2

Hz), 5.62 (1H, dtd, J_1 = 15.2 Hz, J_2 = 6.8 Hz, J_3 = 1.2 Hz), 6.06 (1H, d, J = 8 Hz), 7.21-7.25 (3H, m), 7.27-7.31 (6H, m), 7.36-7.40 (6H, m).

(*E*,2*S*,3*R*)-2-palmitamido-1-trityloxyoctadec-4-en-3-yl benzoate (5) Under a nitrogen atmosphere **3** (100 mg, 128 µmol) and 4-dimethylaminopyridine (DMAP, 15.6 mg, 128 µmol) were dissolved in CH_2Cl_2 (1.3 mL) at room temperature with stirring, followed by the addition of triethylamine (Et_3N, 26mg, 256 µmol). Benzoyl chloride **4** (27 mg, 192 µmol) was then added drop-wise to the flask over 5 min, and the mixture was left to stir overnight. Complete consumption of trityl ceramide **3** was then confirmed by TLC (CH_2Cl_2/EtOAc/Et_3N 98:2:0.1). Dilution in EtOAc was followed with washes in 10% HCl, saturated $NaHCO_3$, and brine prior to drying the organic phase over $MgSO_4$. Purification by flash chromatography (hexanes/EtOAc) following a gradient from 95:5 to 9:1) afforded 103.7 mg (92 %) of **5**. ^{1}H NMR (300 MHz; $CDCl_3$) δ_H 0.90 (6H, t, J = 6.3 Hz), 1.28-1.32 (46H, m), 1.57-1.61 (2H, m), 2.02 (2H, dt, J_1 = 6.9 Hz, J_2 = 6.9 Hz), 2.13 (2H, dd, J_1 = 7.8 Hz, J_2 = 7.2 Hz), 3.22 (1H, dd, J_1 = 9.6 Hz, J_2 = 4.2 Hz), 3.47 (1H, dd, J_1 = 9.6 Hz, J_2 = 3.6 Hz), 4.48-4.56 (1H, m), 5.47 (1H, dd, J_1 = 15.3 Hz, J_2 = 7.5 Hz), 5.71 (1H, br), 5.72 (1H, dd, J_1 = 7.5 Hz, J_2 = 7.2 Hz), 5.90 (1H, dt, J_1 = 15.3 Hz, J_2 = 6.6 Hz), 7.19-7.27 (9H, m), 7.40-7.45 (8H, m), 7.58 (1H, t, J = 7.5 Hz), 7.96 (2H, d, J = 7.5 Hz).

(*E*,2*S*,3*R*)-1-hydroxy-2-(palmitamido)octadec-4-en-3-yl benzoate (6) **5** (80 mg, 91 µmol) was dissolved in 2mL toluene/MeOH (6:4) at room temperature, under nitrogen. A solution of freshly distilled $BF_3{\cdot}Et_2O$ (10% v/v in toluene, 25 mg, 18 µmol) was slowly added to the flask which was then left to stir for two hours, at which point TLC (hexanes/EtOAc 9:1) indicated complete disappearance of **5**. The reaction was quenched with water, extracted with EtOAc, washed with saturated $NaHCO_3$ and brine, and then dried over $MgSO_4$. Flash chromatography

(hexanes/EtOAc 7:3 increasing to 1:1) was used to purify the resulting **6** of which 58.10 mg (70 %) was recovered. ^{1}H NMR (400 MHz; $CDCl_3$) δ_H 0.88 (6H, t, *J* = 6.4 Hz), 1.25-1.37 (46H, m), 1.57-1.63 (2H, m), 2.05 (2H, dt, J_1 = 6.8 Hz, J_2 = 6.8 Hz), 2.17-2.21 (2H, m), 2.88 (1H, dd, J_1 = 4.8 Hz, J_2 = 3.2 Hz), 3.66-3.76 (2H, m), 4.24-4.30 (1H, m), 5.53 (1H, t, *J* = 7.2 Hz), 5.61 (1H, ddt, J_1 = 15.2 Hz, J_2 = 7.6 Hz, J_3 = 1.2 Hz), 5.85 (1H, dt, J_1 = 14.8 Hz, J_2 = 6.8 Hz), 6.04 (1H, d, *J* = 8.8 Hz), 7.44-7.48 (2H, m), 7.59 (1H, tt, J_1 = 7.2 Hz, J_2 = 1.6 Hz), 8.04 (2H, dd, J_1 = 8.4 Hz, J_2 = 1.2 Hz).

***Tert*-butyl 4-(4-nitrobenzo-2-oxa-1,3-diazol-7-ylamino)butylcarbamate (7)** was prepared as described in Chapter 2.

(*E*,2*S*,3*R*)-1-(4-butyl-(4-nitrobenzo-2-oxa-1,3-diazol-7-ylamino)carbamoyl)-2-(palmitamido)octadec-4-en-3-yl benzoate (9) 6 (7.8 mg, 12 µmol) was dissolved in toluene (500 µL) under a nitrogen atmosphere at room temperature; solid carbonyldiimidazole (CDI, 4 mg, 25 µmol) was then added. The mixture was left to stir for 1 hr, at which point TLC analysis (hexanes/EtOAc 1:1) indicated complete consumption of starting material. In a separate flask, **7** (8 mg, 23 µmol) was dissolved in trifluoroacetic acid (TFA, 400 µL) and allowed to stir for 30 min, in the dark, at room temperature (TLC hexane/EtOAc, 1:1). The de-protected NBD-butylamine **8** was concentrated under reduced pressure; it was then re-suspended in benzene and once again concentrated at low pressure to remove residual TFA (repeated twice). Subsequently **8** and Et_3N (5.6 mg, 43 µmol) were dissolved in CH_2Cl_2 (300 µL) under nitrogen. This preparation was slowly added by syringe to the solution in the first flask and stirred overnight in the dark. A new fluorescent spot was observed by TLC (hexanes/EtOAc 1:1) concomitant with the reappearance benzoyl-ceramide **6**- complete conversion was not achieved. The reaction mixture was diluted with EtOAc, washed with 10 % HCl, saturated

$NaHCO_3$ then brine, and finally dried over $MgSO_4$. The crude product was concentrated, loaded onto a preparative TLC plate, and developed in a mobile phase of hexanes/EtOAc 45:55. The major fluorescent band was isolated from the plate to afford 4.2 mg (38 %) of **9**. ^{1}H NMR (400 MHz; $CDCl_3$) δ_H 0.86 (6H, t, *J* = 6.8 Hz), 1.22-1.30 (46H, m), 1.57-1.59 (2H, m), 1.67-1.69 (2H, m), 1.82-1.85 (2H, m), 2.00-2.04 (2H, m), 2.18 (2H, dd, J_1 = 7.6 Hz, J_2 = 6.8 Hz), 3.18-3.21 (1H, m), 3.28-3.31 (1H, m), 3.51-3.53 (2H, m), 4.24-4.26 (2H, m), 4.62 (1H, br), 4.83 (1H, t, *J* = 4.0 Hz), 5.48-5.51 (1H, m), 5.53-5.56 (1H, m), 5.80-5.84 (1H, m), 5.86-5.91 (1H, m), 6.15 (1H, d, *J* = 8.4 Hz), 6.99 (1H, br), 7.42 (2H, dd, J_1 = 7.6 Hz, J_2 = 7.6 Hz), 7.56 (1H, t, *J* = 7.6 Hz), 8.01 (2H, d, *J* = 7.6 Hz), 8.47 (1H, d, *J* = 8.4 Hz).

((*E*,2*S*,3*R*)-3-hydroxy-2-(palmitamido)octadec-4-enyl)-4-(4-nitrobenzo-2-oxa-1,3-diazol-7-ylamino)butylcarbamate (NBD-Ceramide, 10) A solution of **9** (4.2 mg, 5 µmol) was prepared in a mixture of THF/MeOH/H_2O (3:1:1, 500 µL). Solid LiOH (9 mg, 376 µmol) was added, and the solution was allowed to stir for 1 hr, after which complete disappearance of **9** was observed by TLC (hexanes/EtOAc 1:1). The mixture was concentrated under reduced pressure, re-suspended in EtOAc/H_2O and then washed with 10 % HCl, saturated $NaHCO_3$, brine, and then dried over $MgSO_4$. The crude product was purified by reversed-phase HPLC with a SunFire C18 column (Waters Corp., Milford, MA, USA), and eluted with an isocratic mixture (95% EtOH/H_2O) at a flow rate of 0.8 mL/min (t_R = 4.2 min) to obtain 2.3 mg (60 %) of **10**. Detection was by absorbance at 470 nm and fluorescence at 535 nm. ^{1}H NMR (400 MHz; $CDCl_3$) δ_H 0.89 (6H, t, *J* = 7.0 Hz), 1.24-1.33 (46H, m), 1.59-1.63 (2H, m), 1.67-1.80 (2H, m), 1.85-1.96 (2H, m), 2.02-2.07 (2H, m), 2.21 (2H, t, J_1 = 7.6 Hz, J_2 = 7.2 Hz), 2.53 (1H, t, *J* = 7.0 Hz), 3.19-3.24 (1H, m), 3.33-3.39 (1H, m), 3.54-3.57 (2H, m), 3.75 (1H, t, *J* = 5.9 Hz), 4.19-4.24 (2H, m), 4.27-4.30 (1H, m), 4.92

(1H, t, J = 4.7 Hz), 5.50 (1H, dd, J_1 = 15.5 Hz, J_2 = 6.3 Hz), 5.73-5.80 (1H, m), 5.99 (1H, d, J = 8.0 Hz), 6.18 (1H, d, J = 8.7 Hz), 7.03 (1H, br), 8.50 (1H, d, J = 8.7 Hz); ^{13}C NMR (125 MHz; $CDCl_3$) δ_C 14.4, 22.9, 25.4, 26.0, 27.9, 29.4, 29.5, 29.6, 29.7, 29.9, 32.2, 32.5, 37.1, 40.4, 43.9, 53.7, 64.0, 73.5, 128.2, 134.9, 136.7, 144.6, 174.1; MS (ES+) 815.6 (MH^+).

3.5.3 Absorption and Fluorescence Spectroscopy

Small unilamellar vesicles (SUVs) were prepared as previously described in chapter 2 subject to some minor modifications. Lipids and NBD-Cer were dissolved in chloroform, methanol, ethanol, or mixtures thereof as required. Once these organic solutions were mixed in appropriate proportions, the organic solvents were evaporated. The resulting dry lipid films were hydrated in *Milli-Q* water and then sonicated at 60 °C in a bath sonicator to clarity to form SUVs with a final lipid concentration of 1.0 mg/mL for spectroscopic experiments, or 0.5 mg/mL for supported bilayer experiments. Lipid films were stored for up to 1 week at -20 °C prior to use; however, fresh vesicles were prepared on the day of each experiment.

Absorption spectra were measured with a Cary 5000 UV-vis-NIR spectrophotometer. Emission spectra were recorded using a Horiba Jobin Yvon FL-3 21 2tau spectrofluorometer with slit widths of 1 nm. All spectral measurements were performed in oxygenated *Milli-Q* water at 22 °C using a 1-cm path length quartz cuvette. Fluorescence quantum yields were calculated with reference to NBD-DHPE[56] (Φ_{fl} = 0.16 at 2 mol% in SUVs of EPC at a total lipid concentration of 1.0 x 10^{-3} M, pH 7) at an excitation wavelength of 470 nm and absorbance ≤ 0.2. Absorption measurements for vesicle solutions containing the NBD probes were corrected for lipid scattering before calculating Φ_{fl}. This was done by subtracting the absorbance of an unlabelled vesicle solution of the appropriate composition and concentration from each of the

dye-containing samples. Fluorescence lifetimes were measured using the frequency domain method with modulation frequencies in the 2-80 MHz range. Gaussian fits of the raw data were prepared by Dr. Zygmunt J. Jakubek.

3.5.4 Supported Lipid Bilayers

Planar supported bilayers were formed on mica via vesicle fusion. Freshly cleaved mica disks (15-25 μm thick for fluorescence imaging) were glued onto circular cover glasses. To prepare bilayers of DOPC/ESM/Chol or DPPC/ESM/Chol stained with NBD-Cer, 950 μL of 8 mM $CaCl_2$ was first added to a mica/glass slide clamped in a liquid cell, and warmed to 45 °C. 50 μL of a 0.5 mg/mL vesicle suspension was then introduced at the same temperature, and the samples were incubated for 15 min before being gradually cooled to 22 °C over a period of 2 h. Bilayers were gently washed with *Milli-Q* water or buffer to remove adsorbed vesicles before imaging.

3.5.5 pTIRFM/AFM Imaging

3.5.5.1 pTIRFM/AFM Instrumentation

Polarized total internal reflection fluorescence microscopy (pTIRFM) and correlated pTIRFM-AFM were both performed on the same experimental apparatus at room temperature (~22 °C). The imaging system consisted of a NanoWizard II BioAFM (JPK Instruments, Berlin, Germany) mounted on an IX81 inverted optical microscope (Olympus Corporation, Tokyo, Japan) with objective-based total internal reflection fluorescence optics (PLAN-APO N 60X objective, 1.45 NA; Olympus). This ensemble was contained in an acoustic isolation box fabricated in-house, and seated on a Micro 60 active vibration isolation table (Halcyonics/Accurion GmbH, Goettingen, Germany). A fiber-coupled 488 nm Ar ion laser (CVI Melles Griot, Albuquerque, NM) was used for excitation and fluorescence was recorded

through a FF01-536/40 emission filter (Semrock, Rochester, NY). All fluorescence images were captured using a Cascade 512B CCD camera (512 x 512 pixels, 16 x 16 μm pixel size; Photometrics, Tucson, AZ). The size of the excitation spot at the objective could be adjusted using a manually operated micrometer screw to reposition the focusing lens in the illuminator. A second micrometer allowed radial translation of the focused laser beam from the center of the objective aperture (polarized epifluorescence mode) toward its edge in order to achieve TIR (TIRFM mode). For an initial comparison of the effects of laser polarization, images were recorded using TIRF and epifluorescence geometries; the linearly polarized emission from the laser resulted in ~70% axial polarization for TIRF as compared within-plane polarized excitation for epifluorescence.

Drs. Zhengfang Lu and Zygmunt J. Jakubek (National Research Council, Canada) implemented several modifications to the optical microscope's excitation pathway to enable polarized TIRF illumination of samples at the objective. The electric field vector defining the polarization angle of the excitation beam, ψ, could be set by the microscope user to any angle between 0° and 90° by rotating a ½" zero-order, half-wave plate with antireflection coating for 488 nm (Thorlabs, Newton, NJ). The rotation angle for the half-wave plate could be defined to within ±1°, and the plate was held in a manually operated rotation mount that was installed in the NIR filter slot of the microscope turret. The laser polarization extinction ratio (PER) was measured using a linear polarizer and a power meter placed at the objective. For blank mica-glass substrates used to calibrate the half-wave plate and for bilayer imaging experiments, PER values > 100:1 were obtained with the substrates appropriately aligned to control for the birefringence of mica.

3.5.5.2 pTIRFM/AFM Image Acquisition

pTIRFM and pTIRFM/AFM imaging experiments were performed as follows: a sample region of interest (ROI) was brought into focus and *s*- and *p*-polarized images were successively acquired. The exposure time used was 1 s with the camera gain set to 0 for all images. Following pTIRFM acquisition 30 x 30 μm AFM scans were obtained as required in the central area of the ROI. All AFM images were captured using uncoated silicon nitride DNP-S-10 (Veeco, Camarillo, CA) AFM cantilevers with a typical spring constant of 0.12 N/m. Contact mode topographic images were collected at scan rates of 0.7-1 Hz, and continuous adjustments to the set point kept the force exerted on the sample at a minimum. Scans were collected at 512 x 512 pixel resolution and were line fitted with first- to third-order polynomials when necessary. A second pTIRFM acquisition was performed in the ROI upon completion of AFM imaging to monitor the sample for scan-related morphological changes. Once the required images had been obtained a pair of fine-nosed tweezers was used to create a dark stripe or defect in the ROI by cleanly scraping away the lipid bilayer. A final set of *s*- and *p*-polarized images was then obtained in the area under the same acquisition parameters used previously. These images were used to provide a localized background correction for the *s*- and *p*-polarized channels respectively.

3.5.5.3 pTIRFM Image Analysis and Order Parameter Determination

All pTIRFM image analysis and processing was done using National Institutes of Health ImageJ (http://rsb.info.nih.gov/ij, Ver. 1.43 M), which is in the public domain. For each ROI examined in a pTIRFM imaging experiment *s*- and *p*-polarized images were background corrected by subtracting an intensity value to account for any intensity contributions from the

substrate or solution, electronic noise, and excitation leak-through from the microscope optics. This value was independently determined for the *s*- and *p*-polarized images by measuring intensity in the center of the dark defect that had been imaged in the final set of pTIRFM images. The averaged intensity values obtained in this area were then subtracted from the appropriate *s*- and *p*-polarized images of the intact membrane.

Order parameters were subsequently calculated from the background-corrected pTIRFM images using a macro for ImageJ developed by Drs. John Oreopoulos and Christopher M. Yip (University of Toronto, Canada), which was graciously made available to us upon request. The macro accepts the angle of incidence for the excitation laser (α), the indexes of refraction for the medium (n_1) and substrate (n_2) and the *p*- and *s*-polarized pTIRFM images as inputs. For these experiments we used α = 60°, n_1 = 1.3326 (water), and n_2 = 1.5750 (mica). The plug-in calculates factor *B* (see Equation 3-2) for each *ij* pixel (B_{ij}) using a least-squares numerical algorithm. Order parameter values were thus determined on a pixel-by-pixel basis $(P_2)_{ij}$ for each B_{ij}, and were then plotted in a new (P_2) image of the ROI. The order parameter images were color-scaled using ImageJ's FIRE 8-bit lookup table. Order parameters were analyzed using the software's built-in measure and histogram functions. Analysis of pTIRFM images was confined to the central areas of the ROIs (typically 30 x 30 µm) where the TIRF illumination had its peak intensity, was most homogeneous, and free of any interference patterns. Within each ROI 10-15 sample regions were selected for each [P_2] environment (i.e. l_d and l_o phases) based on the size of the features present (for l_o domains square boxes with side lengths of 3-5 pixels were selected). Thus, for every ROI the [P_2] value reported for each environment was the average of at least 10 measurements each encompassing the average value measured from 9-25 pixels.

Unless otherwise stated [P_2] values reported in Table 3-2 are averaged values for a minimum of three ROIs from each of three independently prepared bilayer samples.

3.5.5.4 SMase Treatments and pTIRFM/AFM Imaging

Supported lipid bilayers of DOPC/ESM/Chol stained with **10** were formed as described above. Prior to pTIRFM image acquisition the samples were gently rinsed with SMase buffer for 2 min and allowed to stand for 20-30 min in the dark. pTIRFM and AFM images were then sequentially acquired in a ROI. SMase in buffer (final concentration in the wet cell was 0.2 U/mL) was then introduced by pipette into the solution above the bilayer. Changes in the membrane were monitored by fluorescence until rapid micron-scale lateral reorganization had ceased- typically 15-20 min following enzyme addition. At this point pTIRFM and AFM images were sequentially acquired with the enzyme *in situ*.

3.6 References

1. Veatch, S. L.; Keller, S. L., Seeing spots: complex phase behaviour in simple membranes. *Biochim. Biophys. Acta* **2005,** *1746*, 172-185.

2. Lagerholm, B. C.; Weinreb, G. E.; Jacobson, K.; Thompson, N. L., Detecting microdomains in intact cell membranes. *Annu. Rev. Phys. Chem.* **2005,** *56*, 309-36.

3. Meder, D. M.; Moreno, J. M.; Verkade, P.; Vaz, W. L. C.; Simons, K., Phase coexistence and connectivity in the apical membrane of polarized epithelial cells. *Proc. Natl. Acad. Sci. USA* **2006,** *103*, 329-334.

4. Bagatolli, L. A., To see or not to see: lateral organization of biological membranes and fluorescence microscopy. *Biochim. Biophys. Acta* **2006,** *1758*, 1541-1556.

5. P., C.; Keller, S. L.; Veatch, S. L., Diffusion of liquid domains in lipid bilayer membranes. *J. Phys. Chem. B* **2007,** *111*, 3328-3331.

6. Montes, L. R. A.; Alonso, A.; Goni, F. M.; Bagatolli, L. A., Giant unilamellar vesicles electroformed from native membranes and organic lipid mixtures under physiological conditions. *Biophys. J.* **2007,** *93*, 3548-3554.

7. Ira; Zou, S.; Carter Ramirez, D. M.; Vanderlip, S.; Ogilvie, W. W.; Jakubek, Z. J.; Johnston, L. J., Enzymatic generation of ceramide induces membrane restructuring: correlated AFM and fluorescence imaging of supported bilayers. *J. Struct. Biol.* **2009,** *168*, 78-89.

8. Carter Ramirez, D. M.; Ogilvie, W. W.; Johnston, L. J., NBD-cholesterol probes to track cholesterol distribution in model membranes. *Biochim. Biophys. Acta* **2010,** *1798*, 558-568.

9. Li, L.; Cheng, J. X., Label-free coherent anti-Stokes Raman scattering imaging of coexisting lipid domains in single bilayers. *J. Phys. Chem. B* **2008,** *112*, 1576-1579.

10. De Almeida, R. F. M.; Borst, J.; Fedorov, A.; Prieto, M.; Visser, A., Complexity of lipid domains and rafts in giant unilamellar vesicles revealed by combining imaging and microscopic and macroscopic time-resolved fluorescence. *Biophys. J.* **2007,** *93*, 539-553.

11. Crane, J. M.; Kiessling, V.; Tamm, L. K., Measuring lipid asymmetry in planar supported bilayers by fluorescence interference contrast microscopy. *Langmuir* **2005,** *21*, 1377-1388.

12. Kraft, M. L.; Weber, P. K.; Longo, M. L.; Hutcheon, I. D.; Boxer, S. G., Phase separation of lipid membranes analyzed with high-resolution secondary ion mass spectrometry. *Science* **2006,** *313*, 1948-1951.

13. Popov, J.; Vobornik, D.; Coban, O.; Keating, E.; Miller, D.; Francis, J.; Peterson, N. O.; Johnston, L. J., Chemical mapping of ceramide distribution in sphingomyelin-rich domains in monolayers. *Langmuir* **2008,** *24*, 13502-13508.

14. Touboul, D.; Brunelle, A.; Laprevote, O., Mass spectrometry imaging: towards a lipid microscope? *Biochimie* **2011,** *93*, 113-119.

15. Vobornik, D.; Banks, D. S.; Lu, Z.; Fradin, C.; Taylor, R.; Johnston, L. J., Fluorescence correlation spectroscopy with sub-diffraction-limited resolution using near-field optical probes. *Appl. Phys. Lett.* **2008,** *93*, 163904.

16. Abulrob, A.; Lu, Z.; Baumann, E.; Vobornik, D.; Taylor, R.; Stanimirovic, D.; Johnston, L. J., Nanoscale imaging of epidermal growth factor receptor clustering. *J. Biol. Chem.* **2010,** *285*, 3145-3156.

17. Rice, J. H., Beyond the diffraction limit: far-field fluorescence imaging with ultrahigh resolution. *Mol. BioSys.* **2007,** *3*, 781-793.

18. O'Shea, P.; Somekh, M.; Barnes, W., Shedding light on life. *Phys. World* **2008,** *21*, 29-34.

19. Shaw, J. E.; Epand, R. F.; Epand, R. M.; Li, Z.; Bittman, R.; Yip, C. M., Correlated fluorescence-atomic force microscopy of membrane domains: structure of fluorescence probes determines lipid localization. *Biophys. J.* **2006,** *90*, 2170-2178.

20. Oreopoulos, J.; Yip, C. M., Combined scanning probe and total internal reflection fluorescence microscopy. *Methods* **2008,** *46*, 2-10.

21. Oreopoulos, J.; Yip, C. M., Probing membrane order and topography in supported bilayers by combined total internal reflection fluorescence-atomic force microscopy. *Biophys. J.* **2009,** *96*, 1970-1984.

22. Chiantia, S.; Ries, J.; Chwastek, G.; Carrer, D.; Li, Z.; Bittman, R.; Schwille, P., Role of ceramide in membrane protein organization investigated by combined AFM and FCS. *Biochim. Biophys. Acta* **2008,** *1778*, 1356-1364.

23. Plochberger, B.; Stockner, T.; Chiantia, S.; Brameshuber, M.; Weghuber, J.; Hermetter, A.; Schwille, P.; Schutz, G. J., Cholesterol slows down the lateral mobility of oxidized phospholipid in a supported lipid bilayer. *Langmuir* **2010,** *26*, 17322-17329.

24. Klose, C.; Ejsing, C. S.; Garcia-Saez, A. J.; Kaiser, H. J.; Sampaio, J. L.; Surma, M. A.; Shevchenko, A.; Schwille, P.; Simons, K., Yeast lipids can phase-separate into micrometer-scale membrane domains. *J. Biol. Chem.* **2010,** *285*, 30224-30232.

25. Demchenko, A. P.; Mely, Y.; Duportail, G.; Klymchenko, A. S., Monitoring biophysical properties of lipid membranes by environment-sensitive fluorescent probes. *Biophys. J.* **2009,** *96*, 3461-70.

26. Oreopoulos, J.; Yip, C. M., Combinatorial microscopy for the study of protein-membrane interactions in supported lipid bilayers: Order parameter measurements by combined polarized TIRFM/AFM. *J. Struct. Biol.* **2009,** *168*, 21-36.

27. Oreopoulos, J.; Yip, C. M., Peptide-induced domain formation in supported lipid bilayers: Direct evidence by combined atomic force and polarized total internal reflection fluorescence microscopy. *Biophys. J.* **2010,** *98*, 815-823.

28. Livanec, P. W.; Dunn, R. C., Single-molecule probes of lipid membrane structure. *Langmuir* **2008,** *24*, 14066-14073.

29. Livanec, P. W.; Huckabay, H. A.; Dunn, R. C., Exploring the effects of sterols in model lipid membranes using single-molecule orientations. *J. Phys. Chem. B* **2009,** *113*, 10240-10248.

30. Bernchou, U.; Brewer, J.; Midtiby, H. S.; Ipsen, J. H.; Bagatolli, L. A.; Simonsen, A. C., Texture of lipid bilayer domains. *J. Am. Chem. Soc.* **2009,** *131*, 14130-14131.

31. Anantharam, A.; Onoa, B.; Edwards, R. H.; Holz, R. W.; Axelrod, D., Localized topological changes of the plasma membrane upon exocytosis visualized by polarized TIRFM. *J. Cell Biol.* **2010,** *188*, 415-428.

32. Huckabay, H. A.; Dunn, R. C., Hydration effects on membrane structure probed by single molecule orientations. *Langmuir* **2011,** *27*, 2658-2666.

33. Gidwani, A.; Holowka, D.; Baird, B., Fluorescence anisotropy measurements of lipid order in plasma membranes and lipid rafts from RBL-2H3 mast cells. *Biochemistry* **2001,** *40*, 12422-12429.

34. Veatch, S. L., From small fluctuations to large-scale phase separation: lateral organization in model membranes containing cholesterol. *Semin. Cell Dev. Biol.* **2007,** *18*, 573-582.

35. van Meer, G.; Voelker, D. R.; Feigenson, G. W., Membrane lipids: where they are and how they behave. *Nat. Rev. Mol. Cell Biol.* **2008,** *9*, 112-124.

36. Lopes, S.; Castanho, M., Overview of common spectroscopic methods to determine the orientation/alignment of membrane probes and drugs in lipidic bilayers. *Curr. Org. Chem.* **2005,** *9*, 889-898.

37. Dafforn, T. R.; Rodger, A., Linear dichroism of biomolecules: which was is up? *Curr. Opin. Struct. Biol.* **2004,** *14*, 541-546.

38. Hubbell, W. L.; McConnell, H. M., Molecular motion in spin-labeled phospholipids and membranes. *J. Am. Chem. Soc.* **1971,** *93*, 314-326.

39. Seelig, A.; Seelig, J., Dynamic structure of fatty acyl chains in a phospholipid bilayer measured by deuterium magnetic-resonance. *Biochemistry* **1974,** *13*, 4839-4845.

40. Castanho, M.; Lopes, S.; Fernandes, M., Using UV-Vis linear dichroism to study the orientation of molecular probes and biomolecules in lipidic membranes. *J. Spectrosc.* **2003,** *17*, 377-398.

41. Citra, M. J.; Axelsen, P. H., Determination of molecular order in supported lipid membranes by internal reflection Fourier transform infrared spectroscopy. *Biophys. J.* **1996,** *71*, 1796-1805.

42. Toptygin, G.; Brand, L., Determination of DPH order parameters in unoriented vesicles. *J. Fluoresc.* **1995,** *5*, 39-50.

43. Seelig, J.; Niederbe, W., Deuterium-labeled lipids as structural probes in liquid-crystalline bilayers-deuterium magnetic resonance study. *J. Am. Chem. Soc.* **1974,** *96*, 2069-2072.

44. Vist, M. R.; Davis, J. H., Phase-equilibria of cholesterol dipalmitoylphosphatidylcholine mixtures-H^2 nuclear magnetic-resonance and differential scanning calorimetry. *Biochemistry* **1990,** *29*, 451-464.

45. Zhao, J.; Wu, J.; Heberle, F. A.; Mills, T. T.; Klawitter, P.; Huang, G.; Costanza, G.; Feigenson, G. W., Phase studies of model membranes: Complex behaviour of DSPC/DOPC/Cholesterol. *Biochim. Biophys. Acta* **2007,** *1768*, 2764-2776.

46. Vermeer, L. S.; de Groot, B. L.; Milon, A.; Czaplicki, J., Acyl chain order parameter profiles in phospholipid bilayers: computation from molecular dynamics simulations and comparison with 2H NMR experiments. *Eur. Biophys. J.* **2007,** *36*, 919-31.

47. Lindblom, G.; Oradd, G., Lipid lateral diffusion and membrane heterogeneity. *Biochim. Biophys. Acta* **2009,** *1788*, 234-244.

48. Axelrod, D., Carbocyanine dye orientation in red-cell membrane studied by microscopic fluorescence polarization. *Biophys. J.* **1979,** *26*, 557-573.

49. Axelrod, D., Fluorescence polarization microscopy. *Methods Cell Biol.* **1989,** *30*, 333-352.

50. Sot, J.; Bagatolli, L. A.; Goni, F. M.; Alonso, A., Detergent-resistant, ceramide-enriched domains in sphingomyelin/ceramide bilayers. *Biophys. J.* **2006,** *90*, 903-914.

51. Ariola, F. S.; Mudaliar, D. J.; Walvicka, R. P.; Heikal, A. A., Dynamics imaging of lipid phases and lipid-marker interactions in model biomembranes. *Phys. Chem. Chem. Phys.* **2006,** *8*, 4517-4529.

52. Baumgart, T.; Hunt, G.; Farkas, E. R.; Webb, W. W.; Feigenson, G. W., Fluorescence probe partitioning between L_o/L_d phases in lipid membranes. *Biochim. Biophys. Acta* **2007,** *1768*, 2182-2194.

53. Burghardt, T. P.; Ajtai, K.; Chan, D. K.; Halstead, M. F.; Li, J.; Zheng, Y., GFP-tagged regulatory light chain monitors single myosin lever-arm orientation in a muscle fiber. *Biophys. J.* **2007,** *93*, 2226-2239.

54. Thompson, N. L.; McConnell, H. M.; Burghardt, T. P., Order in supported phospholipid monolayers detected by the dichroism of fluorescence excited with polarized evanescent illumination. *Biophys. J.* **1984,** *46*, 739-747.

55. Sund, S. E.; Swanson, J. A.; Axelrod, D., Cell membrane orientation visualized by polarized total internal reflection fluorescence. *Biophys. J.* **1999,** *77*, 2266-2283.

56. Mazeres, S.; Schram, V.; Tocanne, J. F.; Lopez, A., 7-Nitrobenz-2-oxa-1,3-diazole-4-yl-labeled phospholipids in lipid membranes: differences in fluorecence behaviour. *Biophys. J.* **1996,** *71*, 327-335.

57. Veatch, S. L.; Keller, S. L., Miscibility phase diagrams of giant vesicles containing sphingomyelin. *Phys. Rev. Lett.* **2005,** *94*, 148101-148104.

58. Paprica, P. A.; Baird, N. C.; Petersen, N. O., Theoretical and experimental analyses of optical transitions of nitrobenzoxadiazole (NBD) derivatives. *J. Photochem. Photobiol. A.* **1993,** *70*, 51-57.

59. Goni, F. M.; Alonso, A., Effects of ceramide and other simple sphingolipids on membrane lateral structure. *Biochim. Biophys. Acta* **2009,** *1788*, 169-177.

60. Kang, H. C.; Fisher, P. J.; Prendergast, F. G.; Haugland, R. P., Bodipy: A novel fluorescein and NBD substitute. *J. Cell Biol.* **1988,** *107*, 34a.

61. Pagano, R. E.; Martin, O. C.; Kang, H. C.; Haugland, R. P., A novel fluorescent ceramide analogue for studying membrane traffic in animal cells: accumulation at the golgi apparatus results in altered spectral properties of the sphingolipid precursor. *J. Cell Biol.* **1991,** *113*, 1267-1279.

62. Lopez-Montero, I.; Monroy, F.; Velez, M.; Devaux, P. F., Ceramide: From lateral segregation to mechanical stress. *Biochim. Biophys. Acta* **2010,** *1798*, 1348-1356.

63. Lancet, D.; Pecht, I., Spectroscopic and immunochemical studies with nitrobenzoxadiazolealanine, a fluorescent dinitrophenyl analogue. *Biochemistry* **1977,** *16*, 5150-5157.

Chapter 4

Bhc-caged Ceramides: Spatial and Temporal Control of Ceramide Generation

This Chapter Contains Material Adapted from the Following Manuscripts

1. Kim, Y.A.; Carter Ramirez, D.M.; Costain, W.J.; Johnston, L.J., Bittman, R. A new tool to assess ceramide bioactivity: 6-bromo-7-hydroxycoumarinyl-caged ceramide. *Chem. Commun*. **2011**, *47*, 9236-9238
2. Carter Ramirez, D.M.; Kim, Y.A.; Bittman, R.; Johnston, L.J. Lipid phase separation and protein-ganglioside clustering in supported bilayers induced by photorelease of ceramide. *Submitted.*
3. Carter Ramirez, D.M.; Pitre, S.P.; Kim, Y.A.; Bittman, R.; Johnston, L.J. Photo-uncaging of ceramide in supported lipid bilayers introduces lateral membrane reorganization. *Submitted.*

4.1 Introduction: Towards the Photo-Controlled Release of Ceramide

4.1.1 Photolabile Protecting Groups for Biomolecules

Caged compounds have been increasingly used[1-5] to study molecular processes in biochemistry, biophysics and physiology since the late 1970s, when 2-nitrobenzyl (NB) photolysis was first applied towards understanding a biological problem.[6] Light-activated chemical processes are broadly appealing to life scientists because they can be used to release or "uncage" bioactive compounds with a high degree of spatial and temporal control. Initially only small, low molecular weight compounds were releasable. In the seminal work mentioned above, by Kaplan and coworkers, 1-(2-nitrophenyl)ethyl-caged adenosine triphosphate (NPE ATP) was photolyzed to study the erythrocytic Na : K ion pump. More recently, whole proteins[7] and oligonucleotides[8] have been the subject of caging applications.

Four principal chromophore classes have been most widely used in photo-uncaging reactions involving biomolecules: 1) 2-nitrobenzyl (NB), 2) benzoin (Bnz), 3) *para*-hydroxyphenacyl (pHP), and 4) benzyl (Bz).[9] The fourth category also includes other arylalkyls such as coumaryl (Cou) groups (Figure 4-1). Over 80% of published studies involving photolabile protecting groups have been based on the photoredox chemistry of the NB chromophore (Scheme 4-1).[10] However, NB cages have well-documented limitations: a slow rate of substrate release, absorption maxima situated at short wavelengths (< 350 nm), small two-photon cross-sections and generation of reactive nitroso side products. Much of the work involving other chromophores seeks to remedy some of these shortcomings, particularly in the context of increasing their compatibility with *in vivo* processes. This chapter describes the characterization of (6-bromo-7-hydroxycoumarin-4-yl)methyl (Bhc) caged ceramides,[11] and their application

towards the study of ceramide-mediated membrane reorganization. As such, we will present an overview of the spectroscopic, photochemical and mechanistic properties of coumarin-4-ylmethyl phototriggers, and discuss them in the context of the NB literature.

Figure 4-1. Chemical structures of some chromophores used to cage bioactive compounds. X = leaving group/caged substrate; and R, R_1, X and Y are groups that modulate the electron density around the chromophore.

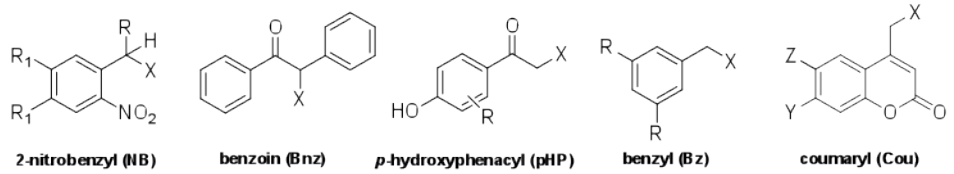

Scheme 4-1. Reaction scheme for the photolysis of generalized nitrobenzyl-caged compounds.[10] X = caged species and R = H, CH_3, CO_2^-. Following irradiation of **I** the photolytic process proceeds with transfer of the benzylic proton to an oxygen of the nitro group to form *Z*-nitronic acid **II**. The decay of aci-nitro anion **III** represents the RDS and is proportional to $[H^+]$ below pH 9. Isomerization to *E*-nitronic acid **IV** allows cyclization to the *N*-hydroxybenzisoxazoline **V**. There is no direct evidence for **V**, as it is assumed to decay immediately to nitrosocarbonyl **VII**. Alternative collapse to hemiacetal **VI** is generally ruled out because accumulation of such an intermediate is not observed. The release of alcohols from an NB cage is a notable exception, for which a rate limiting hemiacetal with $t_{1/2}$ ~ 2s at pH 7 and 23 °C has been observed.

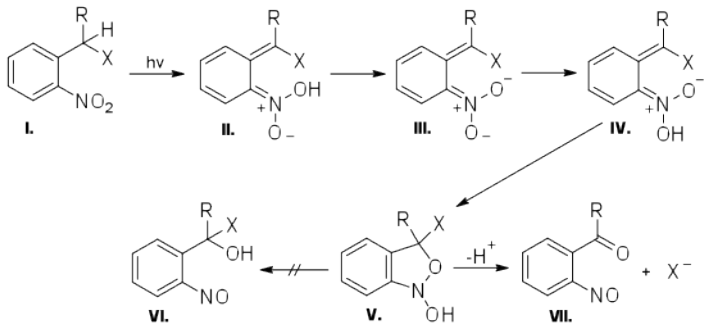

Caging chromophores should possess the following attributes: a) strong absorption at visible or near-infrared wavelengths to diminish cell damage, b) efficient and rapid photorelease processes, c) the cage and its photo by-products should be biologically inert, d) by-products should exhibit a hypsochromic shift in absorption with respect to the cage, e) installation of the caging group should not generate new stereocenters. A photolabile protecting group's utility can be quantified in terms of the efficiency and rate of its photolysis

upon pulse illumination by light at a suitable wavelength. Efficiency of photoconversion refers to the percentage of caged compounds converted to the bioactive species by the light pulse. It is influenced by two factors: 1) the extinction coefficient (ε) indicates the fraction of incident light absorbed at the irradiation wavelength; 2) the quantum yield (Φ) which denotes the fraction of molecules that undergo photolysis to form the desired photoproduct after absorbing a photon.[12]

4.1.2 (Coumarin-4-yl)methyl Phototriggers

(Coumarin-4-yl)methyls are arylalkyl-type photolabile protecting groups that have been used to cage phosphates, amines, alcohols, phenols, carboxylates and other carbonyl compounds.[13] Photolysis cleaves the C-O bond between between the C4 methylene and the leaving group to produce an anion (A^-) as the leaving group and a coumarinyl cation (CM^+), which are protonated and trapped by the solvent respectively (Scheme 4-2). A more detailed mechanistic scheme proposed by Bendig and coworkers for the photocleavage of (coumarin-4-yl)methyl esters outlines the major processes in the release of the substrate from a π,π^* excited singlet state $^1[CM\text{-}A]^*$ (Scheme 4-3).[14] Excitation of the coumarin chromophore is followed by CM-A fragmentation. The bond breaking step that affords the singlet ion pair $^1[CM^+ A^-]$ occurs via a heterolytic pathway with rate constant k_1. $^1[CM^+ A^-]$ hydrolyses to CM-OH and HA with rate constant k_2 or recombines to ground-state CM-A with rate constant k_{rec}. Stabilization of CM^+ by using electron-donating substituents and A^- by delocalizing the anion (increasing acid strength) leads to a strong enhancement of k_1 and a simultaneous diminution of k_{rec}.

Scheme 4-2. Generalized photolysis of a (coumarin-4-yl)methyl caged alcohol. In the specific case of a caged alcohol, protonation of the carbonate anion **A**$^-$ is followed by decarboxylation to afford the free alcohol.[13]

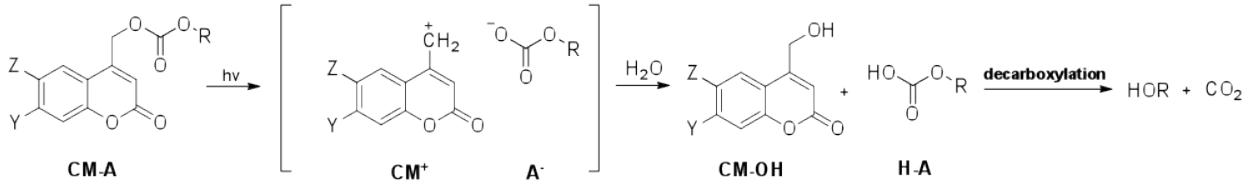

Scheme 4-3. Mechanism of photocleavage of (coumarin-4-yl)methyl esters as proposed by Bendig, Hagen and coworkers.[14]

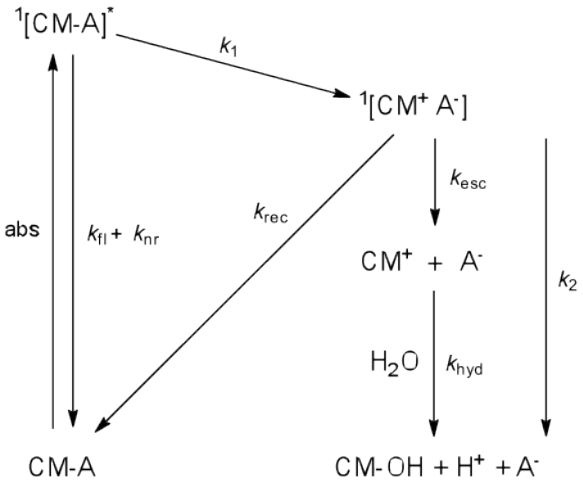

As a class, (coumarin-4-yl)methyl cages offer certain advantages over other phototriggers: 1) large extinction coefficients at wavelengths greater than 300 nm, 2) high efficiency (Φε) at longer UV wavelengths (>350 nm), 3) fast photolysis kinetics, 4) moderate stability (resistance to hydrolysis) in the dark, and 5) large 2-photon excitation cross-sections. In addition, their absorption properties, water solubility and membrane permeability can be optimized via selection of appropriate coumarin ring substituents. The coumarinyl phototriggers reported to date can be grouped into four main sub-types based on the functional substituents on the coumarin: 1) 7-alkoxy group, 2) 6,7-dialkoxy group, 3) 6-bromo-7-alkoxy group, and 4) 7-dialkylamino group (Figure 4-2).[13]

Figure 4-2. Structures and acronyms of (coumarin-4-yl)methyl phototriggers.[13]

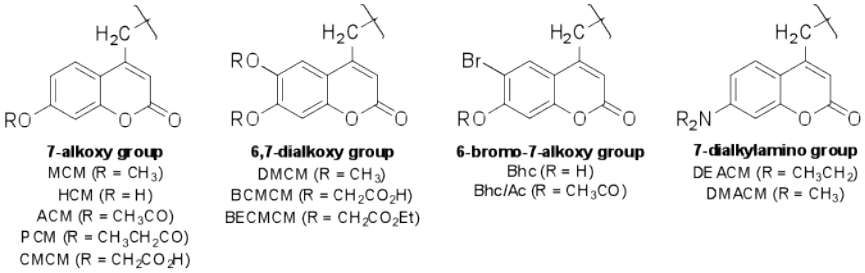

The photochemical, photophysical and physical properties of coumarin-caged compounds depend to a large extent on the nature of the protected functional group/molecule in question. Nonetheless, a comparison can be made regarding the spectroscopic and photochemical characteristics of the four groups of coumarinyl cages alongside a NB-type cage applied to the same substrate (Scheme 4-4).[15] Table 4-1 provides selected photophysical and chemical properties of the four coumarin-4-ylmethyl galactose derivatives, representing the four groups, alongside that of the analogous 4,5-dimethoxy-2-nitrobenzyl (NVOC) cage.[15] Installing electron-donating substituents on C6 or C7 of the coumarin ring red-shifts the absorption maximum. This effect is maximized with the C7 dialkylamino group, which introduces a red shift of more than 80 nm with respect to coumarin-4-ylmethanol, which has its absorption maximum at 310 nm. Most coumarins have strong fluorescence which may overlap with the absorption or emission spectra of commonly used fluorescence probes. This characteristic may complicate the use of fluorescence imaging to monitor specific effects following photo-uncaging of a bioactive molecule. However, coumarin-caged substrates are typically weakly fluorescent, and so the change in fluorescence intensity that occurs upon photorelease can be exploited to monitor the extent of reaction.

Scheme 4-4. Photolysis of 4,5-dimethoxy-2-nitrobenzyloxycarbonyl (NVOC) and (coumarin-4-yl)methoxycarbonyl galactose derivatives.[15]

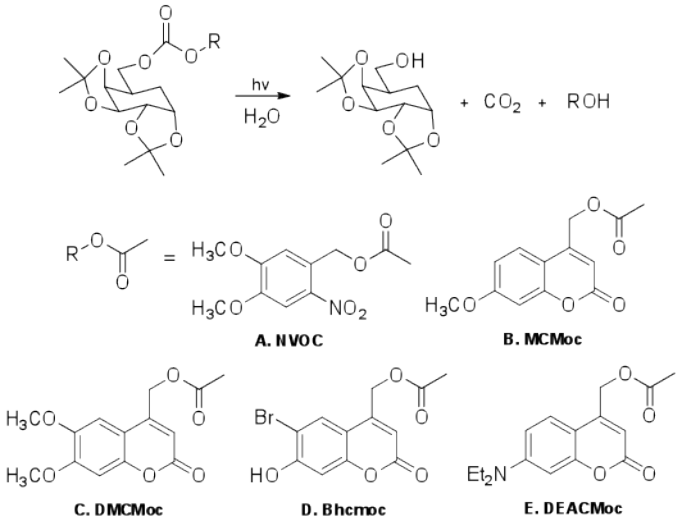

Table 4-1. Selected photophysical an chemical properties of NVOC and (coumarin-4-yl)methoxycarbonyl galactose phototriggers.[15]

	λ_{max} (ε)[a]	ε_{350}	Φ_{350}[b]	$\Phi\varepsilon_{350}$	solvent[c]
A	344 (5400)	5300	3.5×10^{-4}	2	A
B	322 (12100)	4100	2.0×10^{-2}	84	A
	323 (13100)	3400	2.9×10^{-3}	10	C
C	344 (10800)	10400	6.5×10^{-3}	68	A
D	374 (15000)	11500	1.5×10^{-2}	173	A
	376 (14000)	10000	8.3×10^{-3}	83	B
E	396 (17300)	6300	5.8×10^{-3}	37	A

[a] Extinction coefficient (cm^{-1} M^{-1}). [b] Quantum yields for disappearance of starting materials upon 350 nm irradiation. [c] Solvent A: KMops (pH 7.2) containing 0.1% DMSO. Solvent B: KMOPS (pH 7.2) containing 25% acetonitrile. Solvent C: H_2O containing 50% THF.

In 6-bromo-7-hydroxy-substituted coumarins (Bhc) the electron-withdrawing effect of the bromine atom installed at C6 lowers the pK_a of the hydroxyl at C7 from 7.9 (for HCM) to 6.2.[16] Therefore, at pH 7 the phenolate form predominates, and the Bhc group has a single absorption maximum at around 375 nm, with a large extinction coefficient (up to 19,000 $M^{-1}cm^{-1}$). It should be noted, however, that in an acidic environment where the protonated phenolic form is

predominant, the absorption maximum of the Bhc group undergoes a 40-50 nm blue-shift. The effects of halogen substitution on uncaging efficiency were assessed in a study that compared the photolysis quantum yields of four coumarin-caged acetates: HCM-OAc, Chc-OAc, Bhc-OAc, and tBhc-OAc (Figure 4-3).[13] 6-chloro-substitution decreased the photolysis quantum yield by 40% (HCM vs Chc), whereas a 6-bromo-substituent with a much larger heavy atom effect increased it by 150% (HCM vs Bhc). 3,6,8-tribromo-substitution gave a 260% enhancement (HCM vs tBhc-OAc) for a quantum yield of photolysis of 0.065. Taken together these results suggest that introducing an electron-withdrawing substituent at the 6-position is unfavourable for the photolysis reaction because it may impair through-bond electron transfer from the C7 oxygen to the C2 carbonyl in the excited state. However, a heavy atom effect may compensate for this by accelerating the rate of intersystem crossing, and populating the triplet excited state. As such, the cumulative effect of multiple bromine substituents (tBhc vs Bhc) points to the possible existence of a reactive triplet excited state for this particular subtype of coumarin-4-yl cage. One notable quality that sets Bhc apart from the other coumarin-4-ylmethyl triggers is its two-photon chemistry. Bhc caged glutamates with two-photon uncaging cross-sections (δ_u) of close to 1 GM for 740 nm irradiation have been reported. This is more than two orders of magnitude larger than the two-photon cross-sections of most NB triggers.[16]

Figure 4-3. Structures and acronyms of coumarin-caged acetates used in a study of halogen substituent effects.[13]

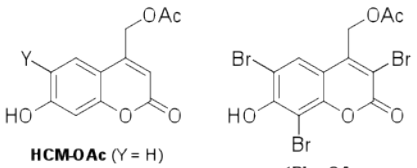

4.1.3 Caged Lipids: Photo-Uncaging of Phosphate, Alcohol and Amine Moieties

Several reports of caged lipid synthesis and their application towards biological studies have emerged in the last two decades. These include diacylglycerols,[15] phosphatidylinositols[17-18] and sphingolipids such as ceramide (Cer) 1-phosphate,[19] sphingosine 1-phosphate,[19-20] sphingosine,[21-22] dehydrosphingosine,[22] and psychosine,[22] as well as several other glycosphingolipids[23] (Figure 4-4). As with the Bhc-caged Cers described in this chapter, in these molecules a polar phosphate, hydroxyl or amine moiety is temporarily masked with a photo-responsive protecting group to supress their biological activity. A NB-caged Cer has been recently described[24] for which biological activity is restored via an O-N acyl transfer-mediated structural change (Figure 4-4 E). Other than the photolysis of Bhc-caged Cers described here, this represents the only light-responsive Cer releasing system to date.

Figure 4-4. Structures of some caged lipid analogs described in the literature. (A) 2-*N*-(2-nitrobenzyl)sphingosine (NB-Sph);[21] (B) (7-(diethylamino)coumarin-4-yl)methyl ester of ceramide 1-phosphate (DEACM-C1P);[19] (C) 2-*N*-(2-nitrobenzyl)psychosine (NB-Psy);[22] (D) (7-(diethylamino)coumarin-4-yl)methyl ester of phosphatidylinositol 3-phosphate (DEACM-PtdIns(3)P/AM);[17] (E) (2-nitrobenzyl) caged ceramide (NB-Cer).[24] Compounds A-D are in their bioactive form following photolysis to cleave the caging chromophores. For NB-Cer E UV irradiation cleaves the NB to unmask the phenolic oxygen. Lactonization ensues, followed by amide bond cleavage, and a subsequent O-N acyl transfer reaction to yield ceramide (Cer).

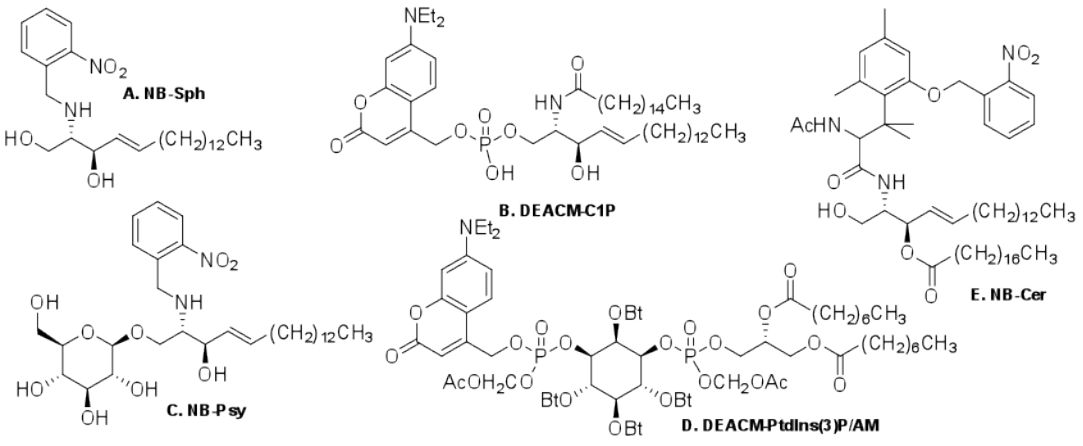

The photophysical and chemical properties of these caged lipids have not been systematically characterized in most cases, as the emphasis in these accounts tends to be on

compound synthesis and assessment of biological activity. However, the physical chemistry of the caging chromophores employed in these systems for lipids has been extensively studied with other substrates. Comparisons of the photochemical properties of ATP (and other phosphates)[13] and glutamate[25] caged with several different groups are among the most comprehensive.

Although such "model" substrates provide an indication of how different caging chromophores perform, the uncaging process for a given phototrigger and substrate pairing will not always proceed with the same efficiency or at the comparable rate. In a recent study several different Bhc-protected hydroxyl-containing compounds were prepared and their photochemical properties examined (Figure 4-5, Table 4-2).[15] This work reported a two-fold difference in quantum yield values between the aliphatic and aromatic carbonates, which were attributed to the difference in thermodynamic stability of the carbonate anions- as predicted from the relative strength of their conjugate acids. Of particular interest in the context of the Bhc-caged ceramides presented here are the study's findings regarding Bhc-caged diacylglycerol (Bhcmoc-diC_8): a blue-shifted absorption maxima with respect to the other caged alcohols in the series, and a decrease in quantum yield as the photolysis progressed. The authors account for the second observation in terms of the hydrophobic aggregates that the diacylglycerol produced in the photolysis forms in aqueous solution. Situating the Bhc-group of remaining caged-substrate in this less polar environment may destabilize the ion pair formed in the first step of the photolysis.

Figure 4-5. Structures of some Bhcmoc-protected hydroxyl containing compounds. (A) Bhc-caged diacylglycerol (Bhcmoc-diC_8); (B) Bhc-caged amino acid ester (Tyr(Bhcmoc)-OMe); (C) Bhc-caged nucleoside (5'-Bhcmoc-adenosine).[15]

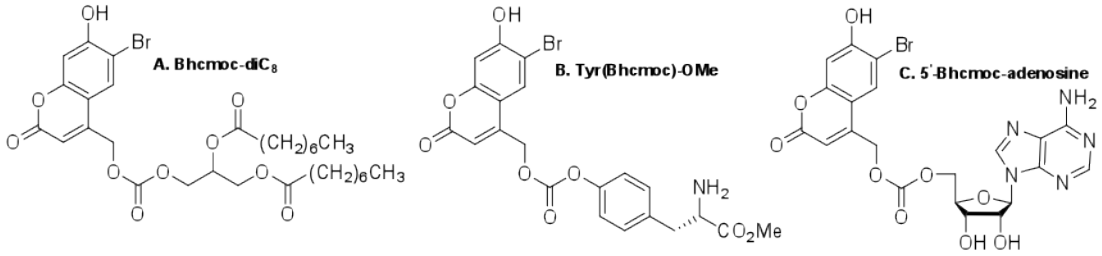

Table 4-2. Selected photophysical and chemical properties Bhcmoc-protected hydroxyl-containing compounds (structures in Figure 4-5). Solvent: KMops (pH 7.2) containing 0.1% DMSO.[15]

	λ_{max} (ε)[a]	Φ_{dis}[b]	$\Phi\varepsilon_{dis}$	Φ_{app}[c]	$\Phi\varepsilon_{app}$	$t_{1/2}$[d]
A	343 (11600)	0.014	160	nd[e]	nd	37
B	372 (13900)	0.022	300	0.020	270	38
C	373 (13700)	0.012	140	0.010	120	467

[a] Extinction coefficient (cm^{-1} M^{-1}). [b] Quantum yields for disappearance of starting materials upon 350 nm irradiation. [c] Quantum yields for appearance of products upon 350 nm irradiation. [d] Half-life (h) in the dark. [e] Not determined.

Several of the caged lipids described above have been used for in vivo studies examining the various lipids' roles as signalling molecules. In these applications the spatially and temporally controlled of release bioactive compounds from an inactive caged form has been of particular value. At the time of writing, however, no caged lipids other than the Bhc ceramides presented herein have been employed in studies involving planar supported lipid bilayers. In the following pages I begin by describing the synthesis and photophysical and chemical characterization of these novel compounds. Subsequently, the membrane restructuring activity of the caged lipids is explored and interpreted in two distinct model membrane systems.

4.2 Results: 6-Bromo-7-hydroxycoumarin-4-ylmethyl-Caged Ceramides

4.2.1 Synthesis of Bhc-Caged Ceramides

Bhc-caged ceramides (**9**, **10**, **13**, and **16**) with sphinganine or sphingosine backbones and amide-linked butyric or palmitic fatty acyl chains were prepared by our collaborators as outlined in Schemes 4-5 and 4-6.[11] Bhc-coumarin **4** was synthesized via the Pechmann condensation[26] of 4-bromoresorcinol **1** and 4-chloroacetoacetate **2** in methanesulfonic acid to afford **3** in 95% yield. 4-(Chloromethyl)coumarin **3** was hydrolyzed in water under reflux, and the resulting diol **4** was chemoselectively protected at the phenolic position using methoxymethyl chloride (MOMCl) in the presence of DIPEA (*N*,*N*-diisopropylethylamine) to give MOM ether **5**. The unprotected primary hydroxyl group of **5** was treated with a phosgene solution to generate chloroformate **6** for use in coupling reactions with the sphingolipids.

Scheme 4-5. Synthesis of Bhc-caged short-chain ceramides. (a) CH_3SO_3H, rt, 2 h, 95%; (b) H_2O, reflux, 2 d, 99%; (c) MOMCl, DIPEA, CH_2Cl_2, 0 °C, 2 h, 89%; (d) phosgene, THF/toluene, 3 h, 0 °C, 94%; (e) DIPEA, DMAP, CH_2Cl_2, 0 °C, 2.5 h, 54% for **8a**, 14% for **8b**; (f) $NaHSO_4{\cdot}SiO_2$, CH_2Cl_2, 2 h, rt, 73% for **9**, 68% for **10**.[11]

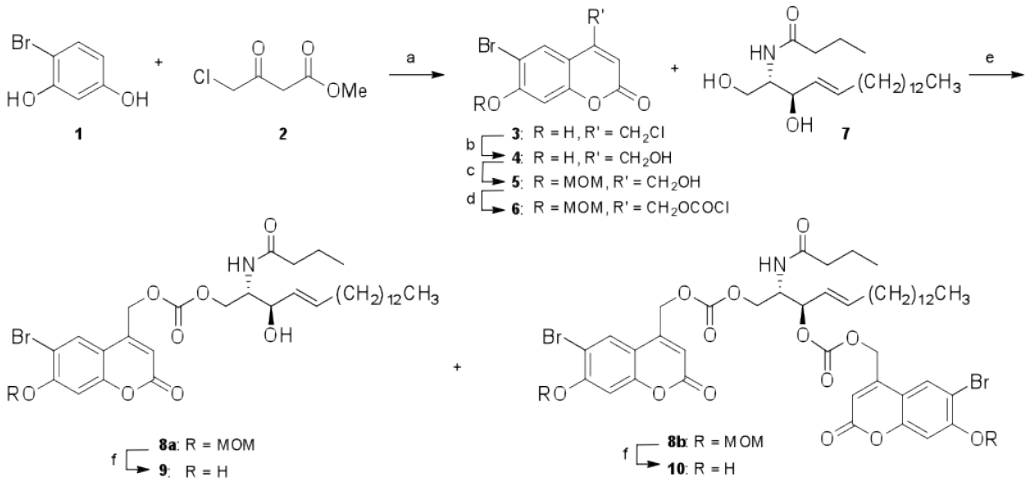

The reaction of unprotected C4-Cer **7** and activated coumarin **6** in the presence of DIPEA and DMAP gave mono- and di-Bhc-caged products, **8a** and **8b** respectively, in a 4:1 ratio. Bhc-caged ceramides **9** and **10** were obtained following removal of the MOM groups with silica-

supported sodium hydrogen sulfate ($NaHSO_4 \cdot SiO_2$).[27] Long-chain ceramides (C16-Cer **11** and C16-dihydroCer **14**) were also used as coupling partners for **6** as shown in Scheme 6. Coupling to the primary hydroxyl group of these sphingolipids was achieved without blocking the allylic hydroxyl group. Formation of di-Bhc-caged products was not observed for either substrate. Steric hindrance arising from the two long hydrocarbon chains of the sphingolipid backbone may explain why **12** and **15** were obtained in low yields relative to **8**. The same mild acidic conditions ($NaHSO_4 \cdot SiO_2$) employed previously were used to cleave the phenolic MOM groups of **12** and **15** to afford the Bhc-caged ceramides **13** and **16**.

Scheme 4-6. Synthesis of Bhc-caged long-chain ceramides. (a) DIPEA, DMAP, THF/CH_2Cl_2 (2:1), rt, 36 h, 25% for **12**, 27% for **15**; (b) $NaHSO_4 \cdot SiO_2$, CH_2Cl_2, 2 h, rt, 70% for **13**, 72% for **16**.[11]

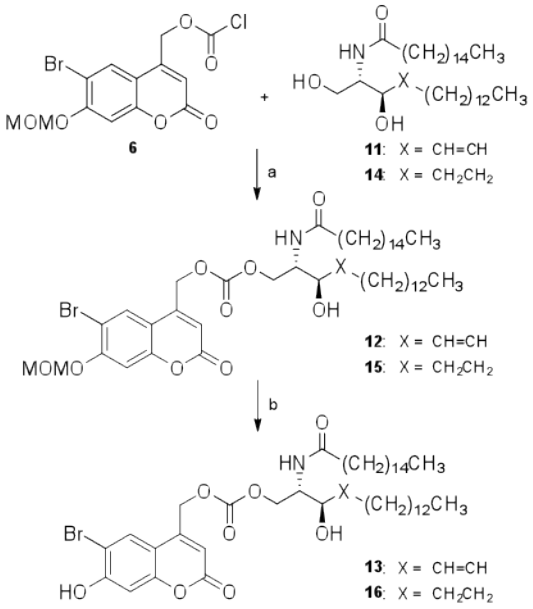

4.2.2 Photophysical and Photochemical Characterization of Caged Ceramides

In order to optimize conditions for photolysis of caged ceramides in supported membranes, we recorded absorption and emission spectra of 6-bromo-7-hydroxy-4-hydroxymethylcoumarin **4** in KMops buffer (Figure 4-6). As indicated in Figure 4-6 A and Table 4-3, the absorption maximum for **4** red-shifted from 328 nm to 366 nm as a function of increasing pH. At a pH of

6.2 corresponding to the reported pK_a of **4**,[16] a broadened absorption spectrum with maxima at 345 and 366 nm was observed, consistent with a mixture of phenol and phenolate anion respectively.

Figure 4-6. Absorption (A) and emission spectra of **4** in KMops as a function of pH. The broad, two-peak absorption of **4** at pH 6.2 is consistent with its reported pK_a of 6.18. Emission was monitored at 374 (B) and 328 nm (C) respectively.

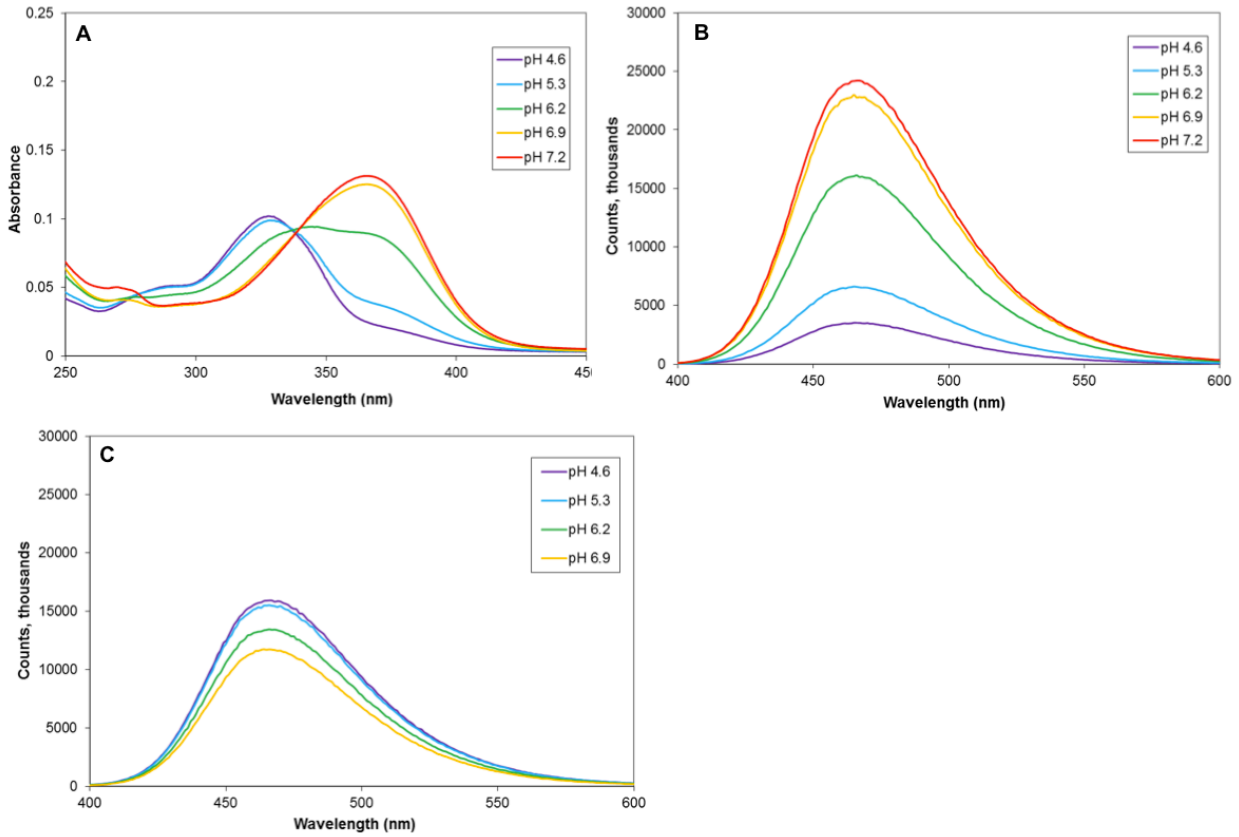

In contrast, all of the emission spectra of **4** exhibited a maximum at 465-467 nm independent of solution pH. The position of the emission peak also remained constant for excitation at both 374 and 328 nm as shown in Figure 4-6 B and C respectively. As pH increased, however, the predominance of the phenolate form of **4** was reflected in the greater absorbance and fluorescence intensity for excitation at the longer wavelength. Conversely, excitation at 328 nm generated the strongest fluorescence from the solution of **4** at the lowest sampled pH, 4.6.

We examined the effect of pH on the fluorescence intensity of **4** by calculating fluorescence quantum yields for excitation at 374 nm, as shown in Table 4-3. Coumarin 460 (Φ_{fl} = 0.59, in ethanol)[28] was selected as the reference standard as it shows good spectral overlap with the phenolate form of **4**. Over the pH range that we examined, the fluorescence quantum yield of **4** decreased from a maximum of 0.49 at pH 7.2 to 0.40 at pH 4.6.

Table 4-3. Photophysical properties of (6-bromo-7-hydroxy-4-hydroxymethyl)coumarin **4** in KMops buffer as a function of pH.

pH	λ_{abs}	λ_{em}	Φ_{fl}[a]
4.6	328	465	0.40
5.3	328	466	0.43
6.2	345, 366[b]	466	0.45
6.9	366	465	0.45
7.2	366	467	0.49

Coumarin 460

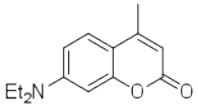

[a] Quantum yields of fluorescence for excitation at 374 nm, with reference to Coumarin 460 (Φ_{fl} = 0.59). [b] Coexistence of protonated (343 nm) and deprotonated (374 nm) forms of **4**.

Figure 4-7 compares the spectral characteristics of **4** and caged dihydroCer **16**. Spectra for **4** were recorded in both KMops buffer (pH 7.4, solvent A) and KMops with 50% ethanol (solvent B); the mixed solvent system was used to ensure complete solvation of **16**. In solvent A the positions of the absorption and emission maxima of **4** were consistent with those recorded in Figure 4-6, although there was a modest decrease in its fluorescence quantum yield (0.47, Table 4-4). Taken together these data suggest that a slight increase in pH has negligible effect on the photophysics of **4** when the phenolate form already strongly predominates. In the solvent mixture B the absorption spectrum of **4** possessed two peaks, at 343 and 374 nm respectively, which confirmed that under these conditions the phenol and phenolate species coexist.

Figure 4-7. (A) absorption and (B) emission spectra of **4** in KMops at pH 7.4 (4A), and **4** and **16** in KMops containing 50% EtOH (4B and 16B respectively).

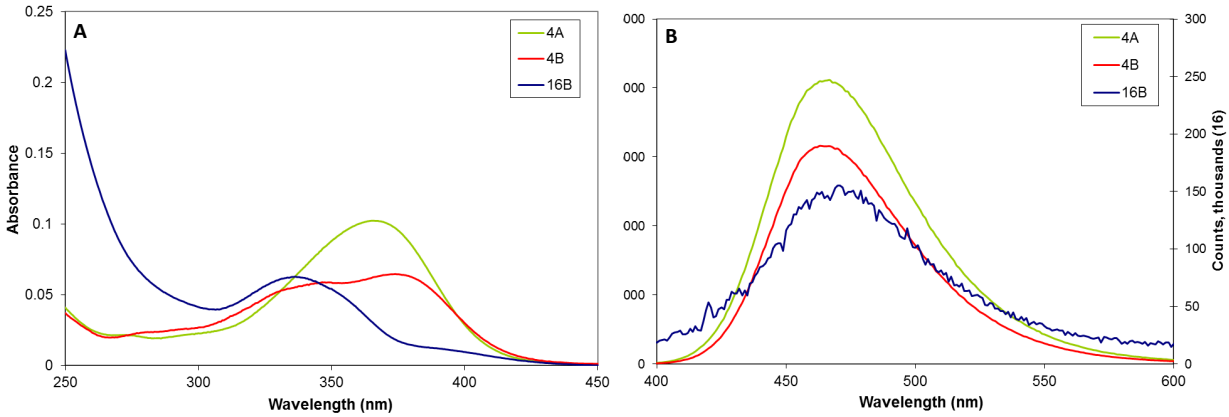

Table 4-4. Photophysical properties of (6-bromo-7-hydroxy-4-hydroxymethyl)coumarin **4** and Bhc-caged **16**.

	λ_{abs} (ε)[a]	λ_{em}	Φ_{fl}[b]	solvent[c]
4	366 (13 600)	466	0.47	A
	343, 374[d]	467	0.50	B
16	338 (11 500)	466	0.02	B

[a] Extinction coefficient (cm^{-1} M^{-1}). [b] Quantum yields of fluorescence for excitation at 374 nm, with reference to Coumarin 460 (Φ_{fl} = 0.59). [c] Solvent A: KMops (pH 7.4), Solvent B: KMops (pH 7.4) containing 50% ethanol. [d] Coexistence of protonated (343 nm) and deprotonated (374 nm) forms of **4**.

In contrast, in solvent B **16** presented a single maximum at 338 nm suggesting that the coumarinyl moiety was in a neutral, protonated state. This could be indicative of hydrogen bonding interactions between the phenolic group of the chromophore and amide or ester moieties in the lipid backbone occurring on either an intra- or intermolecular level if there is some aggregation of caged lipid molecules. Emission spectra for **4** and **16** indicated that for excitation at 374 nm the fluorescence intensity of the caged lipid was about 100-fold less than that of **4**. The fluorescence quantum yield of 0.02 for **16** was also much lower than that of the parent coumarin **4**, which was in keeping with its expected photochemical reactivity.

Starting from a published protocol for Bhc-photoproduct analysis,[16] we optimized a reversed-phase high performance liquid chromatography (HPLC) method that would allow us to separate **4** from the Bhc-caged ceramides **9**, **13**, or **16**, and quantify their abundance in photolytic studies. Figure 4-8 summarizes the general HPLC conditions used. Initially absorbance was monitored at 325 and 375 nm to detect both phenol and phenolate forms of **4** and Bhc-caged dihydroCer **16**. We observed that in the ethanol-rich eluent system used, both **4** and **16** absorbed much more strongly at the shorter wavelength. This finding is consistent with the spectroscopic studies presented above (Figure 4-7), which indicate that in ethanolic solution at near-neutral pH the phenol form of these coumarin derivatives will predominate. Therefore, to facilitate HPLC detection of the coumarins at lower concentrations, we elected to monitor their fluorescence at 480 nm with excitation at 325 nm. Furthermore, as can be seen from the chromatogram in Figure 4-8, injection of a coumarin sample in a mixture of KMops and ethanol produced a "solvent spike" at the beginning of each sample run for both of the absorption wavelengths being monitored. As such, the solvent peak and **4** could not be readily resolved from each other in either absorbance channel. No solvent peak was present in the fluorescence trace, however, and so monitoring this signal greatly simplified relative quantitation of **4** and **16**. Upon elution through a SunFire C18 column on an ethanol-water gradient (75% ethanol rising to 95% over the first three min of the run), **4** gave a retention time of 1.4 min while **16** was detected at 6.5 min. Coumarin **4**'s short retention time is typical for a polar compound of low molecular weight in reversed-phase HPLC, as it would be expected to show a strong interaction with the highly polar mobile phase. Hydrophobic interactions

between the long hydrocarbon chains of **16** and the packing in the column, as well as its weaker association with the solvent, account for its slower migration.

Figure 4-8. Reversed-phase HPLC chromatogram showing the optimized conditions used to separate, detect and quantify **4** and **16**. Absorbance was monitored at both 375 and 325 nm, and fluorescence was detected at 480 nm. Eluent: 75% EtOH(increasing to 95% over the time period 0-3 min), 25% H_2O; flow rate, 0.8mL/min; t_R of **4** 1.4 min, and t_R of **16** 6.5 min. Loading solvent: KMops/EtOH.

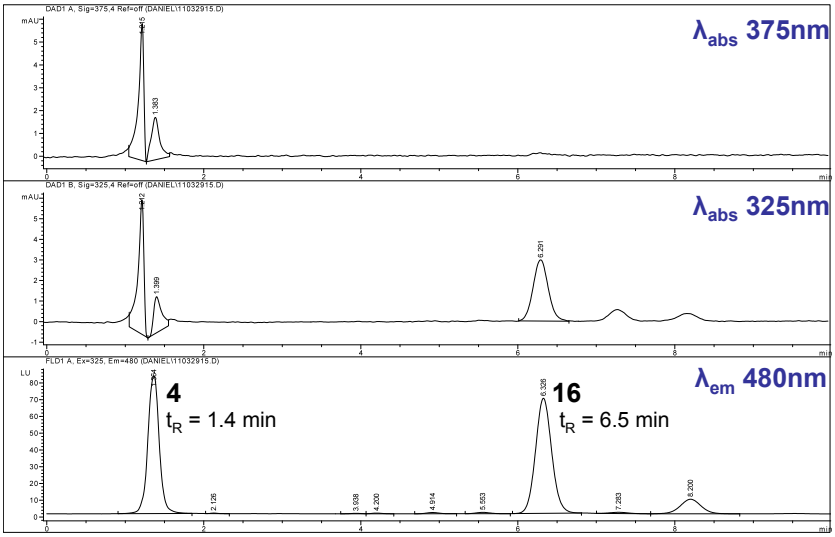

To measure consumption of **16** and monitor the concomitant formation of **4** by HPLC, we required a fluorescent standard that could be used to normalize aliquots drawn at different time points in a photoreaction (Figure 4-9). Initially we sought to use coumarin 460, the same laser dye that was used as a reference for the fluorescence quantum yield measurements. However, the retention times for coumarin 460 and **4** were too similar for their peaks to be resolved in the chromatogram without substantially decreasing the polarity of the eluent. Dropping the solvent polarity also had the undesired effect of greatly increasing the retention time of **16**. Rather than adjust the solvent gradient, we resolved the problem by adopting coumarin 480 as an internal standard for HPLC. The higher molecular weight and larger alkyl groups of this dye resulted in a retention time of 2 min as compared to 1.4 min for **4**, as shown in Figure 4-9. Although the absorption and emission spectra of coumarin 480 (λ_{abs} 390 nm, λ_{em}

466 nm)[29] were red-shifted with respect to coumarin 460 (λ_{abs} 374 nm, λ_{em} 446 nm), a strong fluorescence signal at 480 nm was nonetheless observed with excitation at 325 nm.

Figure 4-9. HPLC was used to monitor the photolysis of **16** and the formation of **4**. Coumarin 480 was used as an internal standard for quantitative analysis. (A) pre-UV; (B) after 240s of 350 nm irradiation in a Rayonet photochemical reactor. Eluent: 75% EtOH (to 95% over the time period 0-3 min), 25% H_2O; flow rate, 0.8mL/min; t_R of **4** 1.4 min, standard 2.0 min, and t_R of **16** 6.9 min.

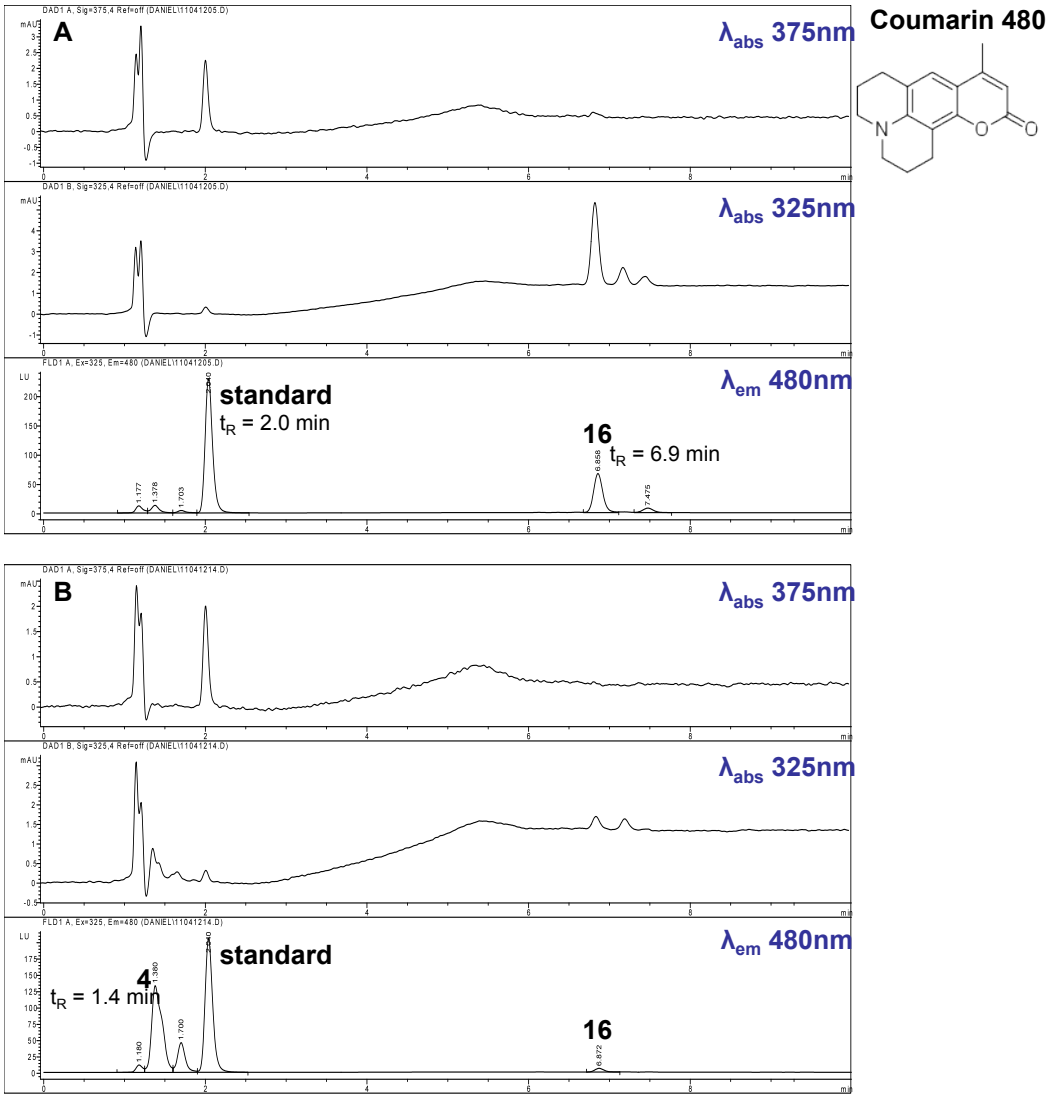

Figure 4-9 A illustrates the starting point for a representative photolysis of **16** performed in KMops containing 50% ethanol. An aliquot of the solution was spiked with coumarin 480, and the resulting chromatogram displayed two major peaks corresponding to the standard and **16**

(t_R of 2.0 and 6.9 min respectively). The relatively weak fluorescence of **16** is attributed to the low fluorescence quantum yield of this Bhc-caged species. A sample taken following 240 s of 350 nm irradiation in a Rayonet photochemical reactor indicated almost complete consumption of **16** and the appearance of a peak at t_R = 1.4 min, which was assigned to **4** (Figure 4-9 B). The time course of photolysis for **16** shown in Figure 4-10 was generated from the fluorescence signals detected for **4** and **16** in chromatograms obtained at discrete time points during the reaction.

Figure 4-10. Time course of photolysis of Bhc-caged ceramide **16** in KMops (pH 7.4) containing 50% EtOH on 350-nm irradiation in a Rayonet photochemical reactor with 4 lamps. Photolysis of **16** (blue) and formation of by-product **4** (red) were quantified by HPLC analysis using coumarin 480 as an internal standard.

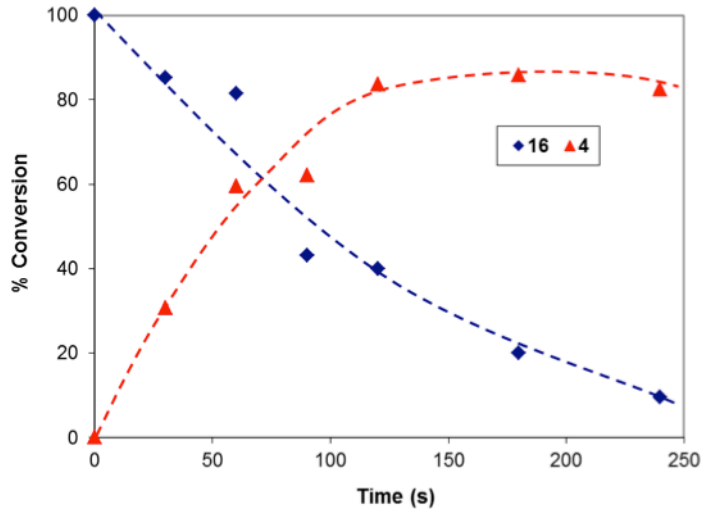

In each chromatogram the area under each of the two peaks was normalized against that of the standard peak. As shown in the time course, less than 10% of the **16** present in the solution prior to irradiation remained following 240 s of irradiation. The plateau in signal intensity observed for the formation of **4** beyond 100 s of irradiation time may be due to photobleaching. We performed a similar degradation study but in the absence of UV light in order to assess the stability of **16** in aqueous solution (data not shown). The resulting time

course of hydrolysis indicated that the half-life of **16** in KMops containing 50% ethanol was about 30 hours at 22 °C.

While the good agreement in HPLC retention times (1.4 min) and spectral characteristics for a clean sample of **4** (Figure 4-8) and the fluorescent photoproduct of **16** (Figure 4-9 B) provided evidence that these two were the same molecular species, further evidence was required to confirm successful release of C16 dihydroCer **14**. To this end, a solution of **16** was photolyzed for 5 min and subsequently analyzed by LC/MS (Figure 4-11). The chromatograms for this analysis were obtained using the same model of column and the same eluent- with the addition of 0.1% formic acid to generate protonated species so as to facilitate MS detection. The chromatogram for the partially photolyzed sample shown in Figure 4-11 A presented peaks with t_R 7.0 min for a mass of 836.5, and t_R 7.5 min with a mass of 540.5; these matched the anticipated masses for **16** and **14** respectively. A commercial sample of C16 Cer **11** was also examined under these conditions (Figure 4-11 B). The calculated mass of 538.5 was as expected for **11**, and the t_R of 7.3 min was in good agreement with that observed for the closely related structure **14**.

Figure 4-11. LC/MS was used to verify the identity of 16 and the expected photoproduct, C16-dihydroceramide **14**. (A) after 5min photolysis. (B) A commercial sample of C16-ceramide **11** was also analyzed under the same conditions. Eluent: 75% EtOH (increasing to 94.9% over the time period 0-3 min), 24.9% H_2O, 0.1% HCO_2H; flow rate, 0.2mL/min; t_R of **16** 7.0 min, t_R of **11** 7.3 min, and t_R of **14** 7.5 min. MS [M+H] *m/z* calcd for **14** using $C_{34}H_{70}NO_3^+$ 540.5, found 540.5.

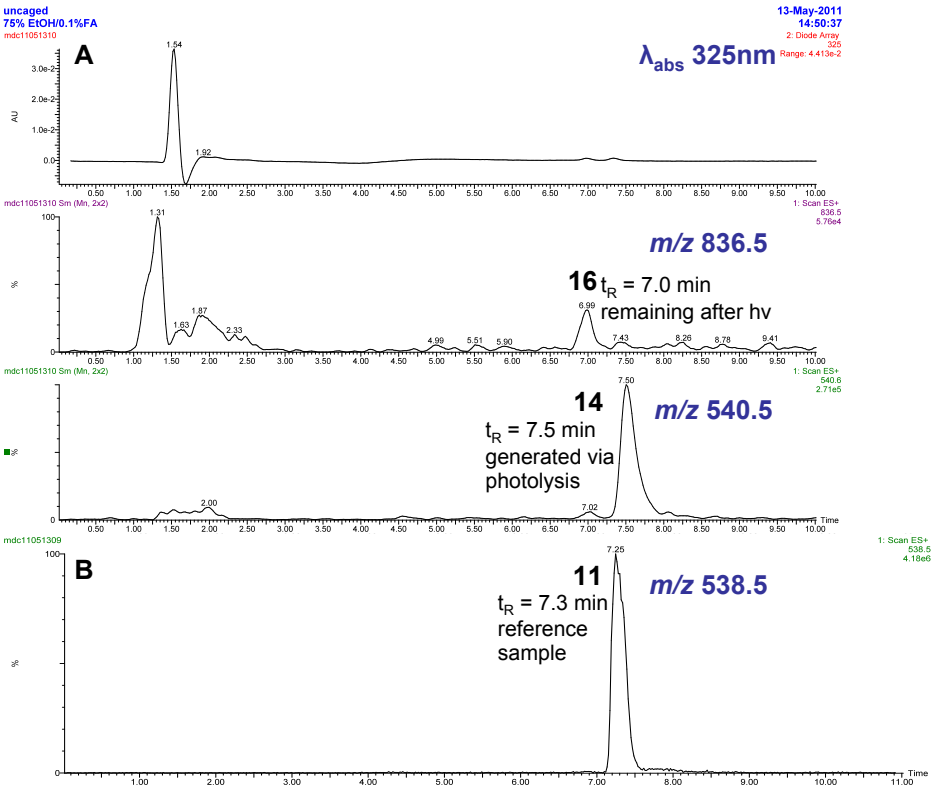

The reversed-phase HPLC protocol used in the studies involving **16** was also succesfully applied towards the separation of Bhc-caged C16 Cer **13** from photoproduct **4**, with t_R 6.8 and 1.4 min respectively (Figure 4-12 A and B). Photolysis involving Bhc-caged C4 Cer **9** was also monitored by HPLC. At 4.6 min, the t_R of **9** was substantially shorter that those of the long N-acyl chain ceramides; this difference can be attributed to a diminution in hydrophobic interactions associated with the decrease in molecular weight.

Figure 4-12. The same reversed-phase HPLC conditions were applied to monitor the photolysis of **13**, which also afforded **4** as a by product. Fluorescence detection at 480 nm was primarily used to assess uncaging. (A) pre-UV; (B) after photolysis. (C) short N-acyl chain caged ceramide **9** could also be resolvedusing this protocol, although its retention time on the column was markedly shorter. Eluent: 75% EtOH (increasing to 95% over the time period 0-3 min), 25% H_2O; flow rate, 0.8mL/min; t_R of **4** 1.4 min, t_R of **9** 4.6 min and t_R of **13** 6.8 min.

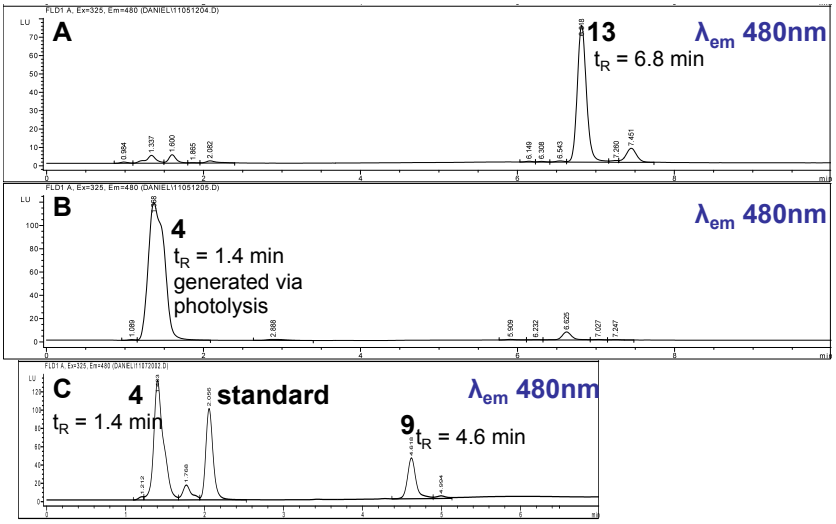

With only a few milligrams each of Bhc-caged ceramides **9**, **13** and **16**, and given our interest in performing direct incorporation studies in lipid membranes, we were unable to carry out a more rigorous photochemical characterization including determination of quantum yields and rate constants of photolysis. However, pursuant to our work with lipids, we did obtain absorption spectra and a photolysis time course for **13** in small unilamellar vesicles (SUVs) (Figure 4-13). Furthermore, we performed a photolysis of **9** in buffered solution using lamp excitation on our fluorescence microscope prior to our bilayer imaging/uncaging experiments (Figure 4-14). These experiments are revisited in further detail in the section on supported membranes that follows below.

Figure 4-13. (A) Absorption spectra of SUVs of DOPC/**13** in 95/5 molar ratios recorded in water. At pH 7.5 **13** is predominantly deprotonated; (B) Time course of caged C16 ceramide photolysis in SUVs of DOPC/ESM/Chol/**13** in 8/7/4/1 molar ratios (DiI-C_{20}(3) 0.5 mol%). Uncaging took place in MQ water with 350nm irradiation in a Rayonet photochemical reactor, and consumption of **13** was quantified by HPLC analysis.

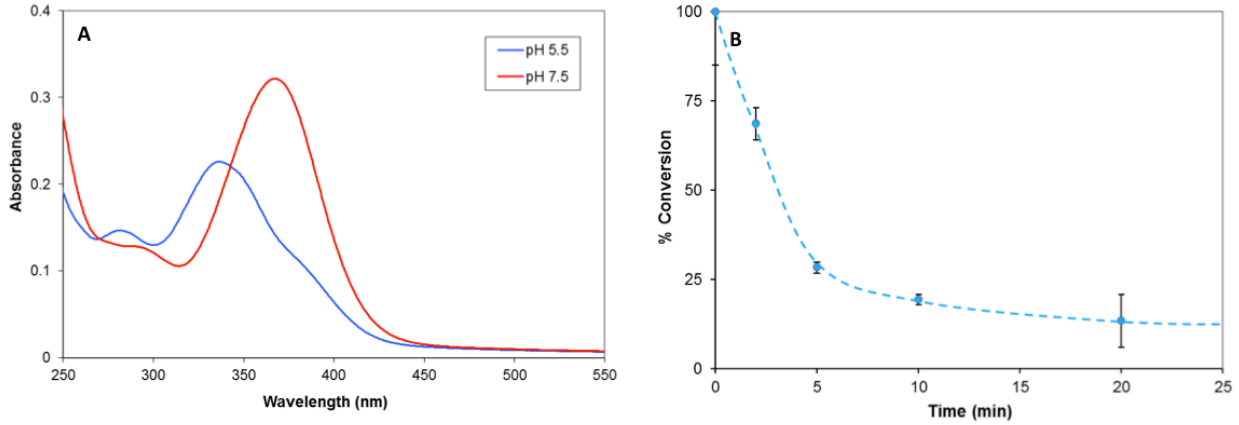

Figure 4-14. Time course of photolysis of Bhc-caged ceramide **9** in KMops (pH 7.4) containing 20% EtOH upon 350-nm irradiation on the confocal fluorescence microscope. Photolysis of **9** (blue) in and formation of by-product **4** (red) were quantified by HPLC analysis using coumarin 480 as an internal standard.

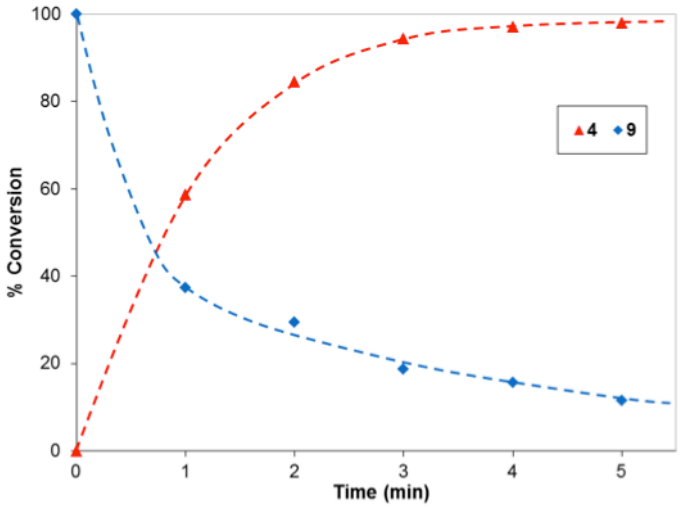

4.2.3 Caged Ceramides in Supported Bilayers of DOPC, ESM and Cholesterol

Mixtures of dioleoylphosphatidylcholine (DOPC), egg SM (ESM),[30] and Cholesterol (Chol), which form coexisting L_d and L_o phases,[31] have been extensively used by several groups including our own to study enzymatic Cer generation in model membranes displaying raft-like phase separation.[32-34] We therefore elected to use a quaternary mixture of DOPC/ESM/Chol/**13**

in 8/7/4/1 molar ratios and containing 0.5 mol% DiI-C_{20}[35] to study the incorporation and photorelease of caged Cer in model membranes. Figure 4-15 provides a representative example of a planar supported bilayer formed in the dark from the caged Cer-containing mixture in water. The DiI-C_{20} fluorescence image (Figure 4-15 A) reveals dark, micrometer-scale L_o domains in a bright L_d bulk phase, indicating that this lipophilic probe preferentially partitions into the disordered environment.[35] Although caged Cer analogues have low fluorescence quantum yields (Table 4-2), the emission of **13** can be used to visualize its relative distribution in the membrane (Figure 4-15 B). The inverted fluorescence contrast for the coumarin channel with respect to the DiI-C_{20} image (bright L_o domains) suggests that the caged lipid is enriched in the ordered phase.

Figure 4-15. Epifluorescence images of a planar supported lipid bilayer composed of DOPC/ESM/Chol/**13** in 8/7/4/1 molar ratios, and stained with DiI-C_{20}(3) (0.5 mol%). (A) L_o domains appear dark in the DiI-C_{20} channel indicating that probe is enriched in the L_d phase. (B) Inverted contrast for the fluorescence of **13** in the same sample region suggests that the caged ceramide analog preferentially partitions into the L_o phase. Images acquired by S. P. Pitre. Scale bar = 4 μm.

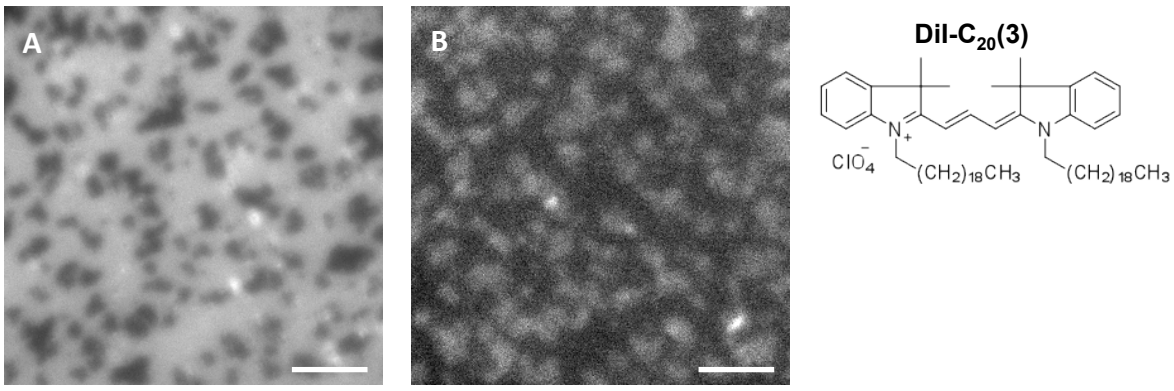

Correlated DiI-C_{20} fluorescence and AFM imaging experiments confirmed the assignment of L_o and L_d phases in the optical images (Figure 4-16 A). Height measurements from the AFM scans showed that the ordered domains were 0.8-1 nm taller than the surrounding fluid phase. This height difference is consistent with reported values for ternary lipid mixtures of

DOPC/ESM/Chol, as well as with those incorporating similar molar fractions of C16-Cer.[36-37] AFM and fluorescence were also used to detect and follow membrane restructuring when C16-Cer **11** was photochemically generated in these supported bilayers. Absorption spectra of **13** in SUVs of DOPC (Figure 4-13 A) had indicated that both protonated and deprotonated forms of the coumarinyl photocage moiety could be excited using the commercial DAPI filter set (λ 377 ± 25 nm) in our fluorescence microscope. A complimentary time course experiment performed on a buffered solution of Bhc-caged C4-Cer **9** demonstrated that this compound was readily uncaged on the same microscope (Figure 4-14). Furthermore, HPLC analysis (Figure 4-13 B) confirmed time-dependent disappearance of **13** in SUVs of DOPC/ESM/Chol/**13** in 8/7/4/1 molar ratios with 0.5 mol% DiI-C_{20} upon irradiation at 350 nm. Figure 4-16 illustrates a photolysis experiment in a supported bilayer formed from vesicles of the same quaternary lipid mixture where an area of interest was irradiated on the microscope for a total of 10 min. During this time the sample was periodically monitored using both imaging techniques. Structural changes first became apparent by AFM (Figure 4-16 B) as small pockets of lower height or slight indentations within the L_o domains. As more C16-Cer was generated with an extended irradiation time, the size and frequency of these features increased, and we were able to discern the largest pockets by fluorescence (Figure 4-16 C, arrows). Closer examination of the AFM scans showed that these pockets are at approximately the same height as the L_d phase, and the DiI-C_{20} fluorescence intensity of the two environments was also comparable. These features continued to evolve after photolysis (Figure 4-16 D). Beyond 20 min post-UV, the bilayer morphology remained essentially unchanged. This suggests that the short-term reorganization of membrane lipids to accommodate the de novo Cer was complete.

Figure 4-16. Caged C16 ceramide photolysis in a supported bilayer of DOPC/ESM/Chol/**13** in 8/7/4/1 molar ratios (DiI-C_{20}(3) 0.5 mol%). This correlated fluorescence and AFM time course reveals the progressive morphological changes that take place in the L_o domains as small amounts of ceramide are generated. (A) $T_{0\ min}$ before UV irradiation; (B) $T_{15\ min}$ after 5 min UV irradiation; (C) $T_{30\ min}$ after a second 5 min UV; (D) $T_{50\ min}$ no further UV. Scale bar = 3 μm.

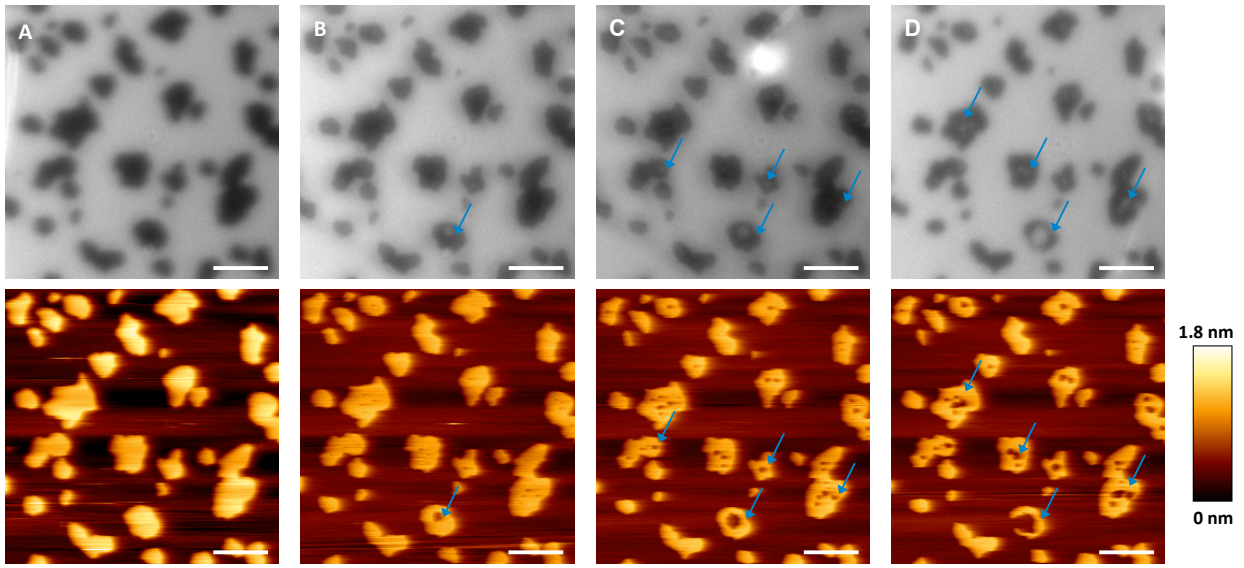

We observed that repeated AFM scanning of a bilayer subsequent to photochemical C16-Cer generation appeared to accelerate the dissolution of L_o domains, particularly in sample regions where smaller sized domains predominated (Figure 4-17). Therefore, we conducted further uncaging experiments where the area of interest was monitored exclusively by fluorescence. This was done to gauge the extent of bilayer restructuring that could arise exclusively from the production of Cer in the absence of any mechanical perturbation caused by the scanning AFM tip. Figure 4-18 describes the progressive disappearance of ordered domains in a typical sample containing 5 mol% caged C16-Cer **13**. Before the uncaging experiment commenced, the iris on the microscope illuminator was closed to give a ~25-μm diameter illumination area for generation of C16-Cer (Figure 4-18 B). After the region of interest was irradiated for 30 min, we monitored the sample for an additional 20 min. By this point the bilayer had ceased to evolve and its morphology appeared relatively stable. During the span of

the 30-min photolysis, the surface coverage of the L_o domains decreased markedly and many of the smaller domains disappeared altogether. Fully opening the iris identified adjacent areas of the bilayer where no Cer had been generated, providing a clear *in situ* comparison of pre- and post-UV membrane morphology (Figure 4-18 A, C).

Figure 4-17. AFM scans of a planar supported lipid bilayer composed of DOPC/ESM/Chol/**13** in 8/7/4/1 molar ratios, and stained with DiI-C_{20}(3) (0.5 mol%). Repeated AFM scanning facilitates the break up of L_o domains following the photochemical generation of ceramide in the lipid membrane. (A) before UV; (B) first scan after 5 min UV; (C) second scan after 5 min UV. Scale bar = 5 μm.

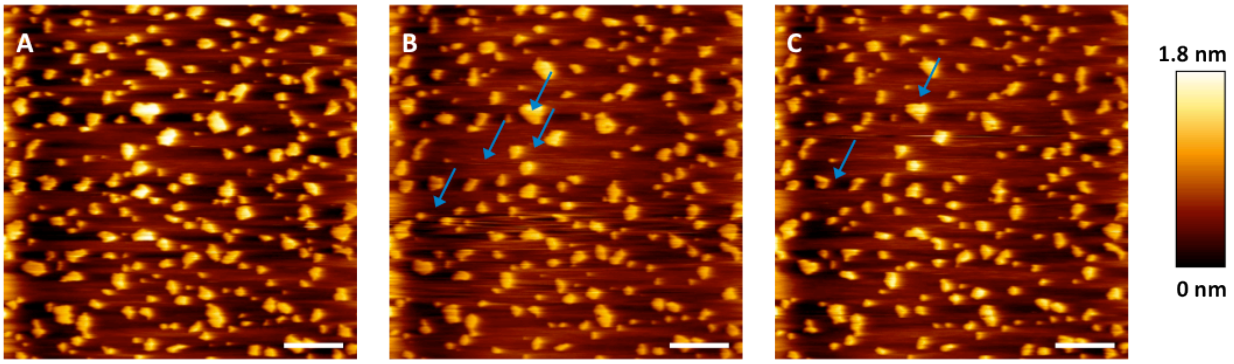

Figure 4-18. As increasing amounts of ceramide are generated with longer irradiation times, L_o domains in a bilayer of DOPC/ESM/Chol/**13** 8/7/4/1 (DiI-C_{20}(3) 0.5 mol%) formed in MQ water decrease in size and gradually disappear. (A) $T_{0\ min}$ before photolysis; (B) closed iris indicating the region to be irradiated; (C) $T_{50\ min}$ 20 min post-30 min UV with the iris opened to reveal adjacent areas of the bilayer not exposed to UV light. Scale bar = 5 μm.

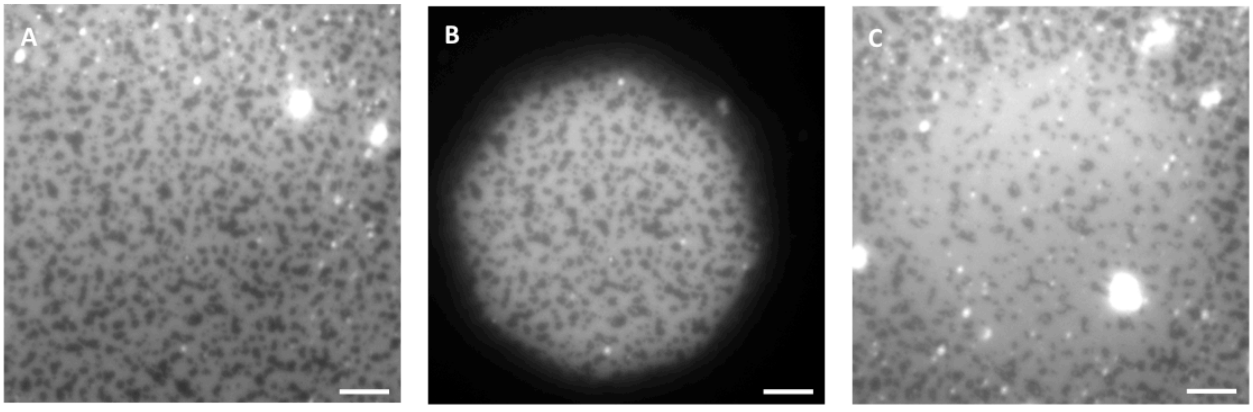

Exposing a bilayer of DOPC/ESM/Chol 2/2/1 containing 0.5 mol% DiI-C_{20} but no caged Cer to UV light for a comparable period of time did not induce any changes in membrane morphology (Figure 4-19). Lipid mixtures containing 5 mol% C16-Cer were also prepared to form bilayers of

DOPC/ESM/Chol/C16-Cer in 8/7/4/1 molar ratios and stained with 0.5 mol% DiI-C_{20}. AFM images of these samples show L_o/L_d phase separation with domains of similar size, shape, and height above the fluid phase as those containing 5 mol% caged C16-Cer or no Cer.[38] We typically observe variability in domain shape and size for phase-separated supported bilayers within and between individual samples. This variability may be attributed to local sample-substrate effects and/or subtle differences in the sample's thermal history.[39-41]

Figure 4-19. UV light does not induce ceramide-mediated bilayer restructuring in the absence of caged ceramide. A supported bilayer of DOPC/ESM/Chol 2/2/1 (DiI-C_{20}(3) 0.5 mol%) was irradiated for 30 minutes. (A) $T_{0\ min}$ before UV; (B) closed iris defining the irradiated region; (C) $T_{30\ min}$ post-UV with iris open. Scale bar = 5 μm.

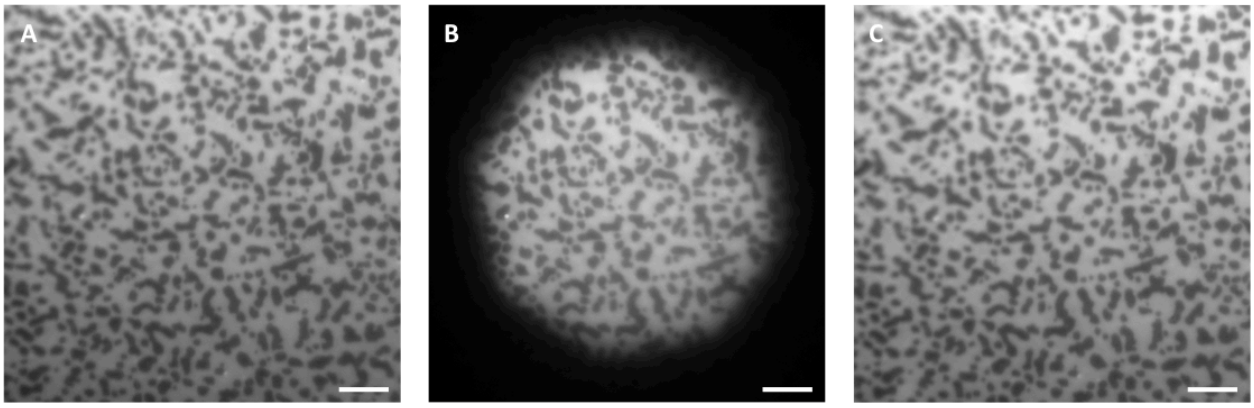

We then examined the effects of generating higher mole fractions of C16-Cer in our model system. Bilayers of DOPC/ESM/Chol/**13** in an 8/6/4/2 molar ratio and containing 0.5 mol% DiI-C_{20} present coexisting L_o/L_d phases with domains comparable to those observed at 5 mol% caged C16-Cer (Figure 4-20). After 30 min of UV irradiation, similar indentations in the ordered domains were observed, with some fragmentation of large domains and disappearance of small domains. The AFM and fluorescence images of these samples provide no evidence for formation of the Cer-rich domains that have been observed previously upon both direct and enzymatic Cer generation.[36-38, 42-46] We did attempt to prepare supported bilayers incorporating higher levels of caged C16-Cer by preparing SUVs of DOPC/ESM/Chol with up to 20 mol% of **13**

(data not shown). These mixtures did not readily form clean bilayers on mica, however, as they were densely covered with adsorbed vesicles even after extensive washing. Following UV irradiation of these samples most of the adsorbed vesicles had disappeared; Cer generation may have promoted vesicle rupturing or desorption. Only modest restructuring of the underlying bilayers took place, on a scale comparable to that observed in the samples incorporating 5 or 10 mol% Cer. These observations suggest that the vesicle deposition protocol we used could not introduce more than about 10 mol% **13** into supported membranes of this lipid mixture.

Figure 4-20. Increasing the caged ceramide content from 5 to 10 mol% of the lipid composition affords bilayers of DOPC/ESM/Chol/**13** in a 8/6/4/2 molar ratio (DiI-C_{20}(3) 0.5 mol%). These samples exhibit L_o domains of similar size and height to those observed at 5 mol%. Photochemical generation of ceramide induces similar time-dependent lipid reorganization that can observed by both fluorescence and AFM. (A) $T_{0\ min}$ before UV; (B) $T_{60\ min}$ 30 min after 30 min UV; (C) AFM of the area acquired 30 min post-UV. Scale bar = 2 μm.

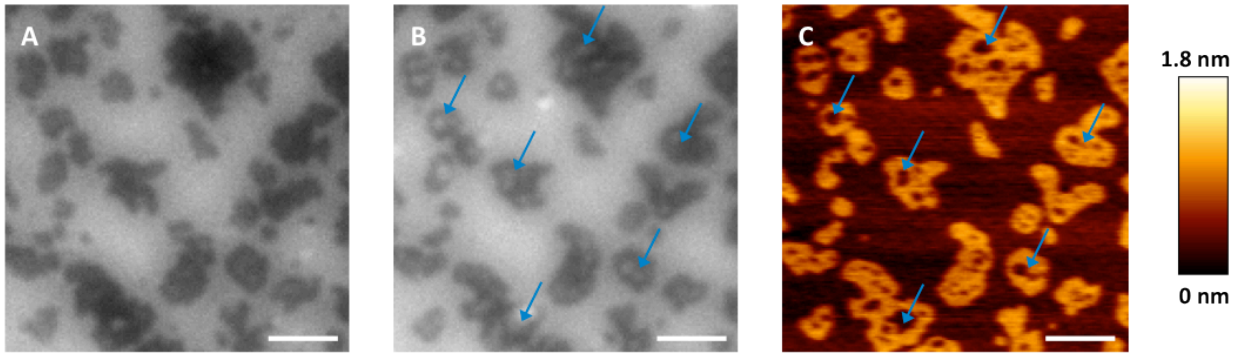

Figure 4-21 describes a photolysis experiment similar to the one illustrated in Figure 4-16 that was performed on a supported bilayer of DOPC/ESM/Chol/**16** in molar ratios of 8/7/4/1 and stained with 0.5 mol% DiI-C_{20}. Correlated AFM and fluorescence images obtained prior to UV irradiation revealed domains that were comparable to those formed from the quaternary mixture containing **13** in terms of their size, shape, height and surface area coverage (Figure 4-21 A). A 10 min photolysis of **16** to generate C16-dihydroCer **14** in the membrane gave rise to small indentations or pits in most of the L_o domains (Figure 4-21B). These subtle changes took

place on a similar timescale to those reported in Figure 4-16, and were most readily observed by AFM. The parallel membrane restructuring behavior observed upon photolysis of **13** and **16** suggests that, at least in this model system, the unsaturation present in the sphingosine backbone of C16-Cer **11** but absent in C16-dihydroCer **14** is not provoking significant differences in the lateral organization of the membrane.

Figure 4-21. Caged C16 dihydroceramide photolysis in a supported bilayer of DOPC/ESM/Chol/**16** in 8/7/4/1 molar ratios (DiI-C_{20}(3) 0.5 mol%). Correlated fluorescence and AFM identify similar initial membrane morphology and comparable changes to those observed in the presence of **13**. (A) $T_{0\ min}$ before UV irradiation; (B) $T_{50\ min}$ following a total of 10 min UV irradiation. Scale bar = 3 μm.

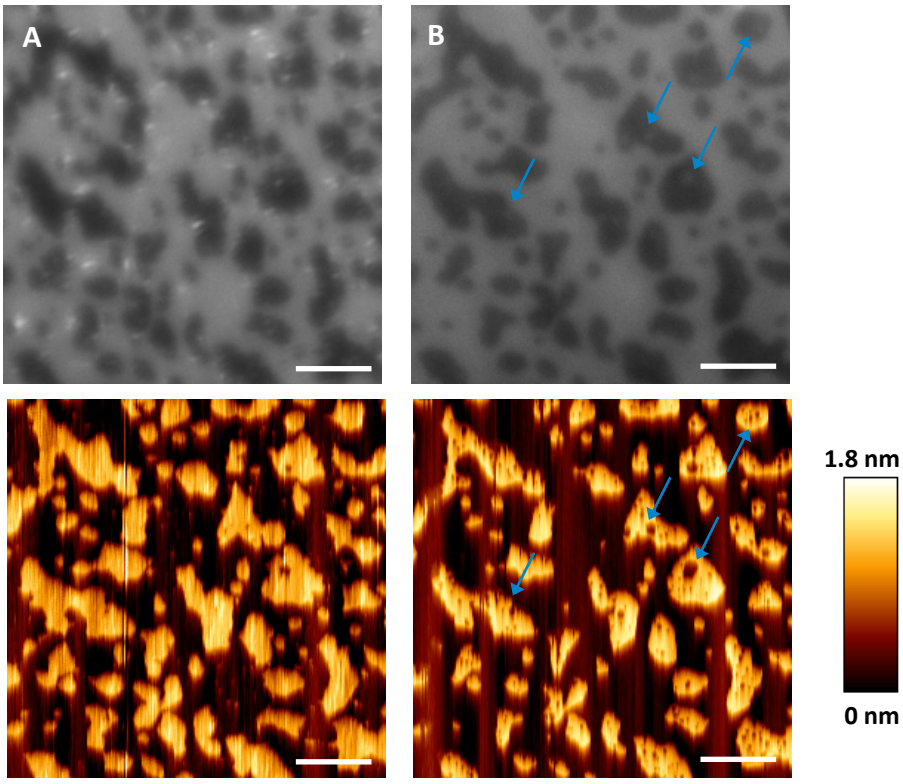

Photolysis of caged C4-Cer, **9**, in DOPC/ESM/Chol lipid bilayers gave qualitatively similar results to those obtained for **13** and **16**. A bilayer prepared from DOPC/ESM/Chol/**9** (8:7:4:1 molar ratio, 0.5 mol% DiI-C_{20}) showed a similar pattern of dark L_o domains surrounded by a fluid phase, with reversed contrast in the coumarin channel, consistent with enrichment of **9** in the L_o domains (Figure 4-22 A, B). The fluorescence contrast was slightly higher, compared to that

obtained in bilayers containing **13**. Changes in bilayer fluorescence after UV irradiation were followed by fluorescence (Figure 4-22 C-F) and showed similar appearance of small regions of fluid phase in the initial L_o domains. Interestingly, in this case, the improved contrast in the coumarin channel allowed visualization of the changes in bilayer morphology following photolysis (Figure 4-22 E).

Figure 4-22. Caged C4 ceramide photolysis in a supported bilayer of DOPC/ESM/Chol/**9** in a 8/7/4/1 molar ratio (DiI-C_{20}(3) 0.5 mol%). (A, B) $T_{0\ min}$ before UV irradiation for DiI and coumarin channels; (C) $T_{5\ min}$ immediately after 5 min UV, DiI channel; (D, E) $T_{20\ min}$ 15 min after UV irradiation for DiI and coumarin channels; (F) $T_{35\ min}$ 30min after UV, DiI channel. Note that the intensity scale is decreased for image (E), due to significant decrease in the coumarin fluorescence following photolysis of **9** and loss of the coumarin fluorophore to the bulk solution. Images acquired by S. P. Pitre. Scale bar = 3 μm.

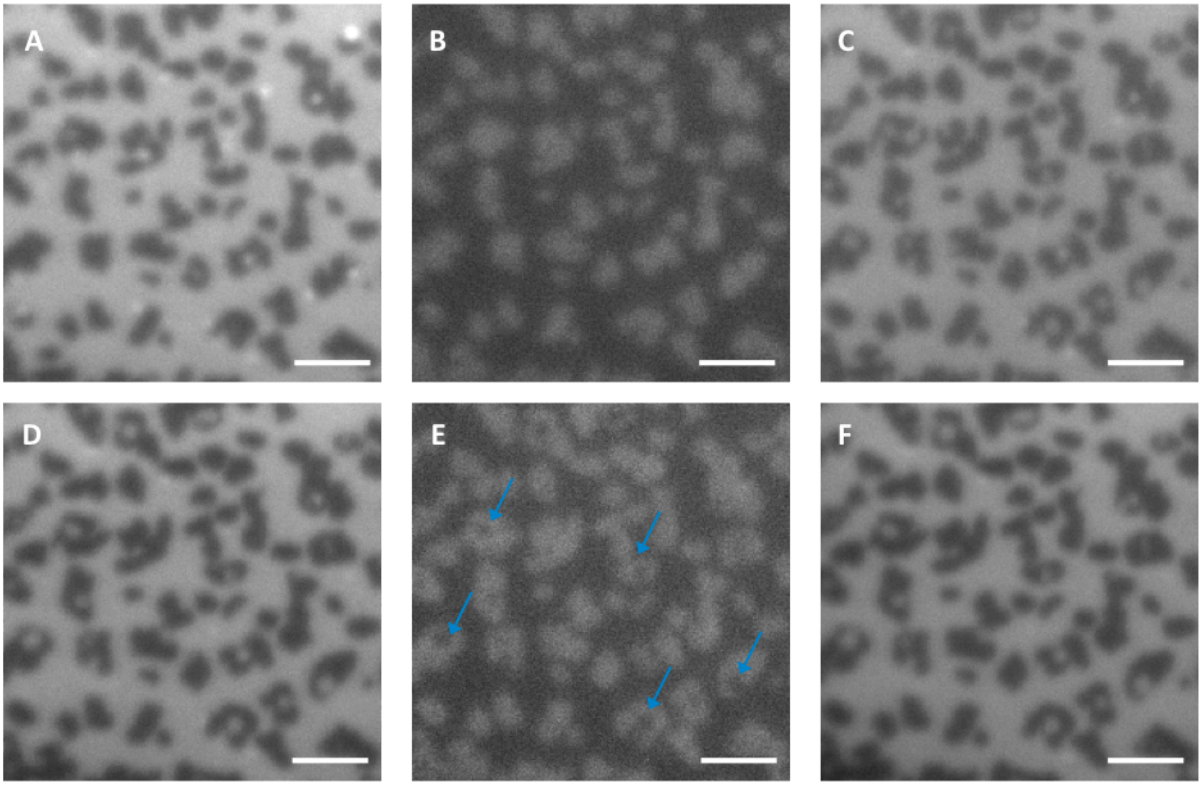

The differences between irradiated and unirradiated areas of the bilayer are evident when the bilayer is imaged with the microscope iris opened, as shown in the larger scale images of the same bilayer measured before and after UV irradiation (Figure 4-23).

Figure 4-23. Fluorescence images showing a larger area of the bilayer for the time course experiment in Figure 4-17 (DOPC/ESM/Chol/**9** in a 8/7/4/1 molar ratio (DiI-C_{20}(3) 0.5 mol%). (A) Before UV irradiation; (B) closed iris denoting the area to be irradiated; (C) after 5 min UV irradiation through the microscope iris with the area irradiated circled, demonstrating that changes in the bilayer are restricted to the irradiated region. Images acquired by S. P. Pitre. Scale bar = 10 μm.

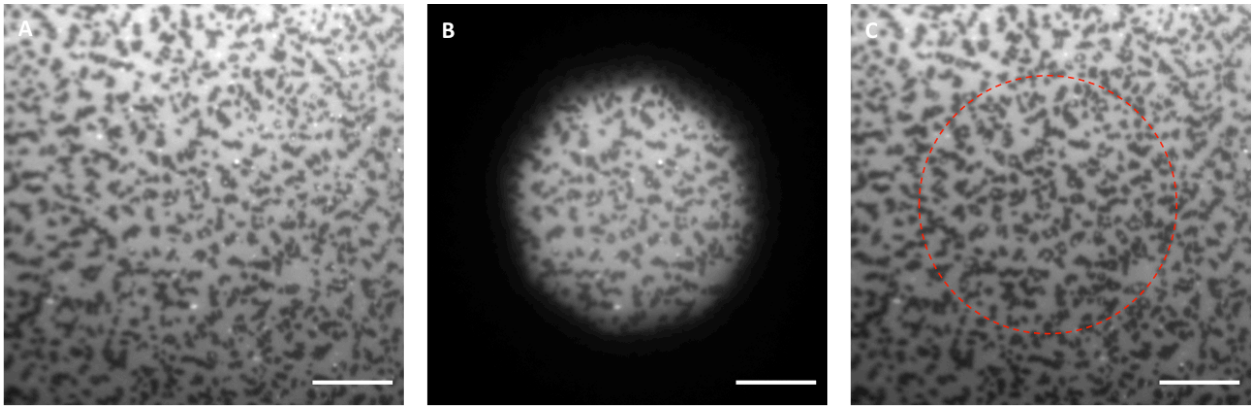

A correlated AFM-fluorescence experiment was also carried out for a DOPC/ESM/Chol/**9** bilayer, as shown in Figure 4-24. Fluorescence images showed morphology changes similar to those in Figure 4-22 and the corresponding before and after UV AFM images confirmed the appearance of many small regions of lower phase in the initial L_o domains. Note that the height of the L_o domains is slightly lower (0.4 – 0.6 nm) than for L_o domains in bilayers containing the C16 analog, **13**.

Figure 4-24. Caged C4 ceramide photolysis in a supported bilayer of DOPC/ESM/Chol/**9** in a 8/7/4/1 molar ratio (DiI-C_{20}(3) 0.5 mol%). (A) $T_{0\ min}$ before UV irradiation; (B) $T_{10\ min}$ immediately after UV irradiation; (C) $T_{40\ min}$ 30 min after UV irradiation; (D, E) AFM images before UV irradiation and after image C. The morphological changes are evident in both fluorescence and AFM images but are clearer with the higher resolution available with AFM. Scale bar = 3 μm.

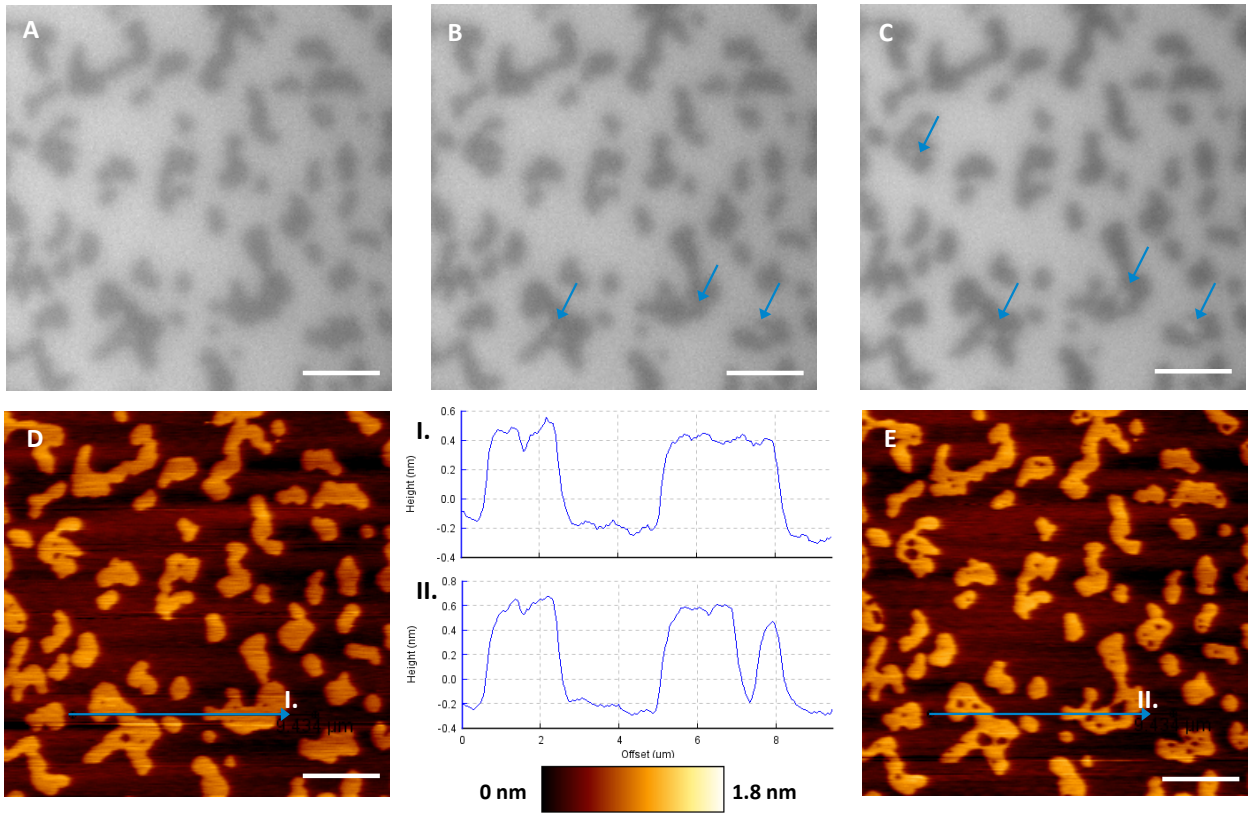

4.2.4 Caged Ceramides in Supported POPC bilayers

Binary mixtures of POPC and long acyl chain-bearing Cers display fluid and gel phase coexistence in GUVs and large unilamellar vesicles (LUVs) containing as little as 4-5 mol% Cer.[47-48] We deposited SUVs composed of POPC/C16-Cer in a 9/1 molar ratio and stained with 0.5 mol% DiI-C_{20} on mica to form phase-separated planar supported bilayers (Figure 4-25). Correlated fluorescence and AFM imaging of these membranes confirmed the presence of round, Cer-rich domains that strongly excluded the fluorescent probe (Figure 4-25 A), and showed heights of approximately 1.2-1.5 nm above the surrounding membrane (Figure 4-25 B). AFM also makes a straightforward distinction between these raised domains and occasional

membrane defects that also appear as dye-excluded regions in the fluorescence image. A second fluorescence image (Figure 4-25 C) acquired after the AFM scan indicates that some of the defects have started to fill in, presumably an effect of the scanning tip. A control experiment showed that UV irradiation had no effect on the morphology of POPC/C16-Cer bilayers (Figure 4-26).

Figure 4-25. A supported bilayer of POPC/C16 Cer in 9/1 molar ratios (DiI-C_{20}(3) 0.5 mol%) imaged by correlated fluorescence and AFM presents similar morphology to POPC bilayers prepared with **13** following ceramide generation. The micron-scale dye-excluded domains in this membrane can be reliably identified as ceramide-rich features. (A) bilayer visualized by fluorescence before AFM scan; (B) contact mode AFM reveals gel-phase domains (light gold areas) that are ~1.5 nm taller than the POPC-rich phase, and some membrane-spanning defects (darker scan regions); (C) in a post-AFM fluorescence image some of these holes can be distinguished from the darker domains, as the defects in the fluid membrane begin to fill in . Scale bar = 5 μm.

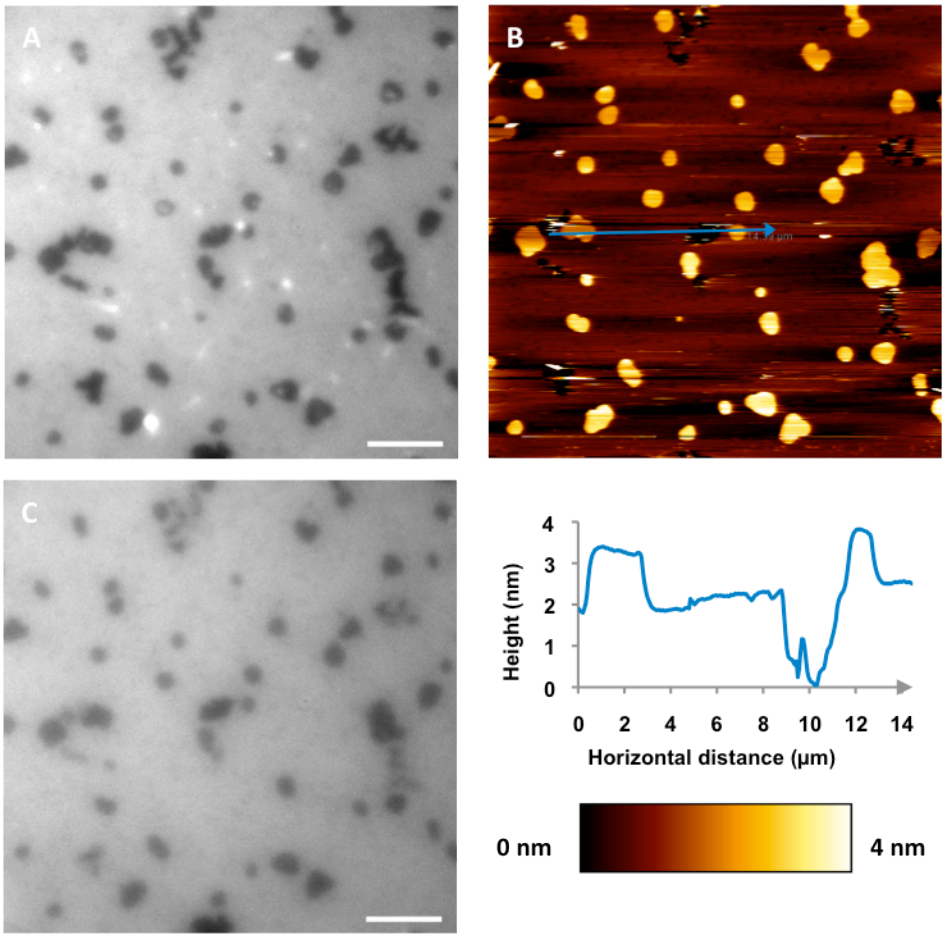

Figure 4-26. UV light does not induce ceramide-mediated bilayer restructuring in the absence of caged ceramide. A supported bilayer of POPC/C16 Cer in 9/1 molar ratios (DiI-C_{20}(3) 0.5 mol%) was irradiated for 10 minutes. (A) $T_{0\ min}$ before UV; (B) closed iris showing the area to be irradiated; (C) $T_{10\ min}$ post-UV. Scale bar = 5 μm.

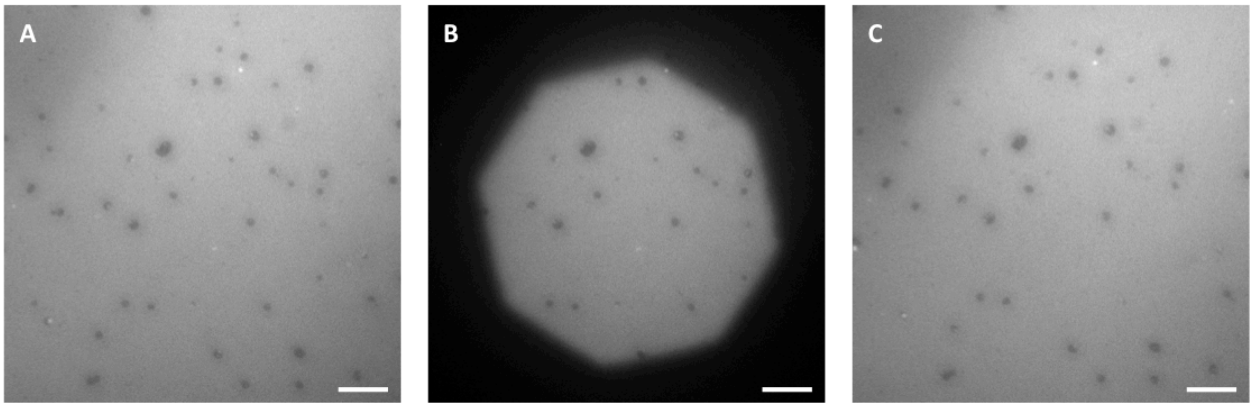

Caged C16-Cer was then substituted for C16-Cer in the parent lipid mixture, to afford SUVs of POPC/**13** in a 9/1 molar ratio and also containing 0.5% $DiIC_{20}$. The resulting supported bilayers exhibited uniform fluorescence intensity suggesting that **13** was homogeneously distributed throughout the membrane, at least at the resolution of optical microscopy (Figure 4-27 A). Correlated AFM and fluorescence imaging confirmed the absence of small nanoscale bilayer domains (Figure 4-28). As before, we used the microscope iris to define a small illumination area for Cer generation (Figure 4-27 B). Following 5 s of UV irradiation an image acquired with the iris fully open revealed an array of small, dye-excluded features in a hexagonal ensemble outlining the area in which photolysis had taken place (Figure 4-27 C). Starting at the periphery of the iris-defined region and moving progressively towards its center, the dark domains had completely disappeared within 10 min of their formation (Figure 4-27 D). Repeating the 5 s photolysis generated a remarkably similar pattern of domains (Figure 4-27 E); once again, the bilayer returned to its initial homogeneous aspect in a matter of minutes. Similar behavior with a well-conserved pattern of domains in the irradiated area was observed following a third (not shown) and fourth (Figure 4-27 E) 5 s UV irradiation. Examination of the

pattern of domains generated during successive irradiations showed two interesting features. First, many of the domains appeared in the same location after successive irradiations, although there were also differences in the domain pattern from one image to the next (examples of both are identified within the blue and red perimeters in Figure 4-27 C, E, F). Second, the area covered by domains had increased significantly by the 4th irradiation.

Figure 4-27. Photorelease of caged C16 ceramide in a supported bilayer of POPC/**13** in molar ratios of 9/1 (DiI-C_{20}(3) 0.5 mol%).(A) $T_{0\ min}$ before UV irradiation the membrane appears uniform by fluorescence, with no visible phase separation; (B) the area where ceramide will be generated is indicated by the reduced iris aperture; (C) following 5 s of UV exposure small, dye-excluded ceramide-rich domains can be observed in the irradiated region; (D) $T_{10\ min}$ the dark domains have disappeared from the iris-defined region, beginning at its periphery and moving progressively towards the centre; (E) a second 5 s photolysis confined to the same area recreates a similar pattern, where most domains correlate well in size and position to those observed in C. As before the membrane re-equilibrates within minutes to give a uniform bilayer (not shown); (F) $T_{29\ min}$ following third and fourth 5 s photolyses, a larger area is covered by domains. Domains encircled in blue reappear in the same location, while domains in red disappear or change. Scale bar = 5 μm.

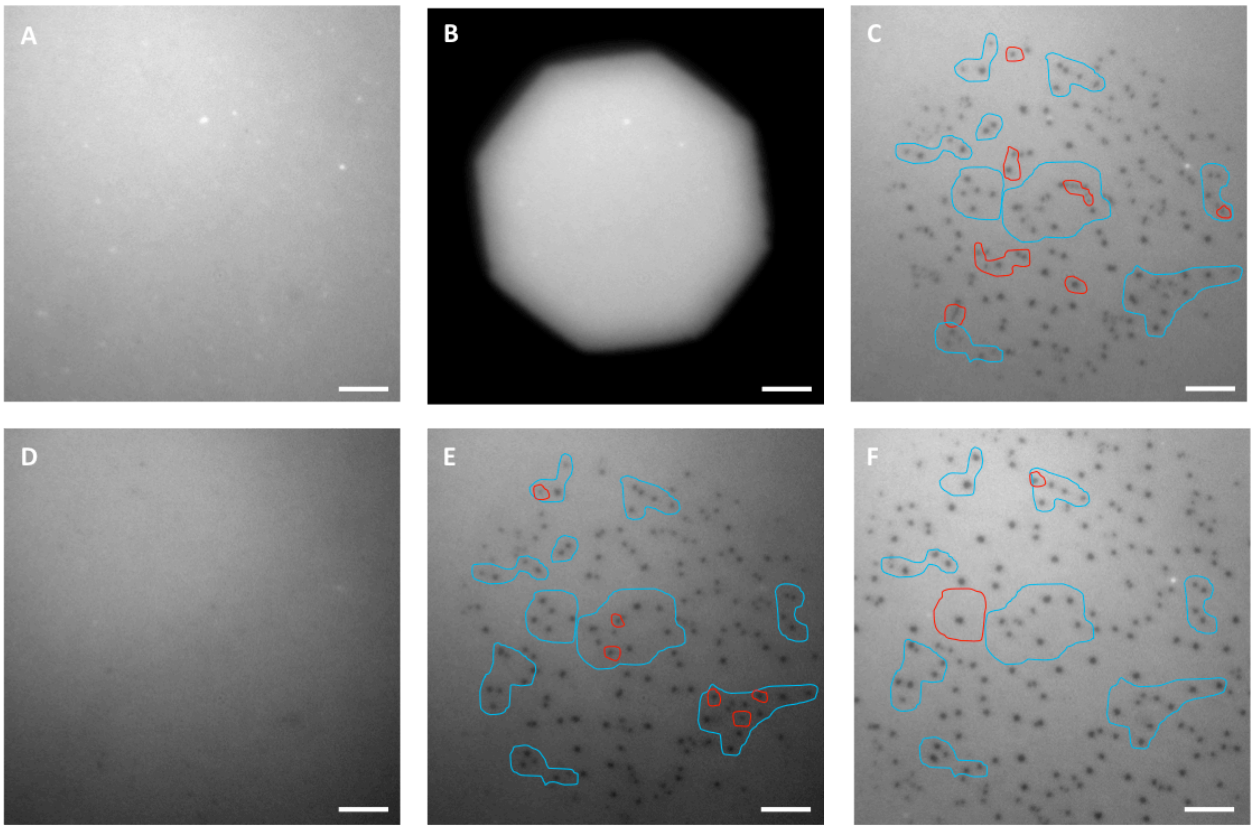

Figure 4-28. A planar supported bilayer of POPC/**13** in molar ratios of 9/1 (DiI-C_{20}(3) 0.5 mol%) presents no discernible phase separation before photolysis of **13**. (A) $T_{0\ min}$ fluorescence image and (B) AFM scan . (C) $T_{20\ min}$ post-AFM image. The bright features due to adsorbed vesicles show a different pattern after the AFM scan. Scale bar = 5 μm.

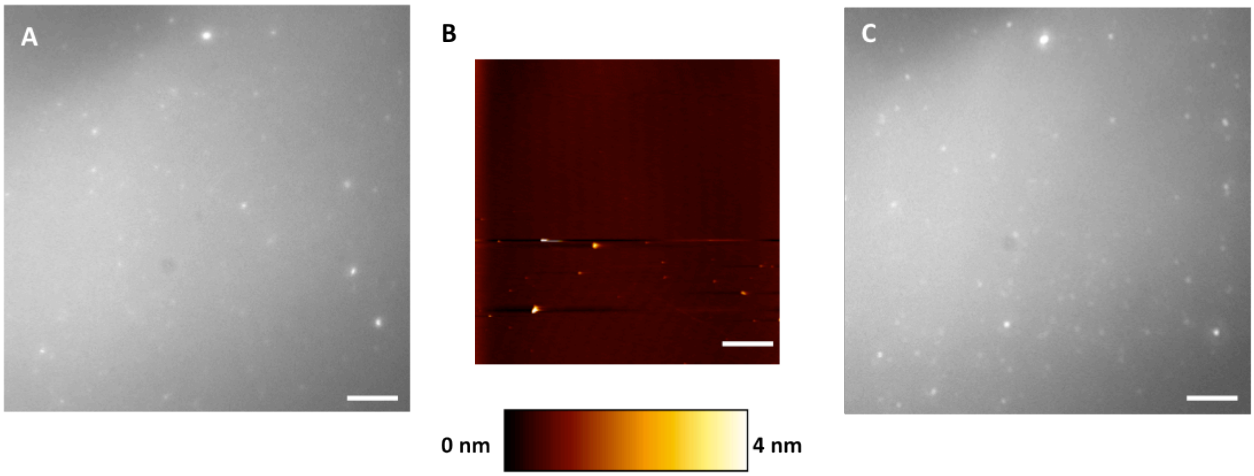

A correlated imaging experiment was performed for the bilayer shown in Figure 4-27. Figure 4-29 A, B shows fluorescence and AFM images obtained immediately after the 4th 5 s irradiation. The dark domains observed by fluorescence correspond to raised features in the AFM image consistent with their assignment to a Cer gel phase. A second fluorescence image obtained immediately after the AFM image (and ~13 min after irradiation) indicated that many of the initial dark domains had disappeared and that domain loss was more pronounced in the region scanned by AFM. This experiment indicated that domain disappearance was enhanced by AFM scanning and that the domains disappeared more slowly after the same region of the bilayer had been irradiated multiple times.

Figure 4-29. Correlated fluorescence and AFM imaging of a supported bilayer of POPC/**13** in molar ratios of 9/1 (DiI-C_{20}(3) 0.5 mol%) following localized photolysis confirms that the dye-excluded features seen by fluorescence are ceramide-rich domains. (A) A zoomed image of the bilayer region shown in Figure 4-27 F, prior to AFM scanning; (B) contact mode AFM shows domains that are ~1.5 nm higher than the bulk membrane; (C) a fluorescence image acquired post-AFM (13 min after image (A) indicates the disappearance of several domains. This is consistent with the ongoing membrane reorganization described in Figure 4-27, and may also reflect interactions between the AFM tip and the sample during scanning. Scale bar = 5 μm.

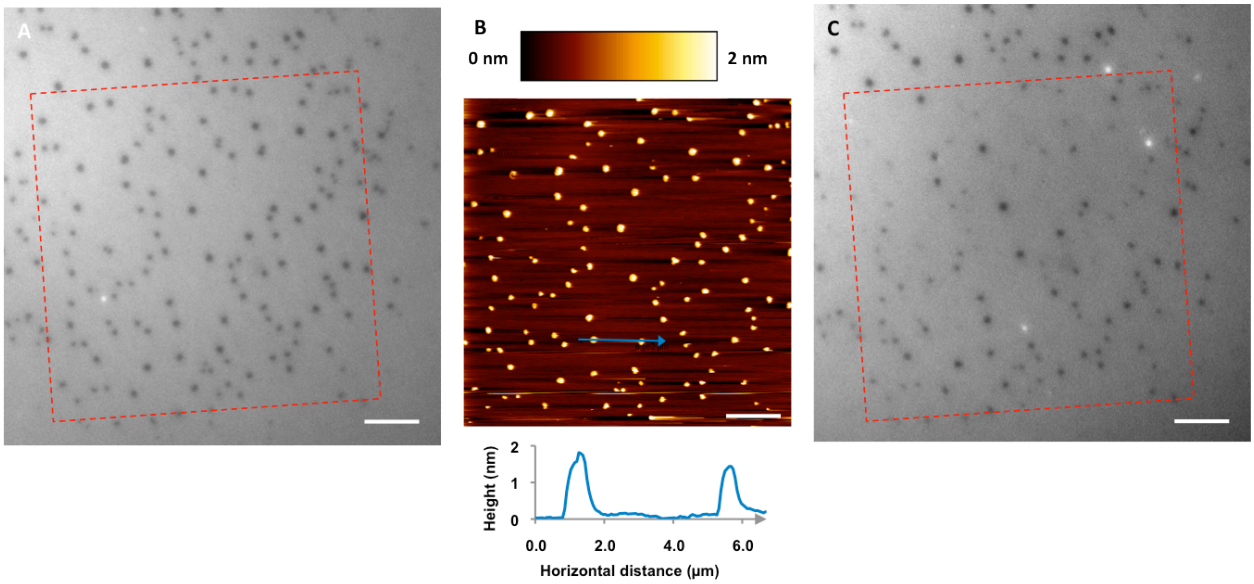

In order to further examine the equilibration of the Cer-enriched domains generated by photo-uncaging of **13**, well-separated regions of a POPC/**13** bilayer were irradiated for different lengths of time, and imaged by fluorescence only to eliminate changes induced by the AFM tip. The area covered by domains increased significantly as the irradiation time was increased (Figure 4-30), with a 1 min irradiation giving domains that covered an area about 80 μm in diameter, versus a 2.5 s irradiation where the domains roughly covered the area outlined by the microscope iris. This effect is much too large to be caused by effects of weaker illumination at the edges of the iris. Successive fluorescence images of the individual irradiated areas indicated that the pattern of domains disappeared in each case, although it took roughly twice as long for this to occur for the larger pattern created by 1 min irradiation compared to the domains generated by 2.5 s irradiation (Figure 4-31).

Figure 4-30. Effects of irradiation time on the observed pattern of dye-excluded domain formation. Several regions of the same bilayer of POPC/**13** in molar ratios of 9/1 (DiI-C_{20}(3) 0.5 mol%) were irradiated through a reduced iris aperture for intervals of varying length: (A) 2.5s; (B) 5s; (C) 15s; (D) 30s; (E) 1min. Scale bar = 10 μm.

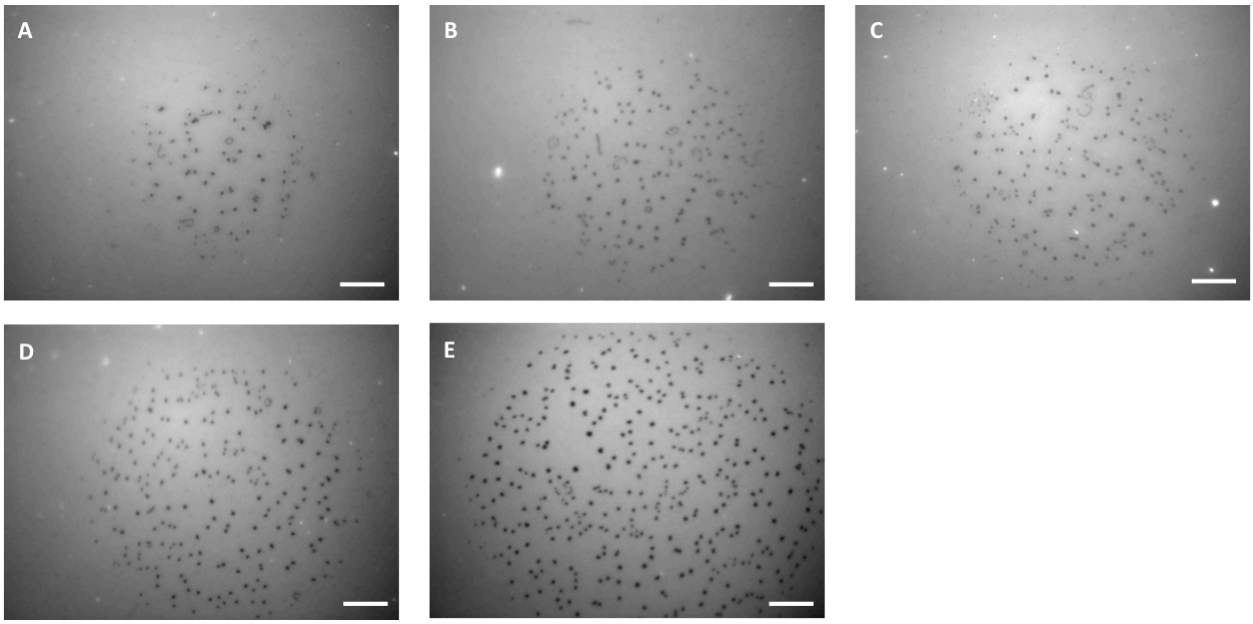

Figure 4-31. Domain disappearance as a function of pattern size. For each irradiation interval shown in Figure 4-30 the region of interest was re-imaged 5 min after the end of the photolysis. (A) 2.5s; (B) 5s; (C) 15s; (D) 30s; (E) 1min. In the area irradiated for 1 min, the domains had almost completely disappeared 10 min post-UV. Scale bar = 10 μm**.**

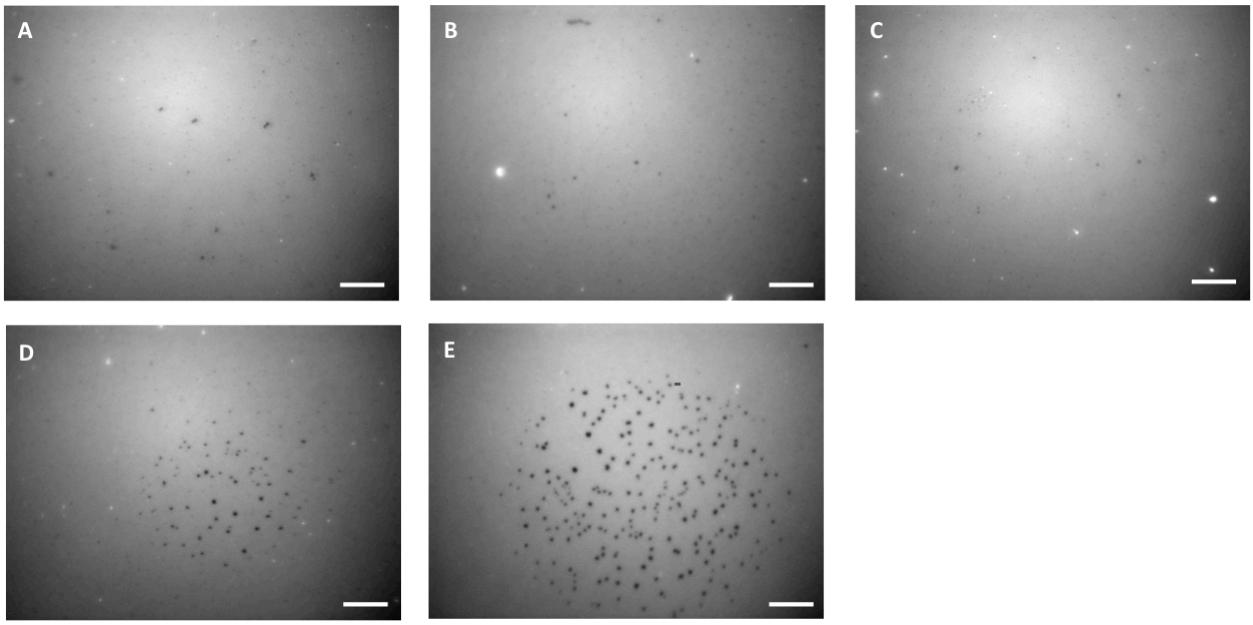

The effects of irradiation time on the area covered by domains and the qualitative changes in their rate of disappearance are hypothesized to result from generation of a high local Cer concentration that is above the threshold for domain formation, followed by lipid diffusion, which dilutes the newly generated Cer into the bulk bilayer. The larger area covered by domains with longer irradiation time indicates an expanding ring of Cer-enriched bilayer resulting from lipid diffusion. The above hypothesis was tested by irradiating an entire bilayer using a small lamp, rather than through the microscope iris. A combination of fluorescence and AFM images showed that small dye-excluded (fluorescence) and raised (AFM) features formed and were stable over a period of >45 min, which included two consecutive AFM images (Figure 4-32). This provides clear evidence that the domains disappear by equilibration of the initial Cer-enriched areas formed within a limited area with the bulk membrane; the equilibration is driven by the concentration gradient created by photo-uncaging of **13** in a spatially restricted region of the bilayer.

The specific binding of the pentameric B subunit of Cholera toxin (Ctx-B) to GM1 ganglioside has been widely exploited in cellular and model membrane studies of raft domains, particularly through the use of fluorescent Ctx-B conjugates.[49-50] In this investigation we examined the distribution of GM1-bound Ctx-B in bilayers before and after photochemical Cer generation. We elected to use supported bilayers of POPC/**13**/GM1 in molar ratios of 90/10/1 and stained with 0.5 mol% $DiIC_{20}$ for our model system. Upon UV irradiation of a small region through the microscope iris, these membranes exhibited Cer-rich domain-forming characteristics similar to those described above (Figure 4-27). Dye-excluded features would form then dissolve, and could be regenerated following repeated UV irradiation (Figure 4-33).

Figure 4-32. Correlated fluorescence and AFM of imaging of a supported bilayer of POPC/**13** in molar ratios of 9/1 (DiI-C_{20}(3) 0.5 mol%) following photolysis of caged ceramide in the whole sample volume confirms that the dye-excluded features seen by fluorescence are ceramide-rich domains. (A) $T_{0\ min}$ before photolysis; (B) $T_{52\ min}$ a second area of the bilayer following 30 min UV exposure of the entire sample; (C) contact mode AFM confirms the presence of gel-phase domains; (D) $T_{75\ min}$ in a fluorescence image taken following two consecutive AFM scans the bilayer appears unchanged, suggesting that the domains are relatively stable, and that the membrane had equilibrated before the AFM images were acquired. Scale bar = 5 μm.

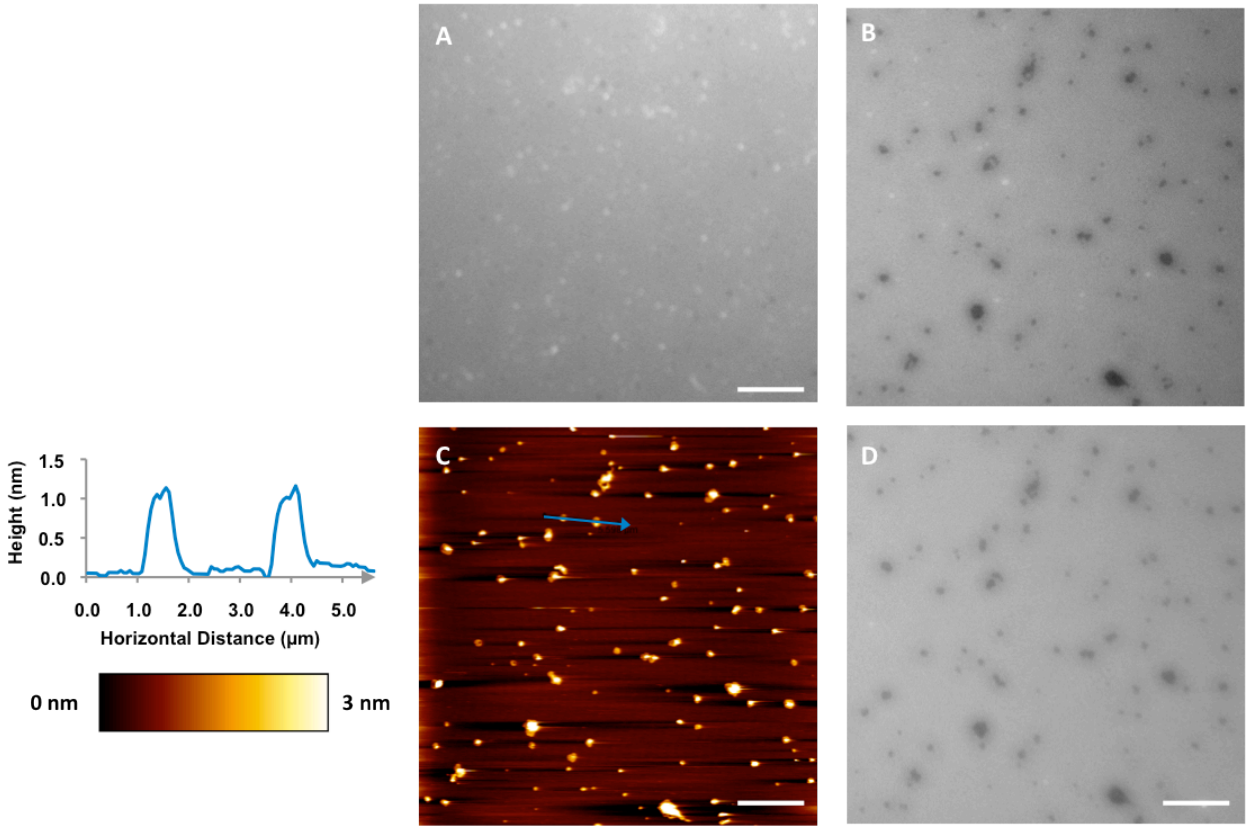

In order to qualitatively assess the partitioning of GM1 between coexisting gel and fluid phases, an entire bilayer of POPC/**13**/GM1 was UV irradiated for 5 min using a small lamp, to form persistent Cer-rich domains. The sample was then incubated in the presence of Alexa 488-labeled Ctx-B for 30 min, washed, and re-imaged by fluorescence (Figure 4-34). When viewed in the $DiIC_{20}$ channel (Figure 4-34 A) the bright fluid phase of the bilayer was punctuated with round, dye-excluded domains comparable to those observed in the absence of both GM1 and Ctx-B. Contrast was inverted in the Alexa 488 channel, with the POPC-rich fluid phase appearing dark relative to the Cer-rich domains (Figure 4-34 B), and indicating that GM1 preferentially

accumulated in the gel phase environment. In a false-colour overlay (Figure 4-34 C) the GM1-containing but $DiIC_{20}$-excluding domains (green) can be readily distinguished from the fluid phase (red) and adsorbed vesicles (orange). The latter features have a comparable Alexa 488 signal to the Cer-rich domains, suggesting that they contain some GM1.

Figure 4-33. Photolysis of caged C16 ceramide in a supported bilayer of POPC/**13**/GM1 in 90/10/1 molar ratios ($DiIC_{20}$(3) 0.5 mol%) induces comparable morphological changes to those observed in bilayers of POPC/**13**. (A) $T_{0\ min}$ before UV; (B) closed iris identifying the area to be irradiated; (C) following 2.5 s of UV exposure small, dye-excluded ceramide-rich domains can be seen in the area exposed to UV light; (D) $T_{5\ min}$ the dark domains have completely disappeared; (E) a second 2.5 s photolysis in the same area recreates dark domains, most of which correspond in size and position to those in C. As before the membrane reassumes a uniform appearance within minutes (not shown); (F) $T_{20\ min}$ following a third 2.5 s interval of localized ceramide generation, a similar distribution of domains is reproduced. Scale bar = 5 μm.

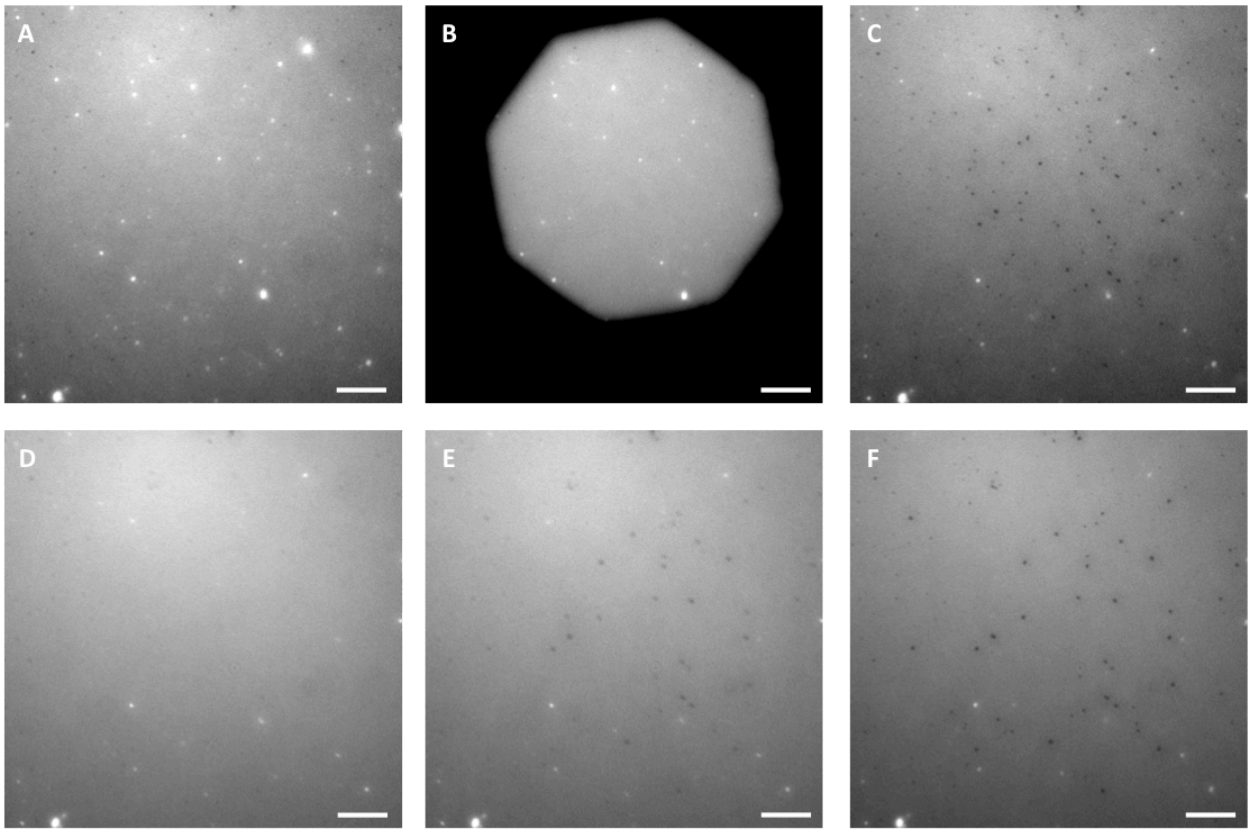

Resonance energy transfer between Alexa 488 and $DiIC_{20}$ could enhance the fluorescence contrast of Ctx-B in the domains with respect to the $DiIC_{20}$-rich fluid phase. To verify that the qualitative enrichment of Ctx-B was not exclusively the product of this effect, we repeated the

above experiment using Alexa 647-labeled Ctx-B (Figure 4-35). The DiI channel showed typical small dark domains, whereas the Alexa 647 channel showed small bright domains that corresponded exactly to the dye-excluded areas in the DiI channel, confirming partitioning of GM1 into the Cer-enriched domains. This is clearly illustrated in the false-color merged image that shows strong enrichment of Ctx-B (red) in the Cer domains that exclude DiI (green). In this case resonance energy transfer between DiI and Alexa 647 will decrease the apparent enhancement of Ctx-B in the ordered domains, but taken together, the two labeling experiments support our conclusion that GM1 partitions into the ordered domains.

Figure 4-34. GM1 ganglioside partitions into crystalline lipid domains formed via light-induced ceramide generation. A supported membrane of POPC/**13**/GM1 in molar ratios 90/10/1 (DiI-C_{20}(3) 0.5 mol%) was UV irradiated for 5 min in buffer (pH 7.4) and subsequently incubated in a dilute solution of Alexa 488-labeled Cholera toxin B subunit (Ctx-B) for 30min, and then gently rinsed. Fluorescence images were then acquired in both (A) DiI-C_{20} and (B) Alexa 488 channels. (C) A false-color composite overlay shows GM1-enrichment in the gel phase domains (green) with respect to The POPC rich-bulk phase (red). Adsorbed vesicles stained with both probes appear yellowish-orange. Scale bar = 3 μm.

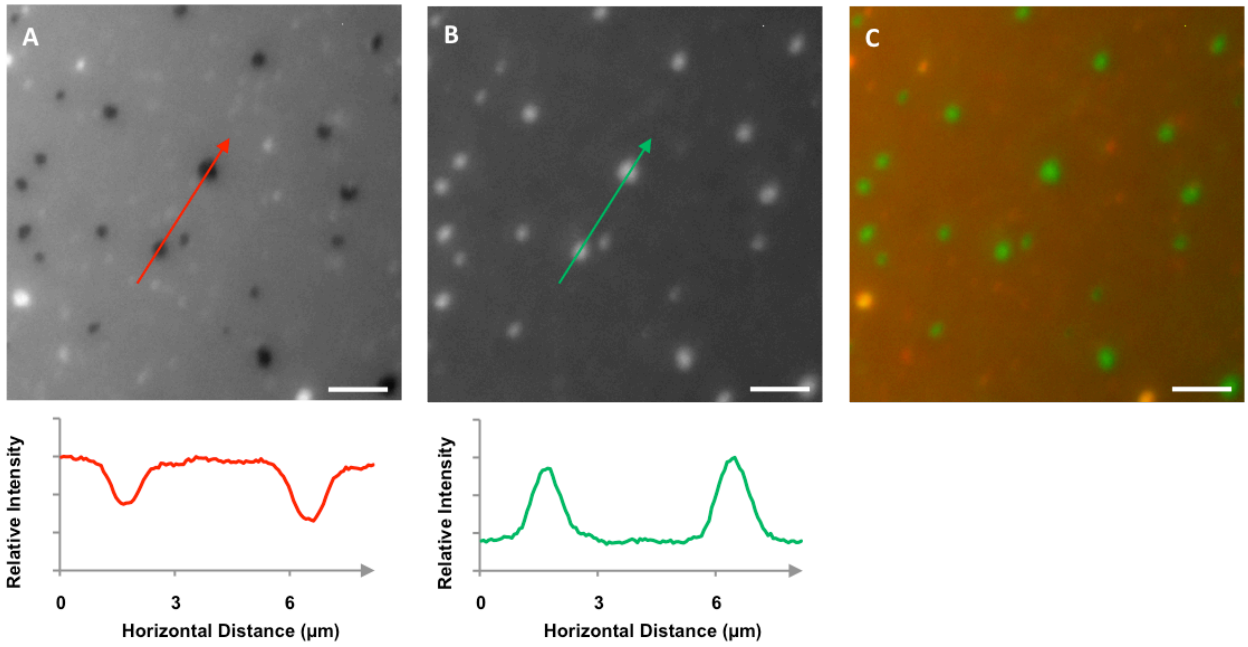

Figure 4-35. GM1 ganglioside partitions into crystalline lipid domains formed via light-induced ceramide generation. A supported membrane of POPC/**13**/GM1 in molar ratios 90/10/1 (DiI-C_{20}(3) 0.5 mol%) was UV irradiated for 30 min in buffer (pH 7.4) and subsequently incubated in a dilute solution of Alexa 647-labeled Ctx-B for 30min, and then gently rinsed. Fluorescence images were then acquired in both (A) DiI-C_{20} and (B) Alexa 647 channels. (C) A false-color composite overlay shows GM1-enrichment in the gel phase domains (red) with respect to the POPC rich-bulk phase (green). Scale bar = 2 μm.

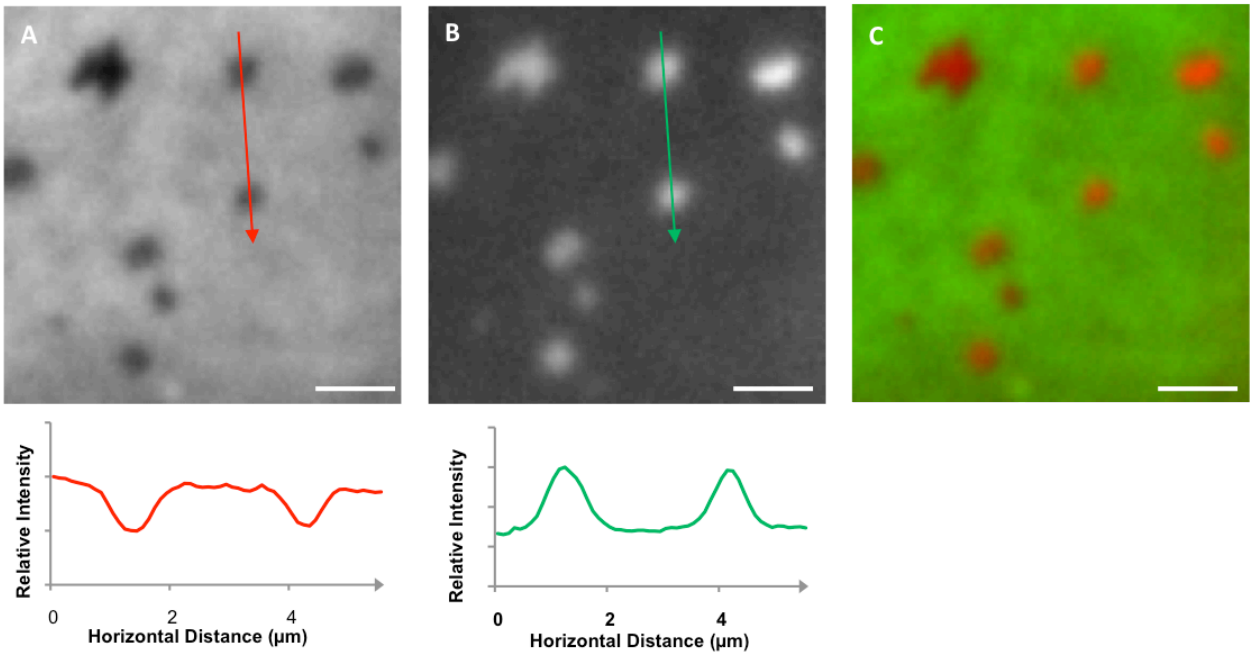

We then proceeded to examine whether photochemical Cer generation could drive the assembly of small, pre-formed protein-bound lipid clusters into larger aggregates. To this end we began by labelling a supported bilayer of POPC/**13**/GM1 with Ctx-B Alexa 488 before performing a photolysis (Figure 4-36 A). Even after extensive rinsing the Ctx-B-bound membrane was covered with a large number of adsorbed vesicles, an effect that was possibly exacerbated by the sample being in a high ionic strength buffer as opposed to MQ water. These vesicles were most apparent in the DiIC_{20} channel. Based on the weak and heterogeneous Alexa 488 signal, at this stage the bound Ctx-B appeared to be scattered throughout the membrane, without much localized enrichment. In bilayers not pre-labelled with Ctx-B 5 s of UV exposure on the microscope was typically sufficient to trigger the formation of dye-excluded domains.

Figure 4-36. Cholera toxin B subunit-bound G_{M1} ganglioside accumulates in photochemically generated ceramide-rich domains. A supported bilayer of POPC/13/GM1 in molar ratios 90/10/1 (DiI-C_{20}(3) 0.5 mol%) was incubated with Alexa 488-labeled Ctx-B for 30min in buffer (pH7.4), and then briefly rinsed. A small area of the sample defined by the microscope iris was then UV irradiated for 1 min. The lateral organization of the membrane before and after photolysis was recorded by fluorescence in both DiI-C_{20} and Alexa 488 channels. (A) $T_{0\ min}$ pre-UV small Ctx-B/GM1 clusters are randomly distributed throughout the region of interest; (B) $T_{1\ min}$ post-UV; areas of higher Alexa 488 Ctx-B fluorescence correlate with dye-excluded gel-phase domains. (C) $T_{20\ min}$ the dark domains have stabilized in size and the fluorescence intensity of labeled Ctx-B/GM1 in these features has increased with respect to the POPC-rich phase. Scale bar = 4μm.

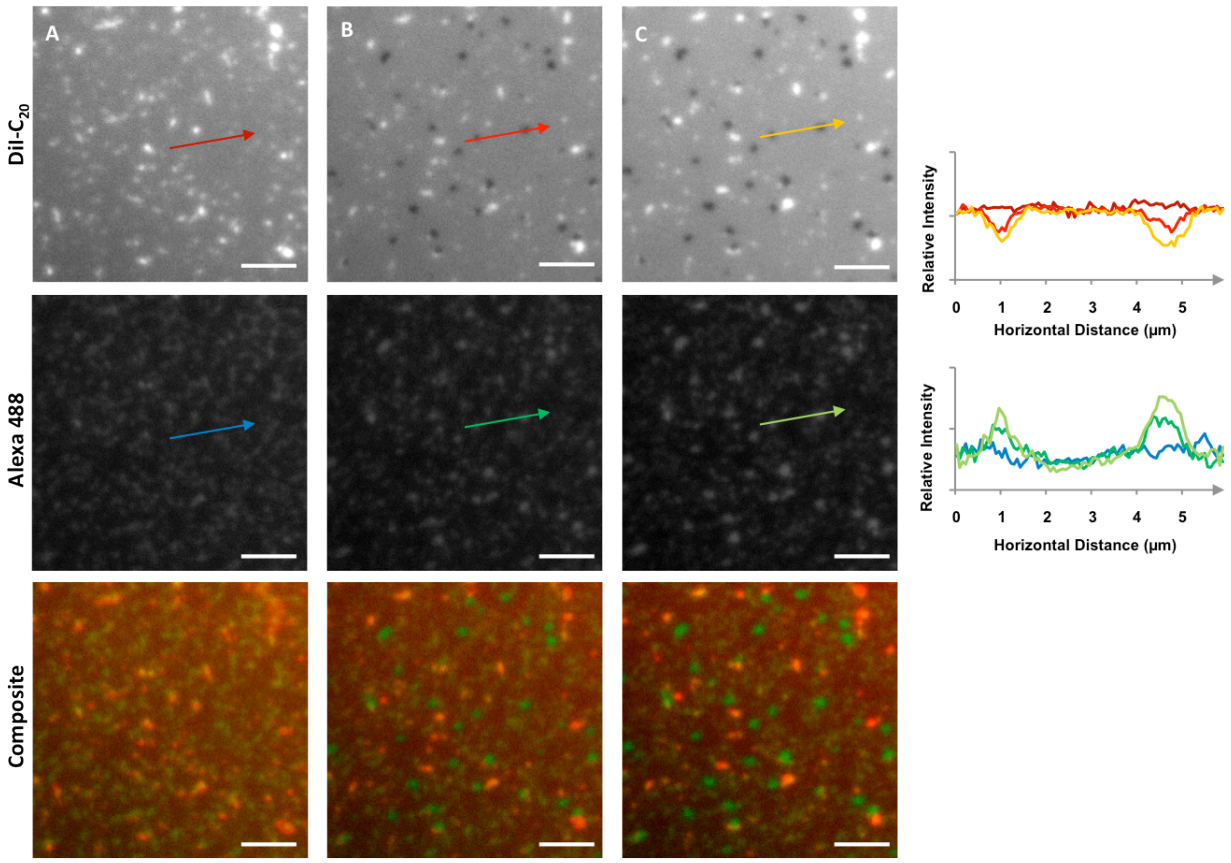

In this case, possibly due to the ordering effect of small Ctx-B/GM1 clusters present in the membrane, Cer-rich domains only appeared following a 1 min photolysis (Figure 4-36 B). As dye-excluded features became visible in the $DiIC_{20}$ channel, the corresponding pixels in the Alexa 488 channel appeared brighter than the bulk membrane. 20 min after the generation of Cer in the membrane, the domains appeared stable, having remained in size for at least 10 min (Figure 4-36 C) Intensity cross sections indicate that over the course of the experiment the intensity of Alexa 488 fluorescence in the gel phase domains had increased as $DiIC_{20}$ intensity in

the same features decreased – a further indication that the process of lateral reorganization proceeded at a relatively slow rate in this case.

Figure 4-37. Cholera toxin B subunit-bound G_{M1} ganglioside accumulates in photochemically generated ceramide-rich domains. A supported bilayer of POPC/**13**/GM1 in molar ratios 90/10/1 (DiI-C_{20}(3) 0.5 mol%) was incubated with Alexa 647-labeled Ctx-B for 30min in buffer (pH7.4), and then briefly rinsed. The sample was then UV irradiated for 30 min. The lateral organization of the membrane before and after photolysis was recorded by fluorescence in both DiI-C_{20} and Alexa 647 channels. (A) $T_{0\ min}$ prior to Ctx-B labelling the bilayer appears uniform and featureless; (B) $T_{30\ min}$ pre-UV small Ctx-B/GM1 clusters are randomly distributed throughout the region of interest; (C) $T_{60\ min}$ post-UV areas of higher Alexa647 Ctx-B fluorescence correlate with dye-excluded gel-phase domains. Scale bar = 2μm.

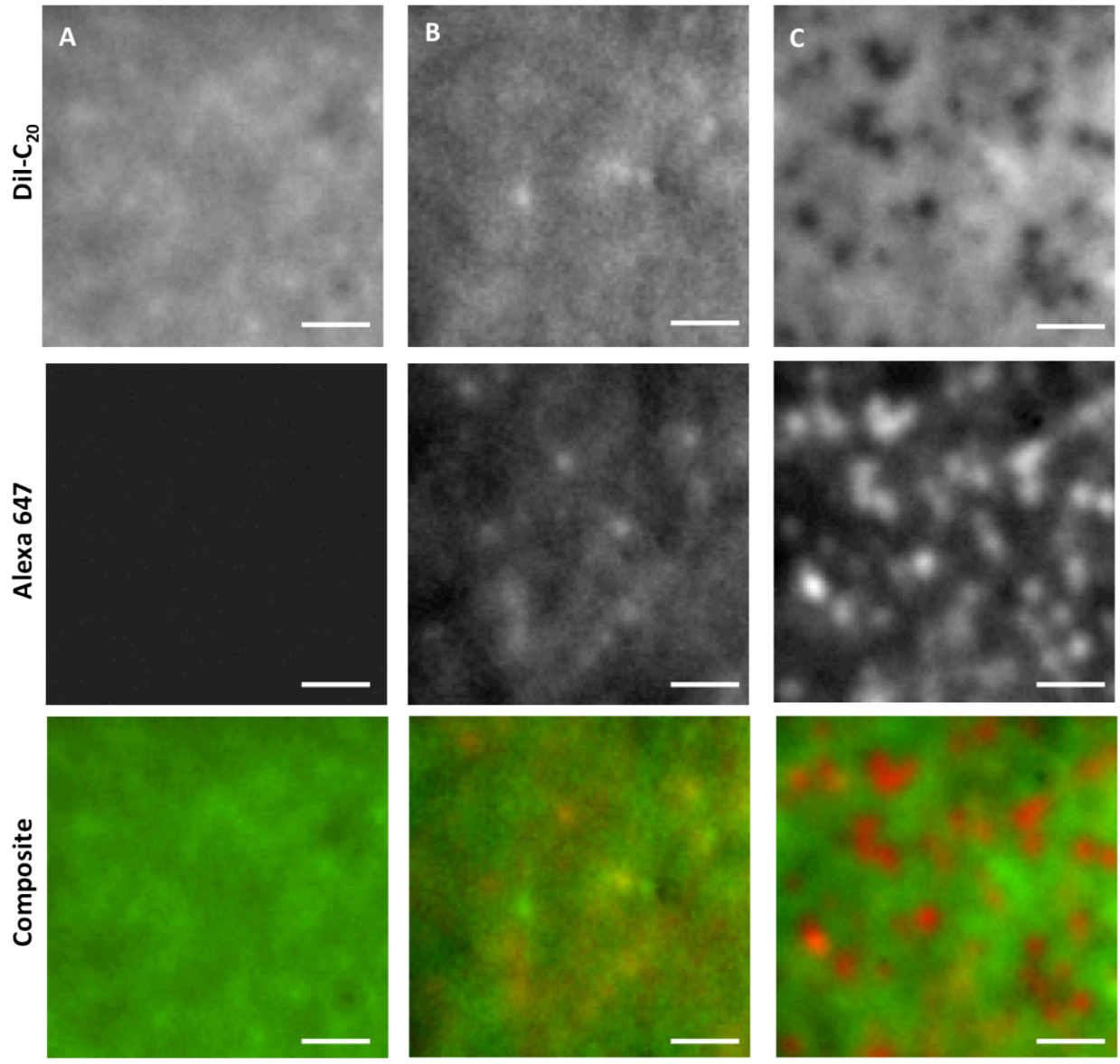

The protein localization experiment in Figure 4-36 was also repeated using Alexa 647-labeled Ctx-B (Figure 4-37). Prior to addition of Ctx-B the bilayer showed uniform fluorescence in the $DiIC_{20}$ channel, with no adsorbed vesicles apparent in the region of interest. After incubating with Ctx-B and rinsing, the bilayer still showed reasonably uniform fluorescence in the DiI channel and diffuse fluorescence with some brighter features in the Alexa 647 channel (Figure 4-37 B), consistent with GM1-Ctx-B distributed throughout the bilayer. After UV irradiation the bilayer changed significantly, with small dye-excluded features appearing in the DiI channel that overlapped well with bright domains observed in the Alexa 647 channel (see merged image, Figure 4-37 C). This confirmed that the photo-uncaging results in partitioning of GM1-Ctx-B into ordered Cer-enriched domains.

In several cases bilayers formed by incubating larger concentrations of lipid vesicles were studied. Increasing the vesicle concentration by a factor of 2 generated bilayers with a substantial number of adsorbed vesicles which could not be removed by prolonged washing with either water or high ionic strength buffer; a representative example is shown in Figure 4-38 for a 9:1 POPC/**13** bilayer containing 1% GM1 and 0.5% DiI-C_{20}. Irradiation of this bilayer led to the disappearance of the adsorbed vesicles in the irradiated area and to formation of the expected ceramide-enriched domains. The domains disappeared rapidly, as observed in earlier samples. A second irradiation with the iris opened to expose a larger area led to the disappearance of the vesicles and formation of domains outside the area of the first irradiation. However, in contrast to earlier results, no additional domains were detected in the central area corresponding to the first irradiation through the closed iris.

Figure 4-38. Photolysis of **13** to generate Cer in vesicles adsorbed to a bilayer of POPC/**13**/GM1 in 90/10/1 molar ratios (DiI-C_{20}(3) 0.5 mol%) may contribute to morphological changes in the supported membrane by promoting vesicle rupturing and/or exchange of lipids between vesicles and the planar bilayer. (A) $T_{0\ min}$ before UV; (B) closed iris identifying the area to be irradiated; (C) following 5 s of UV exposure a few small dye-excluded domains (indicated by the blue arrows) can be seen in the area exposed to UV light; (D) $T_{5\ min}$ the dark domains have completely disappeared; (E) a 5 s photolysis with the iris open generates domains in the areas of the membrane covered with vesicles, but not in the previously irradiated central region; (F) $T_{15\ min}$ these domains appear to be relatively stable and persistent. Scale bar = 8 μm.

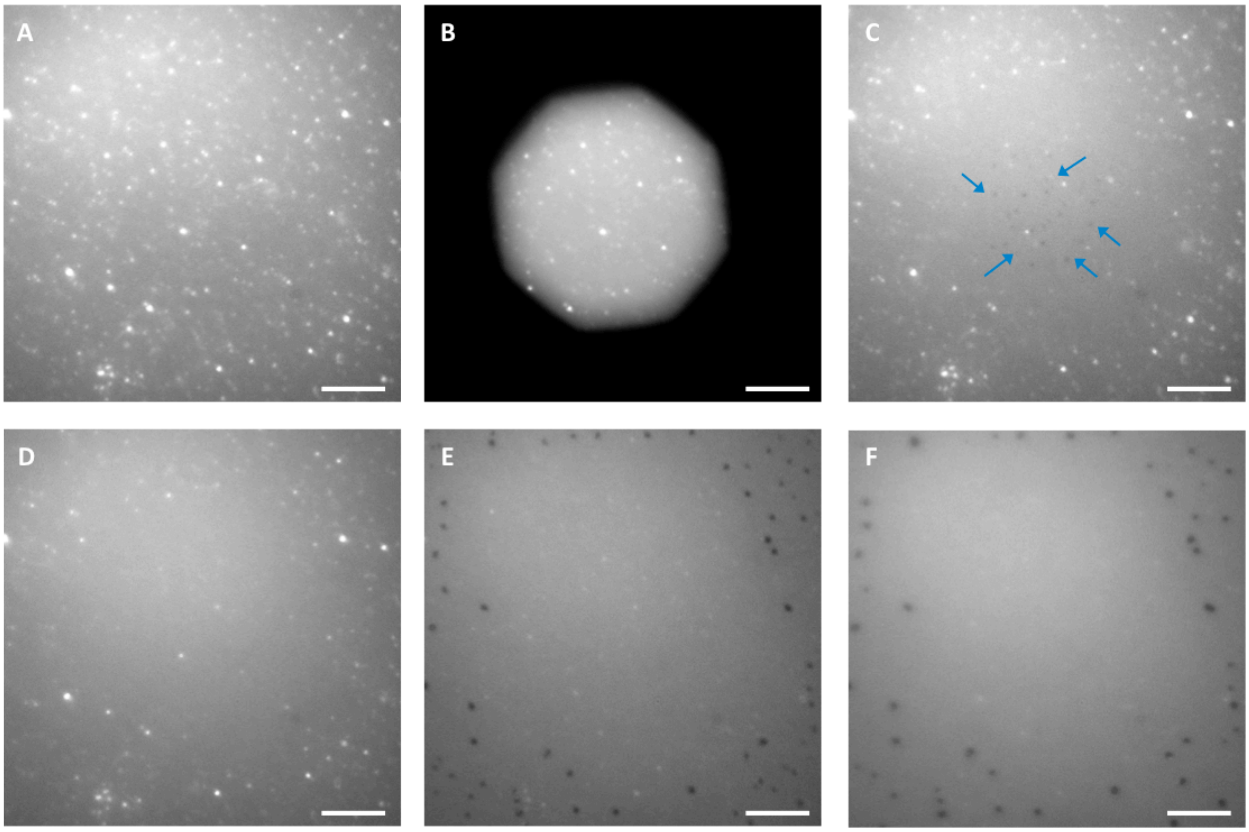

4.3 Discussion: Incorporation and Photorelease of Caged Ceramides in Supported Bilayers

Previous studies have thoroughly characterized the morphology of supported bilayers consisting of DOPC/ESM/Chol by both fluorescence and AFM.[37-38, 46] Our results show that incorporating 5 to 10 mol% caged C16-Cer **13** in SUVs of this ternary mixture, and depositing them onto mica in the presence of calcium produces bilayers that are morphologically very similar. Supported bilayers of DOPC/ESM/Chol in molar ratios of 2/2/1 (Figure 4-19) and

DOPC/ESM/Chol/**13** in ratios of 8/7/4/1 (Figure 4-15) both show L_o and L_d phase coexistence. The dye-excluded domains formed in the two lipid mixtures are comparable in size, shape and surface area coverage. AFM images indicate that the dye-excluded features are 1-1.2 nm taller than the surrounding $DiIC_{20}$-brightened phase (Figure 4-16 A), and thus confirm the assignment of the dark domains as an ESM/Chol-enriched L_o phase.[46] The observed fluorescence of **13** shows that caged C16-Cer successfully incorporates into the membrane (Figure 4-15 B). Furthermore, the inverted contrast of the coumarin fluorescence image with respect to the $DiIC_{20}$ suggests that the caged analog preferentially partitions into the L_o phase. Increasing the amount of **13** in the lipid mixture to 10 mol% (Figure 4-20), or replacing **13** with 5 mol % **16** (Figure 4-21) or **9** (Figure 4-22), did not markedly change the appearance of the supported bilayers.

Generating small amounts of Cer in L_o domains by photo-uncaging **13** leads to a progressive decrease in domain size, and in some cases to complete dissolution (Figure 4-18). Correlated fluorescence and AFM experiments show that small bright pockets form and expand in some of the L_o domains in the minutes following UV irradiation (Fig 4-16 B-D). The fluorescence intensity and heights of these features are comparable to those of the bulk L_d phase. Qualitatively similar results are achieved upon photorelease of **16** and **9** in these phase separated bilayers (Figures 4-21 and 4-22 respectively).

At the examined incorporation level of **13** (5 to 10 mol%), de novo C16-Cer does not form Cer-rich domains, suggesting that a local Cer concentration threshold may be required for gel-like domains to form. Consistent with this, Cer-enriched domains have been reported in DOPC/ESM/Chol bilayers that contain >8 mol% Cer.[36, 38] However, the modest degree of

reorganization observed is in stark contrast with the dynamic formation and dissolution of domains seen in bilayers of POPC/**13** upon UV irradiation (Figure 4-27). The lateral diffusion rates of **13** and C16-Cer in a lipid bilayer are expected to faster in a POPC- or DOPC-rich L_d phase than in an L_o phase rich in ESM and Chol.[51] Fluorescence images of the phase-separated bilayers acquired in the coumarin channel (Figure 4-15) show bright L_o domains, indicating that **13** is probably enriched in this phase. Therefore, the extent of membrane restructuring in these bilayers may be limited by the slower diffusion of C16-Cer in the L_o phase. Micron-scale lateral reorganization may occur on a much longer timescale than in POPC bilayers, as is discussed in more detail below.

It is also possible that bilayers of DOPC/ESM/Chol, in which Cer is generated by photo-uncaging from **13**, do not attain the equilibrium lipid organization produced when Cer is incorporated in vesicles prior to forming supported bilayers. Studies of enzymatic Cer generation in vesicles of a similar ternary lipid mixture have shown that the formation of Cer-enriched domains is sensitive to the amount of Chol; at high Chol content domains are hypothesized to be replaced by a Chol-enriched L_o phase.[52] In the case of supported bilayers, insertion of hydrophobic domains of SMase and translocation of the bound enzyme may contribute significantly to Cer-mediated membrane restructuring by perturbing lipid packing and inducing local disorder.

A ternary POPC/Chol/C16-Cer phase diagram derived from fluorescence measurements in GUVs shows that, in the absence of cholesterol, liquid and solid phase coexistence occurs for as little as 5 mol% Cer.[48] Our fluorescence and AFM experiments in supported bilayers prepared from mixtures of POPC/C16-Cer in 9/1 molar ratios are consistent with this as they exhibit

micron-scale Cer-rich domains (Figure 4-25). The T_m of C16-Cer (90 °C)[53] and the height of these features above the POPC-enriched bulk membrane suggest that they exist in a solid-ordered state (L_β). We can induce similar liquid-solid phase coexistence in bilayers of POPC/**13** upon photorelease of C16-Cer with a high degree of spatial control (Figures 4-27 and 4-29). These supported bilayers are initially homogeneous by both AFM and fluorescence (Figure 4-28); moreover, the ordered domains only appear following UV irradiation. Taken together these observations suggest that the membrane-packing properties of **13** are significantly different to those of free C16-Cer. The Bhc photolabile protecting group that blocks the primary alcohol of C16-Cer in **13** probably prevents the tight packing of Cer molecules that characterizes the L_β phase.

When the entire area of a POPC/**13** bilayer is UV irradiated so as to generate Cer throughout the sample the domains that form are persistent and stable under our AFM imaging conditions (Figure 4-32). In light of existing phase diagram data,[47-48] this L_d and L_β phase coexistence suggests that at least 5 mol% caged C16-Cer is incorporated and photochemically released in these supported membranes. However, when small amounts of C16-Cer are locally generated in bilayers of POPC/**13**, the concentration of Cer is above the threshold for formation of L_β domains in a small area, but not in the bulk membrane. Therefore, the dye-excluded domains are not stable, and disappear within minutes (Fig. 4-27 C, D). This rapid dissolution of Cer-rich domains is consistent with the fast re-equilibration and large diffusion coefficient[51] expected for a liquid-disordered membrane. Developing a more thorough understanding of this domain-forming behavior offers scope for further experiments, but certain aspects of the results presented here merit further discussion.

Some of the domains that form in the irradiated area are conserved over several cycles of formation and disappearance, in what could be termed a “memory” effect in the membrane (Figure 4-27 C-F). Nanoscale clusters of Cer molecules may persist at the locus of each domain, or lipid pinning may occur, and form nucleation sites for the regrowth of features that are large enough to be resolved using conventional fluorescence microscopy. Furthermore, photo-uncaging of **13** in the region of interest is probably creating a Cer concentration gradient in the membrane, as the lipid diffuses away from its site of origin. Repeated irradiations in a small area will impact this equilibration process by adding to the existing pool of Cer. This may explain why the pattern of domains produced by the fourth photolysis (Figure 4-27 F) is more than 40 μm in diameter, and so significantly larger than those formed by the first and second irradiations which are roughly the size of the iris (Figure 4-27 C, E). The same sample was also imaged by correlated AFM and fluorescence following the fourth irradiation cycle (Figure 4-29). Note that in this area, which had been irradiated several times, the Cer-rich domains took longer to disappear in spite of the scanning action of the AFM. The size of the pattern of domains formed in a region of interest is directly related to irradiation time (Figure 4-30). Moreover, the domain patterns show a radial increase in size, which is consistent with the diffusion of Cer away from the area defined by the iris. The time required for the patterns to disappear is also proportional to their size (Figure 4-31), and therefore also to the irradiation time and the amount of Cer that is produced. Together, these experiments provide evidence for the presence of a Cer concentration gradient that responds to the quantity of **13** generated in the region of interest.

Lateral reorganization in bilayers of DOPC/ESM/Chol/**13** after photo-uncaging of C16-Cer from **13** is distinct from both enzymatic Cer generation in supported membranes,[37, 46] and photochemical generation of Cer in the binary mixture of POPC and **13** also examined in this investigation. Specifically, formation of L_β domains is not observed in bilayers of the quaternary lipid mixture, nor do domains dissolve as rapidly or to the same extent. As we propose above, the interaction of SMase with the supported bilayers may increase both the extent and rate at which Cer-mediated micron-scale structural changes occur. Enzymatic remodelling may also proceed more rapidly, and have more extensive morphological effects, by virtue of being able to generate in excess of 5 or 10 mol% Cer. It is nonetheless reasonable, however, to anticipate differences in the level of membrane restructuring observed following photorelease of 5 mol% Cer as compared to 10 mol%. Under our experimental conditions photorelease from **13** in lipid membranes should proceed readily (Figures 4-13 and 4-14); the appearance of Cer-rich domains in bilayers of POPC/**13** following even brief UV exposures supports this assertion.

Our photo-uncaging experiments in bilayers of DOPC/ESM/Chol/**13** were done using significantly longer irradiation times than for the POPC/**13** mixture because we did not observe any changes with shorter UV exposure. The current results suggest that modest restructuring in bilayers of DOPC/ESM/Chol/**13** may in part arise from slower diffusion of lipid molecules in these membranes. However, further experiments are needed to distinguish between the effects of longer irradiation and slower lateral diffusion in the former case. Any effects of restricted diffusion could be amplified if **13** were enriched in the L_o fraction, as it appears to be (Figure 4-15). Also, the ordering effect of cholesterol in the L_d DOPC-rich phase could be a contributing factor. The difficulty we encountered in incorporating higher levels (> 10 mol%) of

13 into supported bilayers points towards an additional consideration, however: the mole fraction of **13** present in the lipid film from which the SUVs are prepared may not be the same as that found in the bilayer formed on the mica support.

Recent studies by Stamou and coworkers suggest that within a given lipid preparation, variations of up to an order of magnitude can be seen in the relative composition (lipid ratio) of individual liposomes.[54-55] Furthermore, smaller liposomes such as SUVs are subject to a greater degree of inhomogeneity (DI) than larger assemblies, GUVs among them. These observations hold true for a variety of lipid compositions and methods of liposome preparation. SUVs made from the mixtures of DOPC/ESM/Chol/**13** we have used here may be more prone to manifesting this degree of heterogeneity than SUVs of POPC/**13**, simply by virtue of containing a greater number of distinct lipid species. Stamou et al also postulate that a compositionally diverse vesicle population should exhibit a broad range of physicochemical properties; this could extend to the kinetics of vesicle rupturing inherent to the process of forming a supported membrane with a well-defined chemical composition.[56] Supported bilayers formed from SUVs of DOPC/ESM/Chol present reproducible morphological features such as the height and area coverage of L_o domains indicative of only a small degree of compositional variation within and among samples. This apparent lipid homogeneity on the mica surface may not extend to the incorporation of caged C16-Cer into the supported membrane. The Bhc moiety on **13** is deprotonated to a significant extent in the aqueous solutions we used to form our SUVs and supported bilayers (Figure 4-13 A). If the SUVs have net negative surface charge, they will experience electrostatic repulsion from the mica substrate. This could lead to a lower concentration of **13** in the supported membrane than concentration of **13** found in the SUVs in

solution. Increasing the loading of Bhc-caged Cer in the vesicles could increase this concentration difference further, particularly if at equilibrium only 5 or 10 mol% of **13** incorporates into the supported bilayer.

Supported bilayers formed from mixtures containing more than 10 mol% **13**, or prepared using more than 25 μg of lipid for mixtures containing 10 mol% or less, were typically extensively covered with adsorbed vesicles (Figure 4-38 A). Calcium chloride was used in sample incubation to promote in deposition of SUVs on mica in order to form supported bilayers more efficiently. Addition of calcium may have increased the number of adsorbed vesicles by masking some of electrostatic repulsion between the phenolate form of **13** and mica; and also directly promote vesicle adhesion by providing coordination sites for phenolates in SUVs and in the supported bilayer. While the bulk of the adsorbed vesicles resisted removal by washing, they largely disappeared following brief UV irradiation. Photo-uncaging of Cer from **13** in these vesicles could have promoted desorption by altering their net surface charge. Work done by Baigl and colleagues with a photosensitive surfactant presents an alternative avenue for discussion: conformational switching of AzoTAB causes GUVs composed of DOPC/DPPC/Chol to burst by reducing the fluidity of the vesicular membranes.[57] The ability of Cer to significantly increase membrane order and form crystalline phases in lipid membranes is well documented. It seems reasonable, therefore, to propose that photochemical Cer generation could de-stabilize the adsorbed vesicles and cause them to rupture and deposit or exchange lipids with the underlying supported bilayer. Figure 4-38 D-E provides a further indication that adsorbed vesicles may exhibit this behavior following photorelease of **13**- namely the formation of Cer-rich domains in the supported membrane concomitant with the disappearance of overlying

vesicles. Significantly, no domains are observed in an adjacent region of the membrane that had been cleared of vesicles in an earlier photolysis (Figure 4-38 B-C).

To date several light-responsive systems have been proposed as triggers to regulate efflux from vesicular or liposomal delivery vehicles.[57-58] Chemical formation of Cer in a lipid bilayer has also been used to drive spontaneous membrane fusion.[59] Photolysis of caged Cer represents an entry point for two plausible mechanisms of controlled release of small molecules encapsulated in vesicles. The first pathway relies on decreasing membrane fluidity to induce vesicle rupturing as outlined above. An alternative or complementary process of increasing membrane permeability following Cer generation, and possible formation of Cer channels can also be envisioned.[60-62]

Parallel fluorescence and atomic force imaging has been used to show that GM1-bound Ctx-B is highly concentrated in Cer-rich domains present in supported model membranes of DOPC/C18-SM/Chol and C18-Cer.[42, 63] The partitioning of GM1 into Cer domains may be favored by increased saturated acyl chain Van der Waals interactions or hydrogen-bond formation between the sphingosine backbones of GM1 and Cer. We first show that introducing 1 mol% GM1 into bilayers of POPC/**13** in 9/1 molar ratios does not change their morphology as assessed by fluorescence microscopy prior to or following photochemical generation of C16-Cer (Figure 4-33). Labelling experiments with Alexa 488 Ctx-B or Alexa 647 Ctx-B after Cer-rich domains have been generated subsequently confirm that GM1 concentrates in these features (Figures 4-34 and 4-35). When a bilayer of POPC/**13** containing GM1-bound Ctx-B is exposed to UV irradiation Cer/GM1 domains form, albeit on a longer timescale than in the absence of Ctx-B (Figures 4-36 and 4-37). Small clusters of GM1 and Ctx-B may already be present in the

membrane, and may increase the overall membrane order. Therefore, slower formation of domains could be due to reduced lateral mobility in the membrane because of these glycolipid-protein aggregates. To put this in context, the following two-component diffusion coefficient has been reported for a fluorescently labelled GM1 in a fluid membrane of DOPC: D_{fast} 3.62 ± 0.77 x 10^{-8} cm^2/s and D_{slow} 0.29 ± 0.13 x 10^{-8} cm^2/s. Bound to Ctx-B these values drop to 0.68 ± 0.15 x 10^{-8} cm^2/s and 0.04 ± 0.01 x 10^{-8} cm^2/s respectively in DOPC.[56] The induced clustering of GM1 demonstrates that photo-uncaging of C16-Cer from **13** can be used to induce lateral segregation in a membrane, and trigger the concentration of a particular lipid species in discrete, highly-ordered domains. This process can be conducted with a degree of spatial and temporal control that cannot be achieved enzymatically.

4.4 Summary of Findings, Significance, and Future Outlook

We characterized the spectroscopic properties of Bhc-caged ceramides **9**, **13** and **16** in buffered aqueous solutions and in SUVs. An HPLC method for separating and quantifying the products of Bhc-caged Cer phototolysis was also developed. We confirmed that UV irradiation of the compounds results in time-dependent release of Cer and the fluorescent by product **4**. Subsequently, this protocol was used to monitor photo-uncaging of the test compounds under several sets of reaction conditions.

The Bhc-caged ceramides were incorporated into supported bilayers of DOPC/ESM/Chol and POPC respectively. We characterized the morphology of these model membranes using a combination of AFM and fluorescence microscopy. Our results in the first lipid mixture showed that at 5 or 10 mol% the Bhc-caged compounds did not change its morphology, and were qualitatively enriched in the “raft-like” L_O domains. Photo-uncaging the caged compounds to

generate Cer in these membranes partially dissolved the domains in the irradiated area. At 10 mol% C16-Cer forms L_β domains in POPC bilayers. In contrast, **13** did not phase-separate in this mixture at a similar loading indicating that the Bhc cage alters the packing properties of the lipid with respect to C16-Cer. Irradiating small regions of POPC/**13** bilayers to generate C16-Cer formed L_β domains that disappeared within minutes as the membranes re-equilibrated. The area coverage and "lifetime" of these domains were directly proportional to the amount of Cer generated, and provided evidence for the existence of a concentration gradient that dispersed the newly generated Cer away from its point of origin.

Supported bilayers of POPC/**13**/G_{M1} were used to show that light-induced membrane compartmentalization of GM1-bound Ctx-B could be achieved upon photorelease of **13**. We propose that a range of raft-associated lipid-anchored proteins could respond in a similar way and concentrate in photochemically generated Cer domains. Further investigations are required to explore the full scope of Bhc-caged ceramides' properties, but they hold promise as tools for characterizing and modulating membrane protein activity. Membrane-based biosensors could also be designed around its demonstrated ability to induce localized, transient and reproducible lateral compartmentalization. Bhc-caged ceramides also represent a potentially useful vehicle for studying ceramide's signalling and cell-cycle regulatory roles *in vivo*.

4.5 Experimental

4.5.1 Chemicals

1,2-Dioleoyl-*sn*-glycero-3-phosphocholine (DOPC), 1-palmitoyl-2-oleoyl-*sn*-glycero-3-phosphocholine (POPC), egg sphingomyelin (ESM), *N*-palmitoyl-*D*-*erythro*-sphingosine (C16:0 ceramide, C16-Cer), and cholesterol were purchased from Avanti Polar Lipids (Alabaster, AL)

and used without further purification. 1,1'-Dieicosanyl-3,3,3',3'-tetramethylindocarbocyanine perchlorate (DiI-C_{20}) was purchased from Molecular Targeting Technologies (Westchester, PA). 7-(Diethylamino)-4-methyl-*2H*-1-benzopyran-2-one (Coumarin 460) and 2,3,6,7-tetrahydro-9-methyl-*1H,5H*-quinolizino(9,1-*gh*)coumarin (Coumarin 480) were obtained from Exciton (Dayton, OH). Recombinant Cholera toxin subunit B conjugated to Alexa Fluor 488 was acquired from Molecular Probes (Eugene, OR). (2*S*,3*R*,4*E*)-2-Butyramido-3-hydroxyoctadec-4-enyl (6-bromo-7-hydroxycoumarin-4-yl)methyl carbonate (caged C4-Cer, **9**), (2*S*,3*R*,4*E*)-2-palmitoylamido-3-hydroxyoctadec-4-enyl (6-bromo-7-hydroxycoumarin-4-yl)methyl carbonate (caged C16-Cer, **13**), and (2*S*,3*R*,4*E*)-2-palmitoylamido-3-hydroxyoctadecyl (6-bromo-7-hydroxycoumarin-4-yl)methyl carbonate (caged C16-dihydroCer, **16**) were synthesized by our collaborators as described previously.[11] Reversed-phase HPLC was used to monitor aliquots of the caged lipids for degradation, and to purify them as required. Optical adhesive 88 was obtained from Norland Products (Cranbury, NJ) and used to glue mica onto cover glass (Fisher Scientific, Hampton, NH). All aqueous solutions were prepared using 18.3 MΩ cm *Milli-Q* water. KMops buffer (100 mM KCl, 10 mM 3-(N-morpholino)-propanesulfonate (Mops), pH 7.4) was used for some imaging and photolysis experiments; and CTx-B buffer (8mM Na_2HPO_4, 20mM NaCl, 2mM NaN_3, pH 7.4) was used for Cholera toxin subunit B labeling experiments. All buffered solutions were passed through a 0.22 μm filter (Millipore, Billerica, MA) before being used. All organic solvents used were HPLC grade from EMD Chemicals (Philadelphia, PA).

4.5.2 Absorption and Fluorescence Spectroscopy

Absorption spectra were measured with a Cary 5000 UV-vis-NIR spectrophotometer. Emission spectra were recorded using a Horiba Jobin Yvon FL-3 21 2tau spectrofluorometer

with slit widths of 1 nm. All spectral measurements were performed at 22 °C using a 1-cm pathlength quartz cuvette. Fluorescence quantum yields were calculated with reference to Coumarin 460 in ethanol (Φ_{fl} = 0.59)[28] at an excitation wavelength of 374 nm and absorbance ≤ 0.1. Working solutions of the compounds were prepared at 5-10 μM to match the absorbance of 5 μM Coumarin 460 at 374 nm.

4.5.3 Photolysis and Photoproduct Analysis

Photolysis was performed in a quartz cuvette containing 3 mL of 5 μM caged substrate in 10 mM KMops buffer containing 100 mM KCl (pH 7.4) with 50% ethanol. The sample was irradiated at 350 nm in a Rayonet photochemical reactor (Southern New England Ultraviolet Co., Branford, CT, USA) equipped with four lamps. Aliquots of 20 μL were removed periodically for analysis. Coumarin 480 (5 μl at 5 μM) was added to each aliquot as an internal standard. Loss of starting material and formation of by-product **4** were monitored by reversed-phase HPLC with a SunFire C18 column (Waters Corp., Milford, MA, USA), and eluted with an ethanol/water gradient (75% ethanol increasing to 95% over 3 min) at a flow rate of 0.8 mL/min. Detection was by absorbance at 325 nm and fluorescence at 480 nm. Preparative HPLC with an ethanol/water mixture (95% ethanol) was used to separate hydrolyzed **4** from the Bhc-caged ceramides in the aliquots used to prepare lipid films for bilayer experiments.

4.5.4 Supported Lipid Bilayers

Small unilamellar vesicles (SUVs) were prepared as previously described in chapter 2 subject to some minor modifications. Lipids, caged C16-Cer, and fluorescent DiI-C_{20} were dissolved in chloroform, methanol, ethanol, or mixtures thereof as required. After these organic solutions were mixed in appropriate amounts, the organic solvents were evaporated. The resulting dry

lipid films were hydrated in *Milli-Q* water and then sonicated at 60 °C in a bath sonicator to clarity to form SUVs with a final lipid concentration of 0.5 mg/mL. Lipid films were stored for up to 1 week at -20 °C prior to use; however, fresh vesicles were prepared on the day of each imaging experiment.

Planar supported bilayers were formed on mica via vesicle fusion. Freshly cleaved mica disks (15-25 μm thick for fluorescence imaging) were glued onto circular cover glasses. To prepare bilayers of DOPC/ESM/Chol/caged-Cer 950 μL of 8 mM $CaCl_2$ was first added to a mica/glass slide clamped in a liquid cell, and warmed to 45 °C. 20-50 μL of vesicle suspension was then introduced at the same temperature, and the samples were incubated for 15 min before being gradually cooled to 22 °C over a period of 2 h. Supported bilayers of POPC/caged C16-Cer and POPC/C16-Cer were similarly prepared by following a shortened 1h incubation at room temperature. Bilayers were gently washed with *Milli-Q* water or buffer to remove adsorbed vesicles before imaging.

4.5.5 Fluorescence Microscopy and Correlated Fluorescence-Atomic Force Microscopy

Fluorescence imaging and correlated fluorescence-atomic force microscopy were both performed on the same experimental apparatus at room temperature (~22 °C). The imaging system consisted of a NanoWizard II BioAFM (JPK Instruments, Berlin, Germany) integrated with an IX81 inverted optical microscope (Olympus Corporation, Tokyo, Japan). Epifluorescence images were obtained using lamp excitation with an Olympus UPlanSAPO 100x, NA = 1.4 oil immersion objective, Cy3, DAPI and FITC WF filter sets (Chroma Technology, Bellows Falls, VT), and a high resolution CoolSNAP CCD camera (Photometrics, Tucson, AZ). Each fluorescence image was background corrected by subtracting a minimum intensity value obtained from an

area of the field of view masked by the closed iris on the microscope. The images were then scaled, cropped, and correlated with the corresponding AFM scans. This series of operations was performed using Image J freeware (NIH, Bethesda, MD).

Caged Cer photolysis experiments were carried out on the same setup using the lamp and DAPI filter set. For most experiments the iris built into the microscope illuminator was used to confine UV irradiation of the sample during caged C16-Cer photolysis to a hexagonal area ~25 μm in diameter. Irradiations of the entire bilayer were done using a small UV lamp (365 nm) positioned directly under the sample. To assess uncaging ability, we irradiated an aqueous dispersion of caged C4-Cer **9** for several minutes on the fluorescence microscope. Post-UV HPLC analysis of the solution confirmed that photolysis of the caged lipid had taken place to afford C4-Cer and 6-bromo-7-hydroxycoumarin **4** (Figure 4-9). A RISE summer student, Spencer P. Pitre, performed some of the SLB imaging and photolysis experiments that have been included in this chapter. His contribution has been acknowledged in the appropriate figure captions.

AFM images were captured using uncoated silicon nitride DNP-S-10 (Veeco, Camarillo, CA) AFM cantilevers with a typical spring constant of 0.12 N/m. Contact mode topographic images were collected at scan rates of 0.7-1 Hz, and continuous adjustments to the set point kept the force exerted on the sample at a minimum. Scans were collected at 512 x 512 pixel resolution and were line fitted with first- to third-order polynomials when necessary.

Solid-supported bilayers of the desired composition were prepared, and fluorescence and AFM images of the same sample area were acquired sequentially after first assessing sample homogeneity over several areas by fluorescence. The sample was irradiated briefly (typically 5-60 sec) and fluorescence and/or AFM images were used to monitor changes in the bilayer.

Typically fluorescence images were acquired before and after AFM scans of the same area to check for changes in membrane morphology occurring during or due to scanning.

4.6 References

1. Mayer, G.; Heckel, A., Biologically active molecules with a "light switch". *Angew. Chem. Int. Ed.* **2006,** *45*, 4900-4921.

2. Ellis-Davies, G. C., Caged compounds: photorelease technology for control of cellular chemistry and physiology. *Nat. Methods* **2007,** *4*, 619-628.

3. Young, D. D.; Deiters, A., Photochemical control of biological processes. *Org. Biomol. Chem.* **2007,** *5*, 999-1005.

4. Lee, H.; Larson, D. R.; Lawrence, D. S., Illuminating the chemistry of life: design, synthesis and applications of "caged" and related photoresponsive compounds. *ACS Chem. Biol.* **2009,** *4*, 409-427.

5. Yu, H.; Li, J.; Wu, D.; Qiu, Z.; Zhang, Y., Chemistry and biological applications of photo-labile organic molecules. *Chem. Soc. Rev.* **2010,** *39*, 464-473.

6. Kaplan, J. H.; Forbush, B.; Hoffman, J. F., Rapid photolytic release of adenosine 5'-triphosphate from a protected analog: utilization by the sodium:potassium pump of human red blood cell ghosts. *Biochemistry* **1978,** *17*, 1929-1935.

7. Loudwig, S.; Bayley, H., In *Dynamic studies in biology: phototriggers, photoswitches and caged biomolecules*, Goeldner, M.; Givens, R., Eds. Wiley-VCH: Weinheim, 2005; pp 253-339.

8. Pirrung, M. C.; Rana, V. S., In *Dynamic studies in biology: phototriggers, photoswitches and caged molecules*, Goeldner, M.; Givens, R., Eds. Wiley-VCH: Weinheim, 2005; pp 341-365.

9. Givens, R.; Kotala, M. B.; Lee, J., In *Dynamic studies in biology: phototriggers, photoswitches and caged biomolecules*, Goeldner, M.; Givens, R., Eds. Wiley-VCH: Weinheim, 2005; pp 95-125.

10. Givens, R., *Dynamic studies in biology: phototriggers, photoswitches and caged biomolecules*. Wiley-VCH: Weinheim, 2005.

11. Kim, Y. A.; Carter Ramirez, D. M.; Costain, W. J.; Johnston, L. J.; Bittman, R., A new tool to assess ceramide bioactivity: 6-bromo-7-hydroxycoumarinyl-caged ceramide. *Chem. Commun.* **2011,** *47*, 9236-9238.

12. Turro, N. J.; Ramamurthy, V.; Scaiano, J. C., *Modern molecular photochemistry of organic molecules*. University Science Books: Sausalito, CA, 2010.

13. Furuta, T., In *Dynamic studies in biology: phototriggers, photoswitches and caged biomolecules*, Goeldner, M.; Givens, R., Eds. Wiley-VCH: Weinheim, 2005; pp 29-54.

14. Schmidt, R.; Giessler, D.; Hagen, V.; Bendig, J., Mechanism of photocleavage of (coumarin-4-yl)methyl esters. *J. Phys. Chem. A* **2007,** *111*, 5768-5774.

15. Suzuki, A. Z.; Watanabe, T.; Kawamoto, M.; Nishiyama, K.; Yamashita, H.; Ishii, M.; Iwamura, M.; Furuta, T., Coumarin-4-ylmethoxycarbonyls as phototriggers for alcohols and phenols. *Org. Lett.* **2003,** *5*, 4867-4870.

16. Furuta, T.; Wang, S. S. H.; Dantzker, J. L.; Dore, T. M.; Bybee, W. J.; Callaway, E. M.; Denk, W.; Tsien, R. Y., Brominated 7-hydroxycoumarin-4-ylmethyls: photolabile protecting groups with biologically useful cross-sections for two photon photolysis. *Proc. Natl. Acad. Sci. USA* **1999,** *96*, 1193-1200.

17. Mentel, M.; Laketa, V.; Subramanian, D.; Gillandt, H.; Schultz, C., Photoactivatable and cell-membrane-permeable phosphatidylinositol 3,4,5-triphosphate. *Angew. Chem. Int. Ed.* **2011,** *50*, 3811-3814.

18. Subramanian, D.; Laketa, V.; Muller, R.; Tischer, C.; Zarbakhsh, S.; Pepperkok, R.; Schultz, C., Activation of membrane-permeant caged PtdIns(3)P induces endosomal fusion in cells. *Nat. Chem. Biol.* **2010,** *6*, 324-326.

19. Lankalapalli, R. S.; Ouro, A.; Arana, L.; Gomez-Munoz, A.; Bittman, R., Caged ceramide 1-phosphate analogues: synthesis and properties. *J. Org. Chem.* **2009,** *74*, 8844-8847.

20. Qiao, L.; Kozikowski, A. P.; Olivera, A.; Spiegel, S., Synthesis and evaluation of a photolyzable derivative of sphingosine 1-phosphate- caged spp. *Bioorg. Med. Chem. Lett.* **1998,** *8*, 711-714.

21. Scott, R. H.; Pollock, J.; Ayar, A.; Thatcher, N. M.; Zehavi, U., Synthesis and used of caged sphingolipids. *Methods Enzymol.* **2000,** *312*, 387-400.

22. Zehavi, U., Synthesis of potentially caged sphingolipids, possible precursors of cellular modulators and second messengers. *Chem. Phys. Lipids* **1997,** *90*, 55-61.

23. Tuchinsky, A.; Zehavi, U., Chemoenzymatic synthesis of potentially caged glycosphingolipids (GSLs): potentially caged *lyso*-G_{M3} and its analogue. *Chem. Phys. Lipids* **1998,** *92*, 91-97.

24. Shigenaga, A.; Hirakawa, H.; Yamamoto, J.; Ogura, K.; Denda, M.; Yamaguchi, K.; Tsuji, D.; Itoh, K.; Otaka, A., Design and synthesis of caged ceramide: UV-responsive ceramide releasing system based on UV-induced amide bond cleavage followed by O-N acyl transfer. *Tetrahedron* **2011,** *67*, 3984-3990.

25. Goeldner, M., In *Dynamic studies in biology: phototriggers, photoswitches and caged biomolecules*, Goeldner, M.; Givens, R., Eds. Wiley-VHC: Weinheim, 2005; pp 76-92.

26. Karimi, B.; Zareyee, D., Design of a highly efficient and water-tolerant sulfonic acid nanoreactor based on tunable ordered porous silica for the von Pechmann reaction. *Org. Lett.* **2008,** *10*, 3989-3992.

27. Ramesh, C.; Ravindranath, N.; Das, B., Simple, efficient and selective deprotection of phenolic methoxymethyl ethers using silica-supported sodium hydrogen sulfate as a heterogeneous catalyst. *J. Org. Chem.* **2003,** *68*, 7101-7103.

28. Jones II, G.; Jackson, W. R., Medium effects on fluorescence quantum yields and lifetimes for coumarin laser dyes. *Chem. Phys. Lett.* **1980,** *72*, 391-395.

29. Exciton. Coumarin 480. www.exciton.com/pdfs/c480.pdf.

30. The predominant species in ESM is *N*-palmitoyl-sphingosylphosphorylcholine (86%), see: *Avanti Polar Lipids*, 2011 Catalog, B 91.

31. Johnston, L. J., Nanoscale imaging of domains in supported lipid membranes. *Langmuir* **2007,** *23*, 5886-5895.

32. Lagerholm, B. C.; Weinreb, G. E.; Jacobson, K.; Thompson, N. L., Detecting microdomains in intact cell membranes. *Annu. Rev. Phys. Chem.* **2005,** *56*, 309-36.

33. Veatch, S. L.; Keller, S. L., Seeing spots: complex phase behaviour in simple membranes. *Biochim. Biophys. Acta* **2005,** *1746*, 172-185.

34. London, E., How principles of domain formation in model membranes may explain ambiguities concerning lipid raft formation in cells. *Biochim. Biophys. Acta* **2005,** *1746*, 203-220.

35. Baumgart, T.; Hunt, G.; Farkas, E. R.; Webb, W. W.; Feigenson, G. W., Fluorescence probe partitioning between L_o/L_d phases in lipid membranes. *Biochim. Biophys. Acta* **2007,** *1768*, 2182-2194.

36. Chiantia, S.; Kahya, N.; Schwille, P., Raft domain reorganization driven by short- and long-chain ceramide: a combined AFM and FCS study. *Langmuir* **2007,** *23*, 7659-7665.

37. Carter Ramirez, D. M.; Ogilvie, W. W.; Johnston, L. J., NBD-cholesterol probes to track cholesterol distribution in model membranes. *Biochim. Biophys. Acta* **2010,** *1798*, 558-568.

38. Ira; Johnston, L. J., Ceramide promotes restructuring of model raft membranes. *Langmuir* **2006,** *22*, 11284-11289.

39. Blanchette, C. D.; Lin, W. C.; Orme, C. A.; Ratto, T. V.; Longo, M. L., Using nucleation rates to determine the interfacial line tension of symmetric and asymmetric lipid bilayer domains. *Langmuir* **2007,** *23*, 5875-5877.

40. Blanchette, C. D.; Orme, C. A.; Ratto, T. V.; Longo, M. L., Quantifying growth of symmetric and asymmetric lipid bilayer domains. *Langmuir* **2008,** *24*, 1219-1224.

41. Blanchette, C. D.; Lin, W. C.; Orme, C. A.; Ratto, T. V.; Longo, M. L., Domain nucleation rates and interfacial line tensions in supported bilayers of ternary mixtures containing galactosylceramide. *Biophys. J.* **2008,** *94*, 2691-2697.

42. Chiantia, S.; Ries, J.; Chwastek, G.; Carrer, D.; Li, Z.; Bittman, R.; Schwille, P., Role of ceramide in membrane protein organization investigated by combined AFM and FCS. *Biochim. Biophys. Acta* **2008,** *1778*, 1356-1364.

43. Ira; Johnston, L. J., Sphingomyelinase generation of ceramide promotes clustering of nanoscale domains in supported bilayer membranes. *Biochim. Biophys. Acta* **2008,** *1778*, 185-197.

44. Fanani, M. L.; Hartel, S.; Maggio, B.; De Tullio, L.; Jara, J.; Olmos, F.; Oliveira, R. G., The action of sphingomyelinase in lipid monolayers as revealed by microscopic image analysis. *Biochim. Biophys. Acta* **2010,** *1798*, 1309-1323.

45. Chao, L.; Gast, A. P.; Hatton, A.; Jensen, K. F., Sphingomyelinase-induced phase transformations: causing morphology switches and multiple-time-domain ceramide generation in model raft membranes. *Langmuir* **2010,** *26*, 344-356.

46. Ira; Zou, S.; Carter Ramirez, D. M.; Vanderlip, S.; Ogilvie, W. W.; Jakubek, Z. J.; Johnston, L. J., Enzymatic generation of ceramide induces membrane restructuring: correlated AFM and fluorescence imaging of supported bilayers. *J. Struct. Biol.* **2009,** *168*, 78-89.

47. Fidorra, M.; Duelund, L.; Leidy, C.; Simonsen, A. C.; Bagatolli, L. A., Absence of fluid-ordered/fluid-disordered phase coexistence in ceramide/POPC mixtures containing cholesterol. *Biophys. J.* **2006,** *90*, 4437-4451.

48. Castro, B. M.; Silva, L. C.; Fedorov, A.; de Almeida, R. F. M.; Prieto, M., Cholesterol-rich fluid membranes solubilize ceramide domains: implications for the structure and dynamics of mammalian intracellular and plasma membranes. *J. Biol. Chem.* **2009,** *284*, 22978-22987.

49. Kenworthy, A. K.; Petranova, N.; Edidin, M., High-resolution FRET microscopy of cholera toxin b-subunit and GPI-anchored proteins in cell plasma membranes. **2000**.

50. Bacia, K.; Schwille, P.; Kurzchalia, T., Sterol structure determines the separation of phases and the curvature of the liquid-ordered phase in model membranes. *Proc. Natl. Acad. Sci. USA* **2005,** *9*, 3272-3277.

51. Ries, J.; Chiantia, S.; Schwille, P., Accurate determination of membrane dynamics with line-scan FCS. *Biophys. J.* **2009,** *96*, 1999-2008.

52. Silva, L. C.; Futerman, A. H.; Prieto, M., Lipid raft composition modulates sphingomyelinase activity and ceramide-induced membrane physical alterations. *Biophys. J.* **2009,** *96*, 3210-3222.

53. Shah, J.; Atienza, J. M.; Duclos, J., R.I.; Rawlings, A. V.; Dong, Z.; Shipley, G. G., Structural and thermotropic properties of synthetic C16:0 (palmitoyl) ceramide: effect of hydration. *J. Lipid Res.* **1995,** *36*, 1936-1944.

54. Larsen, J.; Hatzakis, N. S.; Stamou, D., Observation of inhomogeneity in the lipid composition of individual nanoscale liposomes. *J. Am. Chem. Soc.* **2011,** *133*, 10685-10687.

55. Elizondo, E.; Larsen, J.; Hatzakis, N. S.; Cabrera, I.; Bjornholm, T.; Veciana, J.; Stamou, D.; Ventosa, N., Influence of the preparation route on the supramolecular organization of lipids in a vesicular system. *J. Am. Chem. Soc.* **2012,** *134*, 1918-1921.

56. Richter, R. P.; Berat, R.; Brisson, A. R., Formation of solid-supported lipid bilayers: an integrated view. *Langmuir* **2006,** *22*, 3497-3505.

57. Diguet, A.; Yanagisawa, M.; Liu, Y.; Brun, E.; Abadie, S.; Rudiuk, S.; Baigl, D., UV-induced bursting of cell-sized multicomponent lipid vesicles in a photosensitive surfactant solution. *J. Am. Chem. Soc.* **2012,** *134*, 4898-4904.

58. Sebai, S. C.; Milioni, D.; Walrant, A.; Alves, I. D.; Sagan, S.; Huin, C.; Auvray, L.; Massotte, D.; Cribier, S.; Tribet, C., Photocontrol of the translocation of molecules, peptides, and quantum dots through cell and lipid membranes doped with azobenzene copolymers. *Angew. Chem. Int. Ed.* **2012,** *51*, 2132-2136.

59. Kunishima, M.; Tokaji, M.; Matsuoka, K.; Nishida, J.; Kanamori, M.; Hioki, K.; Tani, S., Spontaneous membrane fusion induced by chemical formation of ceramides in a lipid bilayer. *J. Am. Chem. Soc.* **2006,** *128*, 14452-14453.

60. Perera, M. N.; Ganesan, V.; Siskind, L. J.; Szulc, Z. M.; Bielawski, J.; Biewlaska, A.; Bittman, R.; Colombini, M., Ceramide channels: influence of molecular structure on channel formation in membranes. *Biochim. Biophys. Acta* **2012,** *1818*, 1291-1301.

61. Colombini, M., Ceramide channels and their role in mitochondria-mediated apoptosis. *Biochim. Biophys. Acta* **2010,** *1797*, 1239-1244.

62. Siskind, L. J.; Kolesnick, R. N.; Colombini, M., Ceramide channels increase the permeability of the mitochondrial outer membrane to small proteins. *J. Biol. Chem.* **2002,** *277*, 26796-26803.

63. Carrer, D.; Kummer, E.; Chwastek, G.; Chiantia, S.; Schwille, P., Asymmetry determines the effects of natural ceramides on model membranes. *Soft Matter* **2009,** *5*, 3279-3286.

Chapter 5

Closing Remarks and Future Directions

5.1 Closing Remarks

This thesis describes the development and evaluation of a series of photoactive molecules designed to probe Cer-mediated lipid membrane reorganization. Although they are simplified reductionist models, the supported bilayers employed throughout this study are useful tools for interrogating the fundamental lipid-lipid interactions that underpin the lateral segregation or "raft-like" compartmentalization of membranes in more complex biological systems. Notwithstanding, as discussed previously, the enzymatic generation of Cer in these models has been shown to induce changes that are challenging to interpret because they rapidly and radically alter the topology and phase behaviour of the bilayers. In developing fluorescence-based probes for Chol and Cer, we have addressed some of the uncertainty surrounding the lipid composition and organization of the discrete phases observed following Cer generation. Furthermore, with the photochemical release of Cer from Bhc-caged substrates, we have achieved a superior degree of control over the extent and localization of Cer production than was previously possible using SMase.

The NBD-Chol probes presented in chapter 2 examine the hitherto little-explored approach of attaching a chromophore at the hydroxyl group of Chol. A series of probes was prepared to assess the effects of linker length on the molecules' partitioning between coexisting L_d and L_o phases. The probes were designed using a small, polar chromophore and short, hydrophilic linkers in an effort to conserve or replicate the orientation and packing behaviour of 'free' Chol in lipid membranes. Our study identified an NBD-Chol probe with a partitioning coefficient between L_o and L_d phases approaching that of Chol. Furthermore, we demonstrated the

usefulness of this probe for labelling Chol-containing L_o domains, identifying Chol-depleted Cer-rich membrane regions, and tracking the redistribution of Chol in SMase-treated bilayers.

The same water-soluble linker labelling approach was extended to prepare the NBD-Cer probe which was the subject of chapter 3. Supported bilayers with coexisting L_o and L_d phases stained with this probe exhibited a striking inversion of fluorescence contrast between lipid phases upon visualization by epifluorescence or TIRF microscopy. Subsequent pTIRFM experiments determined that this response was due to preferential excitation of probe molecules in the differentially ordered membrane environments upon systematic variation of the excitation light's polarization. Orientational order parameters calculated from pTIRFM images provided an indirect but quantifiable measure of membrane order by reporting on the orientation of the NBD absorption dipoles. P_2 values for L_o and L_d phases determined with NBD-Cer were consistent with those obtained with fluorescent lipids previously used for pTIRFM. Order parameter measurements on bilayers labelled with NBD-Cer and treated with SMase revealed two significant effects: first, a marked increase in the order of the L_d phase consistent with an increase in its Chol content; second, Chol-depleted Cer-rich domains formed following enzyme activity exhibited a higher degree of orientational order than any regions of the membrane prior to Cer generation.

In chapter 4 we have demonstrated the incorporation and photorelease of Bhc-caged Cers in two distinct supported membrane systems. The caging approach confers a previously unachievable degree of spatial and temporal control in the generation of Cer. We have shown that in supported bilayers of a raft mixture with coexisting L_d and L_o phases, the Bhc-caged Cers are moderately enriched in the L_o phase. Photochemically generating small amounts of Cer in

these model membranes results in the partial dissolution of L_o domains in the irradiated areas. In the second model system, photolysis of caged Cer in homogeneous L_d membranes leads to the near-instantaneous formation of Cer-rich gel domains large enough to be visualized by fluorescence microscopy. Localized Cer generation establishes concentration gradients that, coupled with rapid lateral diffusion, lead to the rapid dissolution of the domains as the membranes re-equilibrate. In contrast, irradiation of whole samples to generate Cer throughout the entire membrane affords thermodynamically stable domains. Notably, we also observed that Cer generation in such bilayers doped with GM1 ganglioside the glycolipid preferentially distributed into the Cer-rich domains. In addition, GM1 complexed to Ctx-B also partitioned strongly into the Cer domains indicating that photochemical generation of Cer may be more broadly employed to induce localized clustering of raft-associated lipid-anchored proteins.

5.2 Future Directions

As our work with Cer and SMase has illustrated, even simple bilayer models can exhibit remarkable complexity when we attempt to characterize their composition, morphology and equilibria. These investigations probing the bulk physicochemical properties of membrane lipids and proteins continue to have merit, because as with other types of fundamental research they form the basis for efforts to interpret the behaviour of complex, multivariate systems. As such, I can envision a number of extensions to the supported bilayer work I have presented in this thesis, some of which I will share below.

However, I believe that in the longer term our interests will move away from model membranes as we pursue a broader line of research that places less emphasis on this highly

specialized biophysical niche. I envision a future focus in one of two areas: either furthering knowledge of the structural and regulatory roles of Cer in vivo; or applications based- tailoring our understanding of membrane dynamics and compartmentalization to develop novel liposomal or interfacial sensing and delivery vehicles.

5.2.1 Further Work with NBD Lipids

As discussed in chapter 2 one of our initial objectives was to design a probe that would partition more strongly into the L_o phase than the Texas Red DHPE we routinely used to stain phase-separated bilayers. We assessed partitioning for our novel NBD-Chol probes on the basis of I_{Lo}/I_{Ld} ratios and K_p values where intensities were corrected for the fluorescence quantum yields of NBD in the L_o and L_d phases. As our subsequent pTIRFM work with NBD-Cer indicated, however, differences in probe orientation in the two distinct lipid environments produce fluorescence images of bilayers where I_{Lo}/I_{Ld} shows considerable dependence on the polarization of the excitation light. As such, a more comprehensive determination of K_p could factor in the orientational dependence of fluorescence intensity, particularly when considering a highly ordered and planar supported membrane.

Our series of NBD-Chols with distinct linker lengths also presents an opportunity to systematically optimize the sensitivity of headgroup labelled pTIRFM membrane probes. The pTIRFM measurements conducted with NBD-Cer in chapter 3 suggest that having a fluorophore reporter linked to the headgroup region of a lipid may provide a better measure of changes in membrane order occurring near the aqueous interface than an acyl chain labelled probe. Tuning the length of the spacer between the fluorophore and lipid core could afford probes that sense lipid order at different " membrane depths" or at the interface of bilayers with

varying thickness. There is rich potential to simultaneously record other ambient information that these probes can offer, particularly given NBD's well-documented utility as a polarity and hydration-sensitive reporter. We have made extensive use of a multimodal fluorescence and AFM imaging approach in this body of work, but the use of NBD lends itself to parallelizing several quantitative fluorescence-based methods including pTIRFM, FLIM and ratiometric imaging.

The correlated pTIRFM-AFM experiments with NBD-Cer in chapter 3 suffered from a significant drawback as far as optical resolution was concerned. Following SMase treatment of the supported bilayers certain morphological changes, such as the appearance of Cer-rich fences around the raft-like domains, were discernible by AFM but not readily apparent in the pTIRFM images. These features ranged from several hundred nm to about one μm in diameter and should be discernible using conventional fluorescence microscopy. Efforts are currently underway in our lab to make the order parameter analysis technique used in these experiments compatible with an Olympus 150x TIRFM objective. The 2.5-fold increase in magnification available with this change in the optical setup will give improved pTIRFM lateral resolution. This in turn may allow us to detect and more accurately measure localized differences in the lipid organization of SMase-treated membranes.

5.2.2 Extensions of Caged Ceramide Work

The supported bilayer work I have presented in chapter 4 raises some intriguing questions regarding the formation and disappearance of Cer-containing domains particularly in the POPC/Caged Cer mixture. How do sample-substrate interactions and lateral diffusion rates/mobility impact the formation of Cer-rich domains? Fluorescence recovery after

photobleaching (FRAP) is one technique that could be used to quantify diffusion rates in these membranes and thus assess the effect of increasing Cer content on membrane fluidity. Substrate effects could be evaluated by substituting glass or functionalized surfaces for mica, or by varying pH and ionic strength to decouple the membrane from the support. GUVs or free-standing membranes are other tools that can be used to asses the dynamics of domain formation in the absence of sample-substrate interactions. What domain patterns and kinetics are observed with higher or lower concentrations of caged Cer? We have yet to examine the effects of generating more than 10 mol % Cer in supported membrane models. However, the existing body of work with SMase suggests that some of the more radical membrane reorganization we have previously observed occurs when a larger fraction of SM is converted to Cer. Given the problems we encountered incorporating > 10 mol % Cer into supported bilayers, vesicles may be a better model in which to conduct such a study.

Vesicles and more specifically GUVs are model systems that could also be used to evaluate the use of caged Cer to direct vesicular binding, association/dissociation or fusion events, and to change membrane properties such as permeability. Several applications such as the controlled delivery and release of therapeutic agents or selective, localized surface modification by vesicle deposition could thus eventually be explored.

In collaboration with W. J. Costain of the National Research Council we have recently demonstrated uptake and controlled release of caged Cer in live cells (J774 murine macrophages). This promising result opens the door for future studies examining effects of additive-free long acyl chain Cer delivery. Prior to this these physiologically relevant Cers had to be administered in suspensions containing decane, due to their poor aqueous solubility and

plasma membrane permeability. Consequently, to date, most investigations involving exogenous delivery of Cer have employed synthetic short acyl chain (C2, C4 or C6) Cers. Other coumarin-caged long chain Cers functionalized to improve intracellular delivery are also being made available by R. Bittman from the City University of New York for us to further this work.

5.3 Claims to Original Research

1. The design and preparation of four novel fluorescent probes for Chol are reported. The photophysical properties of these probes were examined in small unilamellar vesicles (SUVs). One of these NBD-Chols was used to identify Cer-rich domains in supported model membranes, and to visualize the Cer-dependent redistribution of Chol in SMase-treated lipid bilayers.
2. A fluorescent probe for Cer, NBD-Cer, was synthesized and characterized spectroscopically in SUVs. Variation in the fluorescence lifetime of this probe reflected differences in the hydration and polarity of the membrane environment. Orientational order parameters were calculated from pTIRFM data obtained using NBD-Cer incorporated in solid supported bilayers. The probe thus provided an indirect, quantitative measure of lipid packing/order in phase-separated lipid membranes. Changes in order parameter recorded following SMase-treatment of these bilayers reported on localized Cer- and Chol-dependent increases in membrane order.
3. Photorelease of Bhc-caged Cers was successfully demonstrated in buffered aqueous solution, and in SUVs. Analytical HPLC and LC/MS methods were developed to characterize the photoproducts in these systems. Caged Cers were also incorporated

into supported lipid bilayers and uncaged using a fluorescence microscope to induce morphological changes with a high degree of spatial and temporal control. Raft-associated lipid-protein complexes of GM1 ganglioside and Ctx-B were shown to preferentially partition into photochemically generated Cer-rich membrane domains.

5.4 Publications

5.4.1 Published

Kim, Y.A.; **Carter Ramirez, D.M.**; Costain, W.J.; Johnston, L.J.; Bittman, R.; A new to assess ceramide bioactivity: 6-bromo-7-hydroxycoumarinyl-caged ceramide. *Chem. Commun.* **2011**, *47*, 9236-9238

Carter Ramirez, D.M.; Ding, J.; Guan, J.; Vobornik, D.; Carnini, A.; Ogilvie, W.W.; Jakubek, Z.J.; Johnston, L.J., A Forster resonance energy transfer (FRET) approach for enhancing fluorescence contrast in phase-separated membranes. *Can. J. Chem.* **2011,** *89*, 423-432.

Carter Ramirez, D.M.; Ogilvie, W.W.; Johnston, L.J., NBD-cholesterol probes to track cholesterol distribution in model membranes. *Biochim. Biophys. Acta* **2010,** *1798*, 558-568.

Ira; Zou, S.; **Carter Ramirez, D.M.**; Vanderlip, S.; Ogilvie, W.W.; Jakubek, Z.J.; Johnston, L.J., Enzymatic generation of ceramide induces membrane restructuring: correlated AFM and fluorescence imaging of supported bilayers. *J. Struct. Biol.* **2009,** *168*, 78-89.

5.4.2 Submitted or in Preparation

Carter Ramirez, D.M.; Jakubek, Z.J.; Lu, Z.; Ogilvie, W.W.; Johnston, L.J., A new probe to measure changes in orientational order associated with ceramide-mediated membrane reorganization. *In preparation*.

Carter Ramirez, D.M.; Kim, Y.A.; Bittman, R.; Johnston, L.J. Lipid phase separation and protein-ganglioside clustering in supported bilayers induced by photorelease of ceramide. *Manuscript submitted.*

Carter Ramirez, D.M.; Pitre, S.P.; Kim, Y.A.; Bittman, R.; Johnston, L.J. Photo-uncaging of ceramide in supported lipid bilayers introduces lateral membrane reorganization. *Manuscript submitted.*

Appendix

NMR Spectra of Novel Reported Compounds

Chapter 2 – ^{1}H, ^{13}C and DEPT Spectra

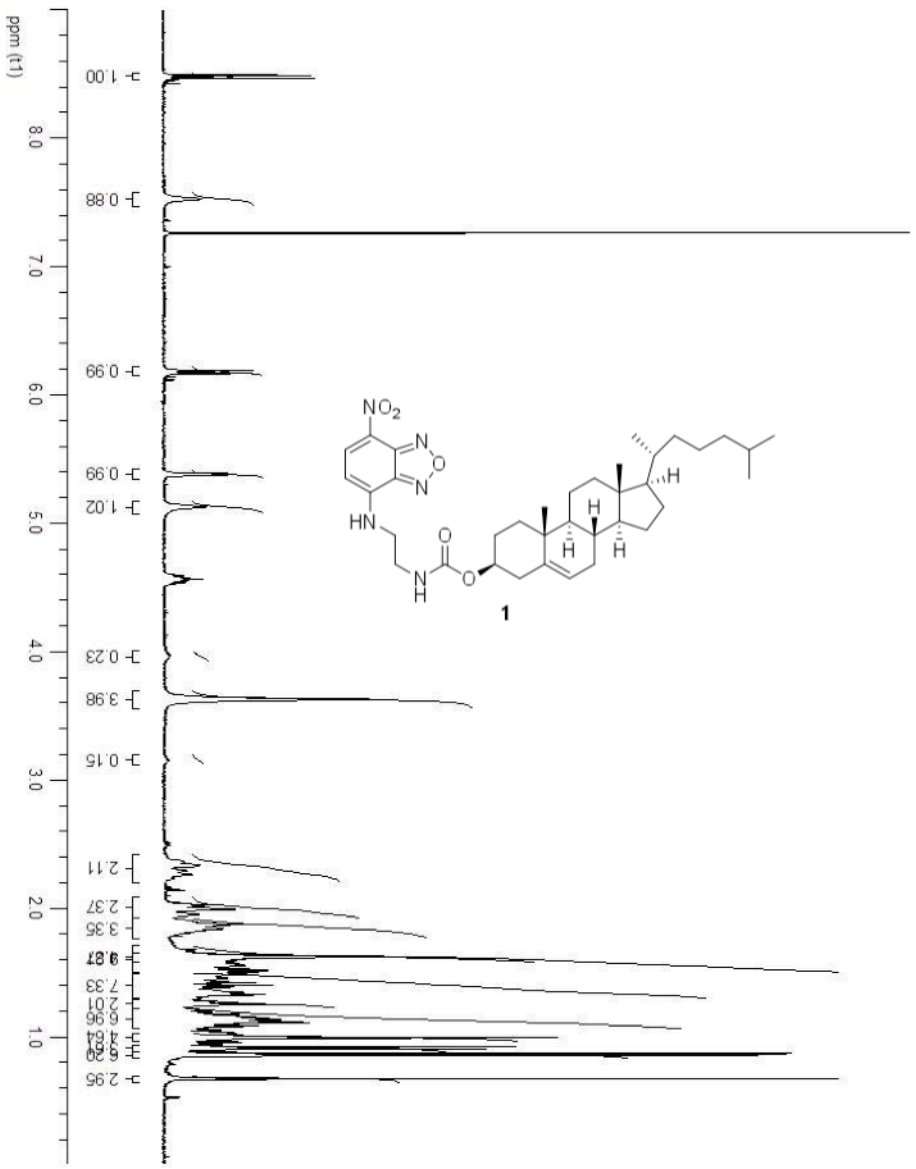
ppm (t1)
8.0
7.0
6.0
5.0
4.0
3.0
2.0
1.0
1.00
0.88
0.99
0.99
1.02
0.23
3.98
0.15
2.11
2.37
3.35
9.87
7.33
2.01
6.96
2.95
NO2
N
O
N
HN
O
N
H
O
H
H
H
H
1

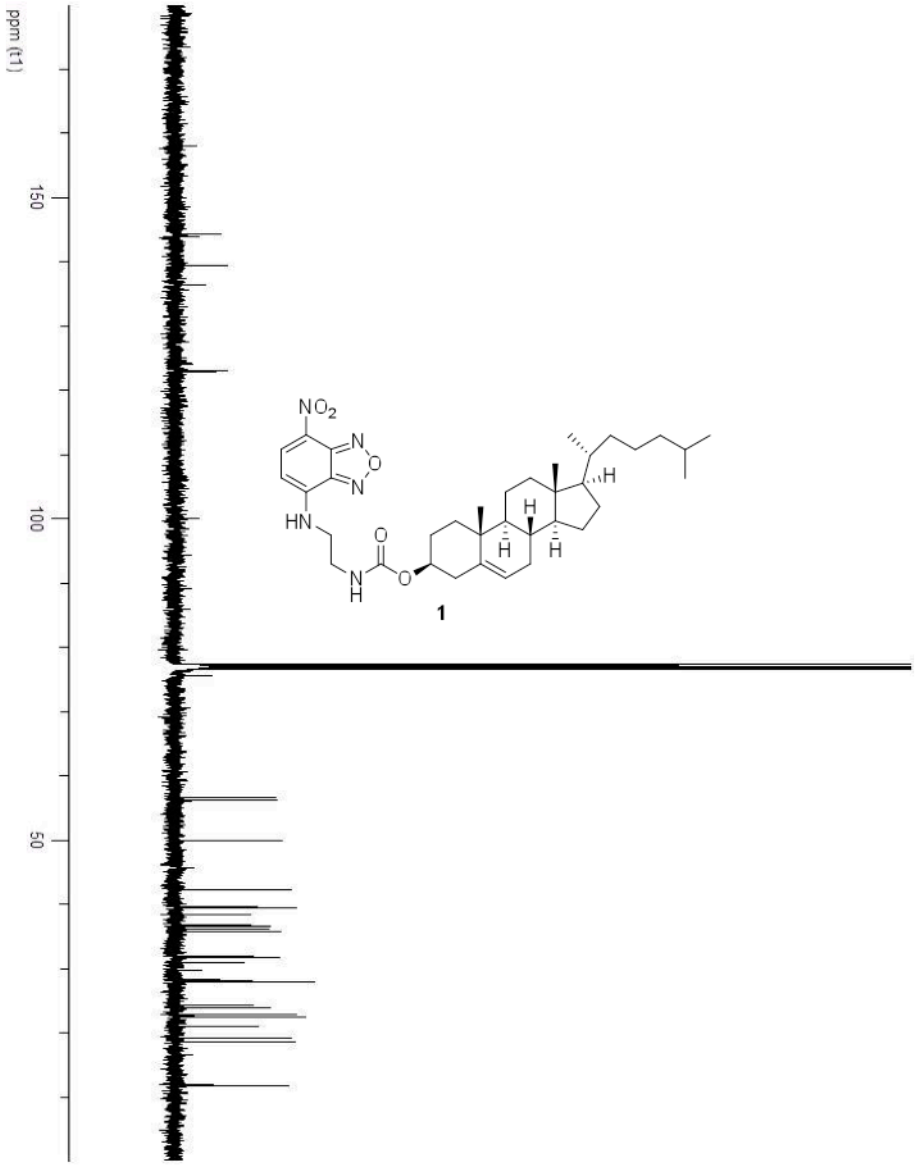
ppm (t1)
150
100
50
NO2
N
O
N
HN
O
O
N
H
H
H
H
1

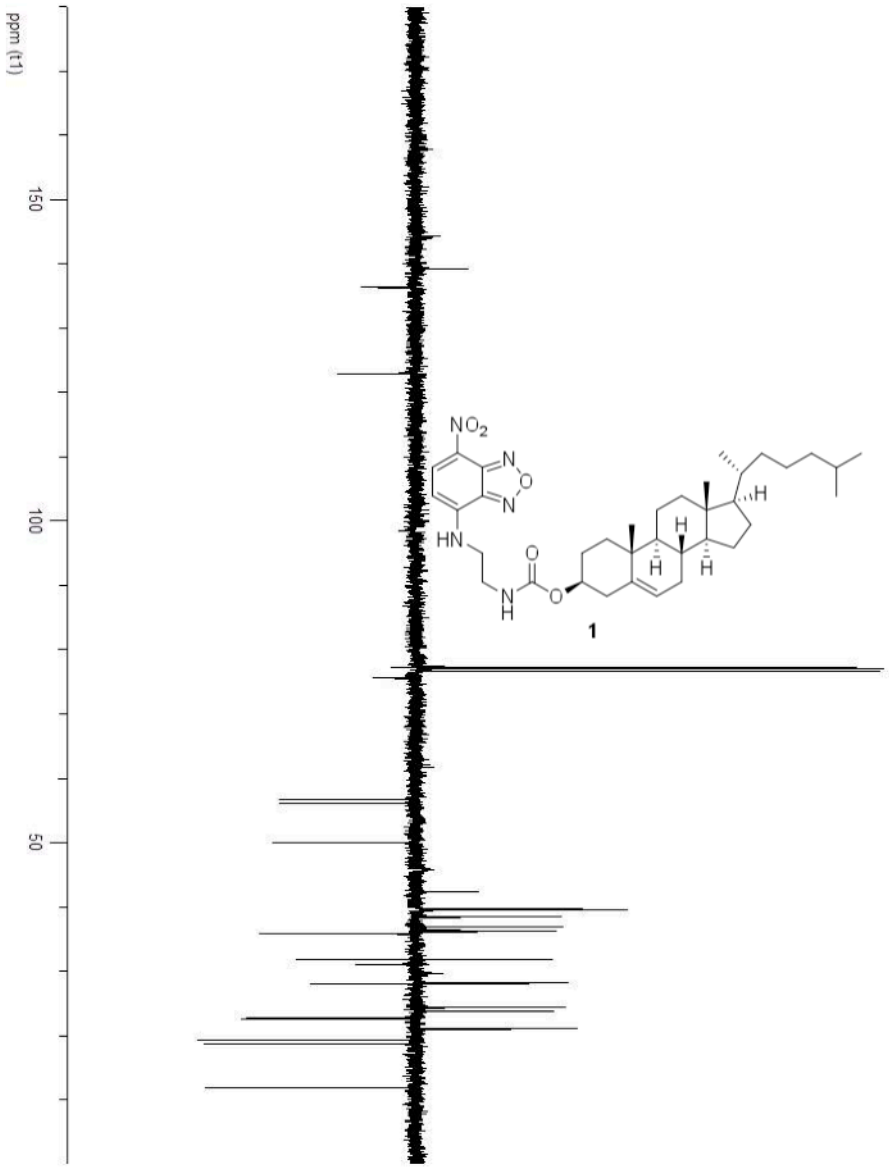
ppm (t1)
150
100
50
NO2
N
O
N
HN
O
NH
O
H
H
H
H
1

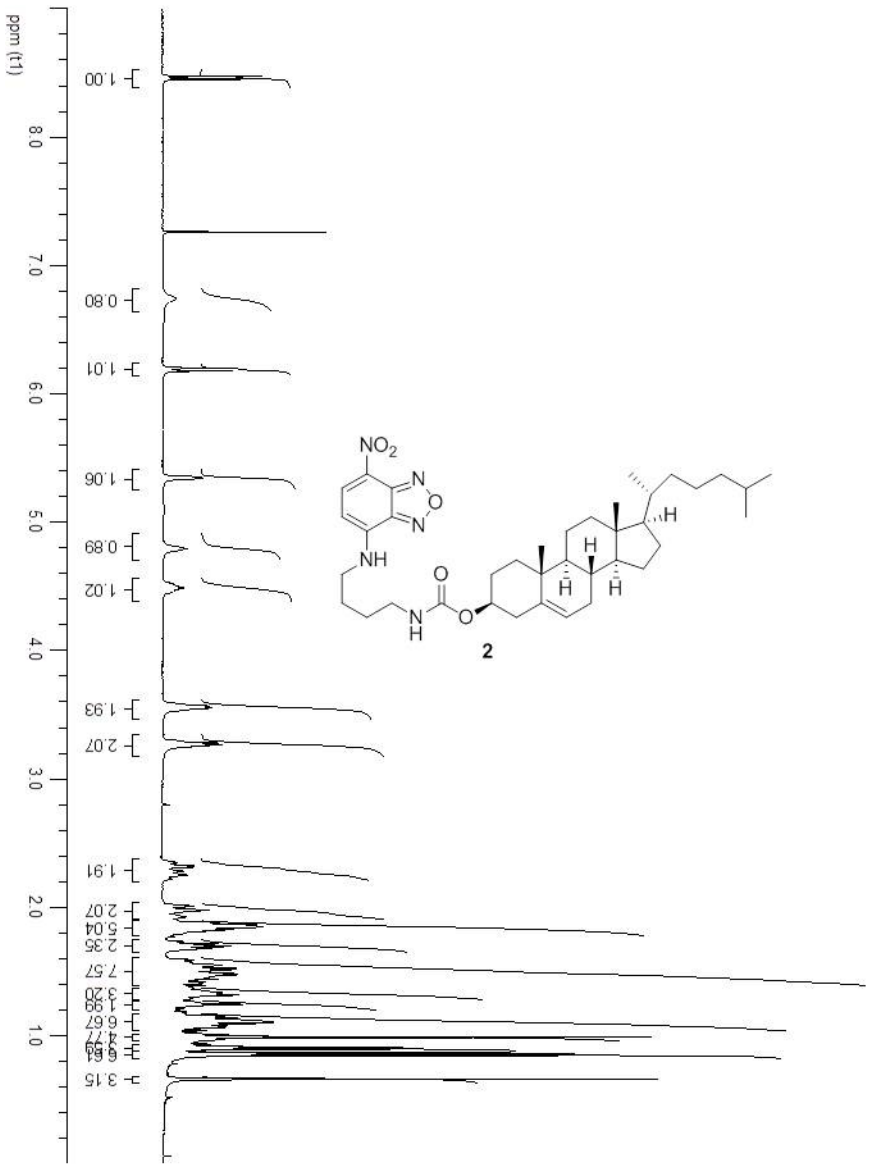
ppm (t1)
8.0
7.0
6.0
5.0
4.0
3.0
2.0
1.0
1.00
0.80
1.01
1.06
0.89
1.02
1.93
2.07
1.91
2.07
5.04
2.35
7.57
3.20
1.99
6.67
3.15
NO2
N
O
N
NH
O
N
H
O
H
H
H
H
2

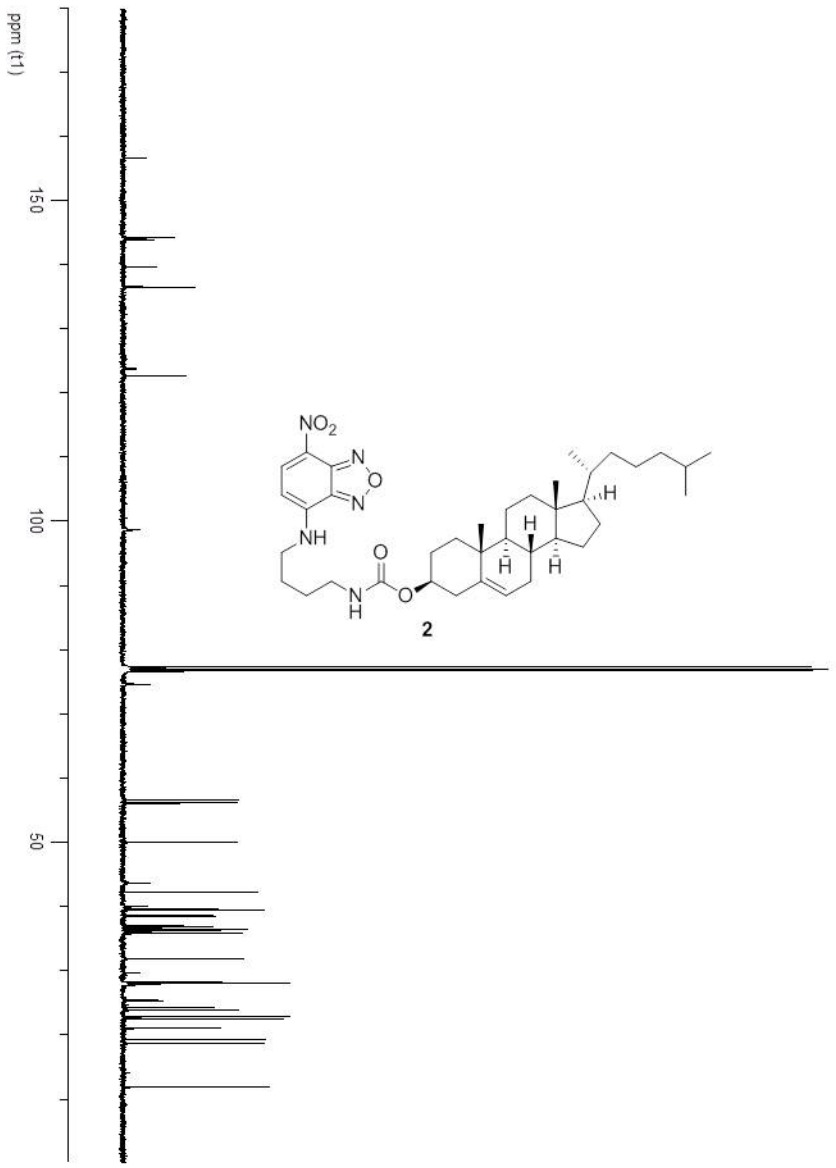
ppm (t1)
150
100
50
NO2
N
O
N
NH
O
N
H
O
H
H
H
H
2

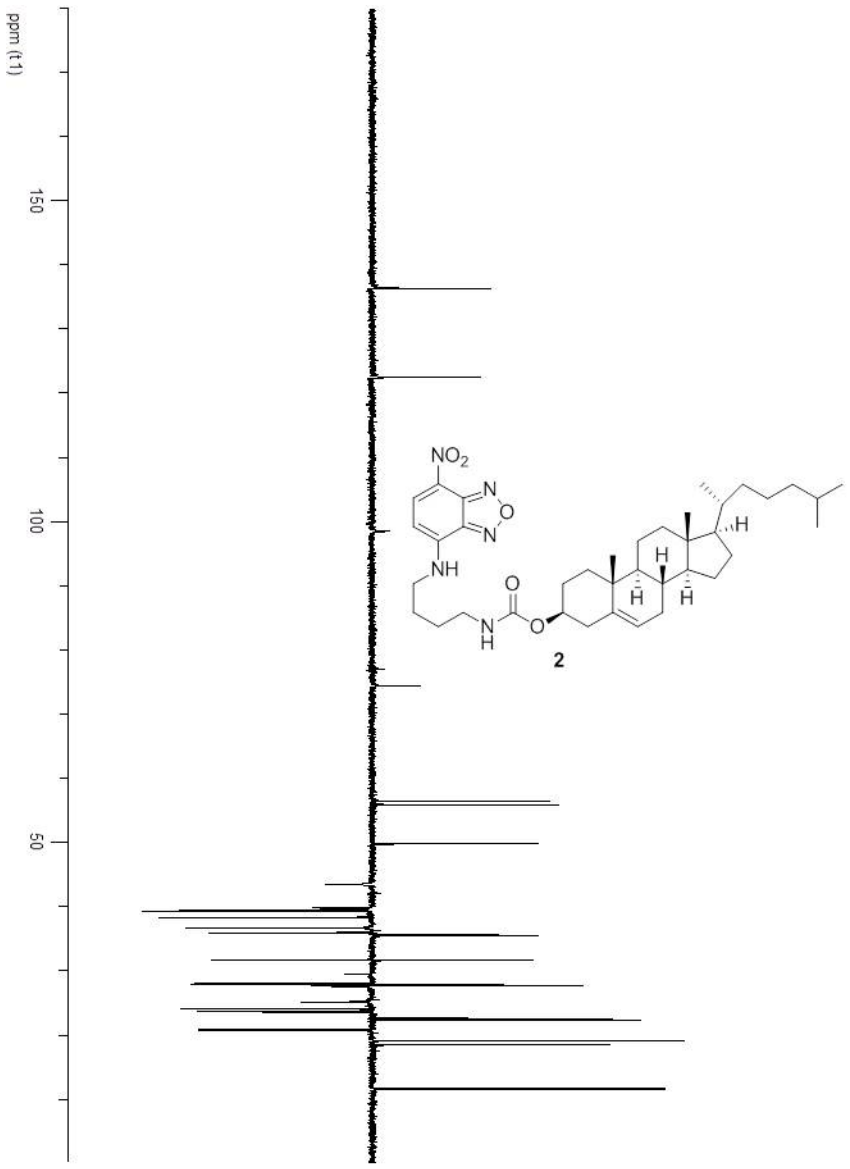
ppm (t1)
150
100
50
NO2
N
O
N
NH
O
N
H
O
H
H
H
H
2

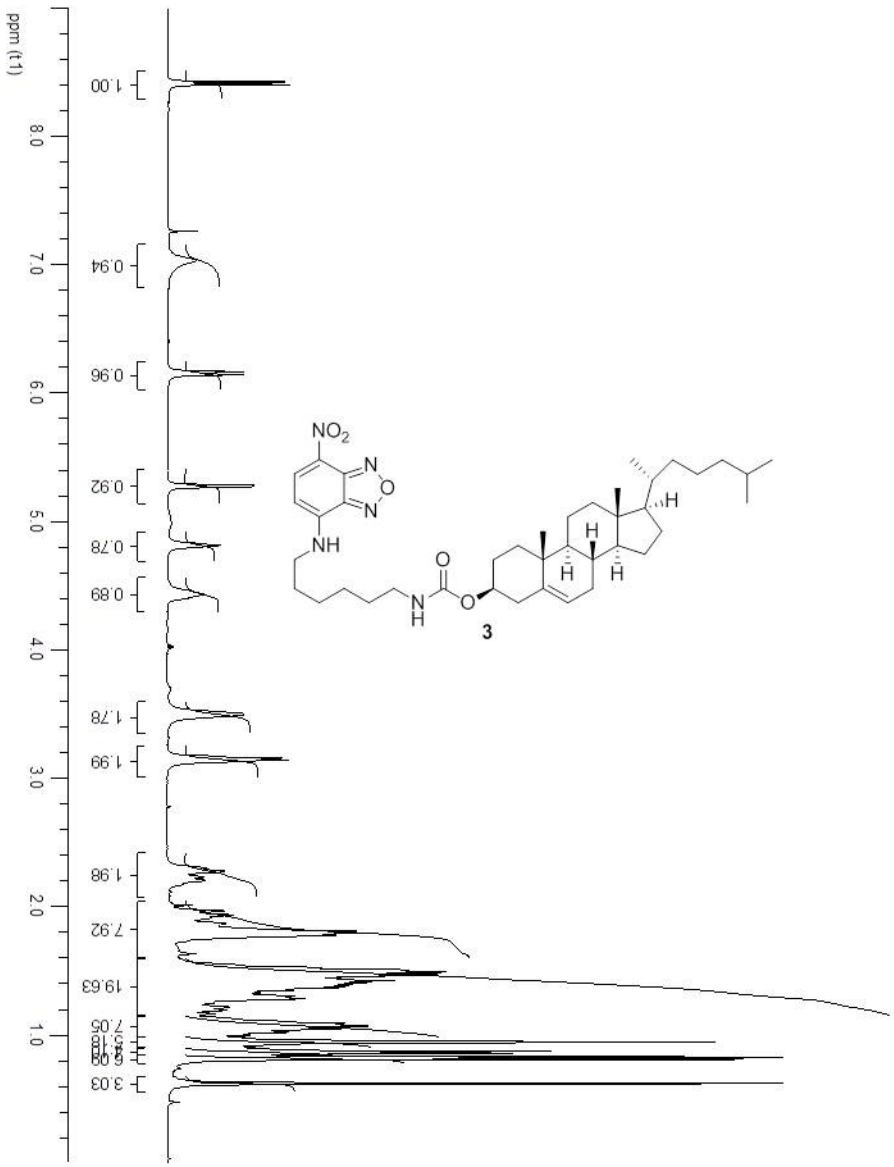
ppm (t1)
8.0
7.0
6.0
5.0
4.0
3.0
2.0
1.0
1.00
0.94
0.96
0.92
0.78
0.89
1.78
1.99
1.98
7.92
19.63
7.05
3.03
NO2
N
O
N
NH
O
N
H
O
H
H
H
H
3

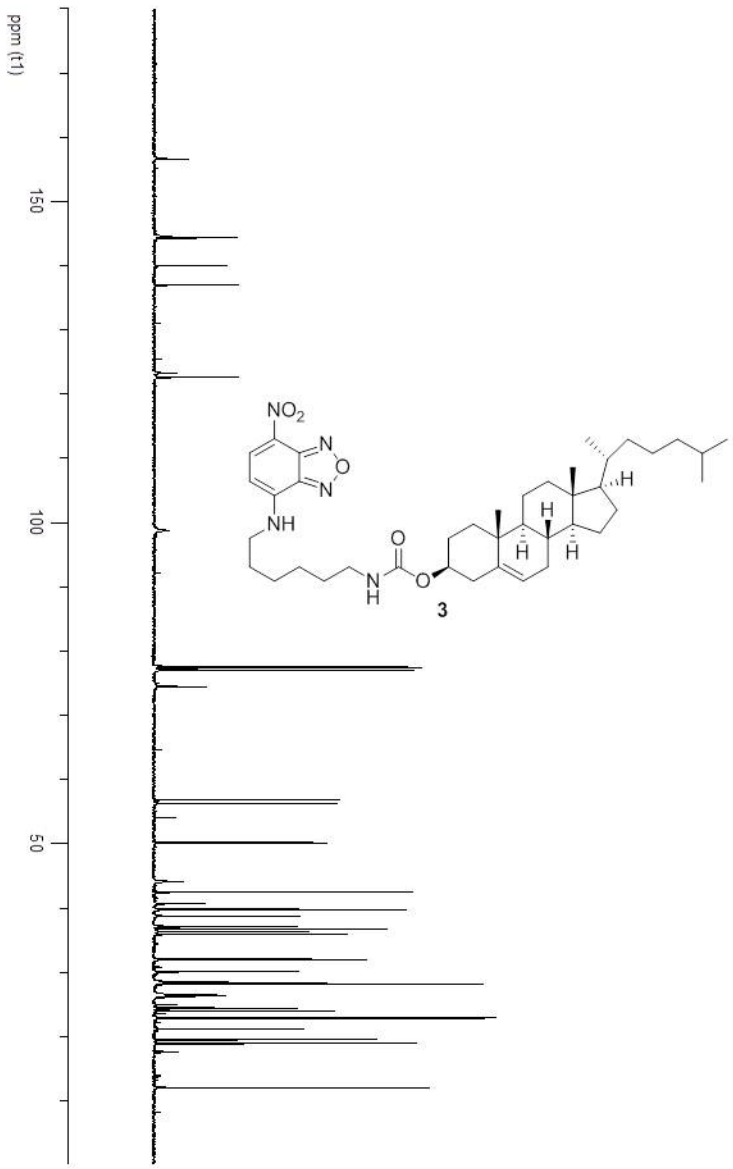
ppm (t1)
150
100
50
NO2
N
O
N
NH
O
N
H
O
H
H
H
H
3

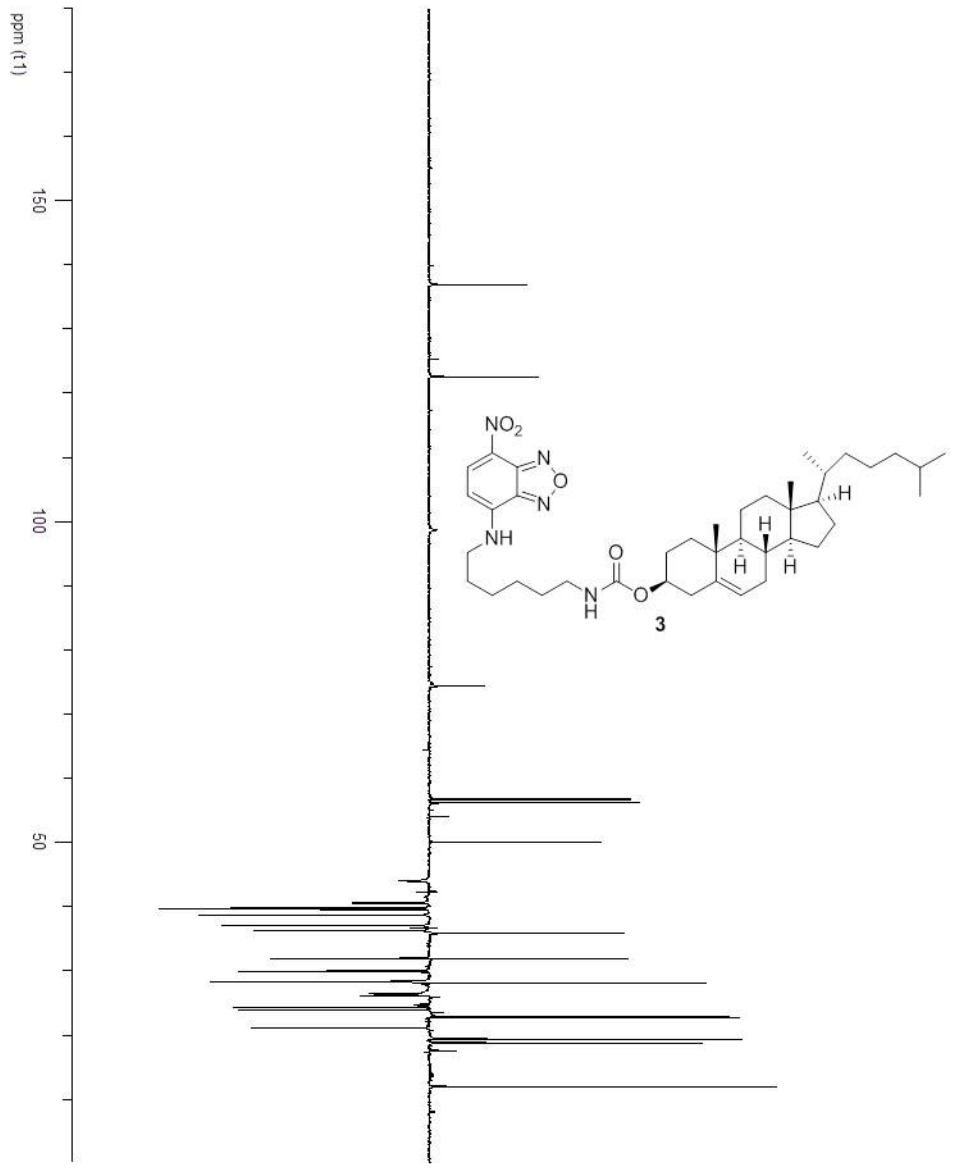
ppm (t1)
150
100
50
NO2
N
O
N
NH
O
N
H
O
H
H
H
H
3

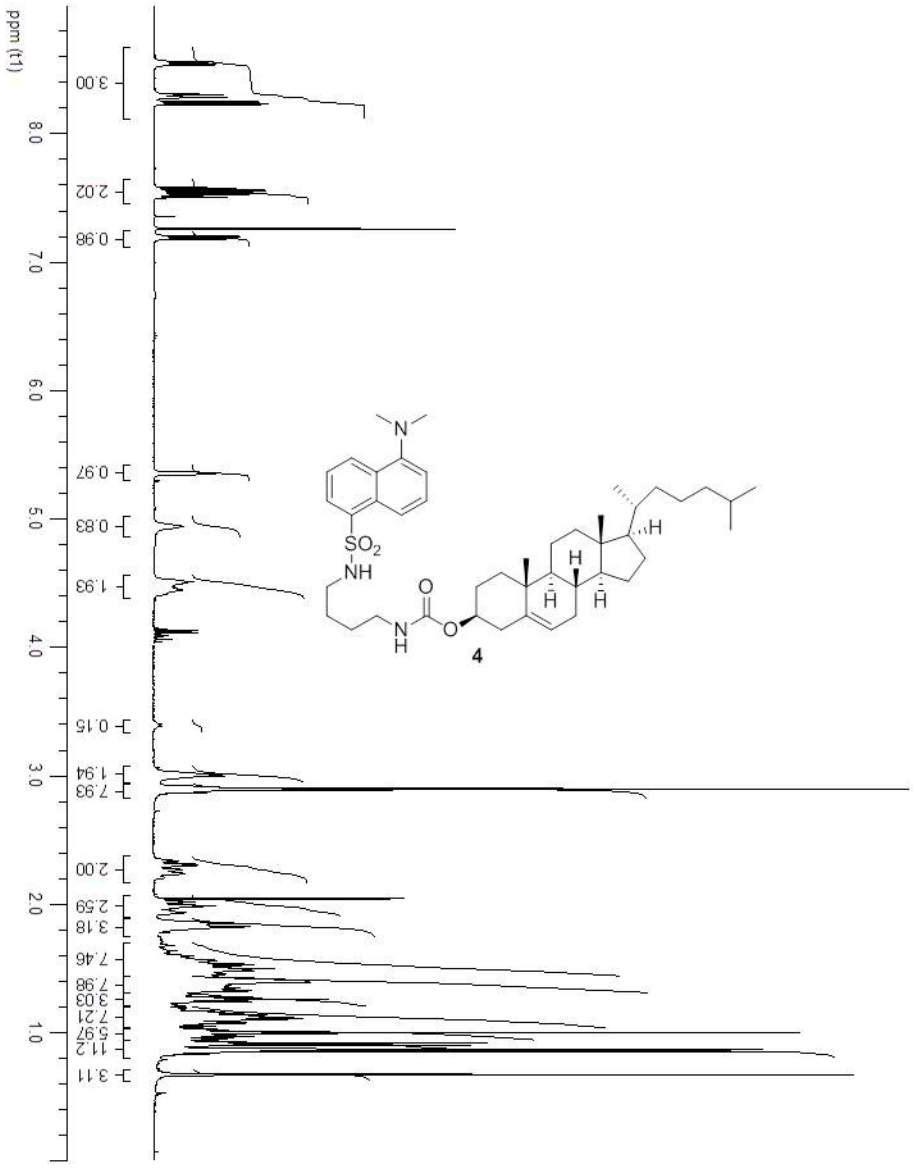
ppm (t1)
8.0
7.0
6.0
5.0
4.0
3.0
2.0
1.0
3.00
2.02
0.98
0.97
0.83
1.93
0.15
1.94
7.93
2.00
2.59
3.18
7.46
7.98
3.03
7.21
5.97
11.2
3.11
N
SO2
NH
O
N
H
O
H
H
H
H
4

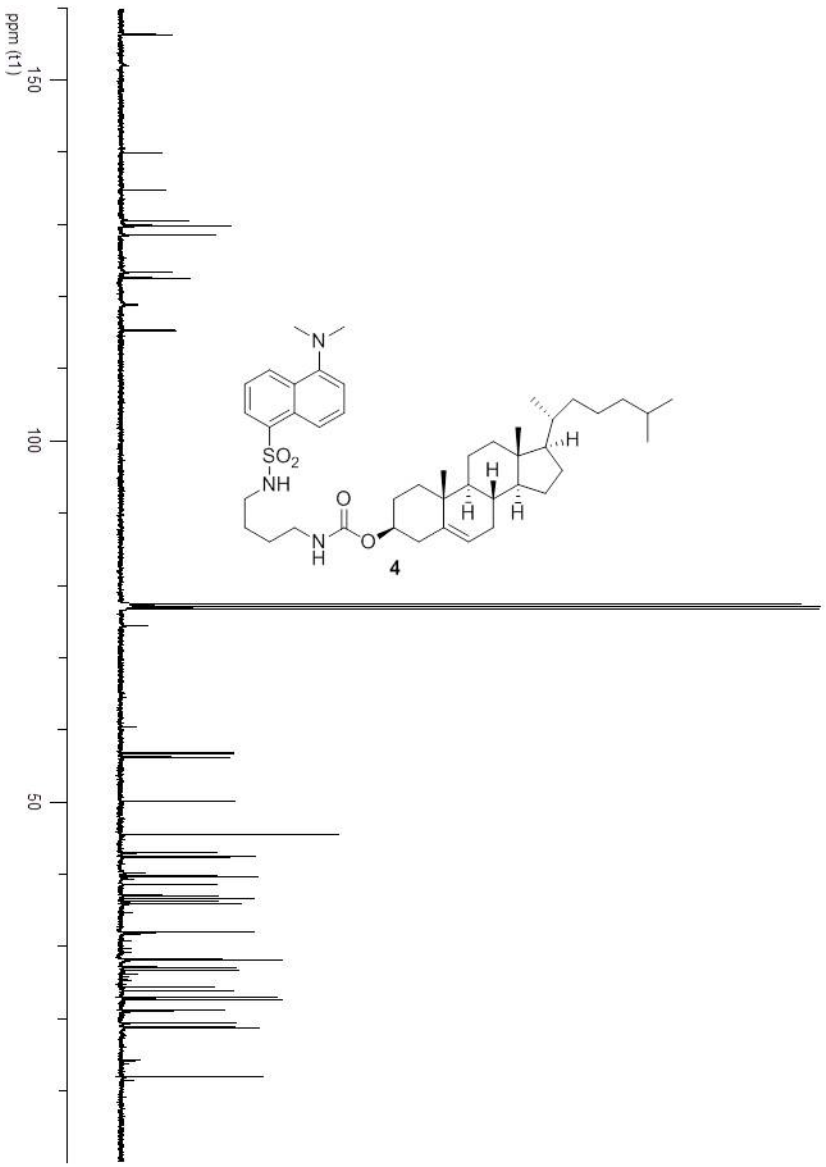
ppm (t1)
150
100
50
N
SO2
NH
O
N
H
O
H
H
H
H
4

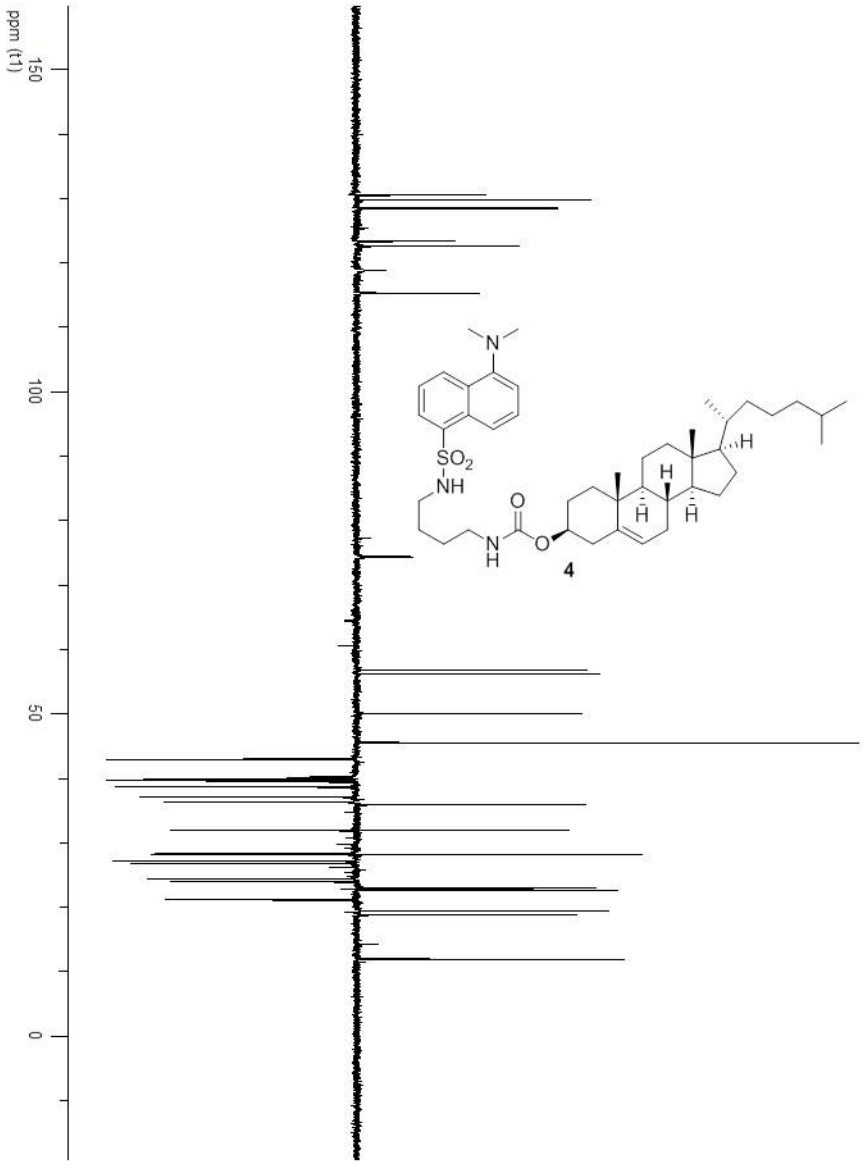
ppm (t1)
150
100
50
0
N
SO2
NH
O
N
H
O
H
H
H
H
4

Chapter 3 – ^{1}H and ^{13}C Spectra

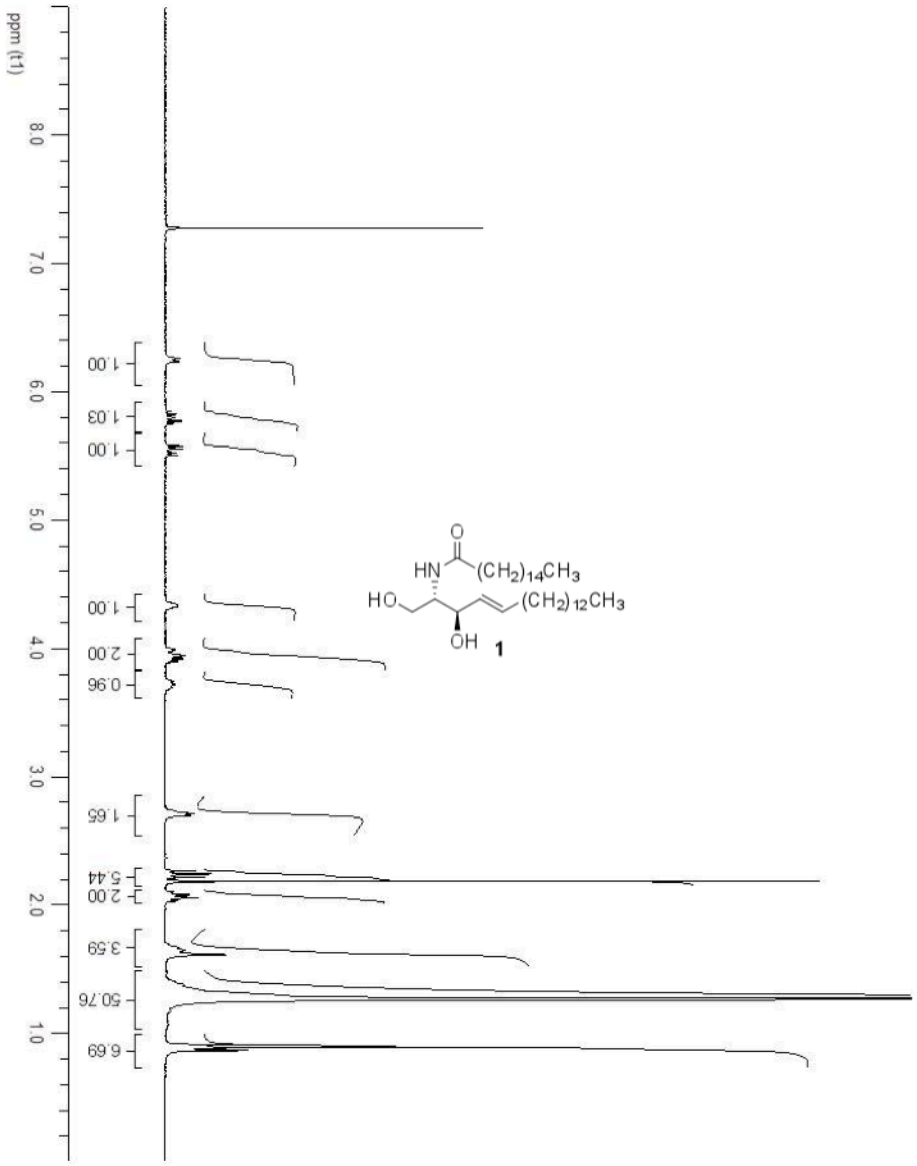
ppm (t1)
8.0
7.0
6.0
5.0
4.0
3.0
2.0
1.0
1.00
1.03
1.00
1.00
2.00
0.96
1.65
5.44
2.00
3.59
50.76
6.69
HN
O
(CH2)14CH3
HO
(CH2)12CH3
OH
1

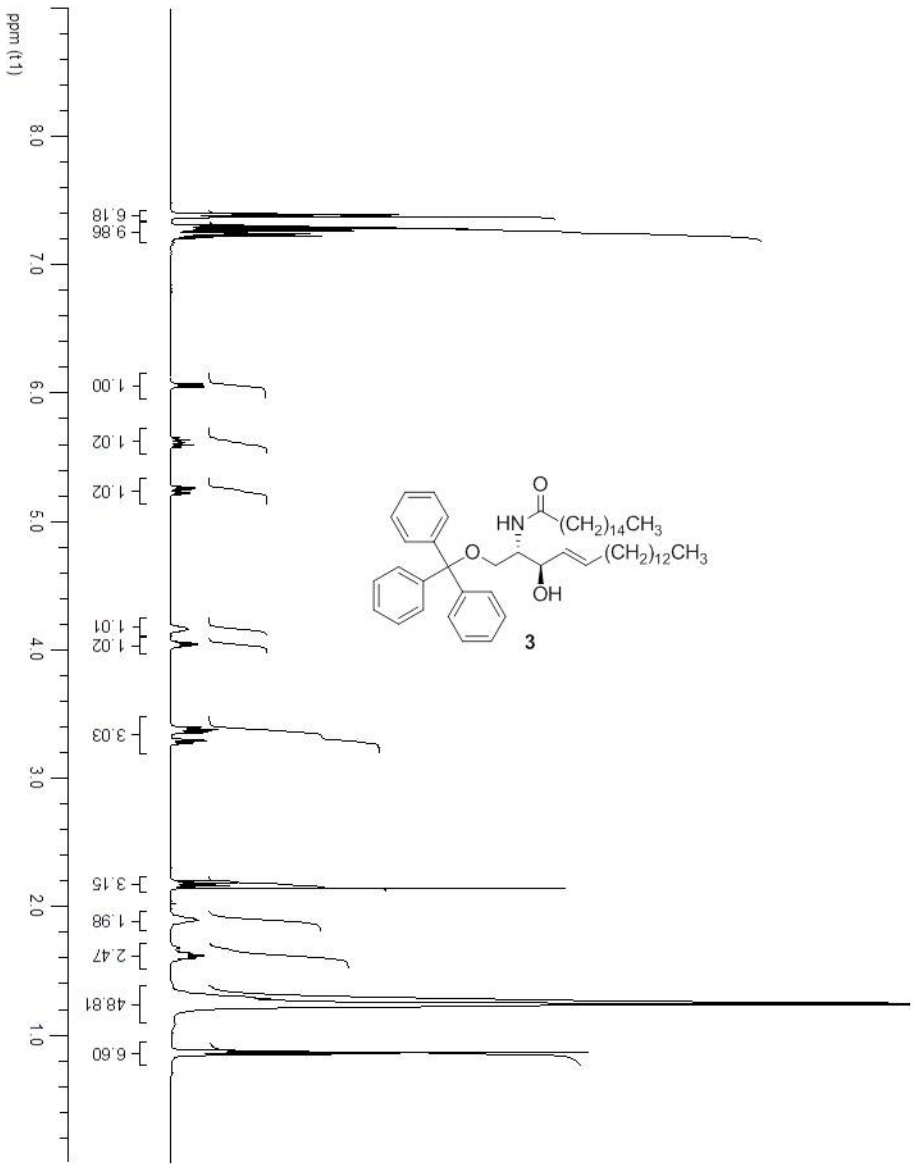
ppm (t1)
8.0
7.0
6.0
5.0
4.0
3.0
2.0
1.0
6.18
9.86
1.00
1.02
1.02
1.01
1.02
3.03
3.15
1.98
2.47
48.81
6.60
HN
O
(CH2)14CH3
O
(CH2)12CH3
OH
3

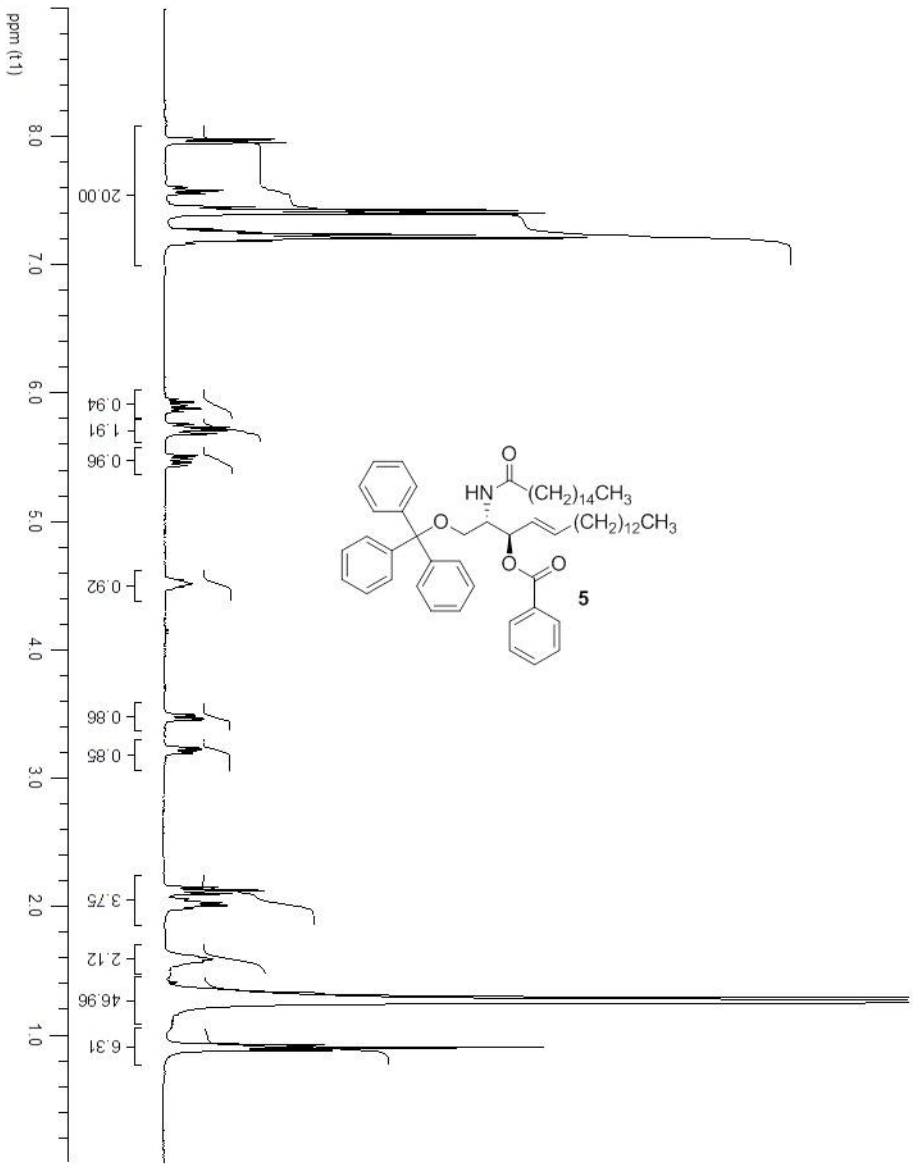
ppm (t1)
8.0
7.0
6.0
5.0
4.0
3.0
2.0
1.0
20.00
0.94
1.91
0.96
0.92
0.86
0.85
3.75
2.12
46.96
6.31
HN
O
(CH2)14CH3
(CH2)12CH3
O
O
O
5

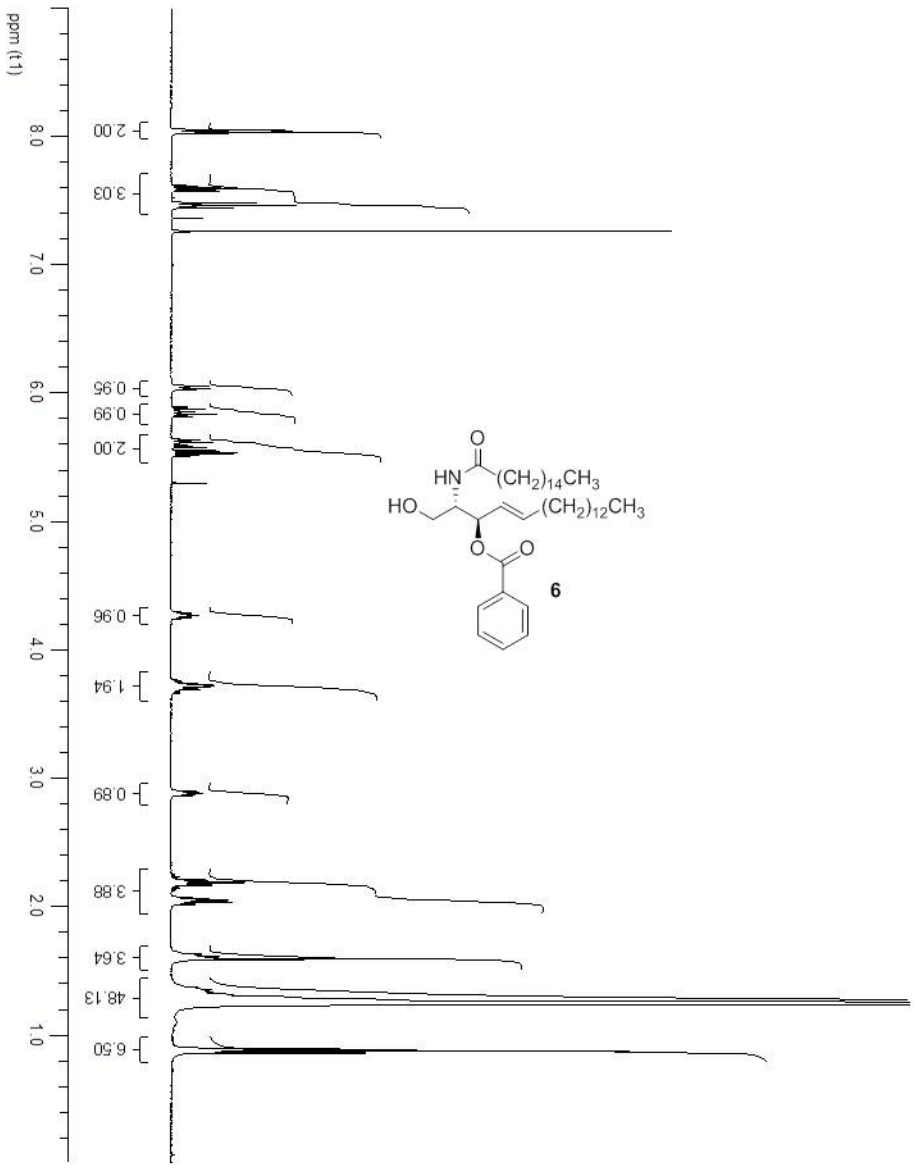
ppm (t1)
8.0
7.0
6.0
5.0
4.0
3.0
2.0
1.0
2.00
3.03
0.95
0.99
2.00
0.96
1.94
0.89
3.88
3.64
48.13
6.50
HN
(CH2)14CH3
HO
(CH2)12CH3
O
O
O
6

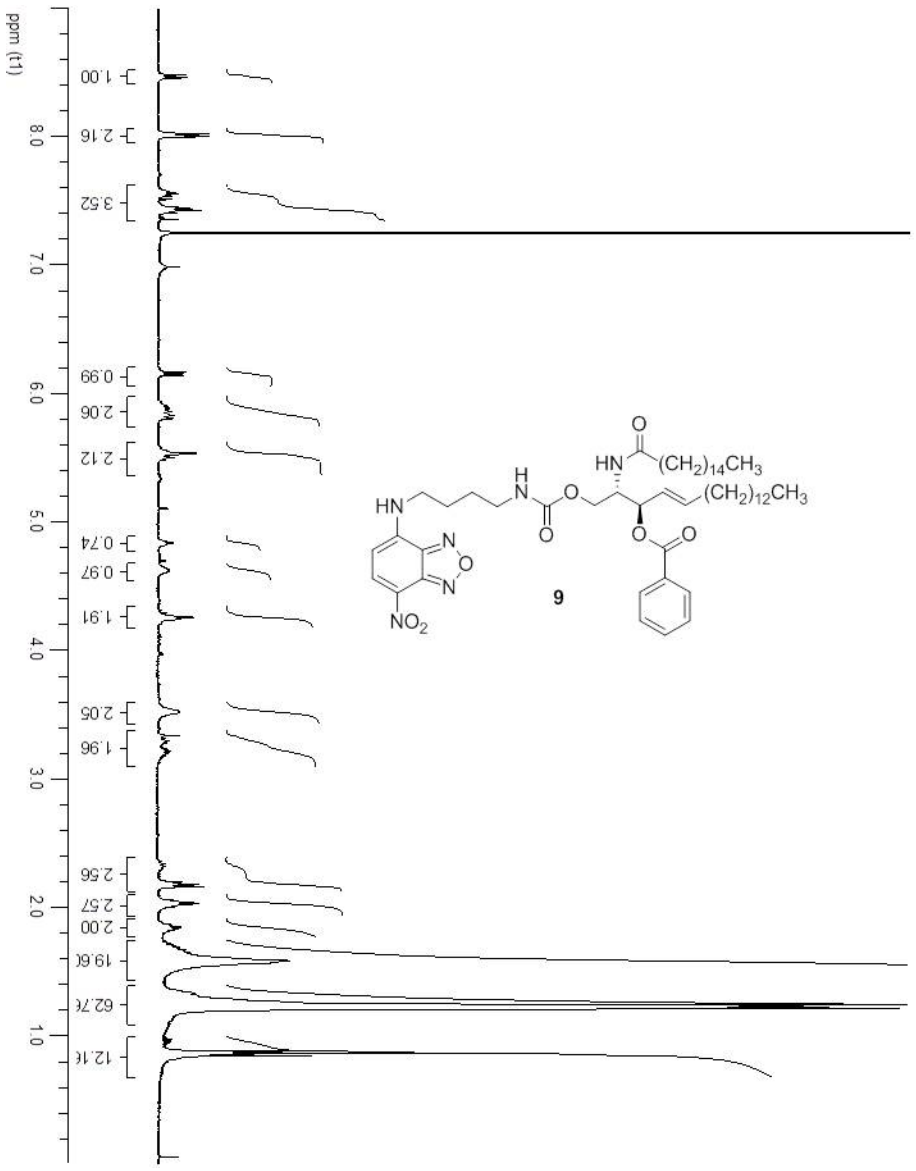
ppm (t1)
8.0
7.0
6.0
5.0
4.0
3.0
2.0
1.0
1.00
2.16
3.52
0.99
2.06
2.12
0.74
0.97
1.91
2.05
1.96
2.56
2.57
2.00
19.6
62.7
12.1
HN
N
O
N
NO2
H
N
O
O
HN
O
(CH2)14CH3
(CH2)12CH3
O
O
9

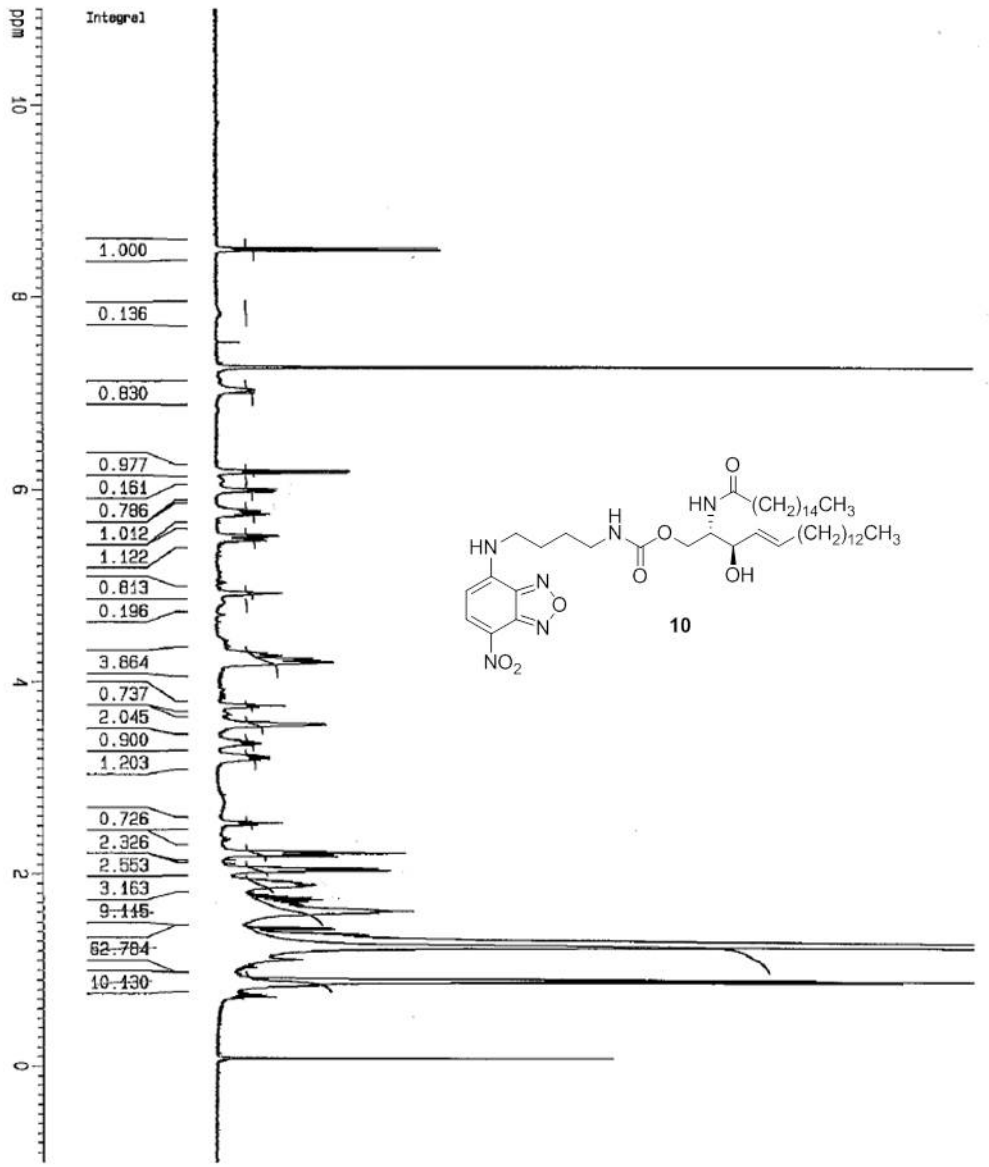
ppm
Integral
1.000
0.136
0.830
0.977
0.161
0.786
1.012
1.122
0.813
0.196
3.664
0.737
2.045
0.900
1.203
0.726
2.326
2.553
3.163
9.115
62.784
10.130
HN
NO2
N
O
N
H
N
O
O
HN
(CH2)14CH3
(CH2)12CH3
OH
10

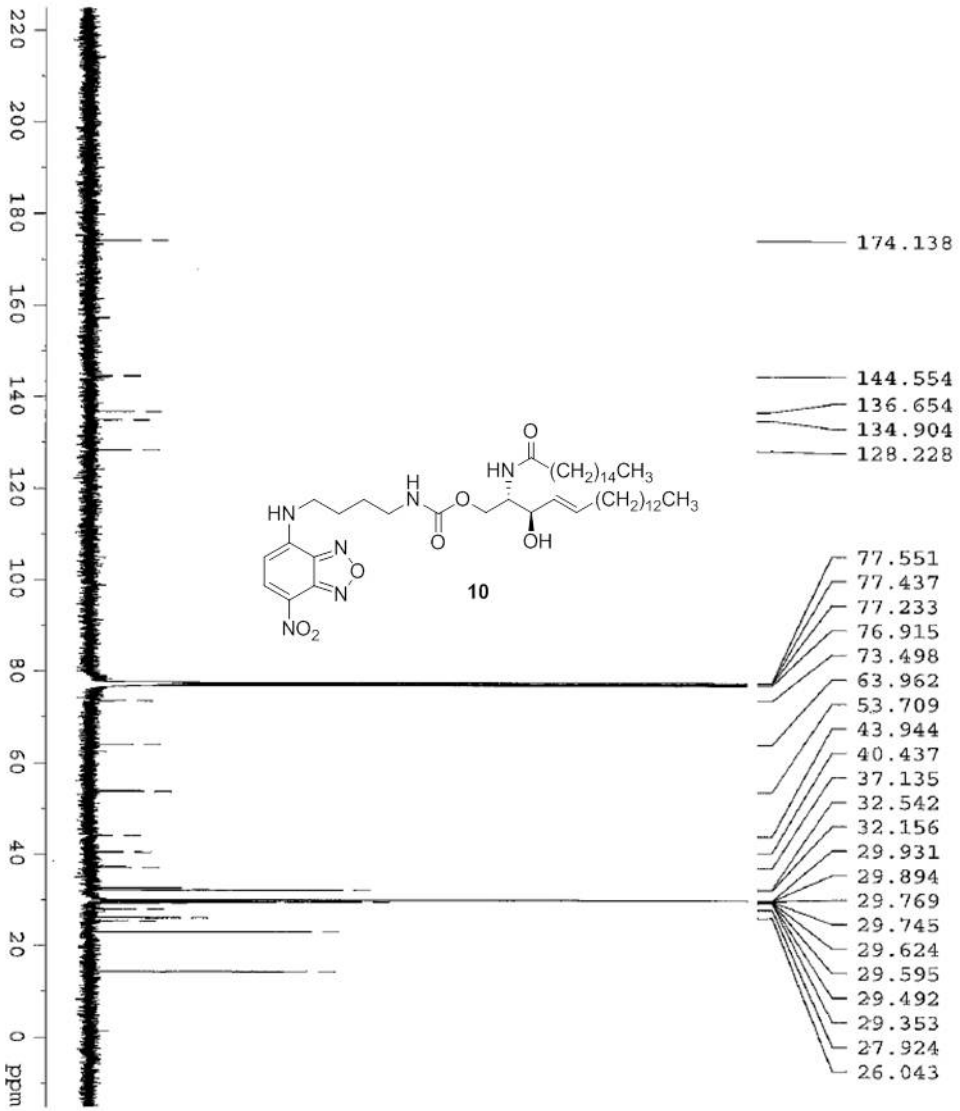
174.138
144.554
136.654
134.904
128.228
77.551
77.437
77.233
76.915
73.498
63.962
53.709
43.944
40.437
37.135
32.542
32.156
29.931
29.894
29.769
29.745
29.624
29.595
29.492
29.353
27.924
26.043
220
200
180
160
140
120
100
80
60
40
20
0
ppm
HN
H
N
O
HN
(CH2)14CH3
(CH2)12CH3
OH
N
O
N
NO2
10